Title
Bare Ice Hydrologic Processes on the Greenland Ice Sheet Ablation Zone

Author
Cooper, Matthew

Publication Date
2020

Peer reviewed|Thesis/dissertation

UNIVERSITY OF CALIFORNIA

Los Angeles

Bare Ice Hydrologic Processes on the Greenland Ice Sheet Ablation Zone

A dissertation submitted in partial satisfaction of the

requirements for the degree Doctor of Philosophy

in Geography

by

Matthew Cooper

2020

ABSTRACT OF THE DISSERTATION

Bare Ice Hydrologic Processes on the Greenland Ice Sheet Ablation Zone

by

Matthew Cooper

Doctor of Philosophy in Geography

University of California, Los Angeles, 2020

Professor Laurence Smith, Chair

The Greenland Ice Sheet is a major contributor to global sea level rise, with recent mass loss dominated by meltwater runoff from the ablation zone, i.e. areas of the ice sheet where annual mass losses exceed gains. In this zone, the winter snowpack melts entirely each summer exposing bare glacier ice. Observations of Greenland's ablation zone suggest the exposed bare ice surface is comprised of low-density ice termed "weathering crust" that may store meltwater, potentially reducing meltwater runoff export to surrounding oceans. Climate models are the primary tools used to forecast future Greenland mass loss, but these models treat the ablation zone as impermeable high-density ice with no meltwater retention capacity. Recent evidence suggests that climate models overpredict meltwater runoff from the ablation zone, which may be linked to weathering crust presence, but diagnosing climate model predictions is difficult because observations of meltwater runoff on the ice sheet surface are extremely rare and weathering crust

presence is undocumented. This dissertation presents the results of four investigations that address this problem by pairing field observations of hydrologic and radiative properties of bare ice collected in Greenland's ablation zone with numerical modeling and analysis of climate model output. The results of these investigations reveal the presence of low-density weathering crust on Greenland's bare ice ablation zone surface and the potential for non-trivial meltwater runoff retention within weathering crust on Greenland's bare ice ablation zone surface. New estimates of spectral radiation attenuation coefficients are quantified and directly applied to a numerical model of spectral and thermodynamic heat transfer in bare ice. This model successfully simulates meltwater runoff from a supraglacial catchment on Greenland's southwest ablation zone surface. Model results suggest that nocturnal refreezing of meltwater stored within weathering crust occurs in Greenland's ablation zone, potentially reducing runoff up to 32% on annual timescales. These findings imply a reinterpretation of refreezing on bare ice as an important control on Greenland's ablation zone surface mass balance and the need to represent this process in climate model predictions of future Greenland mass loss.

The dissertation of Matthew Cooper is approved.

Dennis P. Lettenmaier

Gregory S. Okin

Steven A. Margulis

Laurence Smith, Committee Chair

University of California, Los Angeles

2020

In memory of my mother

TABLE OF CONTENTS

LIST OF FIGURES

LIST OF TABLES

Acknowledgements

Foremost I thank Alexis for her love, patience, and support. I am grateful to have found my partner in life and adventure, who makes the hard work easy and the future bright. I thank my family and friends for their patience and support and for all the fun times during this challenging but rewarding journey. I am grateful for the enthusiasm and generous sharing of ideas from my lab mates Lincoln Pitcher, Kang Yang, Jonathan Ryan, Jessica Fayne, Ethan Kyzivat, Sarah Cooley, Katia Lezine, Mia Bennett, Colin Gleason, and Vena Chu. I thank Clement Miège, Rick Forster, Steve Munsell, Jonathan Ryan, Sarah Cooley, Sasha Leidman, Rohi Muthyala, Charlie Kershner, Brandon Overstreet, Åsa Rennermalm, Samiah Moustafa, Dirk van As, and Marco Tedesco for their help in the field. I thank Kathy Young and the Polar Field Services staff for making our field work possible. I thank Glen Liston for providing his numerical model of ice melt and for hosting me at the Cooperative Institute for Research in the Atmosphere. To the people of Kalaallit Nunaat *Qujanarsuaq*.

I am grateful for the assistance of Kasi McMurray, Matt Zebrowski, Brian Won, Jenée Misraje, and the Department of Geography staff without whom I could not complete this dissertation. I acknowledge financial support from the UCLA Department of Geography, UCLA Graduate Research Mentorship Program, UCLA Department of Geography Travel Grant, and a NASA Earth and Space Science Fellowship. I thank my committee members Dennis Lettenmaier, Greg Okin, and Steve Margulis for overseeing my PhD and for their valuable insight and mentorship. Finally, I express my gratitude to my advisor, Laurence Smith, for his unconditional support of my curiosity, for providing the opportunity to pursue novel, exciting, and important research questions, and most of all for his constant reminder to set my own course and to think differently.

Chapter One is a version of Cooper and Smith (2019). M.G. Cooper and L.C. Smith designed the study. M.G. Cooper wrote the manuscript. L.C. Smith edited the manuscript. This study was funded by the NASA Cryosphere Program grant 80NSSC19K0942 (P.I. Laurence C. Smith), managed by Dr. Colene Haffke, and a graduate fellowship from the NASA Earth and Space Sciences Fellowship Program managed

by Dr. Lin Chambers. The authors thank the Polar Geospatial Center, University of Minnesota, for providing WorldView Imagery© 2018 DigitalGlobe, Inc, Jonathan Ryan, Brown University, for providing Figure 1-9, and the many public and private agencies, universities, and scientists who provided satellite data, processed datasets, and image processing tools that contributed to this work.

Chapter Two is a version of Cooper et al. (2020). M.G. Cooper and L.C. Smith designed the experiment. M.G. Cooper, Å.K. Rennermalm, M. Tedesco, R. Muthyala, S.Z. Leidman, and S.E. Moustafa collected the field data. M.G. Cooper performed the data analysis and wrote the manuscript. L.C. Smith, Å.K. Rennermalm, M. Tedesco, S.Z. Leidman, and J.V. Fayne edited the manuscript. This project was funded by the NASA Cryosphere Program grant 80NSSC19K0942 (P.I. Laurence C. Smith), managed by Dr. Colene Haffke and Dr. Thomas P. Wagner and a graduate fellowship from the NASA Earth and Space Sciences Fellowship Program managed by Dr. Lin Chambers. We thank Polar Field Services for their field support.

Chapter Three is a version of Cooper et al. (2018). Author contribution: M.G. Cooper, L.C. Smith, and Å.K. Rennermalm designed the experiment. M.G. Cooper, C. Miège, Å.K. Rennermalm, L. H Pitcher, J. Ryan, and S. Cooley collected the field data. J. Ryan assisted with Unmanned Aerial System image processing. M.G. Cooper performed the data analysis. M.G. Cooper wrote the manuscript with contributions from all authors. This project was funded by the NASA Cryosphere Program grant NNX14AH93G (P.I. Laurence C. Smith) managed by Dr. Thomas P. Wagner. We thank Professor Robert Hawley of Dartmouth University for the generous lending of the shallow ice corer. We thank Polar Field Services for their field support, Charlie Kershner (George Mason University), Brandon Overstreet (University of Wyoming), Sasha Leidman (Rutgers University), and Rohi Muthyala (Rutgers University) for their field work assistance. We thank Matt Zebrowski (UCLA) for figure production assistance. Data from the Programme for Monitoring of the Greenland Ice Sheet (PROMICE) and the Greenland Analogue Project (GAP) were provided by the Geological Survey of Denmark and Greenland (GEUS) at http://www.promice.dk.

Chapter Four is a version of Cooper et al. (2020; in prep). The numerical model used in this study is available as Matlab© code at https://github.com/mguycooper/icemodel. This project was funded by the NASA Cryosphere Program grant 80NSSC19K0942 (P.I. Laurence C. Smith), managed by Dr. Thorsten Markus, and a graduate fellowship from the NASA Earth and Space Sciences Fellowship Program managed by Dr. Lin Chambers. We thank Polar Field Services for their field support. We thank Dr. Glen E. Liston (Cooperative Institute for Research in the Atmosphere) for providing his numerical model of ice melt.

Curriculum Vitae
MATTHEW GUY COOPER

EDUCATION

2018 **C.Phil.** Geography, University of California, Los Angeles
2015 **M.S.** Water Resources Science, Oregon State University
2008 **B.A.** Environmental Studies, University of California, Santa Cruz

AWARDS & HONORS

2017–20 Earth Science Fellow, National Aeronautics and Space Administration ($125,000)
2018 Outstanding Student Publication, UCLA Department of Geography ($500)
2017 Research Travel Grant, UCLA Department of Geography ($5000)
2016 Graduate Research Fellow, UCLA Graduate Division ($36,000)
2014 Outstanding Conference Presentation, OSU Water Resources Graduate Program ($500)
2009–11 President's List, College of the Sequoias
2003–08 Honor's Program, University of California, Sana Cruz

PUBLICATIONS (5 selected)

2020 **COOPER M.G.**, SMITH L.C., RENNERMALM Å.K., TEDESCO M., MUTHYALA R., LEIDMAN S.Z., MOUSTAFA S.E., AND FAYNE J.V. Spectral measurements of light attenuation in Greenland Ice Sheet bare ice suggest shallower subsurface radiative heating and ICESat-2 penetration depth in the ablation zone *The Cryosphere Discussions* https://doi.org/10.5194/tc-2020-53

2019 **COOPER M.G.** AND L.C. SMITH Satellite remote sensing of the Greenland Ice Sheet ablation zone: a review *Remote Sensing* **11** 2405 https://doi.org/10.3390/rs11202405

2018 **COOPER M.G.**, SCHAPEROW J.R., COOLEY S.W., ALAM S., SMITH L.C. AND LETTENMAIER D.P. Climate elasticity of low flows in the maritime western U.S. mountains *Water Resources Research* **54** 5602–19 https://doi.org/10.1029/2018WR022816

2018 **COOPER M.G.**, SMITH L.C., RENNERMALM Å.K., MIÉGE C., PITCHER L.H., RYAN J.C., YANG K., AND COOLEY S.W. Meltwater storage in low-density near-surface bare ice in the Greenland ice sheet ablation zone *The Cryosphere* **12** 955–70 https://doi.org/10.5194/tc-12-955-2018

2016 **COOPER M.G.**, NOLIN A.W., AND SAFEEQ M. Testing the recent snow drought as an analog for climate warming sensitivity of Cascades snowpacks *Environmental Research Letters* **11** 84009 https://doi.org/10.1088/1748-9326/11/8/084009

THESES

2015 **COOPER M.G.** Modeling elevation-dependent snow sensitivity to climate warming in the data sparse eastern Oregon Cascades, Master of Science, Oregon State University, Corvallis, OR https://ir.library.oregonstate.edu/concern/graduate_thesis_or_dissertations/wm117s33w

TEACHING

2015 Teaching Assistant, University of California, Los Angeles, Department of Geography
2013–15 Teaching Assistant, Oregon State University, Department of Geography
2010–12 Tutor, Calculus and Chemistry, College of the Sequoias, Visalia, CA
2010–12 Tutor, Mathematics, Success in Reading and Math, Visalia, CA

MENTORSHIP

2018–19 Jack Miller, undergraduate researcher, University of California, Los Angeles
2016–17 Wyeth Binder, undergraduate researcher, University of California, Berkeley

LEADERSHIP

2017 Expedition lead, Greenland Ice Sheet, NASA Cryosphere Program
2015–20 Wilderness First Responder, National Outdoor Leadership School
2018 Expedition participant, Greenland Ice Sheet, Lamont Doherty Earth Observatory (courtesy Dr. Marco Tedesco)
2015–18 Expedition participant, Greenland Ice Sheet, NASA Cryosphere Program
2015–17 Event Leader, Sierra Mountaineering Club

EMPLOYMENT

2011–12 Field Technician III, Sierra Nevada Research Institute, UC Merced
2009–11 Field Technician II, Sierra Nevada Research Institute, UC Merced
2006–08 GIS Student Worker III, County of Santa Cruz, Department of Public Works

TECHNICAL REPORTS

2020 **COOPER M.G.**, SMITH L.C., RENNERMALM Å.K., TEDESCO M., MUTHYALA R., LEIDMAN S.Z., MOUSTAFA S.E., AND FAYNE J.V. Optical attenuation coefficients of glacier ice from 350–700 nm *PANGAEA* https://doi.pangaea.de/10.1594/PANGAEA.913508

2018 **COOPER M.G.**, SMITH L.C., RENNERMALM Å.K., PITCHER L.H., RYAN J.C., YANG K. AND COOLEY S.W. Direct measurements of ice density at 1m depth in the Greenland Ice Sheet ablation zone during July 2016 from shallow ice cores *PANGAEA* https://doi.pangaea.de/10.1594/PANGAEA.886748

2015 NOLIN A.W., GRANT G.E., SAFEEQ M., LEWIS S.L., **COOPER M.G.**, AND HEMPEL L.A. Climate change and peak flows: knowledge-to-action to help managers address impacts on streamflow dynamics and aquatic habitat, Northwest Climate Science Center, University of Washington, USA https://www.sciencebase.gov/catalog/item/566edcbbe4b09cfe53ca76b5

SERVICE

2020 Mentor: Mathematics, Engineering, and Science Achievement (MESA), Portland, OR
2011–20 Member: American Geophysical Union
2012–15 Member: Hydrophiles, American Water Resources Association
2010–12 Member: Mathematics, Engineering, and Science Achievement (MESA), College of the Sequoias, Visalia, CA, https://www.cos.edu/mesa
2019–20 Expert review: Geophysical Research Letters, Journal of Hydrology, Remote Sensing of Environment, Remote Sensing, Hydrology and Earth System Sciences
2016 Expert review: Workshop on Observing and Modeling Meltwater Retention Processes in Snow and Firn on Ice Sheets and Glaciers, Geological Survey of Denmark
2014–15 Webmaster: Hydrophiles, American Water Resources Association
2014–15 Event Planner, Pacific Northwest Water Research Symposium, Corvallis, OR
2008 Event Planner, Snapshot Day, Coastal Watershed Council, Santa Cruz, CA
2017–18 Top Writer, Quora, Climate Change, (280k answer views, 8.8k answer upvotes)
2013–20 Contributing Writer, Quora, Climate Change, Hydrology, Atmospheric Sciences

Introduction

Meltwater runoff now accounts for over half of Greenland's contribution to global sea level rise, of which at least 85% originates as melting bare ice on the ablation zone surface (van den Broeke et al., 2016; Machguth et al., 2016; Steger et al., 2017). In the ablation zone, the winter snowpack melts entirely each summer, exposing dark bare glacier ice that absorbs up to three times as much solar radiation as bright snow, owing to its low albedo and melt albedo feedbacks (Box et al., 2012; Ryan et al., 2019). In recent decades, the area of exposed bare ice on Greenland has expanded by up to 50%, driving increased surface melt on the Greenland ablation zone (Bevis et al., 2019; Cooper and Smith, 2019; Noël et al., 2019; Ryan et al., 2019; Tedesco et al., 2011). The full implications of Greenland's enhanced melting for sea level depends on whether this meltwater escapes to surrounding oceans (Harper et al., 2012; Pfeffer et al., 1991). Understanding the processes that control meltwater runoff from the Greenland Ice Sheet bare-ice ablation zone is therefore critical for accurate sea level predictions (MacFerrin et al., 2019; Smith et al., 2015).

Meltwater runoff generated on bare ice is thought to contribute in its entirety to sea level (Steger et al., 2017). This assumption is reflected in global and regional climate models that treat bare ice as a uniform solid ice surface with constant density and no meltwater retention capacity (Reijmer et al., 2012; Steger et al., 2017). Climate model simulations instantly credit ablation-zone meltwater to the global ocean without provision for meltwater retention or runoff processes operating on the bare ice surface (Smith et al., 2017). There is growing evidence that climate models overestimate meltwater runoff on the Greenland ablation zone (Overeem et al., 2015; Rennermalm et al., 2013a; Smith et al., 2017; Yang et al., 2019b). Similar meltwater runoff retention is observed on the ablation zone of glaciers elsewhere, linked to the presence of porous, low-density ice termed "weathering crust" that stores meltwater on ice surfaces and delays its release to downstream environments (Ambach, 1955; Braithwaite et al., 1998; Hastenrath, 1983; Hoffman et al., 2014; Müller and Keeler, 1969; Munro, 1990, 2011).

Weathering crust forms because glacier ice is semi-transparent to solar radiation (Warren, 1982). Sunlight that penetrates bare ice provides a heat source that melts ice internally, generating subsurface meltwater that is stored within the ice matrix (Liston et al., 1999a). Hydraulic conductivity of near-surface glacier ice is low (~10^{-4} m s^{-1}) (Karlstrom et al., 2014; Stevens et al., 2018). Consequently, subsurface melting may slow the transport of surface meltwater to supraglacial streams and rivers that efficiently transport meltwater to surrounding oceans (Smith et al., 2015). Subsurface meltwater may also remain trapped within the ice matrix, where it may refreeze and thereby reduce meltwater runoff export from ice surfaces on interannual timescales (Hoffman et al., 2014; Liston and Winther, 2005).

Climate models are the primary tools used to forecast future Greenland mass loss, but these models currently neglect meltwater retention processes in the ablation zone, including those associated with the understudied phenomenon of weathering crust (Smith et al., 2017). Validating climate model calculations of meltwater runoff and possible retention processes occurring on the Greenland Ice Sheet surface is difficult because measurements of ice sheet surface properties including density, water storage, and meltwater runoff are extremely rare (Rennermalm et al., 2013a, 2013b; Smith et al., 2017). To address this problem, this dissertation uses field measurements of bare ice hydrologic and radiative properties, numerical modeling, and climate model simulations to answer the following research questions:

1) Does solar radiation penetrate bare ice?
2) Can bare ice store meltwater?
3) Does meltwater storage in bare ice explain climate model over-prediction of meltwater runoff?

Chapter One of this dissertation reviews historic and contemporary progress in satellite remote sensing of the Greenland Ice Sheet ablation zone (Cooper and Smith, 2019). The review critically examines a prevailing conceptual model of the ablation zone as homogeneous solid ice with uniform electromagnetic properties. The review concludes that future progress will benefit most from methods that directly address the complexity of the ablation zone surface through multi-sensor, multi-wavelength, and cross-platform datasets and methods.

Chapter Two of this dissertation presents measurements of solar radiation attenuation within glacier ice in Greenland's ablation zone, which are needed to calculate subsurface melting due to internal absorption of solar radiation within ice (Brandt and Warren, 1993). These measurements are used to quantify attenuation coefficients of visible wavelength light within glacier ice and to demonstrate how they can be used to understand interactions between ice surfaces and visible wavelength light sources such as the Ice, Cloud, and land Elevation Satellite-2 (ICESat-2) (Cooper et al., 2020).

Chapter Three of this dissertation presents measurements of bare ice density measured in shallow ice cores in a well-studied catchment on Greenland's southwest ablation zone (Smith et al., 2017; Yang et al., 2018, 2019b). These measurements are used to estimate the amount of meltwater stored in a bare ice weathering crust on Greenland's ablating ice surface (Cooper et al., 2018).

Chapter Four of this dissertation applies a numerical model of spectral radiation and thermodynamic heat transfer (Liston et al., 1999a) to explain climate model simulations of ice sheet meltwater runoff by comparison with direct measurements of ice sheet meltwater runoff collected on Greenland's ablating bare ice surface (Smith et al., 2017). The spectral radiation attenuation coefficients from Chapter Two are used as input to this model. The field measurements of ice density presented in Chapter Three together with measurements of ice sheet surface ablation from a network of ablation stakes installed within the experimental catchment are used as model validation.

1 Satellite remote sensing of the Greenland Ice Sheet ablation zone: a review

Abstract. The Greenland Ice Sheet is now the largest land ice contributor to global sea level rise, largely driven by increased surface meltwater runoff from the ablation zone, i.e. areas of the ice sheet where annual mass losses exceed gains. This small but critically important area of the ice sheet has expanded in size by ~50% since the early 1960s, and satellite remote sensing is a powerful tool for monitoring the physical processes that influence its surface mass balance. This review synthesizes key remote sensing methods and scientific findings from satellite remote sensing of the Greenland Ice Sheet ablation zone, covering progress in 1) radar altimetry, 2) laser (lidar) altimetry, 3) gravimetry, 4) multispectral optical imagery and, 5) microwave and thermal imagery. Physical characteristics and quantities examined include surface elevation change, gravimetric mass balance, reflectance, albedo, and mapping of surface melt extent and glaciological facies and zones. The review concludes that future progress will benefit most from methods that combine multi-sensor, multi-wavelength, and cross-platform datasets designed to discriminate the widely varying surface processes in the ablation zone. Specific examples include fusing laser altimetry, radar altimetry, and optical stereophotogrammetry to enhance spatial measurement density, cross-validate surface elevation change, and diagnose radar elevation bias; employing dual-frequency radar, microwave scatterometry, or combining radar and laser altimetry to map seasonal snow depth; fusing optical imagery, radar imagery, and microwave scatterometry to discriminate between snow, liquid water, refrozen meltwater, and bare ice near the equilibrium line altitude; combining optical reflectance with laser altimetry to map supraglacial lake, stream, and crevasse bathymetry; and monitoring the inland migration of snowlines, surface melt extent, and supraglacial hydrologic features.

1 Introduction

The Greenland Ice Sheet (GrIS) is the second largest ice mass on earth. If the entire ice sheet were to melt, global sea level would rise by about seven meters (van den Broeke et al., 2016). At present, the GrIS is losing mass, consistent with its expected response to anthropogenic climate warming (Ettema et al., 2009;

Hanna et al., 2008; Pattyn et al., 2018; Trusel et al., 2018; Vizcaíno et al., 2008, 2013a, 2013b, 2015). Its mass loss averaged -171 Gt yr^{-1} between 1991 and 2015, equivalent to 0.47 ± 0.23 mm yr^{-1} global eustatic sea level rise (SLR) (van den Broeke et al., 2016). The rate of SLR contribution accelerated to >1 mm yr^{-1} during the latter half of this period with a maximum 1.2 mm contribution in the record melting year 2012 (Bamber et al., 2018; van den Broeke et al., 2016; Hanna et al., 2013; Rignot et al., 2011; Shepherd et al., 2012). Since 2013, satellite gravimetry data suggest mass loss acceleration has stalled but remains negative with an average 0.69 mm yr^{-1} SLR contribution during the 2012–2016 period (Bamber et al., 2018; Bevis et al., 2019; Wouters et al., 2013). Consequently, there is an urgent need to measure and diagnose changes in the GrIS mass balance and satellite remote sensing is a powerful tool for this purpose (Kjeldsen et al., 2015).

The observed GrIS mass loss is being driven by both an increase in solid ice discharge (the physical movement of solid ice into surrounding oceans), and by decreasing surface mass balance (the surplus of surface meltwater runoff and evaporation over snowfall) (Andersen et al., 2015; Bevis et al., 2019; van den Broeke et al., 2009, 2016; Enderlin et al., 2014; Lenaerts et al., 2019; Machguth et al., 2016; Rignot et al., 2011; Shepherd et al., 2012). About 60% of total mass loss since 1991 is explained by increased surface meltwater runoff from the ablation zone and lower elevation areas of the accumulation zone (van Angelen et al., 2014; van den Broeke et al., 2016; Fettweis et al., 2017). This increase is attributed in part to a prevailing pattern of warm, dry, clear-sky conditions during summer in (primarily) west Greenland associated with a persistently negative North Atlantic Oscillation (NAO) atmospheric circulation pattern (Fettweis et al., 2013; Hanna et al., 2016). Since about 2000, the NAO has exacerbated background regional warming of the surface air temperature, leading to enhanced surface melt, reduced summer snowfall, and larger areas of exposed bare ice that further enhance surface melt via melt-albedo feedbacks (van Angelen et al., 2014; Bevis et al., 2019; Box et al., 2012; Fettweis et al., 2013; Hanna et al., 2016; Hofer et al., 2017; Lim et al., 2016; Ryan et al., 2019; Tedesco et al., 2011). In the coming decades, regional warming is expected to drive continued acceleration of surface meltwater runoff (Ettema et al., 2009; Hanna et al., 2008; Pattyn et al., 2018; Trusel et al., 2018; Vizcaíno et al., 2008, 2013a, 2013b, 2015), whereas solid ice

discharge is expected to decline relative to meltwater runoff as the marine terminating ice sheet margins and outlet glaciers thin and retreat (Bevis et al., 2019; Enderlin et al., 2014; Fürst et al., 2015). Consequently, surface processes in the ablation zone, particularly those that control the exposure and melting of bare ice, will play an enhanced role in determining the long-term GrIS mass balance (Bevis et al., 2019; Box et al., 2012; van den Broeke et al., 2016; Franco et al., 2013; Ryan et al., 2019). Already, some 78–85% of the total liquid runoff produced from surface melting is generated in this zone, despite it covering ~22% of the ice sheet's surface area, up from ~15% in the early 1960s (Bader, 1961; Benson, 1962; Box et al., 2012; Machguth et al., 2016; Steger et al., 2017).

Remote sensing plays a critical role in validating ice sheet mass balance and the associated SLR contribution (Kjeldsen et al., 2015). For over three decades, satellite sensors operating in the visible, infrared, and microwave wavelengths of electromagnetic radiation have observed the GrIS (Pritchard et al., 2011). The first spaceborne measurements of GrIS surface elevation were collected in the late 1970s by the National Aeronautics and Space Administration (NASA) Geodetic and Earth Orbiting Satellite-3 (GEOS-3), the NASA Seasat, and the US Navy Geosat oceanographic radar altimeters (Brooks et al., 1978). More recent radar altimetry missions useful for mapping ice sheet elevation change include the Geosat Follow-On (GFO), and the European Space Agency (ESA) European Remote-sensing Satellites 1 and 2 (ERS-1 and ERS-2), the Environmental Satellite (EnviSat), and the Cryosphere Satellite-2 (CryoSat-2). Radar altimetry now provides the longest record of GrIS volume change, owing to this steady progression of international radar altimeter missions extending to the present day (Sørensen et al., 2018).

Historically, ice sheet surface elevation retrieval accuracy from radar altimetry was limited by slope errors in the topographically-complex ablation zone, and uncertain signal penetration depth into snow and firn (Brenner et al., 2007). The laser altimeters on board the NASA Ice, Cloud, and land Elevation Satellites 1 and 2 (ICESat-1 and ICESat-2) and the interferometric mode of the Ku-band (~13.9 GHz) radar altimeter on board CryoSat-2 help redress these issues, and now provide sub-decimeter elevation change accuracy in the ablation zone (Abdalati et al., 2010; Drinkwater et al., 2004). In addition to new satellite laser and radar altimeters, gravimetry emerged in the early 2000s as a wholly novel remote sensing method for measuring

the GrIS mass balance, with the first gravimetric measurements of the GrIS mass balance provided at ~400 km spatial scale by the NASA/German Aerospace Center twin Gravity Recovery and Climate Experiment (GRACE) in 2002 (Pritchard et al., 2011). The GRACE-Follow On (GRACE-FO) satellite launched in May 2018 will continue the GRACE measurement time series for a planned ten years, and adds a new laser ranging interferometer that is expected to improve the satellite-to-satellite distance measurement relative to the GRACE microwave ranging system (Flechtner et al., 2016; Turyshev et al., 2014).

Optical satellite remote sensing provides the longest continuous spaceborne record of the changing GrIS surface. The first spaceborne photographic images of the GrIS were captured in the early 1960s by United States strategic reconnaissance satellites operated under the classified Corona program, followed by the unclassified Nimbus meteorological satellites launched by NASA in the mid-1960s (Bindschadler, 1998; Bjørk et al., 2012; Gallaher et al., 2015). The first multispectral images of GrIS surface reflectance were collected by the Multispectral Scanner (MSS) instrument on the Earth Resources Technology Satellite-1 (later renamed Landsat 1), launched by NASA in 1972 (Freden, 1973). Multispectral imaging spectrometers now provide over three decades of ice and snow surface reflectance from which decadal time series of surface albedo are computed (He et al., 2013; Key et al., 2016). Together with thermal, synthetic aperture radar, and microwave scatterometer imagery, the entire GrIS ablation zone ice surface is imaged daily, and regions of unique ice composition (facies or zones) are mapped and monitored for change (Benson, 1962; Fahnestock et al., 1993). Crevasse fields, superimposed ice, seasonal snowlines, and "dark zones" of anomalously low albedo are all visible in satellite imagery (Nolin and Payne, 2007; Ryan et al., 2019; Tedstone et al., 2017; Wientjes and Oerlemans, 2010; Yang and Smith, 2013). These descriptive zones provide a framework for understanding the spatial organization and physical processes operating on the ablation zone ice surface, and their temporal evolution including surface meltwater presence, outcropping of entrained dust, and the inland migration of the seasonal snowline and supraglacial meltwater lakes (Gledhill and Williamson, 2018; Hall et al., 2006; Ryan et al., 2019; Tedesco et al., 2011; Wientjes and Oerlemans, 2010). Increasingly, ultra-high-resolution commercial satellite and drone imagery is used

to recover unprecedented spatial detail, resolving surface features such as cryoconite holes and supraglacial rivers less than one meter in width (Bhardwaj et al., 2016; Legleiter et al., 2014; Ryan et al., 2018).

Previous reviews of satellite remote sensing of glaciers and ice sheets exist (e.g. Bindschadler, 1998), including recent reviews focused on regional climate modeling of the GrIS surface mass balance (van den Broeke et al., 2017; Lenaerts et al., 2019). Other reviews have focused on satellite altimetry and gravimetry of the combined Greenland and Antarctic ice sheet mass balance (Pritchard et al., 2011; Quincey and Luckman, 2009; Rémy and Parouty, 2009), the global land ice contribution to SLR during the satellite era (Bamber et al., 2018), polar science applications of spaceborne wind scatterometers (Long, 2017), satellite remote sensing of polar climate change (Hall, 1988), principles and theory of remote sensing methods for glaciology (König et al., 2001), remote sensing of Andean mountain glacier mass balance (Bamber and Rivera, 2007), optical remote sensing of Himalayan glaciers (Racoviteanu et al., 2008), glaciological applications of unmanned aerial vehicles (Bhardwaj et al., 2016), and many more specialized reviews of snow and ice optical or hydrologic properties with relevance to glaciological research (Bell, 2008; Carsey, 1992; Chu, 2014a; Deems et al., 2013; Dietz et al., 2012; Dozier and Painter, 2004; Frei et al., 2012; Gardner and Sharp, 2010; Irvine-Fynn et al., 2011; Nolin, 2010; Pitcher and Smith, 2019; Rennermalm et al., 2013b; Richter-Menge et al., 1991; Warren, 1982). To the authors' knowledge no review has focused specifically on satellite remote sensing the GrIS ablation zone, a small but critically important area of the ice sheet with unique physical processes and strong potential to expand in coming years.

This review summarizes platforms, methods, and data products used for remote sensing of the GrIS ablation zone, and some process-level discoveries that these data have produced. Because the ablation zone is defined as those areas where mass losses exceed gains, the review focuses exclusively on mass loss processes. The review is organized as follows: Section 2 defines key concepts relevant to the GrIS mass balance, surface mass balance, and energy balance. Section 3 reviews radar and laser (lidar) altimetry of GrIS surface elevation change. Section 4 reviews satellite gravimetric measurements of the GrIS mass balance. Section 5 reviews optical remote sensing of the GrIS ablation zone surface reflectance and albedo. Section 6 reviews active and passive microwave, thermal, and multi-angular remote sensing of glaciological

zones, surface melt extent, and surface roughness. Throughout the review we provide suggestions for future research directions and opportunities in the context of present and future missions. Glossaries of satellite remote sensing sensors, platforms, and managing agencies discussed in this article are provided in Appendices A–D. The review concludes with a short synthesis and recommendations for future research.

2 Ice sheet mass balance, surface mass balance, and energy balance

Before reviewing satellite remote sensing of the GrIS ablation zone, we briefly define key concepts and terminology that are discussed throughout the review. Ice sheets and glaciers gain mass through snowfall and lose mass through sublimation, meltwater runoff, and solid ice discharge. Following Lenaerts et al. (2019) and van den Broeke et al. (2017), the mass balance MB of an ice sheet is usually written as:

$$MB = SMB - D \tag{1}$$

where SMB is surface mass balance and D is solid ice discharged to surrounding oceans. The components of MB are commonly expressed in units of mass per time (e.g. kg yr^{-1} or Gt yr^{-1}), mass per unit area per time (e.g. kg m^{-2} yr^{-1}), and mass per unit area per time normalized by density of liquid water (e.g. m water equivalent, m w.e. yr^{-1}) (Lenaerts et al., 2019).

The SMB is the sum of mass inputs and outputs at the ice surface:

$$SMB = P - E - ER_{ds} - R \tag{2}$$

where precipitation P is the sum of liquid precipitation $\mathrm{P_{liquid}}$ (e.g. rain) and solid precipitation $\mathrm{P_{solid}}$ (e.g. snow), E is the sum of evaporation and sublimation, ER_{ds} is net snow erosion, and runoff R is the sum of the liquid water balance:

$$R = M + P_{\mathrm{liquid}} + CO - RF - RT \tag{3}$$

where M is surface meltwater production, CO is condensation, RF is refreezing, and RT is liquid water retention e.g. water stored in lakes, aquifers, or under capillary tension in snow and ice. The GrIS ablation zone SMB is dominated by P_{solid} and M with the remaining terms representing smaller but uncertain components (Box and Steffen, 2001; van den Broeke et al., 2016; Cooper et al., 2018; Forster et al., 2014; Rennermalm et al., 2013a). The accumulation and ablation zones of the ice sheet are defined as those areas

where the local $SMB > 0$ and the local $SMB < 0$, respectively. The equilibrium line altitude (ELA) separates the two zones where local $SMB = 0$ (van den Broeke et al., 2017).

The total change in ice sheet surface elevation over time (the quantity observed by spaceborne altimeters) is usually defined as:

$$\frac{dH}{dt} = \frac{SMB}{\rho_\mathrm{s}} + \frac{BMB}{\rho_\mathrm{b}} + \frac{D}{\rho_\mathrm{i}} + v_\mathrm{c} + v_\mathrm{br} \quad (4)$$

where dH/dt is total change in surface elevation (m yr^{-1}), SMB (kg m^{-2} yr^{-1}) is surface mass balance, ρ_s (kg m^{-3}) is surface snow, firn, and/or ice density, BMB (kg m^{-2} yr^{-1}) is basal mass balance, ρ_b (kg m^{-3}) is basal ice density, v_c (m yr^{-1}) is vertical velocity due to snow or firn compaction, v_br (m yr^{-1}) is vertical bedrock velocity (e.g. glacial isostatic adjustment), and ρ_i is solid ice density (Sørensen et al., 2011; Zwally et al., 2011). The vertical velocity terms contribute to dH/dt but are not associated with change in MB.

Equation (4) is used to estimate volumetric changes in the polar ice sheets, and also to estimate MB. This requires correction for the vertical velocity terms and an estimate of ρ_s, which for the ablation zone is typically taken as a constant value between 830 kg m^{-3} and 917 kg m^{-3} (Cuffey and Paterson, 2010) whereas for snow and firn above the ELA, measured or modeled values of ρ_s are necessary to convert dH/dt to SMB (Sørensen et al., 2011). In some cases, all but the first term on the right hand side of Equation (4) can be neglected and the local SMB can be inferred from remotely sensed dH/dt (Sutterley et al., 2018).

The energy available for melting snow or ice is determined by the sum of positive and negative heat fluxes at the surface, referred to as the surface energy balance SEB (W m^{-2}):

$$\begin{aligned} SEB &= SW_\mathrm{NET} + LW_\mathrm{NET} + SHF + LHF + G_\mathrm{S} \\ &= SW_\mathrm{in}(1-\alpha) + LW_\mathrm{in} - \sigma T_\mathrm{sfc}^4 + SHF + LHF + G_\mathrm{S} \end{aligned} \quad (5)$$

where SW and LW are shortwave (solar) and longwave (terrestrial) radiation fluxes, SHF and LHF are the turbulent surface fluxes of sensible and latent heat (which are proportional to the aerodynamic surface roughness length, ζ (m^{-1})), G_S is subsurface (conductive) heat flux, α is the broadband surface albedo, or the ratio of upwelling (reflected) solar radiation to downwelling (incoming) solar radiation ($SW_\mathrm{up}/SW_\mathrm{in}$), σ is the Stefan Boltzmann constant (5.67 x 10^{-8} W m^{-2} K^{-2}), and T_sfc is the ice surface kinetic temperature.

In Equation 5, all heat fluxes have units W m^{-2} and are defined positive toward the surface (van den Broeke et al., 2017).

If T_{sfc} reaches the melting temperature of ice, positive SEB provides melt energy ME (W m^{-2}) and liquid meltwater M is produced. The dominant source of ME for the GrIS is SW_{NET} (van den Broeke et al., 2008). Typical values of α are 0.9 for freshly fallen snow, 0.6 for melting snow, and 0.4 for bare glacier ice (Gardner and Sharp, 2010). This wide variability in α demonstrates the critical role of albedo in modulating the SEB and consequently M in the GrIS ablation zone (Box et al., 2012; Ryan et al., 2019; Tedesco et al., 2011).

3 Ice surface elevation change

The magnitude of GrIS dH/dt and its spatio-temporal variability has been quantified for nearly four decades using spaceborne radar (Radio Detection and Ranging) altimetry (Brooks et al., 1978; Helm et al., 2014a; Khvorostovsky, 2012; Sørensen et al., 2018; Thomas et al., 2008; Zwally et al., 1983, 1989), and since 2001 using spaceborne laser altimetry (Bolch et al., 2013; Csatho et al., 2014; Ewert et al., 2012b; Felikson et al., 2017; Slobbe et al., 2008; Zwally et al., 2002). Recent advances in laser and radar altimeter precision and spatial resolution allow discrimination of dH/dt in slower-flowing, land-terminating sectors of the GrIS ablation zone, principally caused by change in SMB rather than D (Pritchard et al., 2009; Sole et al., 2008). For the accumulation zone, regional climate models and firn compaction models are used to partition the component of dH/dt caused by change in SMB from those caused by change in firn density and D (McMillan et al., 2016; Zwally et al., 2005). The following subsections summarize spaceborne radar altimetry of the GrIS, providing an historical perspective that emphasizes major challenges and advances in the field, and identifies future opportunities for radar altimetry observations of the GrIS ablation zone.

3.1 Radar altimetry

Conventional radar altimeters are nadir pointing single-beam radars that transmit and receive tens to thousands of microwave pulses per second, yielding ground measurement footprint diameters on the order 1–10 km posted at 0.3–0.6 km along-track spacing (Brenner et al., 2007; Ekholm et al., 1995; Martin et al.,

1983). An estimate of dH/dt is obtained by comparing measurements at crossover points, where an earlier satellite ground track intersects a later one (Zwally et al., 1989). Two critical factors affect the accuracy of radar altimeter elevation retrievals over ice sheets: 1) variation in topographic slope, which controls the average distance between the altimeter and the measured ground footprint surface (Bamber et al., 1998; Brenner et al., 1983, 2007), and 2) changes in the electrical permittivity of the ice sheet surface, which controls the reflection, transmission, and absorption of the microwave signal (Davis, 1993b, 1996; Mätzler and Wegmüller, 1987; Ridley and Partington, 1988).

For typical radar altimeter frequencies (Ku-band ~13 GHz), solid ice and liquid water are highly reflective whereas dry snow and firn are semi-transparent, with Ku-band penetration depths on the order of several meters (Davis and Zwally, 1993; Nghiem et al., 2005). Spatial and temporal variations in signal penetration depth caused by seasonal bare ice exposure, snow and firn densification, surface meltwater presence, and refreezing of meltwater introduce spurious height change signals that are poorly quantified for the GrIS but are estimated to exceed >0.50 m in some cases (Nilsson et al., 2015; Scott et al., 2006; Sørensen et al., 2015). Variations in surface slope dominate radar altimeter accuracy in the topographically-complex bare-ice ablation zone, with slope-induced errors that exceed >20 m for slopes >1° (Bamber et al., 1998; Brenner et al., 2007; Davis, 1996). The recent CryoSat-2 radar altimeter mission employs synthetic aperture radar (SAR) and interferometric synthetic aperture radar (InSAR) technologies which decrease the effective along-track footprint diameter to the order 0.1–0.3 km and provide cross-track slope from InSAR processing (Helm et al., 2014a). Together with denser orbital-track spacing and advances in waveform retracking, topographic mapping of ice sheet ablation zone areas is accurate to within a few meters on average, and dH/dt to within sub-meter uncertainty relative to laser altimetry (Gourmelen et al., 2018; Gray et al., 2017; Helm et al., 2014a).

3.1.1 Radar altimetry sensors and datasets

The first satellite altimeter measurements of surface topography for the Greenland Ice Sheet were made by the GEOS-3, Geosat, and Seasat oceanographic Ku-band altimeters (Table 1-1) (Brooks et al., 1978; Martin

et al., 1983; Partington et al., 1989; Thomas et al., 1983; Zwally et al., 1983). Their geographical coverage was limited to ±72° but the data they collected showed it was possible to calculate volumetric changes in the polar ice sheets from space, providing proof of concept for future polar-orbiting altimeters (Zwally et al., 1989). A first demonstration using GEOS-3, Geosat, and Seasat data found that for areas south of <72°N, the GrIS thickened by 23 ± 6 cm yr^{-1} between 1978–1986, with enhanced snowfall in a warmer climate hypothesized to explain the observed thickening (Zwally, 1989). These early missions supported important developments in waveform retracking, slope correction, and physical and empirical models for subsurface volume scattering (Brenner et al., 1983; Davis, 1993a; Martin et al., 1983; Ridley and Partington, 1988). These corrections are critical for accurate elevation retrieval and reliable change detection (Davis, 1995, 1997). For example, Davis et al. (1998) used an improved geodetic model and an improved retracking model to reinterpret the earlier findings of Zwally et al. (1989), finding a smaller 1.5 ± 0.5 cm yr^{-1} thickening for the period 1978–1986 that highlighted the importance of slope- and signal penetration-correction.

The ESA European Remote-sensing Satellite (ERS-1) carried the first polar-orbiting radar altimeter, extending coverage of the polar ice sheets to ±81.5° (Thomas et al., 2008). Together with the follow-on ERS-2 and EnviSat missions, these satellites provided near complete GrIS coverage and 21 years of continuous data acquisition (Sørensen et al., 2018). The first digital elevation model (DEM) spanning the entire GrIS surface was produced from combined ERS-1 and Geosat altimetry data, supplemented by stereo-photogrammetric and cartographic data sets, with pan-GrIS average accuracy -0.33 ± 6.97 m (Bamber et al., 2001; Ekholm, 1996). ERS-1/2 altimetry data were used to discriminate thinning rates in the ablation zone (defined as <1500 m a.s.l.) of -2.0 ± 0.9 cm yr^{-1} from accumulation zone (>1500 m a.s.l.) thickening of 6.4 ± 0.2 cm yr^{-1} with an overall net thickening of 5.4 ± 0.2 cm yr^{-1} for the period 1992–2003 (Johannessen et al., 2005). To extend the temporal coverage and increase spatial measurement density, Khvorostovsky and Johannessen (2009) developed an algorithm to merge ERS-1/2 and EnviSat datasets and detect and eliminate inter-satellite biases. For the period 1992–2008, their dataset suggests net thinning of the GrIS initiated around 2000, and accelerated between 2006–2008, with a thickening of 4.0 ± 0.2 cm yr^{-1} above 1500 m a.s.l. and thinning of -7.0 ± 1.0 cm yr^{-1} below 1500 m a.s.l. (Khvorostovsky, 2012).

Conventional radar altimeters such as the instruments included on ERS-1/2 and EnviSat were optimized for detecting elevation over open oceans and low-gradient polar ice sheet interiors with mean accuracies typically <0.2 m for ice sheet surface slopes <0.2° (Bamber et al., 1998; Brenner et al., 2007). Elevation accuracy and dH/dt uncertainty is much higher for the topographically complex ablation zone due to their large spatial measurement footprint and wide orbital track spacing, with slope errors >20 m for slopes >1° and systematic biases over rough surfaces (Arthern et al., 2001; Bamber et al., 1998; Brenner et al., 2007; Thomas et al., 2008). Careful processing has been used to discriminate ablation zone thinning rates using ERS-1/2 and EnviSat altimetry data, including repeat-track analysis, but the accuracy of these data and their process-based interpretation is ambiguous owing to the aforementioned slope errors and sparse spatial measurement density in the ablation zone (Levinsen et al., 2015; Sørensen et al., 2015; Su et al., 2016, 2018).

The CryoSat-2 satellite (launched April 2010) provides continuity with ERS-1/2 and EnviSat and employs SAR delay-Doppler along-track processing and interferometric cross-track processing (Gourmelen et al., 2018; Wingham et al., 2006). CryoSat-2 is the first ESA radar altimeter dedicated to polar studies, with orbital coverage to ±88° and 1.6 km cross-track spacing at 70°. CryoSat-2 carries two Ku-band SAR/Interferometric Radar Altimeter (SIRAL) systems. SIRAL operates in three distinct modes depending on location: 1) low resolution mode (LRM) over open ocean and ice sheet interiors, 2) synthetic aperture radar mode (SAR) over sea ice and coastal regions, and 3) SAR interferometric mode (SARIn) over ice sheet margins. The SARIn mode employs two SAR instruments oriented across the satellite track. Interferometric phase processing of the dual waveforms provides cross-track slope at ~0.3 km along-track resolution (Gray et al., 2013; Parrinello et al., 2018).

Over mild slopes (<1°), phase unwrapping (Wingham et al., 2006) of CryoSat-2 interferometric data provides 5 km wide-swath elevation retrievals with two orders of magnitude more individual measurements per surface area than any prior radar altimeter (Gourmelen et al., 2018; Gray et al., 2013, 2017). The first spatially continuous swath DEMs were generated from CryoSat-2 data for areas of the Devon Ice Cap and western GrIS with ± 3 m precision (Gray et al., 2013, 2017). Swath processing provides

information about within-swath topography that is not provided by traditional radar processing techniques. For example, Gray et al. (2017) demonstrated a novel method for supraglacial lake water surface elevation retrievals in the ablation zone from CryoSat-2 swath retrievals, and provide a detailed technical description of swath processing.

The SIRAL system nominally resolves dH/dt to 3.3 cm yr^{-1} near the ice sheet margins and 0.7 cm yr^{-1} in the ice sheet interior, at 104 km^2 and 106 km^2 spatial scale, respectively (Parrinello et al., 2018). Using three years (2011–2014) of CryoSat-2 standard retrievals and an updated threshold retracking algorithm, a new pan-GrIS DEM was generated with 3 ± 15 m elevation accuracy relative to ICESat over 80% of the GrIS and 5 ± 65 m accuracy over 90% of the GrIS (Figure 1-1) (Helm et al., 2014a). These data suggest reliable CryoSat-2 elevation retrievals remain limited to areas of the ablation zone with surface slope <1.5° (Figure 1-1). Elevation change from these data suggests a 2.5 factor increase in pan-GrIS volume loss (-375 ± 24 km^3 yr^{-1}) compared with the ICESat (2003–2009) period, with large losses concentrated in the west and southeast marginal ablation zones (Helm et al., 2014a). A separate analysis of the same data combined with a firn density model found an equivalent mass loss of 269 ± 51 Gt yr^{-1} (McMillan et al., 2016).

Currently operating beyond its design lifetime, CryoSat-2 will be succeeded by the SAR Radar Altimeter (SRAL) on board Sentinel-3A/B, and by the AltiKa Ka-band radar altimeter on board the Satellite with ARgos and ALtiKa (SARAL) (Table 1-1). SARAL is a joint French Space Agency (CNES) and Indian Space Research Organisation (ISRO) oceanographic mission launched in 2013 with secondary goal to monitor polar ice sheet surface elevations (Verron et al., 2015). SARAL has the same 35-day repeat orbit as EnviSat and ERS-1/2 but the AltiKa instrument operates at Ka-band (~36 GHz), thereby offering unique opportunities for cross-platform validation of prior Ku-band radar altimeters (Rémy et al., 2014). In particular, the Ka-band should improve diagnosis of Ku-band signal penetration bias, owing to its higher (~36 GHz) signal frequency with ~10× lower theoretical penetration depth into dry snow relative to Ku-band, higher spatial resolution (~8 km footprint and 175 m along-track spacing), and higher pulse-repetition frequency (Chander et al., 2015; Rajkumar et al., 2015; Rémy et al., 2015; Su et al., 2018). SARAL also

provides an independent record of ice sheet dH/dt. Using the 1-km ICESat DEM for the period 2003–2005 (DiMarzio, 2007) as a baseline, data from SARAL-AltiKa for the period 2014–2016 was used to estimate a pan-GrIS volume loss rate of 247 km^3 yr^{-1}, with the largest basin-scale volumetric decreases found in the north- and northwest (Suryawanshi et al., 2019).

3.1.2 Current challenges and future opportunities

Progress in waveform retracking and SAR/InSAR technology has improved radar altimetry performance over complex terrain, but retracking errors over rough surfaces and spatiotemporal variations in signal penetration depth remain important sources of uncertainty. Reliable performance in the ablation zone appears limited to areas with surface slope <1.5° (Figure 1-1), and signal penetration biases may exceed 0.5 m in the lower accumulation zone (Gray et al., 2015, 2017; Nilsson et al., 2015; Sørensen et al., 2015). Nevertheless, radar altimetry provides the longest record of GrIS dH/dt and two challenges stand out for leveraging this unique dataset: 1) homogenization of the inter-mission and cross-platform methods and datasets used to detect dH/dt (Levinsen et al., 2015; Schröder et al., 2019), and 2) better understanding of spatial and temporal changes in snow, firn, and ice permittivity caused by surface meltwater presence, meltwater percolation, and ice lens formation (Gray et al., 2015; Nilsson et al., 2015). These challenges are closely related. For example, methods such as waveform smoothing, waveform model fitting, and optimal thresholding increase absolute accuracy, but at the expense of homogenization required for statistical change detection (Davis, 1995, 1997; Davis et al., 2000). In other cases, waveform retracking may mask real dH/dt signals (Alley et al., 2007). Similarly, real changes in snow and firn permittivity may introduce false dH/dt signals, such as the apparent 56 ± 26 cm elevation increase attributed to ice lens formation in the percolation zone following the 2012 melt event (Nilsson et al., 2015). Here, the SARAL-AltiKa Ka-band altimeter may provide new opportunities for diagnosing radar penetration bias and waveform interpretation. In addition, its replication of the ERS-1/2 and EnviSat repeat orbit will improve the statistical reliability of along-track change detection (Rémy et al., 2014).

In contrast to the percolation zone, the ablation zone is typically conceptualized as homogenous solid ice with uniform electromagnetic properties. Ku-band backscatter over the bare ice ablation zone is dominated by surface scattering from the rough (and seasonally saturated) ice surface but volume scattering has received little direct study and may be important over superimposed ice, seasonally-snow covered surfaces, or areas with multi-modal surface roughness distributions (Rott and Mätzler, 1987). Penetration depths at C- and L-band exhibit an order of magnitude range over bare ice surfaces on the GrIS, possibly reflecting variations in ice thermal structure and surface roughness (Rignot et al., 2001). Similar comparisons at Ku-band do not exist to our knowledge, but could be facilitated by dual-frequency radar altimeters such as SRAL or RA-2, or by comparison with SARAL-AltiKa Ka-band altimetry (Table 1-1). Factors that affect bare ice microwave permittivity include its grain size, temperature, porosity, water content, crystal structure, and chemical and physical impurity content (Irvine-Fynn et al., 2006; Kendrick et al., 2018; Pettersson et al., 2004; Warren and Brandt, 2008). Although slope errors dominate elevation retrieval uncertainty in the ablation zone, seasonal and spatial variations in ablation zone surface properties and their effect on radar backscatter may be an overlooked source of uncertainty (Scott et al., 2006; Su et al., 2018). Conversely, this variation and its effect on waveform shape could provide new opportunities for understanding the ablation zone, such as detecting water surface elevation change in supraglacial lakes, or inferring changes in near-surface ice structure related to physical weathering of solid ice, or estimating seasonal snow thickness using dual-frequency radar, as was recently demonstrated for Arctic sea ice using combined CryoSat-2 and SARAL-AltiKa retrievals (Gray et al., 2017; Guerreiro et al., 2016; Kendrick et al., 2018).

At the ice-sheet scale, knowledge of snow, firn, and ice density is the main source of uncertainty for conversion between ice sheet volume change and mass change (Pritchard et al., 2011). Density changes are caused by snow and firn compaction and by meltwater refreezing, which both affect waveform interpretation by changing the scattering properties of the snow and firn (McMillan et al., 2016; Nilsson et al., 2015). Field investigations suggest ice lenses are widespread in the percolation zone and have thickened in recent decades (Machguth et al., 2016; Vandecrux et al., 2019). The vertical and horizontal distribution

of meltwater percolation and refreezing is difficult to model and may not be accurately represented by regional climate models (van As et al., 2016; Vandecrux et al., 2019). Although these features present challenges for dH/dt detection, they also provide unique opportunities for characterizing snow and firn processes, including detection of extreme melt events, ice lens formation, and snow accumulation rates following ice lens formation (Nghiem et al., 2005).

3.2 Laser Altimetry

Laser altimeters use lidar (light detection and ranging) technology to measure the two-way travel time of narrow-beam monochromatic laser pulses transmitted between the altimeter and the earth's surface. In contrast to radar altimetry, signal penetration in ice and snow is minimal at common lidar wavelengths (visible and near-infrared) and the narrow laser beam illuminates a much smaller ground area which reduces slope errors over complex terrain (Brenner et al., 2007, 2012). The small laser footprint increases absolute accuracy but may also introduce uncertainty because interpolation between narrow footprints is needed to obtain spatially continuous elevations (Felikson et al., 2017). Laser altimeters are sensitive to atmospheric scattering and lack the all-weather capability of radar altimeters but are uniquely adept at measuring local surface elevation in the topographically complex ablation zone, allowing resolution of thinning rates at the scale of individual outlet glaciers and providing benchmark datasets for altimeter accuracy (Csatho et al., 2014; Howat et al., 2008). The following subsections summarize spaceborne laser altimetry of the GrIS, emphasizing the operational performance of ICESat, and future opportunities for laser altimetry observations of the GrIS ablation zone from the recently launched ICESat-2.

3.2.1 Laser altimetry sensors, methods, and datasets

The NASA Lidar In-space Technology Experiment (LITE), flown on the Discovery Space Shuttle in September 1994, was the first spaceborne lidar (Winker et al., 1996). LITE was focused on the vertical structure of clouds and aerosols and provided operational proof of concept. The NASA Geoscience Laser Altimeter System (GLAS) on board the ICESat satellite (2003–2009) (Table 1-1) was the first spaceborne lidar designed for polar science. GLAS transmitted short pulses of near infrared (1064 nm) light for surface

altimetry and visible green light (532 nm) for vertical distribution of clouds and aerosols (Zwally et al., 2002). The ICESat mission was marked by several important innovations in polar altimetry including unprecedented spatial resolution (70 m footprint, 172 m along-track spacing, and 3 cm vertical resolution), geographic coverage to ±86°, and the use of narrow-beam 1064 nm laser which reduced sensitivity to both slope errors and signal penetration into snow and firn (Shuman et al., 2006).

An important design objective of ICESat was to measure ice sheet surface elevation change over regions of high surface slope and complex topography, with primary mission objectives to measure spatially-averaged (104 km^2) ice sheet surface elevation to <15 cm absolute accuracy and elevation change to <1.5 cm yr^{-1} accuracy (Pritchard et al., 2011; Zwally et al., 2002). Field validation suggests operational absolute accuracy achieved 2 ± 3 cm for optimal conditions (Fricker et al., 2005). At-a-point measurement precision is ± 3 cm over the ice sheets and repeat crossover measurement uncertainty is typically 10–15 cm (Shuman et al., 2006; Siegfried et al., 2011), and up to 59 cm in regions of high surface slope (Brenner et al., 2007). Performance is affected by forward scattering of the return signal by intervening clouds, detector saturation, uncertain laser pointing angle, and laser transmit power decline (Abshire et al., 2005; Brenner et al., 2007; Fricker et al., 2005).

The ICESat payload included three separate laser systems. Technical issues with the lasers prevented planned continuous operation and instead data collection took place during 18 separate campaigns (Abshire et al., 2005; Schutz et al., 2005). Campaigns were designated by the laser system used and the campaign-specific orbital repeat frequency. For example, the first laser system operated for 38 days in an 8-day calibration and validation mode repeat frequency before it failed (Schutz et al., 2005). The second and third laser systems operated in campaign mode with 91-day repeat frequency constituting individual campaigns ~33 days in length separated by 4–6 months. Inter-campaign range biases up to ~20 cm have been found (Borsa et al., 2014; Siegfried et al., 2011). The biases owe in part to a coding error in the ICESat signal processing algorithm that has since been corrected (Borsa et al., 2014). On-orbit and post-processing bias corrections were developed to compensate for orbital drift and systematic laser orientation

(pointing) errors, but residual inter-campaign biases are an important measurement uncertainty in the ICESat data (Ewert et al., 2012a; Siegfried et al., 2011; Sørensen et al., 2011).

As with all spaceborne altimeters, the ICESat orbit followed ascending and descending orbital reference tracks with crossover reference points at the ascending and descending orbit intersections (Figure 1-2). Several factors affect geolocation of ICESat ground footprints at repeat-track and crossover locations. These include orbital vibrations, orbital drift, random errors in ICESat's laser orientation determination system, and declines in laser transmit power through time that modify the illuminated footprint diameter (Fricker et al., 2005; Luthcke et al., 2005; Schutz et al., 2005). These factors produce both real and apparent deviations between illuminated ground tracks and reference tracks up to a few hundred meters (Schenk and Csatho, 2012; Shuman et al., 2006). Consequently, exact co-located repeat track and crossover point measurements are extremely rare, and spatial interpolation is required to recover dH/dt at-a-point, which has become a central challenge for ICESat data interpretation (Schenk and Csatho, 2012). To estimate pan-GrIS dH/dt, an additional spatial interpolation of the point dH/dt estimates is typically performed, which is complicated by temporal differences among the point dH/dt estimates (e.g. Sørensen et al., 2011).

As detailed by Felikson et al. (2017), four methods have been developed to recover dH/dt from ICESat data: 1) repeat tracks (RTs), 2) crossovers (XOs), 3) overlapping footprints (OFPs), and 4) surface fitting methods such as triangulated irregular networks (TINs). The Surface Elevation Reconstruction and Change (SERAC) method (Schenk and Csatho, 2012) combines elements of RT and XO (Felikson et al., 2017). Alberti and Biscaro (2010) summarize the ICESat orbital parameters in detail and describe a flexible algorithm for determining RT and XO points from them.

The XO method calculates dH/dt at the ascending and descending orbital crossover points. The method was originally developed for radar altimetry and was expected to be the primary method for interpreting ICESat data (Zwally et al., 2002). The method was used to estimate a relative elevation accuracy for ICESat of 0.14–0.59 m depending on surface slope (Brenner et al., 2007). Using ICESat XO points as reference values, absolute accuracies for ERS-1/2 and EnviSat radar retrievals are ~0.10–0.56 m for surface slopes <0.1° but are 2.27 m on average and up to 30 m for surface slopes exceeding 0.7° (Brenner

et al., 2007). These differences demonstrate the utility of laser altimetry for validating radar altimetry but also suggest caution when combining retrievals at discrete locations with high surface slopes and/or topographic variability (c.f. Bamber et al., 1998).

The RT method calculates dH/dt from repeat measurements at reference points along the reference tracks, which increases spatial measurement density and coverage relative to XO points (Yi et al., 2005). However, RT points are typically further apart than XO points, which may increase slope errors (Felikson et al., 2017). Owing to higher measurement density, the RT method has seen greater operational use than the XO method and is more appropriate for local or regional scale analysis (Felikson et al., 2017). The RT method was combined with Advanced Spaceborne Thermal Emission and Reflection Radiometer (ASTER) digital elevation model differencing, which together suggest an average volume loss in southeast Greenland of ~108 km^3 yr^{-1} for the period 2003–2005 (Howat et al., 2008). Concentrated thinning of narrow outlet glaciers contributed less volume loss than dispersed but smaller thinning over larger interior areas, highlighting the enhanced capability of laser altimetry for observing local-scale processes in the ablation zone (Howat et al., 2008).

The OFP method uses both XO and RT points but requires that the laser footprints of repeat measurements overlap. ICESat footprints are ellipses with 50–90 m major axis length (Schenk et al., 2014). The overlapping criterion is determined by a predefined semi-major axis distance between laser footprints (Slobbe et al., 2008). In principle, the method does not account for slope between footprints but slope corrections have been applied, for example to validate ICESat with NASA Airborne Topographic Mapper (ATM) laser altimeter data (Thomas et al., 2005). Using a similar method, an average 0.07 m offset was found between NASA airborne LVIS lidar and ICESat elevation retrievals over the GrIS (Hofton et al., 2008). The OFP method has greater spatial coverage owing to combined use of RT and XO points. Consequently, dH/dt uncertainty appears to be lowest among methods (Felikson et al., 2017). The method was used to estimate an average thickening of 0.02 m yr^{-1} (equivalent to 21 km^3 yr^{-1} volumetric change) for areas above 2000 m a.s.l. and an average thinning of -0.24 m yr^{-1} (168 km^3 yr^{-1}) below 2000 m a.s.l. for the

period 2003–2007 (Slobbe et al., 2008). Thinning rates near the margin were found to be slightly larger than estimates from other methods due to greater sample size and coverage in the ablation zone.

The TIN method (Pritchard et al., 2009) is similar to RT as it aggregates all available along-track measurements within a predefined distance around each RT reference point. Unlike the standard RT method, a TIN surface is fitted to a subset of points at each RT reference point collected within a reference two-year time period. dH/dt is estimated from all combinations of surface elevation measurements outside the reference period relative to the TIN surface. The TIN surface implicitly accounts for cross-track and along-track slope and sacrifices temporal resolution for both spatial resolution and reference period consistency. Using the TIN method, ICESat dH/dt uncertainty was estimated to be ±0.07 m yr^{-1} at 1σ level (Pritchard et al., 2009). However, the method may systematically under-sample some areas of the ice sheet margin with insufficient points to fit the TIN, leading to underestimated total ice sheet volume change (Felikson et al., 2017). Qualitatively, each method shows a similar pattern of increasing ice thinning along the ice sheet margins with the highest thinning rates along the southern coasts, especially in the marine-terminating Jakobshavn Isbrae region and in southeast Greenland. Across methods, pan-GrIS volume loss ranges from ~200–275 km^3 yr^{-1} during the ICESat era (Felikson et al., 2017).

3.2.2 ICESat-2 and future opportunities

The Advanced Topographic Laser Altimeter System (ATLAS) was launched September 2018 onboard the Ice, Cloud, and land Elevation Satellite-2 (ICESat-2) (Table 1-1). ATLAS is a dual-beam single-photon counting laser altimeter marked by several improvements to the ICESat/GLAS measurement strategy (Abdalati et al., 2010; Markus et al., 2017). These include its dual-beam laser, organized into three pairs with 90 m beam separation and 3.3 km pair separation. Each beam has nominal 17 m spatial footprint diameter and 0.7 m along-track measurement spacing (Figure 1-4). This configuration permits determination of cross-track slope, increases spatial measurement density, and increases local measurement accuracy (Markus et al., 2017). ICESat-2 mission requirements include determination of ice sheet dH/dt to 0.4 cm yr^{-1} accuracy (0.25 cm yr^{-1} for outlet glaciers) when averaged over 100 km^2 areas (Markus et al.,

2017). Data collection began on Oct 14, 2018, with initial ICESat-2 data products released on June 7, 2019, including an initial release of the ATLAS/ICESat-2 L3A Land Ice Height (ATL06), Version 1 (Smith et al., 2019), which provides mean ice sheet surface elevation averaged along 40 m segments of ground track posted at 20 m along-track spacing (Figure 1-5) (https://nsidc.org/data/ATL06/).

In addition to an improved multi-beam configuration, the ATLAS instrument will transmit laser pulses at 532 nm wavelength, which will enhance both photon-return density and optical penetration capability relative to the GLAS instrument on ICESat. Water, both in liquid and solid form, is nearly transparent to 532 nm light. For example, the path length in pure water required to attenuate 532 nm light to 50% of its incident intensity is ~16 m, whereas this path length is ~0.01 m for 1064 nm light, owing to an ~1400-fold respective increase in the imaginary index of refraction of water (Hale and Querry, 1973; Pope and Fry, 1997). Consequently, ICESat-2 laser pulses at 532 nm will effectively "see through" liquid water and thereby facilitate spaceborne measurement of supraglacial lake, stream, and water-filled crevasse bathymetry (Brunt et al., 2016). Conversely, reflectivity of glacier ice and snow is near maximum at 532 nm owing to the extremely low absorption coefficient of ice and extremely high scattering efficiency from ice grains and air bubbles (Warren et al., 2006). This enhanced reflectivity should produce higher photon-return density relative to 1064 nm laser but will also include a non-zero volume scattering component that could introduce a range bias similar to radar penetration into snow and firn (Gardner et al., 2015; Greeley et al., 2017).

ICESat-2 research to date has focused on pre-mission proof of concept, airborne and ground validation, and sensor calibration (Brunt et al., 2014, 2017; Farrell et al., 2011). In addition to its unique ability to map surface water bathymetry, other novel applications of laser altimetry to the ablation zone that will benefit from ICESat-2 continuity include assimilation of dH/dt observations into transient ice flow simulations (Larour et al., 2014), fusion of multi-sensor (e.g. stereophotogrammetry or radar altimetry) datasets to increase the spatial density of surface elevation measurements (Schenk et al., 2014), and application of lidar-based snow grain size and surface roughness retrievals independent of or in combination with optical sensors (Nolin, 1998; Yang et al., 2017b). Comparison between ice sheet surface elevation

change estimates by laser altimetry and regional climate model (RCM) SMB is another area that is under explored (Sutterley et al., 2018). Such comparisons require accurate knowledge of the surface density and change in surface elevation due to ice dynamic motion, and therefore are most appropriate for bare ice areas during summer when surface melting dominates the elevation change signal (Sutterley et al., 2018). Finally, it was recently reported that the CryoSat-2 science team is considering adjusting the satellite's orbit to overlap its ground tracks with those of ICESat-2 once every ~2 days (Lenaerts et al., 2019). If so, these overlapping data would provide cross-platform dH/dt validation and could be used to infer changes in the CryoSat-2 Ku-band penetration depth into snow and firn.

4 Remote Sensing of mass balance

Three methods are used to estimate MB from satellite remote sensing: 1) changes in ice sheet surface elevation from altimetry, 2) the mass budget or input-output method, and 3) time-variable gravimetry (Mouginot et al., 2019). Satellite and airborne altimeters measure dH/dt which is converted to MB using modeled firn density and modeled SMB to partition D. The input-output method uses remotely-sensed ice sheet surface velocity and ice sheet thickness to calculate D for outlet glacier drainage basins and uses modeled SMB to calculate MB. Satellite gravimetry measures changes in earth's gravity field to directly estimate MB. The methods are complementary and largely independent, and together provide a comprehensive view of spatial and temporal patterns in the GrIS MB, since 2002 for gravimetry, 1992 for altimetry, and 1972 for IOM (Mouginot et al., 2019). We review each method below and compare estimates of MB from each.

4.1 Converting ice surface elevation change to mass change

Satellite altimeters observe total change in ice sheet surface elevation, which includes both real and apparent changes in ice sheet thickness. Glaciers and ice sheets thicken from snow accumulation and thin by melting, sublimation, horizontal ice flow, snow redistribution, and increases in ice, snow, and firn density. Apparent changes in ice sheet thickness are caused by vertical motion of underlying bedrock. Converting altimetric measurements of dH/dt to change in ice volume and mass balance requires an estimate of each individual

contribution to dH/dt, and correction for each term in Equation (4) that is not associated with change in ice volume and/or change in mass balance.

The typical procedure for estimating each term on the right-hand side of Equation 4 involves obtaining SMB from a climate model and defining the accumulation and ablation zones as those areas where SMB is positive and negative, respectively, separated by the ELA where modeled $SMB = 0$ (Sørensen et al., 2011). Above the ELA, positive dH/dt is caused by net accumulation and ρ_s is estimated with a firn density model, whereas negative dH/dt is caused by ice dynamics and ρ_s is solid ice density (typically taken as 917 kg m^{-3}). Below the ELA, dH/dt is caused by both negative SMB and D, and solid ice density is used to convert both to mass (Csatho et al., 2014; Kuipers Munneke et al., 2015; McMillan et al., 2016; c.f. Sørensen et al., 2011). The v_c term causes an apparent change in mass that is estimated with a firn compaction model and removed from dH/dt (Li and Zwally, 2011). The v_{ice} term is negligible, BMB is negligible in the accumulation zone and very small (~0.015–0.020 m yr^{-1}) in the ablation zone, and v_{br} contributes about 1 GT yr^{-1} in apparent mass change that can be corrected or ignored (Fahnestock et al., 2001; Sørensen et al., 2011).

When corrected for the terms in Equation 4, ICESat altimetry data suggest mass loss rates of -191 ± 23 Gt yr^{-1} to -240 ± 28 Gt yr^{-1} for the period 2003–2008 (Sørensen et al., 2011). The spread arises from the choice of dH/dt interpolation method (Section 3.2.1) and, more substantially, the choice of firn density model. Removal of v_c reduces mass loss rates by 33–36 Gt yr^{-1}, almost all of which is due to compaction in the zone between the ELA and 2000 m a.s.l. (Sørensen et al., 2011). Despite the uncertainties associated with firn densification, good agreement is found between altimetry and mass balance estimates from GRACE, which suggest mass loss of -230 ± 33 Gt yr^{-1} during the period 2002–2009 (Velicogna, 2009), -179 ± 25 Gt yr^{-1} for 2002–2007 (Wouters et al., 2008), and -237 ± 20 Gt yr^{-1} for 2003–2008 (van den Broeke et al., 2009). Applying the same methods as Sørensen et al. (2011), Greenland's peripheral ice caps lost mass at -28 ± 11 Gt yr^{-1} (0.08 ± 0.03 mm yr^{-1} SLR equivalent), representing 20% of total GrIS mass loss during the ICESat era (Bolch et al., 2013).

A combined analysis of ICESat data and airborne laser altimeter data from the NASA Airborne Thematic Mapper (ATM) suggest a mass loss rate of -243 ± 18 Gt yr^{-1} (0.68 ± 0.05 mm yr^{-1} SLR equivalent) for the 2003–2009 period (Csatho et al., 2014). The SERAC method was used to combine ICESat and ATM XO and RT points and an SMB model was used to diagnose spatial differences in thinning, likely representing the most comprehensive analysis of spatiotemporal variability in dH/dt and its attribution to SMB vs D for the ICESat era. Negative SMB accounted for 52% of total mass loss and accelerated during the study period. Persistent SMB decreases were concentrated in the southwest and southeast marginal ablation zones but an acceleration in thinning due to SMB was also observed in the northwest. On average, dynamic thinning of outlet glaciers decelerated during the study period, but large spatiotemporal variability was found with some outlets accelerating, owing to local scale controls on ice dynamics (e.g. bed geometry). Regionally, the largest contribution to D was from southeast outlet glaciers, with the largest thinning rates observed on Helheim and Kangerdlugssuaq glaciers and on Sermeq Kujalleq (Jakobshavn Isbræ) in the west. As with prior studies (e.g. Thomas et al., 2006), a slight thickening of the interior ice sheet above the ELA was found.

4.2 The input-output method

Satellite altimetry is unique in that it provides spatially resolved estimates of mass changes, but attribution of dH/dt to SMB vs D requires estimating SMB with a regional climate model and treating D as a residual. Alternatively, the input-output method (IOM) is used to calculate D directly from remotely sensed ice surface velocity and outlet glacier geometry (van den Broeke et al., 2009; Enderlin et al., 2014; Mouginot et al., 2019; Rignot et al., 2004, 2008; Rignot and Thomas, 2002; Shepherd et al., 2012). Ice surface velocity is obtained from offset-feature tracking of optical (Bindschadler and Scambos, 1991; Fahnestock et al., 2016; Joughin et al., 2018; Lucchitta and Ferguson, 1986; Rosenau et al., 2015) or interferometric SAR imagery (Joughin, 2002; Joughin et al., 1995, 1998, 2000; Mouginot et al., 2017; Rignot et al., 1995), and outlet glacier (flux gate) geometry from airborne radar soundings of ice sheet thickness (Bamber et al., 2013; Gogineni and Yan, 2014; Gogineni et al., 2001), or a mass conservation approach that combines the

two, recently with fjord bathymetry and for the entire ice sheet (Millan et al., 2018; Morlighem et al., 2011, 2017; Morlighem and Willis, 2016).

As with altimetric surveys of dH/dt, the IOM reveals a complex spatial pattern of ice sheet mass loss concentrated in narrow outlet glaciers along the coastal margins, with longer term (e.g. 1990–present) mass losses concentrated in the southeast and the Jakobshavn basin in the west, and recent (post 2005) increases concentrated in the northwest (Enderlin et al., 2014; King et al., 2018; Mankoff et al., 2019; Mouginot et al., 2019; Rignot et al., 2004). In general, a small number of isolated glaciers drive the majority of D with just four (Sermeq Kujalleq, Kangerdlugssuaq, Køge Bugt, and Ikertivaq South) accounting for ~50% of total D acceleration during the period 2000–2012 (Enderlin et al., 2014; Howat et al., 2011; Mouginot et al., 2019). The IOM provides the longest record of D and therefore uniquely places recent MB trends in a long term context. For example, although negative SMB accounts for approximately 60% of MB for the period 1990–present, the proportion is reversed for the period 1972–2018, although debate exists about the exact contributions (King et al., 2018; Mankoff et al., 2019; Mouginot et al., 2019).

The recent availability of digital bed elevation models, ice surface velocity mosaics, and digital surface elevation models for the entire ice sheet provide new insight into the spatial and temporal drivers of GrIS MB at the scale of individual outlet glaciers and their upstream drainage basins (Howat et al., 2014; Joughin et al., 2018; Morlighem et al., 2017; Mouginot et al., 2017). Mouginot et al. (2019) reconstruct 46 years of MB for 260 individual outlet glaciers for the period 1972–2018, using surface velocity constructed from all available SAR (ALOS/PALSAR, ENVISAT/ASAR, RADARSAT-1/2, and Sentinel-1b) and Landsat-8 optical imagery (Mouginot et al., 2017), ice thickness from BedMachine v3 (Morlighem et al., 2017), and surface topography from the Greenland Ice Mapping Project DEM (Howat et al., 2014), WorldView DEMs, and historical orthophotographs (Korsgaard et al., 2016). The MB switched from +47 ± 21 Gt yr^{-1} in 1972–1980 to -187 ± 17 Gt yr^{-1} in 2000–2008, and -286 ± 20 Gt yr^{-1} in 2010–2018, within the bounds of most estimates from altimetry and GRACE for the latter two periods. As in Enderlin et al. (2014), they find four glaciers (ibid) control half the mass loss during 2000–2012, but for the 1972–2018

study period Ikertivaq South gained mass while Steenstrup-Dietrichson in northwest, Humboldt in north, and Midgårdgletscher in southeast join the three others as dominant drivers of mass loss. The largest single historical contributor is Sermeq Kujalleq (Jakobshavn Isbræ), which has experienced long term retreat and episodic rapid acceleration (Joughin et al., 2004) including the disintegration of its floating ice tongue between 2000–2003 and rapid retreat of its calving front (Figure 1-6) (Alley, 2005; Andersen et al., 2019; Joughin et al., 2004, 2008; Luckman and Murray, 2005; Moon and Joughin, 2008). Whereas ice discharge has historically been dominated by the southeast, northwest, and western sectors, they conclude that the north and northeast sectors are of greatest importance to future sea level rise owing to their present-day slow velocities and potential for large increases in D.

4.3 Time variable gravimetry and the twin-GRACE mission

The NASA/German Aerospace Center twin Gravity Recovery and Climate Experiment (GRACE) satellites (2002–2017) are conceptually unique from all other remote sensing platforms because they do not measure interaction between the earth and electromagnetic radiation (Tedesco, 2015). As the twin GRACE satellites orbit, their proximal distance varies with earth's gravitational pull. These small changes in their acceleration are used to measure variations in the density of earth at ~400–500 km spatial resolution. Consequently, GRACE provides the only direct measurement of ice sheet MB and independent validation of MB estimates made from satellite altimetry and RCMs (Figure 1-7) (Ramillien et al., 2006, 2008; Velicogna and Wahr, 2006).

As an independent dataset, many studies have combined or compared GRACE MB with satellite altimetry or other traditional remote sensing techniques (Kjeldsen et al., 2013). GRACE MB has been compared to ERS radar altimetry (Su et al., 2015), to surface melt extent from MODIS thermal imagery (Hall et al., 2008b), and to MB from combined RCM SMB and InSAR derived D (Sasgen et al., 2012a). These comparisons confirmed earlier findings from both satellite altimetry and RCMs that the GrIS MB declined at an accelerating rate during the post-2002 period (Su et al., 2015; Velicogna, 2009; Velicogna and Wahr, 2013). GRACE MB estimates range from -191 ± 21 Gt yr^{-1} between 2002–2009 (Ewert et al.,

2012b) to -244 ± 6 Gt yr^{-1} between 2002–2016, with an acceleration of -28 ± 9 Gt yr^{-2} during this period (Harig and Simons, 2016). An updated analysis of GRACE data suggests the negative MB acceleration halted in 2013 owing to suppression of surface runoff production in west Greenland caused by a shift in the North Atlantic Oscillation to its cool phase (van Angelen et al., 2014; Bevis et al., 2019).

The accuracy of GRACE data is inherently limited by its spatial resolution, with accuracy decreasing as spatial resolution increases (Harig and Simons, 2012; Ramillien et al., 2008; Wouters et al., 2008). Sophisticated signal processing methods are required to determine the optimal spatial resolution and to quantify the spatial dependence of signal processing error (Velicogna and Wahr, 2013; Wahr et al., 2006; Watkins et al., 2015). For example, north-south oriented spatially correlated errors ("striping") are a persistent issue (Swenson and Wahr, 2006). Most early methods used the Mascon approach to extract the GRACE signal onto a geometric grid (Velicogna and Wahr, 2005, 2006). Recent work has shown spherical Slepian functions theoretically maximize spatial resolution of the GRACE signal (Harig and Simons, 2016). The Slepian solutions were used to extract MB trends at previously unresolvable scale, showing nearby Baffin Island and Ellesmere Island MB trends of -22 ± 2 and -38 ± 2 Gt yr^{-1}, respectively (Harig and Simons, 2016). In addition to signal processing errors, the glacial isostatic adjustment effect on the GRACE signal is ~5–20 Gt yr^{-1} for the GrIS but is uncertain (Barletta et al., 2008; Sasgen et al., 2012b).

The GRACE Follow-On (GRACE-FO) mission (launched May 22, 2018) is the successor to the GRACE mission (Flechtner et al., 2014). GRACE-FO uses the same orbital acceleration measurement technology as the original GRACE mission and will continue the GRACE measurement time series for a planned ten years. In addition to providing gravity time series continuity, GRACE-FO will test a laser ranging interferometer that is expected to improve the satellite-to-satellite distance measurement relative to the GRACE microwave ranging system (Flechtner et al., 2016; Turyshev et al., 2014). Following a period of in-orbit checks, GRACE-FO entered the science phase of its mission in January, 2019 (Greicius, 2018). The first GRACE-FO Level-1 data products were released on May 24, 2019, and Level-2 gravity field products were released June 10, 2019, with planned monthly release updates thereafter (NASA/JPL-Caltech, 2019).

5 Remote sensing of ice surface reflectance and albedo

Surface albedo modulates the absorption of shortwave radiation by ice and snow surfaces (Warren, 1982). Shortwave radiation is the dominant contributor to melt energy in the GrIS ablation zone (van den Broeke et al., 2008). Consequently, albedo is an important control on the production of surface meltwater and, by extension, the SMB (van Angelen et al., 2014). Satellite remote sensing instruments measure multispectral reflectance, which is used to estimate albedo (Schaaf et al., 2002). Remotely sensed albedo is used to understand spatial patterns in surface melting, as input to land surface models and regional climate models that simulate the SMB, and as a diagnostic marker of the changing ice surface (van Angelen et al., 2012; Box et al., 2012; Nolin and Stroeve, 1997; Ryan et al., 2019; Tedesco et al., 2016). The following subsections summarize key terminology relevant to spaceborne measurement of surface reflectance and albedo, the sensors and datasets used to retrieve the GrIS surface albedo, observed changes in GrIS albedo and their diagnosis, and current challenges and future opportunities for understanding the GrIS ablation zone albedo.

5.1 Definition of reflectance, BRDF, and albedo

Standardized nomenclature for reflectance quantities were defined in terms of incident and reflected beam geometry by Nicodemus et al. (1977) and later adapted for common optical remote sensing measurement configurations (Di Girolamo, 2003; Martonchik et al., 2000; Schaepman-Strub et al., 2006; Snyder, 2002). Here we briefly review key definitions of reflectance quantities, following Schaepman-Strub et al. (2006). Spectral radiance, L, is the radiant flux in a beam per unit wavelength and per unit area and solid angle of that beam, with SI units [W m^{-2} sr^{-1} nm^{-1}]. Reflectance is the ratio of exitent radiant flux density (radiant exitance, M) [W m^{-2}] to incident radiant flux density (irradiance, E) [W m^{-2}], where both the incident and exitent radiance are integrated across the beam geometry [sr] and radiant spectrum [nm] (Schaepman-Strub et al., 2006). For passive optical remote sensing measurements, the incident beam geometry is hemispherical and is composed of both direct-beam and diffuse solar radiation (Figure 1-8). The exitent (reflected) beam geometry is conical, defined by the sensor instantaneous field of view (IFOV), and is

composed of both direct-beam and diffuse reflected solar radiation, corresponding to the hemispherical-conical reflectance function (HCRF) described by Schaepman-Strub et al. (2006).

The bidirectional reflectance distribution function BRDF [sr^{-1}] describes the scattering of an infinitesimal beam of incident light from one direction in a hemisphere into another direction, and is defined as the ratio of directional reflected radiance L_r [W m^{-2} sr^{-1}] to incident irradiance E_i [W m^{-2}]:

$$BRDF = \frac{dL_r(\theta_i, \phi_i, \theta_r, \phi_r)}{dE_i(\theta_i, \phi_i)} \quad (6)$$

where θ_i and θ_r are the incident and reflected viewing angle, respectively, and ϕ_i and ϕ_r are the incident and reflected azimuth angles, respectively. As a ratio of infinitesimal quantities, the BRDF is a theoretical construct that cannot be directly measured, but describes the intrinsic reflectance properties of a surface from which measurable quantities can be derived (Schaepman-Strub et al., 2006). For example, integration of the BRDF across $\theta_r(0 \rightarrow \pi/2)$ and $\phi_r(0 \rightarrow 2\pi)$ yields bihemispherical reflectance, or what is commonly called albedo.

Viewing geometry is important because every natural earth surface is an anisotropic reflector. For example, snow and ice are strongly forward scattering at the particle scale, especially at visible wavelengths, but ice surfaces can be strongly backward scattering due to surface roughness (Nolin et al., 2002). Consequently, an estimate of the BRDF is required to convert directional reflectance measured by satellite remote sensing instruments to albedo. To achieve this, the BRDF for each satellite ground footprint is estimated (not measured) from repeat directional reflectance measurements collected over time and therefore under varying illumination conditions (Schaaf et al., 2002) or collected instantaneously by spaceborne multi-angular instruments (Stroeve and Nolin, 2002). A complete technical discussion of the BRDF is available from Schaepman-Strub et al. (2006).

5.2 Optical reflectance and albedo sensors and datasets

Spatially- and temporally-consistent repeat measurements of surface reflectance, and estimates of BRDF and albedo for the Greenland Ice Sheet are provided by satellite-borne imaging spectrometers including the NASA Moderate Resolution Imaging Spectroradiometer (MODIS), the NASA Multi-angle Imaging

SpectroRadiometer (MISR), and the National Oceanic and Atmospheric Administration's Advanced Very High Resolution Radiometers (AVHRR) (Table 1-2) (Bindschadler et al., 2001; Stroeve, 2001; Stroeve et al., 2006; Stroeve and Nolin, 2002). Other notable spaceborne sensors providing surface reflectance that have been used to study the GrIS ablation zone include the Enhanced Thematic Mapper Plus (ETM+) on board Landsat 7, the Operational Land Imager (OLI) on board Landsat 8, the ASTER on board Terra, the High Resolution imagers on board the Satellite Pour l'Observation de la Terre (SPOT 1-7), the Global Land Imager (GLI) on board the Advanced Earth Observing Satellite II (ADEOS-2), the Multispectral Imager (MSI) on-board Sentinel-2, and the Ocean Colour and Land Instrument (OLCI) on board Sentinel-3A/B (Table 1-2) (Arnold et al., 2014; Georgiou et al., 2009; Hori et al., 2007; Pope et al., 2016; Sohn and Jezek, 1999; Wang et al., 2018; Yang et al., 2019a).

The NOAA Extended AVHRR Polar Pathfinder (App-X) product provides surface broadband all-sky albedo and a suite of surface radiative flux and cloud property variables on a 25 km equal area grid twice-daily for the period 1982 to present for the Arctic and Antarctic regions (Key et al., 2014). The AVHRR App-X product provides a continuous record of GrIS surface albedo and an important climatological dataset (Tedesco et al., 2016). An early demonstration of AVHRR surface albedo retrieval revealed a region of anomalously dark ice in the southwestern GrIS ablation zone later termed the "Dark Zone" (Section 5.3) (Knap and Oerlemans, 1996). Although rigorous quality control procedures are applied during dataset production (Key et al., 2016), its utility for investigations of GrIS ablation zone albedo may be limited by geolocation errors, four-channel spectral resolution, and inter-mission biases (Box et al., 2006; Stroeve et al., 2001). Spatial and spectral resolution are both improved with MODIS, which measures surface reflectance in 30 narrow spectral bands at 250–500 m spatial resolution.

Higher spectral and/or spatial resolution reflectance products are provided by Landsat, MISR, SPOT, Sentinel, and other spaceborne spectrometers (Table 1-2). Various albedo estimations exist for most sensors (Liang, 2001). Many rely on the MODIS BRDF or empirical conversions from narrowband reflectance to broadband albedo, and for others (e.g. MISR) a unique BRDF and physically-based albedo estimation exists (Greuell and Oerlemans, 2004; Stroeve and Nolin, 2002). Most studies of the GrIS albedo

have used MODIS albedo owing to the development of operational, publicly available data products spanning nearly two decades. Two MODIS albedo products are currently available: 1) the 500-m Terra/Aqua MODIS 8-day BRDF/Albedo product (MCD43) and, 2) the 500-m Terra daily snow/ice cover and BRDF/Albedo product (MOD10A) (Schaaf et al., 2002; Stroeve et al., 2013, 2006). The MCD43 algorithm uses cloud-free, multi-date, atmospherically corrected input data from combined Terra (MOD09) and Aqua (MYD09) directional surface reflectance retrievals to estimate a unique BRDF for each MODIS pixel in the seven MODIS 'Land' bands (1–7) every eight days. Albedo is calculated using this BRDF estimation for each of bands 1–7, and also for three broad-bands (0.4–0.7, 0.7–3.0, and 0.4–3.0 um) (Schaaf et al., 2002; Stroeve et al., 2013).

The MOD10A algorithm is a daily product that uses the discrete-ordinate radiative transfer (DISORT) model to convert MOD09 daily directional surface reflectance to spectral albedo (Klein and Stroeve, 2002). The daily frequency of the MOD10A product makes it particularly useful for studies of the GrIS ablation zone, where day-to-day albedo variability is substantial (Ryan et al., 2017b, 2019). Both the MCD43 and MOD10A retrieval algorithms require cloud-free images, as identified by the MOD35 cloud mask. For the MCD43 product, data gaps within the 16-day period window may result in under-sampling of the BRDF, requiring use of a backup BRDF algorithm. Albedo values estimated with the backup algorithm are generally considered less reliable, and quality flags are provided to distinguish between them (Schaaf et al., 2011).

The accuracy of MODIS albedo over the GrIS has been evaluated by comparison with surface-based measurements of albedo at Greenland Climate Network (GC-Net) automatic weather stations (AWS) (Steffen et al., 1996). The MCD43 product has an average root mean squared difference (RMSD) of ±0.07 and mean bias +0.022 relative to AWS albedo, which has ±0.035 RMSD uncertainty relative to precision pyranometer measurements (Stroeve et al., 2005, 2013). The MCD43 RMSD is reduced to ±0.04 when only the highest-quality flagged values are used (Stroeve et al., 2005). MODIS albedo accuracy is reduced at high solar zenith angle (SZA) (Stroeve et al., 2005, 2006). For example, Wang and Zender (2010) found large MCD43 albedo bias relative to GC-Net AWS albedo in the dry-snow zone for SZA>55^{o}. However,

these biases are mostly eliminated if only the highest-quality flagged values are used as recommended (Schaaf et al., 2011). In general, the MODIS albedo products are not recommended for comparison with surface measurements for SZA>70^{o} (Schaaf et al., 2011; Stroeve et al., 2005).

Relative to three AWS stations in the southwestern GrIS ablation zone, the MOD10A albedo is lower by up to 0.10 and by 0.06 on average during July for the period 2009–2016 (Ryan et al., 2017b). The low bias is attributed to inadequate sampling of surface heterogeneity by the AWS, which are preferentially located on flat areas of bare ice rather than areas of lower albedo such as meltwater channels or crevasses that influence the satellite albedo (Ryan et al., 2017b). Using one day of high quality in situ spectral albedo measurements (N=232) collected within two MODIS satellite pixel ground footprints in the southwest GrIS ablation zone, Moustafa et al. (2017) showed that the MODIS Collection V006 daily blue-sky albedo was accurate to within -0.04 to +0.07 for the homogeneous surface of one pixel and was biased low by -0.04 to -0.07 for the heterogeneous surface of the second pixel. As in Ryan et al. (2017b), the low bias was attributed to under sampling of dark meltwater channels and shadowed crevasses. In addition to spatial heterogeneity, comparisons between satellite albedo and surface measurements are complicated by factors including spatial scale, sensor spectral sensitivity, and whether hemispherical or directional reflectance is measured (Schaaf et al., 2011; Stroeve et al., 2005). Owing to these varied processes, ground validation of satellite albedo products for the GrIS ablation zone is challenging and satellite retrieval uncertainty is enhanced relative to the interior snow covered accumulation-zone surface, especially at sub-pixel scale (Moustafa et al., 2015, 2017; Ryan et al., 2017b).

5.3 Dark ice in the ablation zone: albedo trends and drivers

Satellite albedo retrievals provide an important marker of the changing ice surface. The MOD43 data suggest the GrIS area-averaged albedo for June, July, and August (JJA) decreased by -0.044 between 2000–2012 (Stroeve et al., 2013). The JJA albedo anomaly during the record 2012 pan-GrIS melt event (Nghiem et al., 2012) was more than two standard deviations below the period mean. The most negative albedo trends are observed for the southern and western ice sheet ablation area where July albedo trends are -0.12

to -0.24 per decade, attributed to both reduced seasonal snow cover duration and increased bare ice exposure during this period (Box et al., 2012; Stroeve et al., 2013; Tedesco et al., 2011). The MOD10A product indicates a similar JJA albedo trend of -0.083 averaged over the GrIS ablation zone for the period 2000–2010 (Box et al., 2012) and -0.078 for the period 2000–2013 (Alexander et al., 2014). Although MOD10A reflectance data suggest a modest brightening of the ablation zone since 2013 that likely reflects anomalously cold and snowier spring and summer conditions during this period (Ryan et al., 2019; Tedstone et al., 2017), there is strong potential for melt-albedo feedbacks to accelerate negative SMB in the coming years (2012; Franco et al., 2013).

For the ablation zone, spatial and temporal albedo variability is driven foremost by the seasonal snowline position and its control on bare ice exposure (Figure 1-9) (Ryan et al., 2019). Where snow is present, snow grain growth is the strongest modifier of surface albedo (Nolin and Stroeve, 1997; Tedesco et al., 2016). Bare ice albedo is scale dependent but is principally controlled by air bubble size and shape distribution, , shadowing by cracks and crevasses (Dadic et al., 2013; Moustafa et al., 2017), and by ice grain metamorphism, surface meltwater presence, and exposure and deposition of mineral and biological light absorbing impurities (LAI) (Benning et al., 2014; Goelles and Bøggild, 2017; Ryan et al., 2018; Tedesco et al., 2016; Tedstone et al., 2017; Wientjes and Oerlemans, 2010; Yallop et al., 2012). The darkening effect of LAI is particularly apparent in satellite images of the GrIS ablation zone that reveal foliated bands of "dark ice" with anomalously low albedo relative to surrounding ice (Figure 1-10) (Greuell and Knap, 2000; Knap and Oerlemans, 1996; Wientjes et al., 2012; Wientjes and Oerlemans, 2010). The wavy appearance of these foliated bands and their static position indicate their provenance as outcropping ice layers rich in dust deposited during past millennia (Bøggild et al., 1996; Wientjes et al., 2011, 2012; Wientjes and Oerlemans, 2010).

The spatial extent of bare ice and albedo variability within the bare ice zone exerts a primary control on ice sheet albedo and surface meltwater production in the ablation zone (Box et al., 2012; Ryan et al., 2019). Shimada et al. (2016) used MODIS/Terra surface reflectance to quantify the regional distribution of bare ice and dark ice extent during July for the period 2000–2014. The spatial extent of bare ice ranged

from 5–16% of the GrIS surface area, dark ice ranged from 4–10%, and both exhibited a positive trend (4.4% yr^{-1} for bare ice and 7.6% yr^{-1} for dark ice) with the greatest expansion in the southwest ablation zone. Bare ice extent was strongly correlated ($r = 0.66$) with air temperature, whereas dark ice extent was weakly correlated with air temperature and was negatively correlated with solar radiation, suggesting that bare ice weathering by solar radiation may reduce dark ice extent and increase surface albedo in the GrIS ablation zone (Figure 1-11).

Recent work highlights the darkening effect of biological LAI on bare ice albedo, including assemblages of biologically-active dust termed "cryoconite" that melt quasi-cylindrical holes into the ice (Figure 1-11) (Hodson et al., 2010) and distributed communities of algae and cyanobacteria that inhabit the ice surface (Uetake et al., 2010). For example, Tedstone et al. (2017) applied the bare ice and dark ice detection algorithm from Shimada et al. (2016) to MODIS surface reflectance imagery of the southwest ablation zone during June-July-August for the period 2000–2016. In contrast to Shimada et al. (2016), they conclude that distributed algae blooms, rather than bare ice weathering and cryoconite hole growth, likely explains dark ice dynamics in their study region, owing to the synchronous and abrupt timing of dark ice exposure across the study area and the progressive rather than episodic increase in dark ice extent from June to August. In general, the deepening of cryoconite holes into the ice surface appears to limit their regional effect on albedo, especially at low sun angle (Figure 1-11d) whereas distributed LAI that accumulate on the ice surface appear to control bare ice darkening in the GrIS ablation zone (Ryan et al., 2018; Stibal et al., 2017). Understanding seasonal and interannual relationships between bare ice structure, mineral and biological LAI, and bare ice albedo driven by cryoconite hole deepening and removal, weathering crust growth and decay, rotting and removal of superimposed ice, and variations in ice grain and air bubble geometry remain important areas of research that currently elude confident detection by satellite remote sensing (Chandler et al., 2015; Cook et al., 2017b; Cooper et al., 2018; Shimada et al., 2016; Tedstone et al., 2017).

5.4 Current challenges and future opportunities

Contemporary research on GrIS ablation zone surface reflectance and albedo is focused on understanding and diagnosing agents of albedo change (Tedesco et al., 2016). Important questions remaining unresolved include whether observed reductions in GrIS snow albedo are caused by enhanced snow grain metamorphism due to a warming climate (Nolin and Stroeve, 1997), or by deposition of LAI such as dust and black carbon from industrial emissions and/or forest fire (Goelles and Bøggild, 2017). These questions cannot currently be answered owing to spectral and radiometric limitations of existing spaceborne optical sensors and inadequate surface validation measurements (Ryan et al., 2017b; Tedesco et al., 2015). For example, it is unlikely that the albedo-reducing effect of industrial black carbon emissions on relatively clean accumulation zone snow can be detected from space (Warren, 2013; Zege et al., 2008). Similarly, it is unknown if bare ice albedo reduction due to deposition or emergence of inorganic mineral LAI can be distinguished using satellite imagery from albedo reduction due to biological LAI (Cook et al., 2017b; Goelles and Bøggild, 2017).

To date, efforts to remotely sense changing bare ice albedo have focused on quasi-physical proxies such as "darkening" in broad spectral bands (Ryan et al., 2018; Tedstone et al., 2017). Hyperspectral reflectance is used to map the albedo reducing effect of LAI including snow algae and dust in mountain environments and valley glaciers elsewhere (Painter et al., 2001; Takeuchi et al., 2006). However, ice algae are taxonomically distinct from snow algae (Yallop et al., 2012), and optical methods developed by the snow albedo community need to be adapted to detect ice algae or separate its effect on ice albedo from inorganic impurities or variations in ice grain size and structure (Cook et al., 2017b; Goelles and Bøggild, 2017). At present, no spaceborne hyperspectral imager operates over the polar regions, although several hyperspectral missions are planned for the coming years (Transon et al., 2018). Recently, multispectral reflectance imagery from the OLCI on-board Sentinel-3A was used to infer the spatiotemporal distribution of ice algal blooms in the southwest GrIS ablation zone, providing insight into the capability of enhanced spectral resolution for diagnosing albedo change in the polar regions (Wang et al., 2018). While this represents an important first step toward bioalbedo detection from space, additional ground validation of

cellular optical properties specific to the microbial communities on the GrIS surface is needed to discriminate the individual drivers of bare ice albedo reduction using satellite remote sensing (Cook et al., 2017b, 2017a).

6 Mapping surface melt and glaciological zones

Mapping of surface zones or facies such as dry snow, wet snow, and bare ice was pioneered by Benson (1962), and later mapped across the GrIS using both ERS SAR imagery (Fahnestock et al., 1993) and Seasat-A scatterometer backscatter (Long and Drinkwater, 1994). In contrast to the climatological facies of Benson (1962), the concept of radar glacier zones was introduced to distinguish dynamic zones driven by the seasonal cycle of surface melt onset, surface roughening, and snowline migration, thereby revealing the seasonal extent of the bare ice ablation zone (Forster et al., 1996; Smith et al., 1997). Multi-angular optical reflectance together with derived surface roughness provides an independent method to map glacier zones on the GrIS with particular relevance to ablation zone studies owing to the unique ability of angular reflectance to detect crevasse fields and the lower limit of superimposed ice (Nolin and Payne, 2007). These classification approaches are complemented by an extensive legacy of surface melt detection studies using active microwave backscatter, and thermal and passive microwave brightness temperature, which together provide a comprehensive view of the ablation zone surface and changes in ice sheet melt extent with time (Abdalati and Steffen, 1995; Fettweis et al., 2011; Hall et al., 2006; Jezek et al., 1994; Mote, 2007).

6.1 Active microwave detection of surface melt and glacier zones

SAR imagers measure radar backscatter (image brightness) at (typically) C-band (5 GHz) and Ku-band (14 GHz) frequencies (Table 1-3). Backscatter strength, or the normalized radar cross-section (σ^o), is principally controlled by the complex electrical permittivity of the ice surface and by geometric properties including ice surface roughness, grain size, incidence angle, and ice thermal and physical structure (Fahnestock et al., 1993; Shi and Dozier, 1993). Variations in σ^o associated with these controls are used to map zones of unique snow and ice composition on glacier and ice sheet surfaces (Ashcraft and Long, 2006). An early demonstration of the method used variations in C-band SAR image brightness to map zones of dry snow,

percolation, wet snow, and bare ice, extending the early facies work of Benson (1962) into the satellite era (Fahnestock et al., 1993). Cold, dry, fine-grained snow in the accumulation zone appears dark in C-band imagery, whereas the percolation zone and wet snow zone appear bright, owing to reflections from refrozen ice lenses in the snow/firn column (Jezek et al., 1994). The bare ice zone is distinguished from the wet snow zone using differential brightness between winter and summer images and the bright reflections of rough, crevassed surfaces (Fahnestock et al., 1993; Partington, 1998).

C- and Ku-band wind scatterometers measure σ^o at both vertical (VV) and horizontal (HH) polarization and are used to map the timing of melt onset and the seasonal progression of surface melt extent (Nghiem et al., 2001; Smith et al., 1997). As with SAR, the method exploits the strong reduction in σ^o caused by presence of liquid water at or near the ice surface. Relative to SAR imagers, scatterometers provide σ^o at coarse spatial resolution but high temporal resolution, for example 25 km grid size twice-daily for the SeaWinds on NASA's Quick Scatterometer (QuikSCAT) (Nghiem et al., 2001). Resolution enhancement techniques increase effective resolution to ~8–10 km (Early and Long, 2001).

Surface melt on the GrIS and peripheral ice caps has been detected by the Seasat-A scatterometer (SASS), the Advanced Microwave Instrument-Scatterometer (AMI-SCAT) on ERS-1/2, and the SeaWinds scatterometer on both NASA's Quick Scatterometer (QuikSCAT) and ADEOS-2 (Table 1-3) (Ashcraft and Long, 2006; Hicks and Long, 2011; Long and Drinkwater, 1994; Nghiem et al., 2001; Smith et al., 2003; Wismann, 2000). Methods to detect surface melt include single-channel absolute σ^o thresholds (Wismann, 2000), diurnal σ^o variability (relative thresholds) (Nghiem et al., 2001), physical and statistical model-based methods (Hicks and Long, 2011), and dual-frequency/polarization thresholds that also use the diurnal difference between ascending and descending orbital passes (Li et al., 2017). The diurnal method exploits contrasts in σ^o caused by diurnal melt-freeze cycles. The use of relative thresholds reduces errors from sensor drift, cross-mission biases, or step changes in surface properties such as ice lens formation that affect absolute thresholds (Nghiem et al., 2005). In addition to discrete melt onset, time-integrated σ^o reduction is used to infer seasonal melt intensity (Hicks and Long, 2011; Smith et al., 2003; Wismann, 2000).

In addition to mapping surface melt onset and extent, seasonal changes in σ^o are used to infer the timing and spatial extent of ice layer formation in snow and firn (Jezek et al., 1994; Nghiem et al., 2005; Wang et al., 2007). Understanding ice layer formation is important because meltwater refreezing increases firn density without reducing mass and raises the effective backscattering surface detected by radar altimeters, leading to errors in radar mass balance estimates (Section 3.1.3). Nghiem et al. (2005) developed a field-validated method that relates threshold increases in QuickSCAT HH-polarized σ^o before and after melt seasons to ice layer formation in the GrIS percolation zone. The method also provides a basis for estimating snow accumulation by integrating σ^o reduction following ice layer formation. The method assumes threshold increases in σ^o are caused by enhanced reflections from newly formed ice layers whereas the gradual attenuation of σ^o following ice layer formation is caused by new snow accumulation. Wang et al. (2007) applied the method to 5 years of enhanced-resolution QuickSCAT imagery (Long and Hicks, 2005) and found extensive increases in ice layer formation following a short 3-day melt event in 2002, highlighting the disproportionate impact of extreme melt events on ice layer formation.

6.2 Passive microwave and thermal radiometry

At thermal and microwave wavelengths (beyond about 3 um) spectral radiance (converted via the Planck function to brightness temperature, T_b) is approximately linear with T_sfc: $T_\mathrm{b} = \varepsilon * T_\mathrm{sfc}$, where ε is the material emissivity (Wan and Dozier, 1989). Whereas σ^o is dramatically reduced by liquid water in snow, T_b is dramatically increased, forming the basis for surface melt detection threshold algorithms, typically using a threshold value below freezing to indicate melting (Abdalati and Steffen, 1995; Chang et al., 1976; Mote et al., 1993). Passive microwave radiometers measure background microwave emission at (primarily) K-band (~19 GHz) and Ka-band (~37 GHz) frequencies and various combinations of VV and HH polarization (Table 1-4). In contrast to the higher spatial resolution (~10 km^2) but lower temporal resolution (weeks to months) of spaceborne active microwave sensors, passive microwave sensors provide T_b twice-daily at ~25–50 km^2 spatial resolution and complete ice sheet coverage. Melt detection methods using T_b include single-channel thresholds (Mote et al., 1993; Mote and Anderson, 1995), dual

frequency/polarization combinations (cross polarized gradient ratio XPGR) (Abdalati and Steffen, 1995, 2001), and diurnal amplitude variations (DAV) on ascending and descending passes (Ramage and Isacks, 2002; Tedesco, 2007). As with σ^o, microwave T_b is strongly modified by liquid meltwater presence at the ice sheet surface but typically does not provide information about the internal snow or firn structure (Tedesco, 2015; Wismann, 2000).

With more than 30 years of continuous data collection, pan-GrIS spatial coverage, and all-weather capability, spaceborne passive microwave radiometers provide unique insight into the climatic drivers of ice sheet surface mass balance processes, including changes in the location and extent of surface melting (Figure 1-12) (Abdalati and Steffen, 1995, 2001; Bhattacharya et al., 2009; Fettweis et al., 2011; Mote, 2007; Tedesco, 2007; Tedesco et al., 2013). Data from the Special Sensor Microwave/Imager (SSM/I) suggests the area of active surface melt over the GrIS has approximately doubled since the early 1990s, with a 40,000 km^2 yr^{-1} trend during this period (Fettweis et al., 2011; Tedesco, 2007). Data from the Scanning Multichannel Microwave Radiometer (SMMR, 1978-1987) and SSM/I were used to characterize the effects of the Mt. Pinatubo eruption on GrIS surface melt patterns (Abdalati and Steffen, 1997). Surface melt extent from SSM/I has been correlated with downstream sediment plume concentrations in Greenland fjords driven by ice sheet meltwater discharge (Chu et al., 2009), to validate surface melt extent calculated from surface energy balance models (Mernild et al., 2010, 2011), and to quantify extreme events such as the record July 2012 melt event when 98.6% of the GrIS surface was actively melting (Nghiem et al., 2012; Tedesco et al., 2013).

Thermal radiance (~3–14 μm) is used to map T_{sfc} and provides an additional method for surface melt detection (Stroeve et al., 1996). Variations in thermal and optical radiance form the basis for mapping "reflectance zones" to characterize melt presence and changes in thermal structure on glacier surfaces (Hall et al., 1987). Whereas σ^o and microwave T_B are primarily diagnostic of melt presence, both at or near the surface, thermal radiance is diagnostic of the surface "skin" temperature, and provides little to no information about subsurface temperature, meltwater presence, or snow and firn structure. Consequently, thermal T_{sfc} is strictly an indicator of surface melt and, together with the higher spatial and radiometric

resolution of thermal sensors such as MODIS, provides an independent method for validating active and passive microwave melt presence products (Hall et al., 2009; Välisuo et al., 2018). When combined with microwave melt presence and remotely sensed albedo, thermal T_{sfc} may improve discrimination of surface and subsurface melt areas and diurnal variations in melt-freeze cycles (Hall et al., 2009). As with microwave surface melt detection, thermal radiance melt detection has been used to validate modeled surface melt (Fettweis et al., 2011; Mernild et al., 2010), and to study the spatiotemporal variation of surface melt extent and duration on the GrIS and its relation to climatic variability (Hall et al., 2006, 2008a, 2008b, 2013; Välisuo et al., 2018).

The primary spaceborne thermal sensors used to obtain T_{sfc} are MODIS and AVHRR. The NOAA Extended AVHRR Polar Pathfinder (App-X) product provides T_{sfc} on a 25 km polar equal-area grid twice-daily for the period 1982 to present (Key et al., 2014). As with the AVHRR albedo product (Section 5.2), there are spectral, radiometric, and inter-mission homogenization issues that limit its utility (Hall et al., 2012). The MODIS land surface temperature product (MOD11A1) uses the split-window technique developed for AVHRR to calculate T_{sfc} from radiance at 10.78 μm and 11.77 μm (Wan and Li, 2008). The MOD11A1 data are provided on a 1 km grid globally for clear-sky conditions as discriminated by the MOD35 cloud mask. The MOD11A1 product is accurate to ± 1 ºC on average over snow and ice surfaces and agrees to within ± 0.5 ºC with T_{sfc} calculated from ASTER and Landsat ETM+ thermal radiance over the GrIS (Hall et al., 2008a). Surface melt extent from MOD11A1 corresponds closely to surface melt inferred from QuickSCAT using the diurnal σ^{o} method (Hall et al., 2009).

The Greenland Ice Surface Temperature (IST) product is an enhanced version of MOD11A1 that provides IST and binary melt absence/presence for the period 2000–2014 on a 1.25 km polar stereographic grid for the GrIS (Hall et al., 2012, 2013). For values of T_{sfc} near 0 ºC, the IST data are -0.5 ºC cooler than surface-based T_{sfc} measurements collected at Summit Station (Koenig and Hall, 2010; Shuman et al., 2014). The bias increases to -5.0 ºC for values of T_{sfc} near -60 ºC and increases with SZA, suggesting the bias may be related to reduced accuracy of the MOD35 cloud mask at high SZA. Under-sampling of T_{sfc} during

warm inversions with dense cloud coverage may also introduce bias but this effect has not been systematically evaluated (Koenig and Hall, 2010; Shuman et al., 2014). In general, spaceborne thermal T_{sfc} retrievals are effective for detecting surface melt during clear-sky conditions but are sensitive to the atmospheric aerosol and water vapor profile (Hall et al., 2012; Stroeve and Steffen, 1998). To overcome cloud-cover data gaps, Välisuo et al. (2018) gap-filled the IST product with modeled values of T_{sfc} from the European Centre for Medium-Range Weather Forecasts ERA-Interim reanalysis.

6.3 Multi-angular reflectance and surface roughness

The Multi-angle Imaging SpectroRadiometer (MISR) measures coincident-in-time bi-directional radiance in four spectral bands between 450–850 nm at 0° (nadir), 26.1, 45.6, 60.0, and 70.5° fore and aft of nadir. Reflectance is provided on a 275 m grid and 9-day global coverage to ±83° (Table 1-2.) (Nolin et al., 2002). The normalized difference angular index (NDAI) was developed to estimate ice surface roughness from MISR angular reflectance (Nolin et al., 2002). The method uses an empirical relationship between MISR red band reflectance at 60° fore and aft of nadir and ATM lidar-derived surface roughness to develop spatially-continuous maps of surface roughness over ice sheets and sea ice (Nolin and Mar, 2019). The MISR NDAI and near-infrared albedo (Section 5.2) were used to map unique signatures of surface glaciological features in the western GrIS ablation zone including crevasse fields, wet snow, and bare glacier ice (Nolin and Payne, 2007). With this approach, MISR angular reflectance appears to provide a unique method for detecting the superimposed ice zone, and may improve identification of changes in crevasse field roughness relative to SAR and optical sensors (Nolin et al., 2002; Nolin and Payne, 2007).

Surface roughness controls ice-atmosphere interactions via the aerodynamic roughness length and the net vapor flux, an understudied component of the GrIS SMB (Boisvert et al., 2017; Box and Steffen, 2001). The MISR surface roughness product (Nolin and Mar, 2019) was used to define the aerodynamic roughness length of the BMF13 vapor flux model to improve the spatial realism of net vapor flux in the ablation zone where roughness is highly variable (Boisvert et al., 2017). The average annual modeled vapor flux was 14.6 ± 3.6 Gt yr^{-1}, or 6 ± 2% of annual SMB for the period 2003–2014. The average annual

difference between modeled vapor flux with and without MISR roughness was 30 ± 15%. In addition to angular reflectance, surface roughness has been quantified from ICESat and ATM laser altimetry waveforms (Li et al., 2016; van der Veen et al., 2009; Yi et al., 2005). The forthcoming ICESat-2 laser altimeter may provide additional capability for measuring surface roughness on the GrIS, for example using the multi-sensor lidar-angular reflectance approach of Nolin and Mar (2019) and Nolin et al. (2002), which may also be useful for radar altimetry waveform interpretation of the leading edge of the beam footprint (Helm et al., 2014a).

6.4 Future opportunities for mapping the changing GrIS ablation zone surface

The GrIS surface is undergoing rapid change, driven by increased surface meltwater production in the ablation zone. Spaceborne SAR imagers, wind scatterometers, and passive microwave, thermal, and angular radiometers are used to map and monitor diagnostic features of change on the ablation zone surface including surface melt presence and extent, subsurface ice layer formation, ice surface temperature, and ice surface roughness. These characteristic features are used to define and map the dry snow zone, wet snow zone, percolation zone, superimposed ice zone, and the bare ice zone. Mapping of supraglacial hydrologic features including meltwater lakes, rivers, and moulins stands out as an additional research priority (c.f. Pitcher and Smith, 2019), in particular their expansion and inland migration toward sensitive (e.g. high elevation) areas of the ice sheet (Gledhill and Williamson, 2018; Hoffman et al., 2018; Poinar et al., 2015). Other diagnostic markers of change detectable in satellite imagery include end of summer snowline position (Figure 1-9) (Ryan et al., 2019), the lower limit of superimposed ice (Nolin and Payne, 2007), and the lower limit of the slush zone (Greuell and Knap, 2000). Multi-sensor methods, for example optical imagery combined with SAR imagery or scatterometry, shows promise for detecting dynamic regions characterized by changing snow, firn, and ice surface types, including supraglacial lakes and slush fields obscured by snow or clouds, and may reduce detection bias caused by cloud cover (Cooley and Christoffersen, 2017; Koenig et al., 2015; Miles et al., 2017).

7 Conclusion

For over forty years, earth observing satellites sensitive to visible, infrared, and microwave electromagnetic radiation, together with gravimetry, have documented the patterns of change on the GrIS ablation zone surface. Satellite remote sensing data show an ablation zone expanded in size, its albedo and surface elevation lower in response to enhanced melting and ice discharge, and an ice sheet transition from steady state to negative mass balance that now represents the largest land ice contributor to global sea level rise. Already, some 78–85% of the total liquid runoff produced from surface melting is generated in the bare ice ablation zone, despite it covering ~22% of the ice sheet's total surface area, up from ~15% in the early 1960s (Bader, 1961; Benson, 1962; Box et al., 2012; Machguth et al., 2016; Steger et al., 2017). Although often conceptualized as a uniform surface of solid ice, the ablation zone is a dynamic region with widely varying electromagnetic properties controlled by diverse physical, biological, and hydrologic processes. Future progress in remote sensing the ablation zone will likely benefit most from methods that directly address this complexity, for example using multi-sensor, multi-wavelength, and cross-platform datasets. Examples include fusing radar and laser altimetry with optical stereophotogrammetry to discriminate and diagnose causes of surface elevation change (Schenk et al., 2014), or fusing radar and laser backscatter with optical imagery to discriminate snow, ice, liquid water, and refrozen meltwater in sensitive areas near the equilibrium line altitude (Koenig et al., 2015; Miles et al., 2017). Other areas of opportunity recommended for future research include spaceborne detection of subsurface refrozen meltwater and its effects on radar backscatter, which requires additional in-situ validation (Nghiem et al., 2005; Nilsson et al., 2015), the partitioning of ablation zone thinning into ice dynamic and surface mass balance components (Csatho et al., 2014), cross-validation of ice surface elevation change from altimetry with modeled surface mass balance (Sutterley et al., 2018) and modeled ice dynamic motion (Larour et al., 2014), spaceborne diagnosis of changing bare ice albedo (Wang et al., 2018) and grain size (Yang et al., 2017b), and monitoring the inland migration of snowlines, surface melt extent, and surface hydrologic features including lakes, streams, and moulins (Gledhill and Williamson, 2018; Ryan et al., 2019).

8 Tables

Table 1-1. Summary of radar and laser altimeter remote sensing platforms, instruments, temporal coverage, observed wavelength, and managing agencies.

Platform*	Instrument[Ŧ]	Temporal Coverage	Observed Wavelength	Agency[§,Ɣ]
Radar altimeters				
GEOS-3	ALT	1975 - 1978	13.9 GHz (Ku)	NASA
Seasat	ALT	1978 (110 days)	13.6 GHz (Ku)	NASA
Geosat	GRA	1985 - 1990	13.5 GHz (Ku)	DoD/NASA
ERS-1	RA	1991 - 2006	13.8 GHz (Ku)	ESA
ERS-2	RA-2	1995 - 2011	13.575 GHz (Ku), 3.2 GHz (S)	ESA
GFO	GFO-RA	1998 - 2008	13.5 GHz (Ku)	DoD/NASA
EnviSat	RA-2	2002 - 2012	13.575 GHz (Ku), 3.2 GHz (S)	ESA
CryoSat-2	SIRAL	2010 - present	13.9 GHz (Ku)	ESA
SARAL	ALtiKA	2013 - present	36 GHz (Ka)	ISRO/CNES
Sentinel-3A/B	SRAL	2016 - present	13.6 GHz (Ku), 5.4 GHz (C)	ESA
Laser altimeters				
ICESat	GLAS	2003 - 2009	1.064 μm, 0.532 μm	NASA
ICESat-2	ATLAS	2018 - present	1.064 μm, 0.532 μm	NASA
Aircraft	ATM	1977 - present	1.064 μm	NASA
Aircraft	LVIS	1998 - present	1.064 μm	NASA
Aircraft	MABEL	2012 - 2014	1.064 μm, 0.532 μm	NASA

* See Appendix A for expanded acronyms

Ŧ See Appendix B for expanded acronyms

§ See Appendix C for expanded acronyms

Ɣ Managing agencies are identified by WMO OSCAR database (Table D1) and may not reflect joint collaborations

Table 1-2. Summary of optical and near-infrared remote sensing platforms, instruments, temporal coverage, observed wavelengths, and managing agencies.

Platform*	Instrument[†]	Temporal Coverage	Observed Wavelength	Agency[§,¥]
Nimbus 1-4	AVCS/IDCS	1964 - 1980	(1 band) 0.45-0.65 µm	NASA
Landsat 1-5	MSS	1972 - 2013	(4 bands): 0.55-0.955 µm	NASA/USGS
GOES 1-15	VISSR	1975 - present	(5 bands): 0.62-12 µm	NASA/NOAA
Seasat	VIRR	1978	(2 bands): 0.49-0.94, 10.5-12.5 µm	NASA
TIROS-N, NOAA-6,8,10	AVHRR	1978 - 2001	(4 bands): 0.63-11 µm	NOAA/NASA
NOAA 7,9,11-14	AVHRR/2	1981 - present	(5 bands): 0.63-12 µm	NOAA
Landsat 4-5	TM	1982 - 2013	(7 bands): 0.485-11.45 µm	NASA
Spot 1-3	HRV	1985 - 2009	(3 bands): 0.55-0.83 µm	CNES/Spot
ERS-1	ATSR	1991 - 2000	(4 bands): 1.6-12.0 µm	ESA
JERS-1	OPS	1992 - 1998	(8 bands): 0.52-2.40 µm	JAXA
ERS-2	ATSR-2	1995 - 2011	(7 bands): 0.55-12.0 µm	ESA
ADEOS	POLDER	1996 - 1997	(9 bands): 0.44-0.91 µm	CNES
ADEOS	AVNIR	1996 - 1997	(4 bands): 0.42-0.89 µm	JAXA
Spot 4	HRVIR	1998 - 2013	(4 bands): 0.55-1.63 µm	CNES/Spot
NOAA15-19, MetOp A-C	AVHRR/3	1998 - present	(6 bands): 0.63-12.0 µm	NOAA/EMSO
Landsat 7	ETM+	1999 - present	(7 bands): 0.49-11.45 µm	NASA/USGS
Ikonos-2	OSA	1999 - present	(4 bands): 0.45-0.86 µm	DigitalGlobe
EO-1	Hyperion	2000 - 2017	(242 channels): 0.35-2.5 µm	NASA/USGS
EO-1	ALI	2000 - 2017	(9 bands): 0.44-2.2 µm	NASA/USGS
Aqua, Terra	MODIS	2000 - present	(36 bands): 0.412-14.2 µm	NASA
Terra	MISR	2000 - present	(4 bands)[¥]: 0.446-0.867 µm	NASA
Terra	ASTER	2000 - present	(14 bands): 0.56-11.3 µm	NASA
QuickBird-2	BGIS2000	2001 - 2015	(4 bands): 0.45-0.9 µm	DigitalGlobe
ADEOS-2	POLDER	2002 - 2003	(9 bands): 0.44-0.91 µm	CNES
ADEOS-2	GLI	2002 - 2003	(36 bands): 0.38-11.95 µm	JAXA
EnviSat	MERIS	2002 - 2012	(15 bands): 0.39-1.04 µm	ESA
EnviSat	AATSR	2002 - 2012	(7 bands): 0.55-12.0 µm	ESA
Spot 5	HRG / HRS	2002 - 2015	(4 bands): 0.55-1.63 µm	CNES/Spot
ALOS	AVNIR-2	2006 - 2011	(4 bands): 0.46-0.82 µm	JAXA
WorldView-1	WV60	2007 - present	(1 band): 0.45-0.90 µm	DigitalGlobe
GeoEye-1	GIS	2008 - present	(4 bands): 0.45-9.2 µm	DigitalGlobe
WorldView-2	WV110	2009 - present	(8 bands): 0.40-1.04 µm	DigitalGlobe
Suomi NPP	VIIRS	2011 - present	(22 bands): 0.41-12.01 µm	NASA
Spot 6	NAOMI	2012 - present	(4 bands): 0.48-0.82 µm	CNES/Spot
Landsat 8	OLI	2013 - present	(9 bands): 0.44-2.19 µm	USGS/NASA
Landsat 8	TIRS	2013 - present	(2 bands): 10.9, 12 µm	USGS/NASA
Spot 7	NAOMI	2014 - present	(4 bands): 0.48-0.82 µm	CNES/Spot
WorldView-3	WV-3 Imager	2014 - present	(29 bands): 0.40-2.365 µm	DigitalGlobe

Sentinel-2A/B	MSI	2015 - present	(13 bands): 0.444-2.202 μm	ESA
GeoEye-2	SpaceView^{TM} 110	2016 - present	(4 bands): 0.45-9.2 μm	DigitalGlobe
Sentinel-3A/B	OLCI	2016 - present	(21 bands): 0.40-1.02 μm	ESA
GCOM-C1	SGLI	2017 - present	(19 bands): 0.38-12.0 μm	JAXA

* See Appendix A for expanded acronyms

Ŧ See Appendix B for expanded acronyms

§ See Appendix C for expanded acronyms

Ɣ Managing agencies are identified by WMO OSCAR database (Table D1) and may not reflect joint collaborations

¥ Observed fore and aft of nadir @ 26°, 45°, 60°, 70.5°

Table 1-3. Summary of active microwave (synthetic aperture radar and microwave scatterometer) remote sensing platforms, instruments, temporal coverage, observed frequencies, and managing agencies.

Platform*	Instrument Ŧ	Temporal Coverage	Observed Frequency	Agency§
Synthetic Aperture Radar				
Seasat	SAR	1978 (110 days)	1.275 GHz (L)	NASA
ERS-1	AMI-SAR	1991 - 2006	5.3 GHz (C)	ESA
JERS-1	SAR	1992 - 1998	1.2 GHz (L)	JAXA
ERS-2	AMI-SAR	1995 - 2011	5.3 GHz (C)	ESA
RADARSAT-1	SAR	1995 - 2013	5.3 GHz (C)	CSA
EnviSat	ASAR	2002 - 2012	3.2 (S), 5.3 (C), 13.6 GHz (Ku)	ESA
ALOS	PALSAR	2006 - 2011	1.2 GHz (L)	JAXA
RADARSAT-2	SAR	2007 - present	5.3 GHz (C)	CSA
TerraSAR-X	SAR-X	2007 - present	9.6 GHz (X)	DLR/EADS
TanDEM-X	SAR-X	2010 - present	9.6 GHz (X)	DLR/EADS
CryoSat-2	SIRAL	2010 - present	13.9 GHz (Ku)	ESA
Sentinel-1A	SAR-C	2014 - present	5.4 GHz (C)	ESA
ALOS-2	PALSAR-2	2014 - present	1.2 GHz (L)	JAXA
Sentinel-1B	SAR-C	2016 - present	5.4 GHz (C)	ESA
Scatterometers				
Seasat	SASS	1978 (110 days)	14.6 GHz (Ku)	NASA
ERS-1	AMI-SCAT	1991 - 2006	5.3 GHz (C)	ESA
ERS-2	AMI-SCAT	1995 - 2011	5.3 GHz (C)	ESA
ADEOS	NSCAT	1996 - 1997	14.0 GHz (Ku)	JAXA
QuikSCAT	SeaWinds	1999 - 2009	13.4 GHz (Ku)	NASA
ADEOS-2	SeaWinds	2002 - 2003	13.4 GHz (Ku)	JAXA/NASA
MetOp A-C	ASCAT	2006 - present	5.3 GHz (C)	EOMS/ESA

* See Appendix A for expanded acronyms

Ŧ See Appendix B for expanded acronyms

§ See Appendix C for expanded acronyms

Ɣ Managing agencies are identified by WMO OSCAR database (Table D1) and may not reflect joint collaborations

Table 1-4. Summary of passive microwave remote sensing platforms, instruments, temporal coverage, observed frequencies, and managing agencies.

Platform*	Instrument[Ŧ]	Temporal Coverage	Observed Frequency	Agency[§]
Nimbus-5	ESMR	1972 - 1983	19 GHz	NASA
Nimbus-6	ESMR	1975 - 1983	37 GHz	NASA
Seasat	SMMR	1978 (110 days)	7, 10, 18, 21, 37	NASA
Nimbus-7	SMMR	1978 - 1994	7, 10, 19, 37 GHz	NASA/NOAA
DMSP F08,10-15,18	SSM/I	1987 - present	19, 22, 37, 86 GHz	DoD/NOAA
DMSP F16-19	SSMIS	1987 - present	19, 22, 37, 92 GHz	DoD/NOAA
ERS-1	ATSR	1991 - 2006	24, 37 GHz	ESA
GFO	WVR	1998 - 2008	22, 37 GHz	DoD/NASA
ADEOS-2	AMSR	2002 - 2003	7, 10, 19, 24, 37, 89A, 89B GHz	JAXA/NASA
Aqua	AMSR-E	2002 - 2011	7, 10, 19, 24, 37, 89 GHz	NASA
ERS-2, EnviSat	MWR	2002 - 2012	24, 37 GHz	ESA
GCOM-W1	AMSR-2	2012 - present	7 (dual), 10, 19, 37, 89 GHz	NASA/JAXA
Sentinel 3A/B	MWR	2016 - present	24, 37 GHz	ESA

* See Appendix A for expanded acronyms

Ŧ See Appendix B for expanded acronyms

§ See Appendix C for expanded acronyms

Ɣ Managing agencies are identified by WMO OSCAR database (Table 1-5) and may not reflect joint collaborations

9 Figures

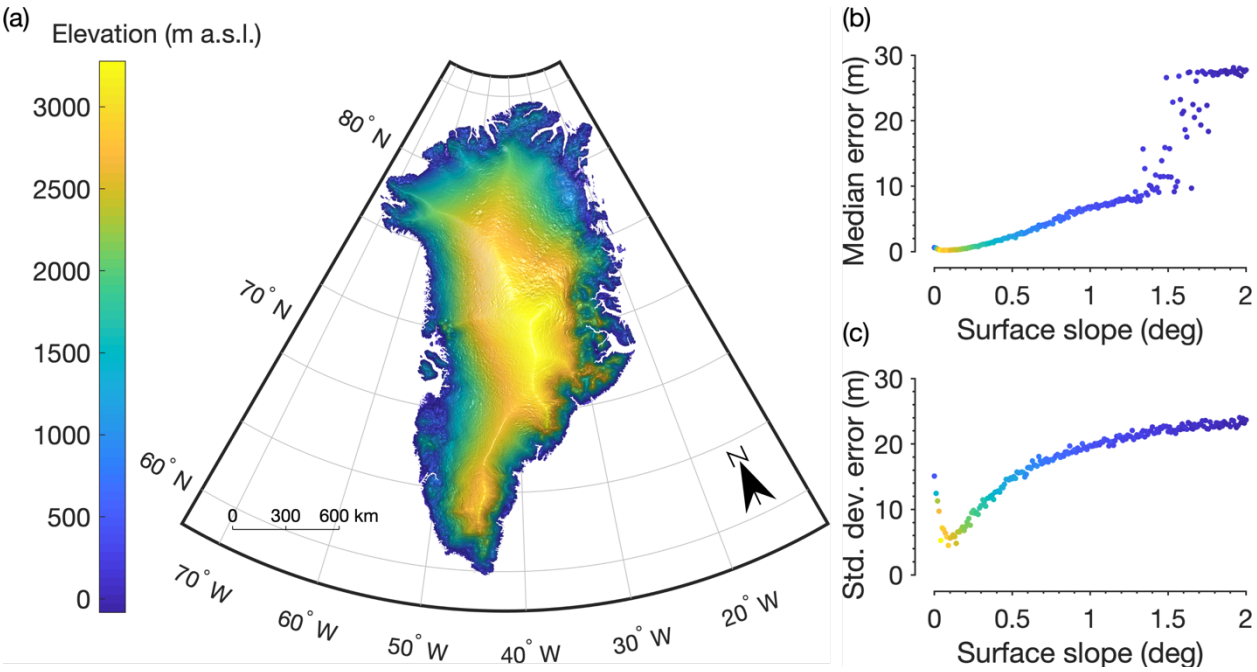

Figure 1-1. (a) Digital elevation model (DEM) of the Greenland Ice Sheet surface created from the European Space Agency (ESA) level 1B CryoSat-2 radar altimetry waveform product (Helm et al., 2014a), with slope indicated by shaded relief; (b) Median error (difference between CryoSat-2 DEM and ICESat elevations) vs surface slope, with elevation indicated by colormap in (a); (c) Standard deviation of error vs surface slope, with elevation indicated by colormap in (a). The median and standard deviation of error are calculated from the CryoSat-2 DEM error grid binned by slope with 0.01o bin size, following Helm et al. (2014a) (Figure 9). The median and standard deviation of error increase with slope with a step shift toward higher error at slopes >1.5o. Elevation and slope values calculated from the DEM indicate that 16% of the ice sheet area has surface slope >1.5o, and nearly all (95%) such areas have elevation <2000 m a.s.l., which is generally representative of the ablation zone (calculations performed by the first author). The error grid was produced by first calculating elevation differences between the CryoSat-2 DEM and individual ICESat elevations (campaign 3F, 3G, and 3H), corrected for elevation change between the individual ICESat observation and the DEM reference time (1 Jul 2012), and then calculating a weighted error as a function of surface roughness, surface slope, and number of cross-validation data points (Helm et al., 2014a). The DEM and associated error grid is publicly available at https://doi.pangaea.de/10.1594/PANGAEA.831394 (Helm et al., 2014b).

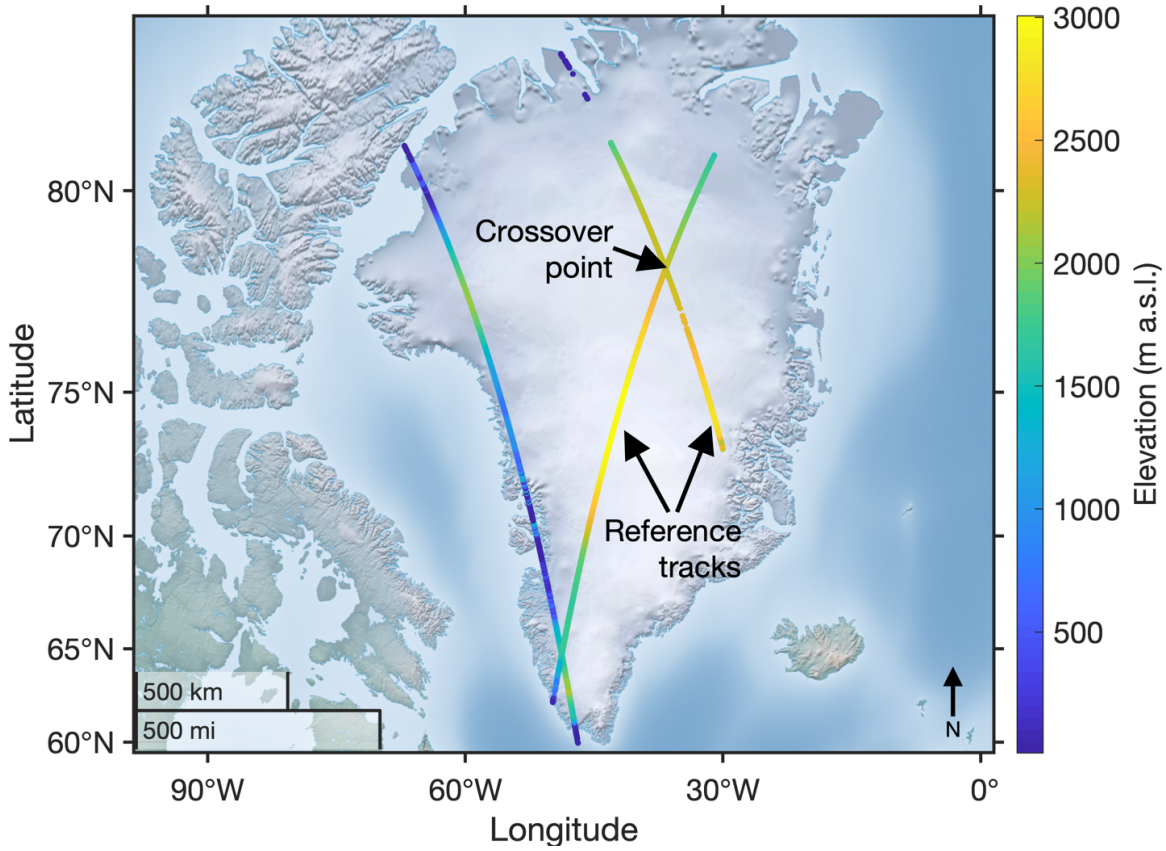

Figure 1-2. Example of GLAS/ICESat orbital reference tracks, crossover point, and 27,766 unique surface elevation measurements collected on 20 February 2003 obtained from the GLAS/ICESat L2 Antarctic and Greenland Ice Sheet altimetry Data (GLAH12), Version 34 (https://nsidc.org/data/GLAH12/). ICESat data are produced by the GLAS Science Team at the ICESat Science Investigator-led Processing System (I-SIPS) at NASA/GSFC and are archived by the National Snow and Ice Data Center (NSIDC) DAAC.

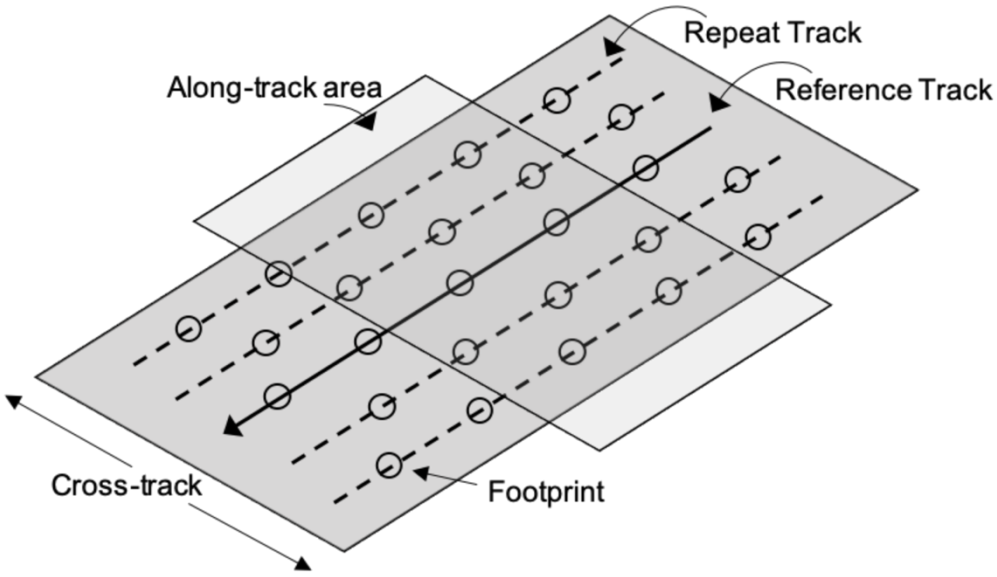

Figure 1-3. Illustration of altimeter (e.g. ICESat) reference track and repeat tracks. Repeat tracks are parallel to reference tracks but separated in the cross-track direction. An area of interest in the along-track direction is used to collect ground footprint measurements that are spatially interpolated to recover the area-average surface elevation and subsequent change in area-average surface elevation dH/dt. In practice, repeat tracks are often not parallel owing to orbital variations and, in the case of ICESat laser altimetry, footprint diameter may change owing to laser transmit power variation.

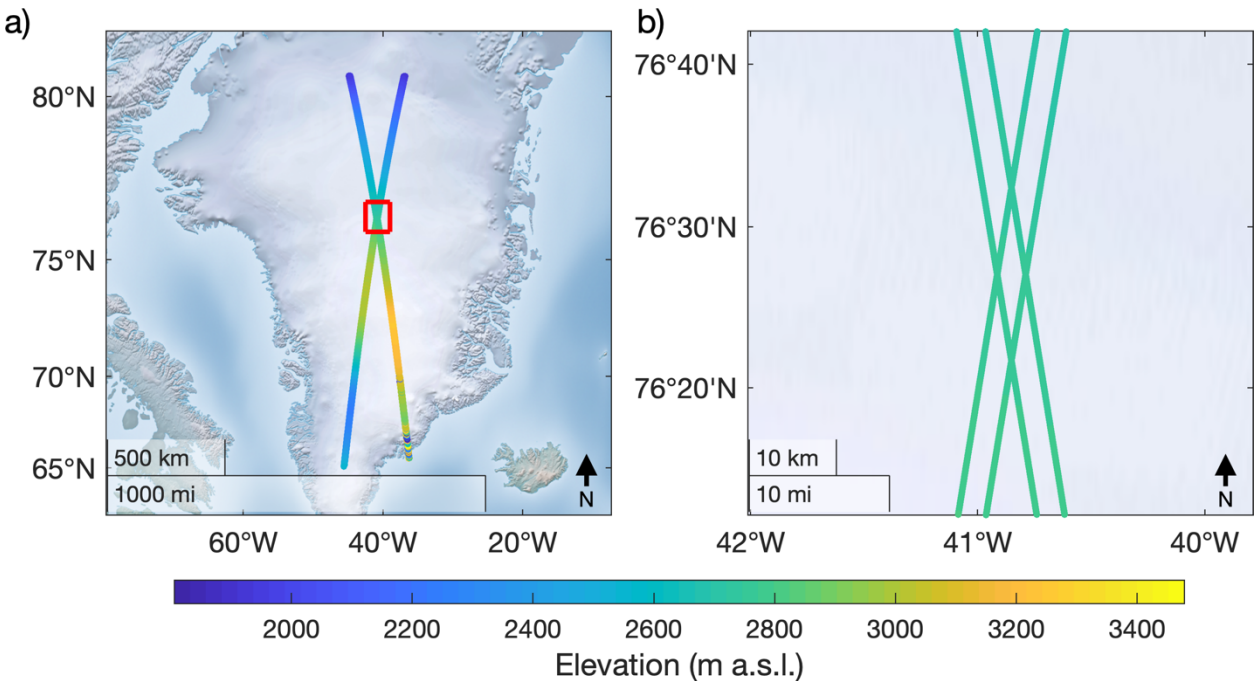

Figure 1-4. (a) Example of ATLAS/ICESat-2 Level-3A data product Land Ice Height, Version 1 (ATL06), representing 304,550 unique surface elevation measurements collected on 18 October 2018 (Smith et al., 2019); (b) Example crossover location (red box inset in (a)) showing the ICESat-2 multi-beam configuration (two beam-pairs shown, the third beam-pair was not included in ATL06 Version 1 at this time and location). Single-beam altimeters such as ICESat give one crossover measurement at each crossover location, and the cross-track slope cannot be determined in the along-track direction. The ICESat-2 multi-beam configuration allows determination of cross-track slope and gives multiple unique crossover measurements at each crossover location (up to nine possible, four shown in this example).

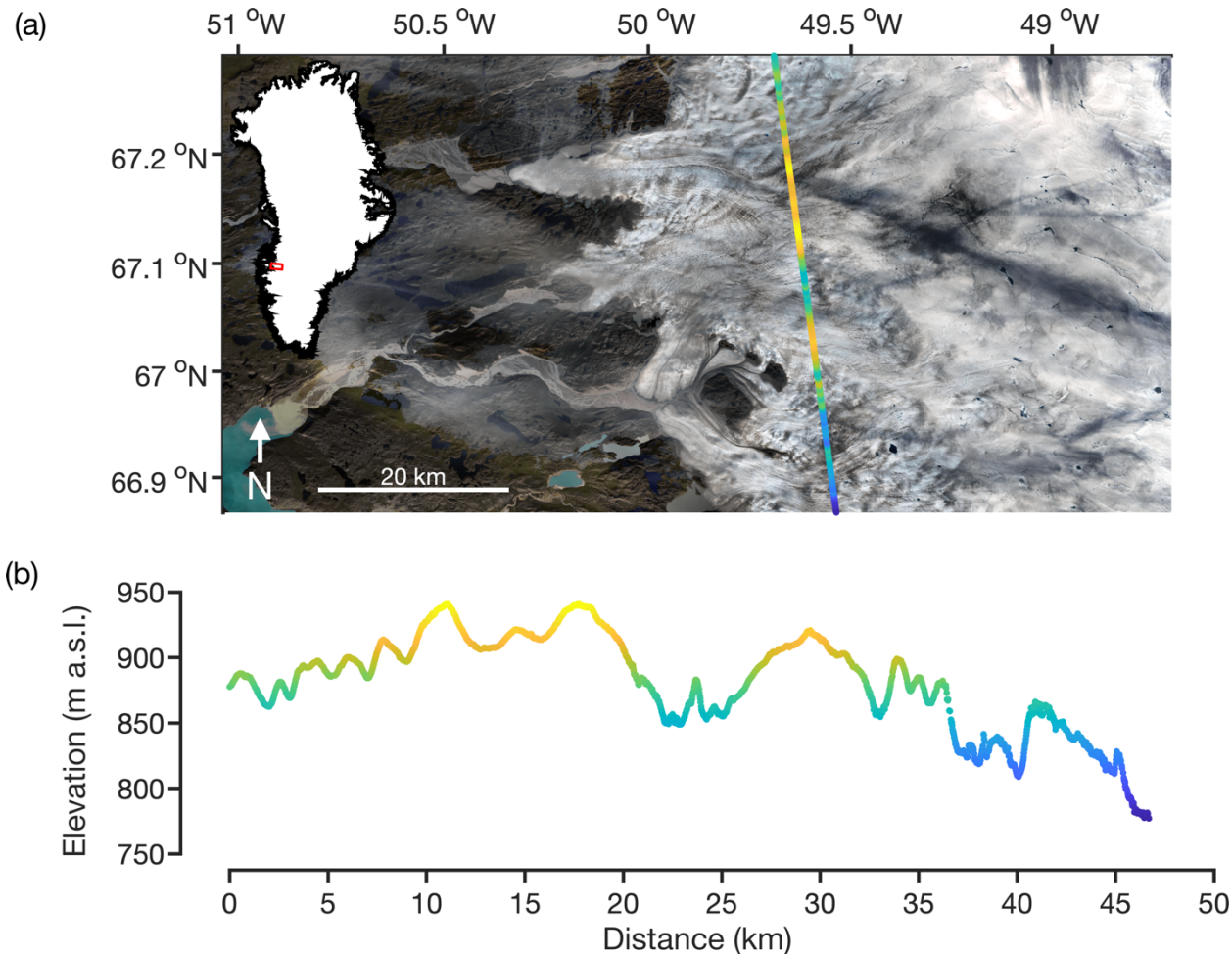

Figure 1-5. (a) Example of ATLAS/ICESat-2 Level-3A data product Land Ice Height, Version 1 (ATL06) (Smith et al., 2019), collected on 24 October 2018 in the western Greenland Ice Sheet ablation zone. Background image is Landsat 8 Operational Land Imager 30 m resolution image (RGB: band 4 (red), 3 (green), and 2 (blue))collected on 24 August 2018. Inset is Greenland Ice Mapping Project (GIMP) ice mask (Howat et al., 2014) with red box showing extent of image area; (b) Elevation profile for ground track profile 3, right beam ('gt3r'), for the north to south track shown in (a), showing the rough, crevassed ice surface in the marginal ablation zone. ATL06 elevations represent mean surface elevation averaged along 40 m segments of ground track, posted at 20 m along-track spacing.

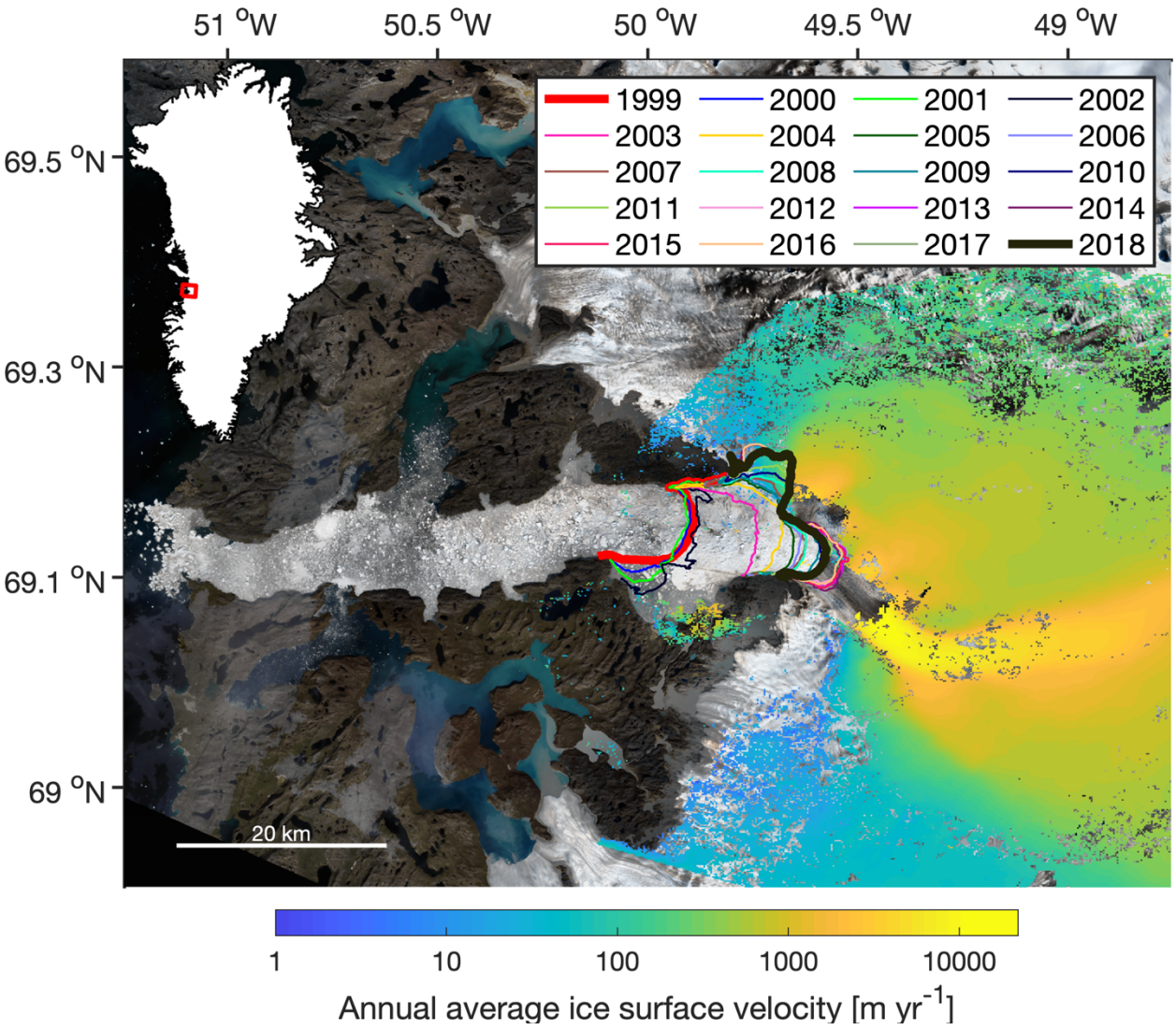

Figure 1-6. The largest single contributor of ice discharge *D* from the Greenland Ice Sheet to the global ocean during recent decades is Sermeq Kujalleq (Jakobshavn Isbræ), shown here in a 27 July 2017 Landsat 8 Operational Land Imager 30 m resolution image (RGB: band 4 (red), 3 (green), and 2 (blue)). The annual average ice surface velocity for the period 2011–2016 is shown for upstream areas, calculated from Landsat-8 (optical), Sentinel-1, and RADARSAT-2 (interferometric SAR) image processing (Mouginot et al., 2017). The maximum surface velocity value is 12,000 m yr^{-1}. Calving fronts, which mark the terminus position of the outlet glacier where ice is discharged to the ocean, are mapped from Landsat-7, Landat-8, and Sentinel-2B optical imagery (Andersen et al., 2019). Sermeq Kujalleq has lost 137 km^2 of surface area between 1998–2018 (compare thick red line to thick black line) with a series of large episodic retreats occurring between 2000–2003 resulting in near complete disintegration of its floating ice tongue (Joughin et al., 2004, 2008). It's flow speed has nearly doubled since the early 1990s with upstream thinning rates exceeding 15 m yr^{-1} (Alley, 2005). Inset is Greenland Ice Mapping Project (GIMP) ice mask (Howat et al., 2014) with red box showing extent of image area.

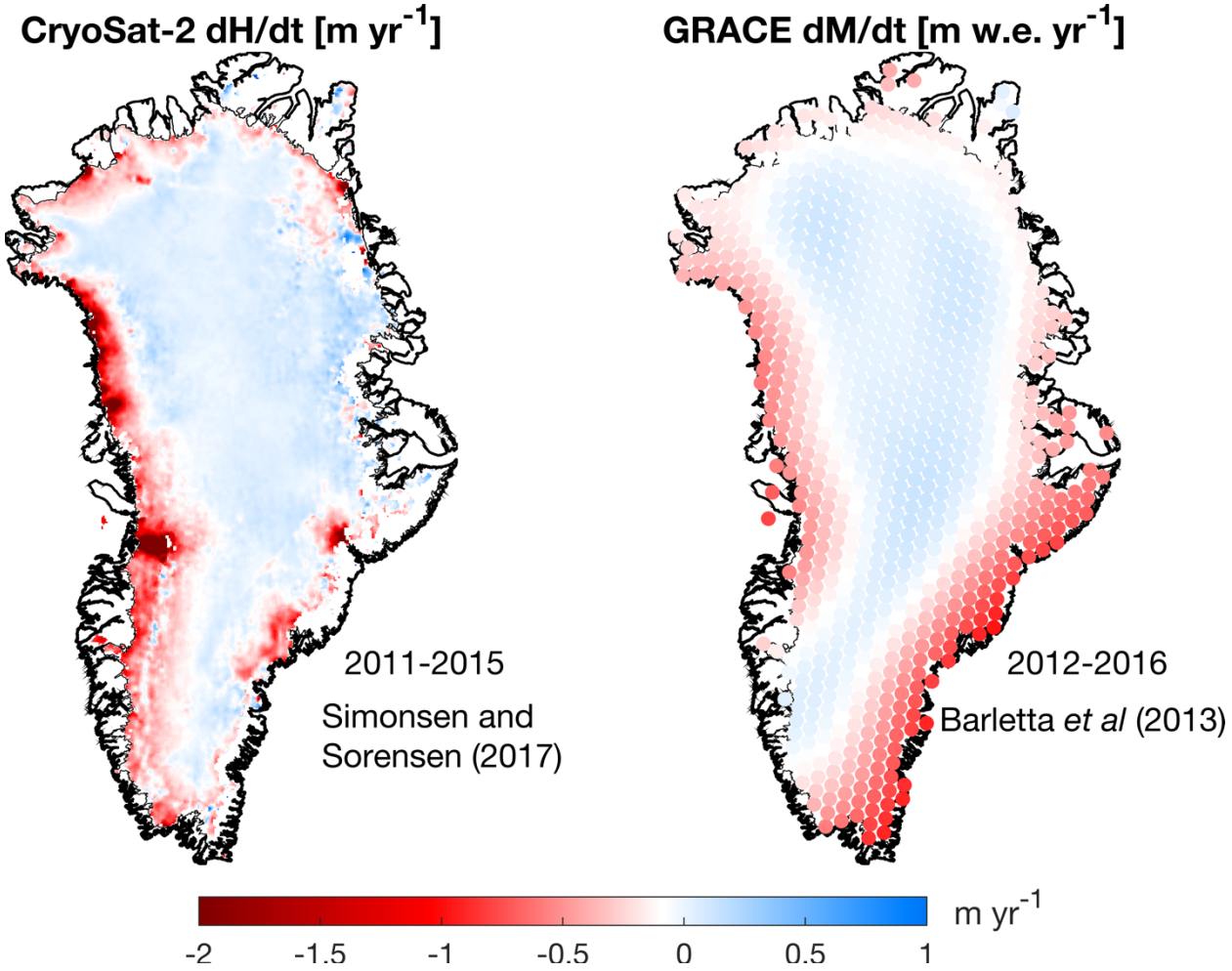

Figure 1-7. Comparison of ice surface elevation change dH/dt [m yr^{-1}] from CryoSat-2 radar altimetry with mass change dM/dt [m w.e. yr^{-1}] from GRACE. Both missions observe similar spatial patterns, with mass losses concentrated in the southeast and western sectors, and a slight thickening of the interior. Altimetry resolves rapid thinning concentrated in narrow outlet glaciers along the coastal margins. The CryoSat-2 Surface Elevation Change (SEC) product version 2.2 is based on the ESA Baseline C CryoSat-2 product and is provided at 1 km grid spacing as a five-year average for the period 2011–2015 (Simonsen and Sørensen, 2017). The GRACE mass balance product is produced by the Danish Institute of Space (DTU Space) and is provided as a five-year average for the period 2012–2016 with 500 km nominal spatial resolution (Barletta et al., 2008). Both datasets are Essential Climate Variables provided by the ESA Climate Change Initiative and are available online at http://products.esa-icesheets-cci.org.

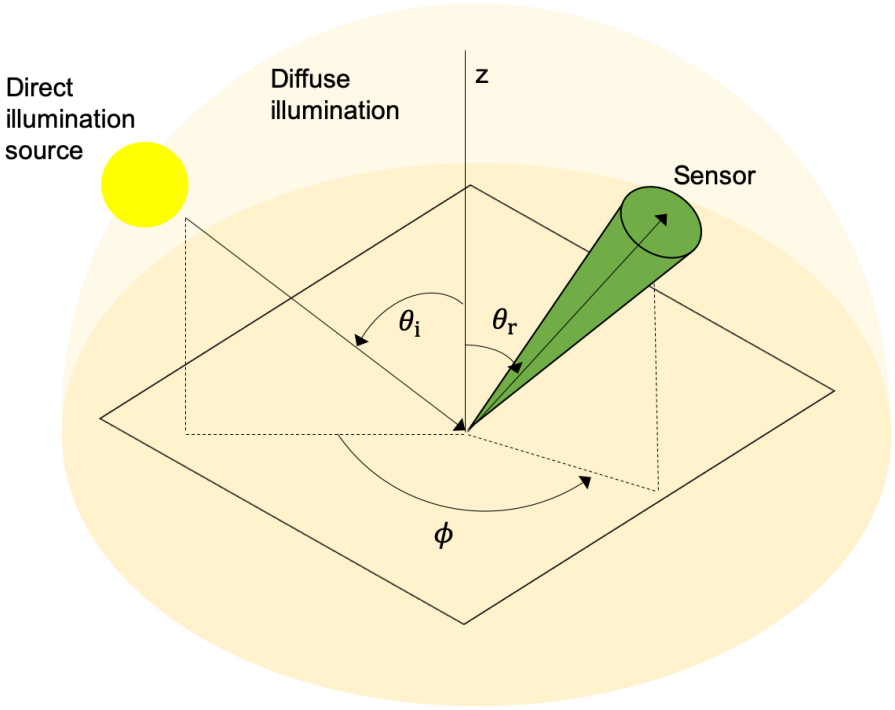

Figure 1-8. Diagram of incident and reflected viewing angles for a directional light source with direct and diffuse (hemispherical) incoming radiance and conical reflected radiance, adapted from Schaepman-Strub *et al.* (2006). The incident viewing angle (θ_i), reflected viewing angle (θ_r), and the azimuth angle (ϕ) together define the angular coordinates of both the directional illumination and the light reflected toward the sensor, with respect to the surface normal, z.

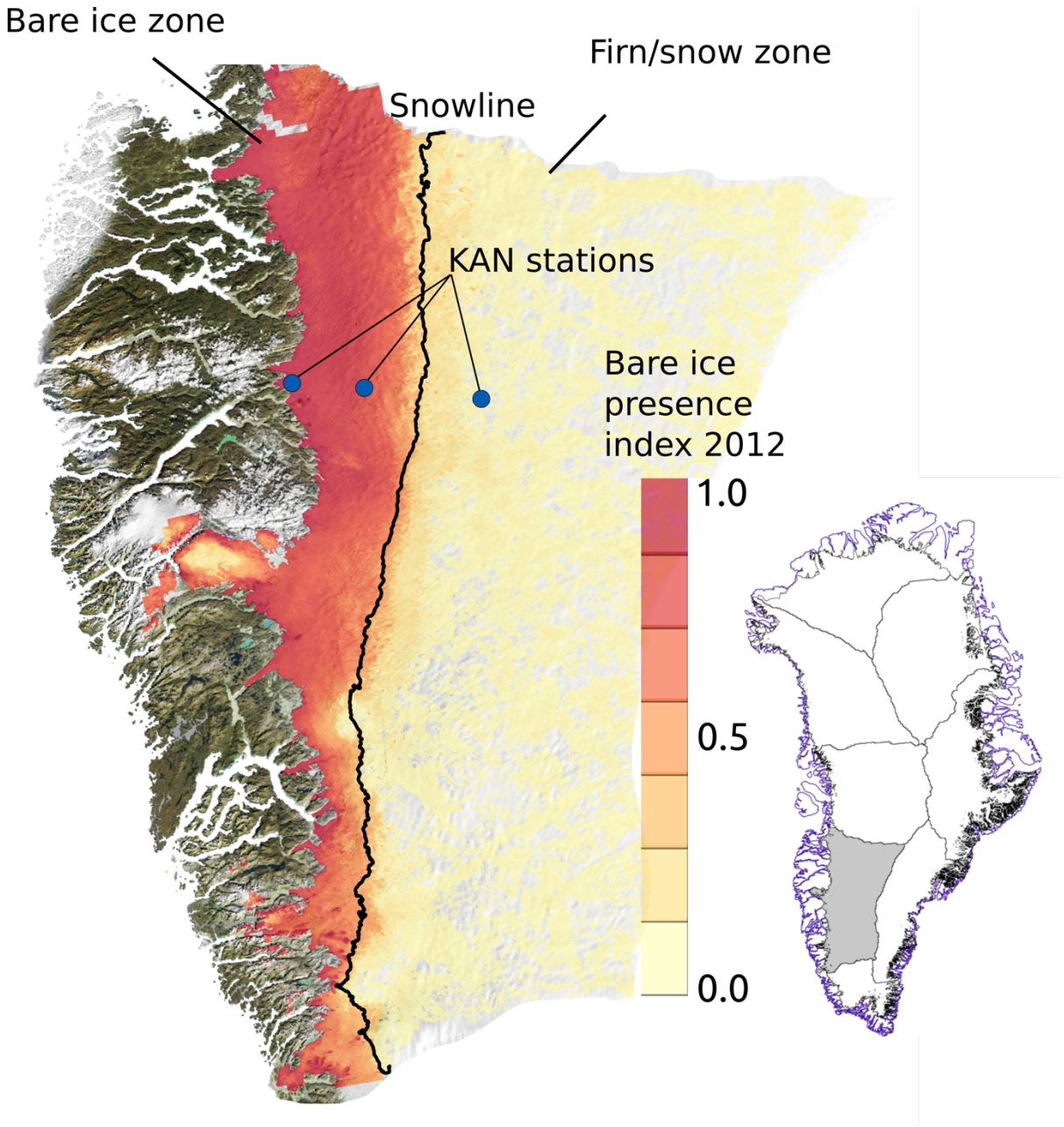

Figure 1-9. The average end-of-summer (maximum) snowline position for the southwest sector of the Greenland Ice Sheet during the period 2001–2017 as determined from MODIS MOD09GA surface reflectance, reprinted with permission from Ryan et al. (2019) (courtesy Johnathan Ryan, Brown University). Daily reflectance maps for June, July, and August were classified into bare ice, snow-covered, and water-covered pixels using supervised random forest classification. The bare ice presence index is an exposure frequency representing the fraction of total days classified as bare ice for each pixel. The average end-of-summer snowline elevation is 1520 ± 113 m in this sector with interannual variation ±385 m. Interannual snowline variability explains 53% of MOD10A albedo variability (Ryan et al., 2019).

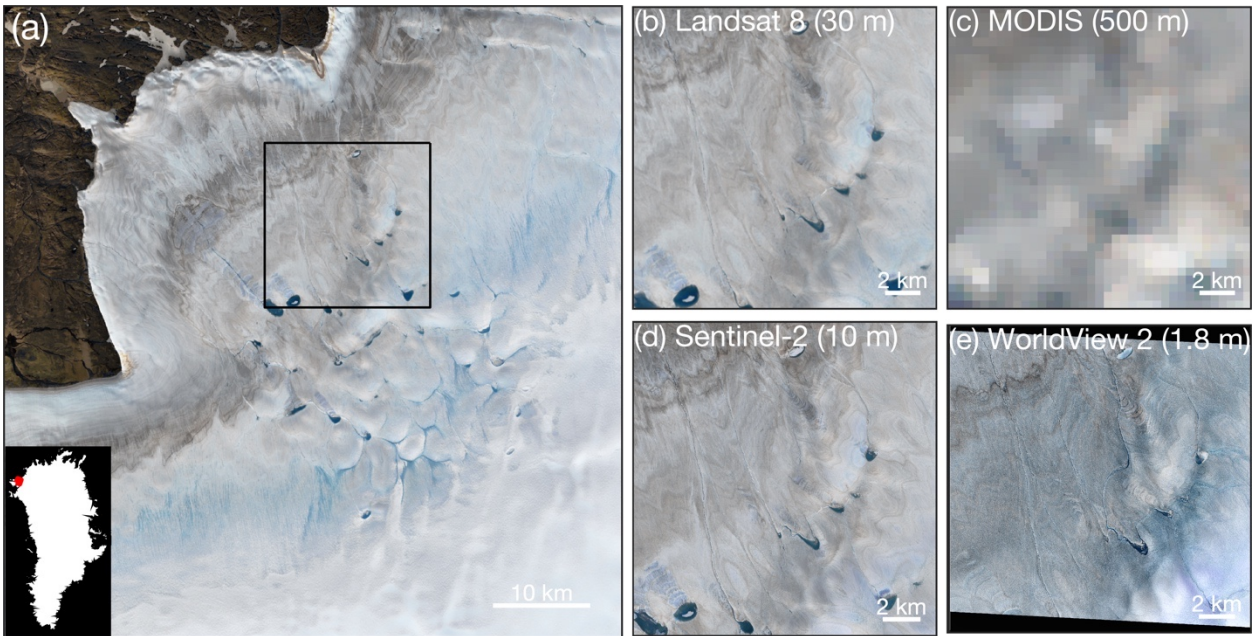

Figure 1-10. Satellite images of the ablation zone proximal to Inglefield Land in northwest Greenland (78.64 ºN, 65.89 ºW), showing bands of outcropping dust in bare ablating ice, supraglacial lakes and rivers indicating melting ice, and what appears to be snow, firn, or otherwise non-melting ice that may indicate the approximate location of the summer snowline. (a) Landsat-8 Operational Land Imager 30 m resolution image (RGB: bands 4 (red), 3 (green), and 2 (blue)) acquired on 16 July 2016. Elevations in this image range from 600 m a.s.l. at the ice sheet edge to ~1500 m a.s.l.; (b) Same as (a) but for detail box; (c) MODIS/Terra MOD09A1 500 m resolution 8-day composite image (RGB: bands 1 (red), 4 (green), and 3 (blue)) acquired on 27 July – 03 August 2016; (d) Sentinel-2 Multispectral Imager 10 m resolution image (RGB: bands 4 (red), 3 (green), and 2 (blue)) acquired on 23 July 2016. (e) WorldView-2 image (RGB: bands 5 (red), 3 (green), and 2 (blue)) resampled to 1.8 m resolution (native resolution: 0.5 m) acquired 03 September 2019. Images in (b)-(e) demonstrate the range of spatial resolutions typically used for studying the ablation zone.

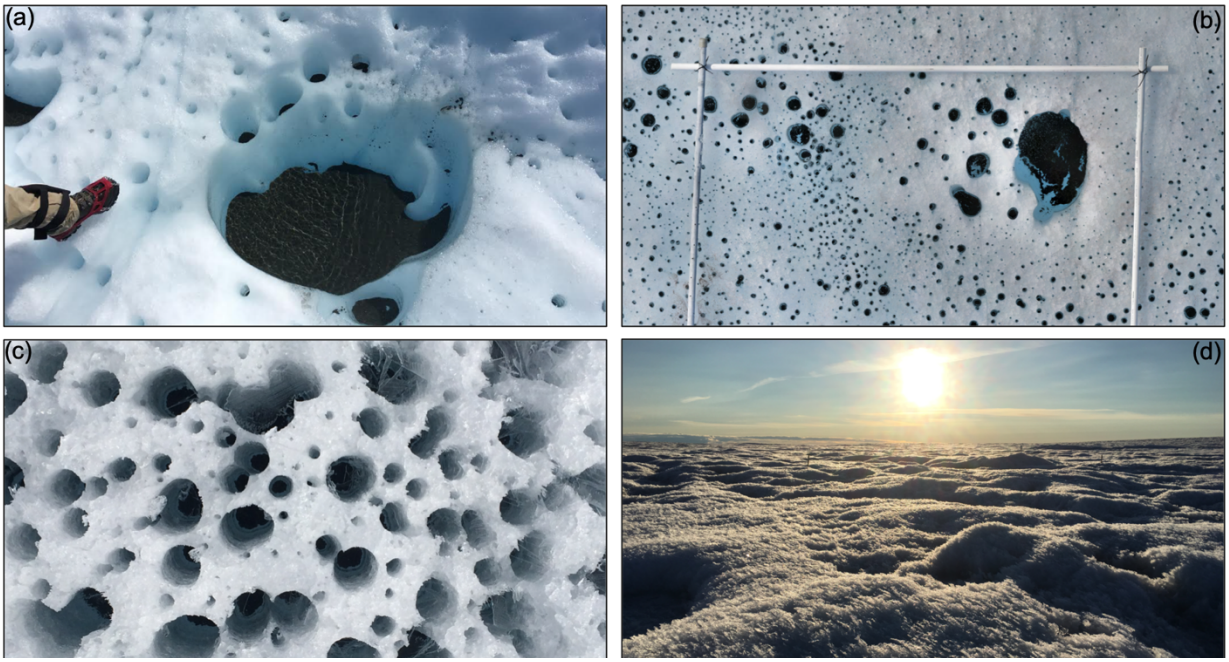

Figure 1-11. Images of cryoconite hole-studded ice surface in the western Greenland Ice Sheet ablation zone, collected at (a) ~850 m a.s.l.; (b) ~950 m a.s.l.; and (c) ~1200 m a.s.l. along an elevation transect outside Kangerlussuaq (Søndre Strømfjord). At the low and mid-elevation sites, the ice surface is glazed and smooth, and the water table within the cryoconite holes is nearly coincident with the ice surface. At the high-elevation site (c), the surface is rougher, and evidence of nocturnal refreezing is visible. (d) same location as (c), showing the rough, weathered ice surface at low sun angle, reprinted from Cooper et al. (2018). Quadrat shown in (b) is 3 m wide. Cryoconite holes in (c) are on the order 1–5 cm wide. Seasonal weathering of the ice surface, including cryoconite hole deepening and removal, exerts a primary control on ice roughness and grain morphology but its effect on bare ice albedo has received little direct study (Shimada et al., 2016).

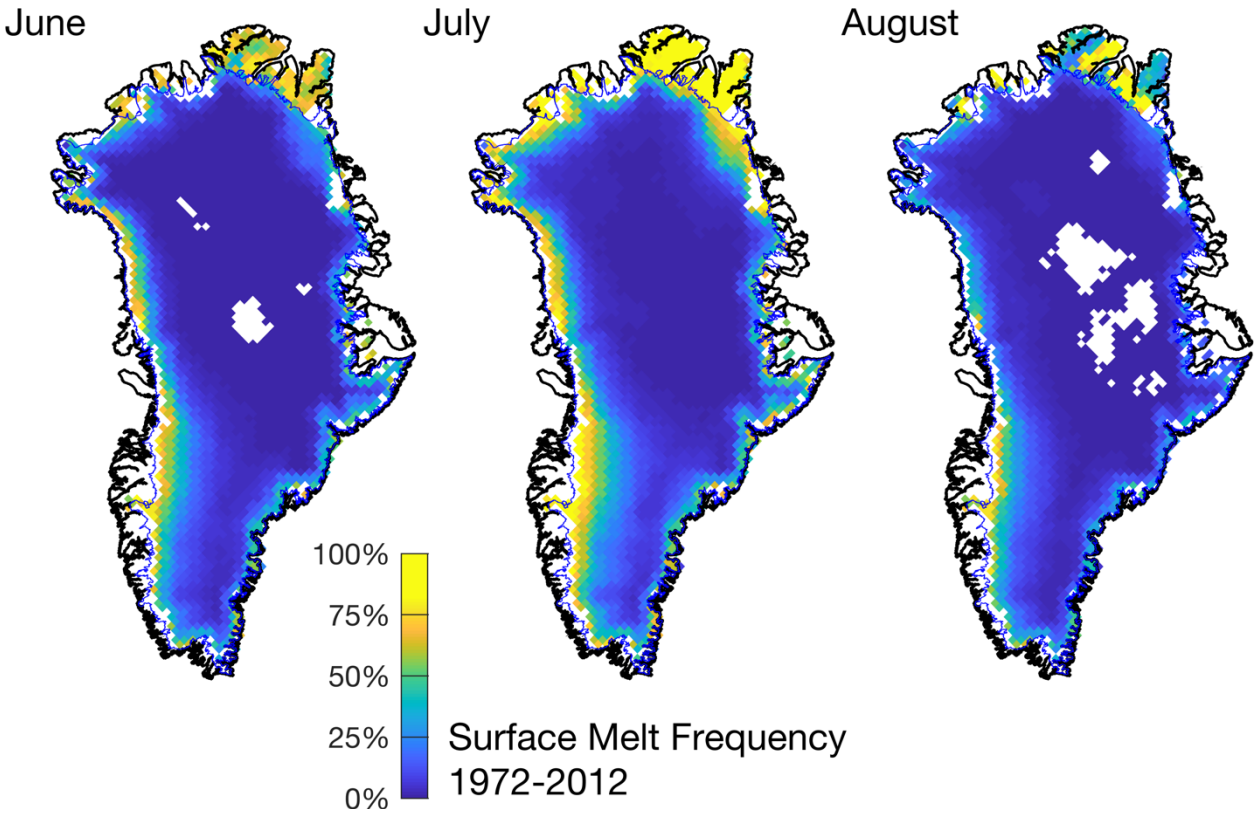

Figure 1-12. Surface melt presence frequency-of-occurrence during the summer melting season (June–August) for the period 1972–2012 from passive microwave brightness temperature observed by the Scanning Multichannel Microwave Radiometer (SMMR), the Special Sensor Microwave/Imager (SSM/I), and the Special Sensor Microwave Imager/Sounder (SSMIS). Areas experiencing zero melt presence frequency are colored white. Surface melt presence provides a sensitive indicator of changing climatic conditions over the Greenland Ice Sheet, including the July 2012 extreme melt event when surface melt prevailed over the entire ice sheet for the first time in the satellite era (Nghiem et al., 2012). Surface melt frequency is calculated by the authors from the NASA MEaSUREs Greenland Surface Melt Daily 25 km EASE-Grid 2.0 data set (Mote, 2014).

Appendix 1-A. Glossary of select remote sensing satellite platforms

ADEOS	ADvanced Earth Observing Satellite
ADEOS-2	ADvanced Earth Observing Satellite-2
ALOS	Advanced Land Observing Satellite
CryoSat	Cryosphere Satellite
DMSP	Defense Meteorological Satellite Program
EnviSat	Environmental Satellite
EO-1	Earth Observation-1
ERS-1	European Remote-sensing Satellite-1
ERS-2	European Remote-sensing Satellite-2
GCOM-W1	Global Change Observation Mission – Water “Shizuku”
GCOM-C1	Global Change Observation Mission – Climate “Shikisai”
GEOS-3	Geodetic and Earth Orbiting Satellite-3
GEOSAT	GEOdetic SATellite
GFO	GEOdetic SATellite Follow On
GOES	Geostationary Operational Environmental Satellites
GRACE	Gravity Recovery and Climate Experiment
ICESat	Ice, Cloud, and land Elevation Satellite
ICESat-2	Ice, Cloud, and land Elevation Satellite-2
JERS-1	Japanese Earth Resource Satellite-1
Landsat	Land Satellite
MetOp	Meteorological Operational satellite program
NOAA	National Oceanic and Atmospheric Administration
QuickSCAT	Quick Scatterometer
RADARSAT	Radar Satellite of the Canadian Space Agency
SPOT	Satellite Pour l’Observation de la Terre
SARAL	Satellite with Argos and ALtiKa
Suomi NPP	Suomi National Polar-orbiting Partnership
TerraDEM-X	TerraSAR-X add on for Digital Elevation Measurements
TerraSAR-X	Synthetic Aperture Radar X-band
TIROS	Television Infrared Operational Satellite

Appendix 1-B. Glossary of select remote sensing satellite sensors

AATSR	Advanced Along Track Scanning Radiometer
ALI	Advanced Land Imager
ALT	Radar Altimeter
AltiKa	Ka-Band Altimeter
AMI	Advanced Microwave Instrument
AMSR	Advanced Microwave Scanning Radiometer
AMSR-2	Advanced Microwave Scanning Radiometer 2
AMSR-E	Advanced Microwave Scanning Radiometer – Earth Observing System
ASAR	Advanced Synthetic-Aperture Radar
ASCAT	Advanced Scatterometer
ASTER	Advanced Spaceborne Thermal Emission and Reflection radiometer
ATLAS	Advanced Topographic Laser Altimeter System
ATM	Airborne Topographic Mapper
ATSR	Along Track Scanning Radiometer
ATSR-2	Along Track Scanning Radiometer-2
AVCS	Advanced Vidcon Camera System
AVHRR	Advanced Very High Resolution Radiometer
AVNIR	Advanced Visible and Near Infrared Radiometer
AVNIR-2	Advanced Visible and Near Infrared Radiometer type 2
BGIS2000	Ball Global Imaging System 2000
C-SAR	C-band Synthetic Aperture Radar
ESMR	Electrically Scanning Multichannel Radiometer
ETM+	Enhanced Thematic Mapper Plus
GIS	GeoEye Imaging System
GLAS	Geoscience Laser Altimeter System
GLI	Global Land Imager
GRA	Geosat Radar Altimeter
GRACE	Gravity Recovery and Climate Experiment
HRG	High Resolution Geometric
HRS	High Resolution Stereoscopic
HRV	High Resolution Visible
HRVIR	High Resolution Visible and Infrared
Hyperion	Hyperspectral Imager
IDCS	Image Dissector Camera System
LVIS	Land, Vegetation and Ice Sensor
MERIS	MEdium Resolution Imaging Spectrometer
MISR	Multi-angle Imaging SpectroRadiometer
MODIS	Moderate Resolution Imaging Spectroradiometer
MSI	Multispectral Imager
MSS	Multispectral Scanner
MWR	Microwave Radiometer
NAOMI	New AstroSat Optical Modular Instrument
NSCAT	NASA Scatterometer

OLCI	Ocean and Land Colour Instrument
OLI	Operational Land Imager
OSA	Optical Sensor Assembly
OPS	Optical Sensor
PALSAR	Phased-Array type L-band SAR
PALSAR-2	Phased-Array type L-band SAR
POLDER	Polarization and Directionality of the Earth's Reflectances
RA	Radar Altimeter
RA-2	Radar Altimeter 2
SAR	Synthetic Aperture Radar
SASS	SEASAT-A Satellite Scatterometer
SGLI	Second generation Global Imager
SIRAL	Synthetic Aperture Interferometric Radar Altimeter
SMMR	Scanning Multichannel Microwave Radiometer
SSM/I	Special Sensor Microwave / Imager
SSMIS	Special Sensor Microwave Imager/Sounder
TIRS	Thermal Infrared Sensor
TM	Thematic Mapper
VIIRS	Visible/Infrared Imager Radiometer Suite
VIRR	Visible and Infrared Radiometer
VISSR	Visible and Infrared Spin Scan Radiometer
WV3-Imager	WorldView-3 Imager
WV60	WorldView-60 camera
WV110	WorldView-110 camera
WVR	Water Vapor Radiometer

Appendix 1-C. Glossary of public and private remote sensing sponsoring agencies

CNES	French Space Agency
CSA	Canadian Space Agency
DLR	German Aerospace Center
DoD	Department of Defense (United States)
EADS	European Aeronautic Defense and Space Company
EOMS	European Organisation for Meteorological Satellites
EOSAT	Earth Observation Satellite Company
ESA	European Space Agency
ISRO	Indian Space Research Organisation
JAXA	Japanese Aerospace Exploratory Agency
JPL	Jet Propulsion Laboratory
NASA	National Aeronautics and Space Administration (US)
NASDA	National Space Development Agency of Japan
NOAA	National Oceanic and Atmospheric Administration (US)
USGS	United States Geological Survey

Appendix 1-D. List of online satellite remote sensing information repositories

Table 1-5. List of online repositories of satellite remote sensing platforms, sensors, and managing agency information

Managing organization	Repository name	URL
World Meteorological Organization	Observing Systems Capability Analysis and Review (OSCAR)	https://www.wmo-sat.info/oscar/spacecapabilities
NASA	NASA Space Science Data Coordinated Archive (NSSDCA)	https://nssdc.gsfc.nasa.gov/nmc/
ESA	Earth Observation Portal (eoPortal)	https://directory.eoportal.org/web/eoportal/satellite-missions

2 Spectral measurements of light attenuation in Greenland Ice Sheet bare ice suggest shallower subsurface radiative heating and ICESat-2 penetration depth in the ablation zone

Abstract. Light transmission into bare glacial ice affects surface energy balance, bio-photochemical cycling, and light detection and ranging (LiDAR) laser elevation measurements but has not previously been reported for the Greenland Ice Sheet. We present in-ice solar irradiance measured over the spectral range 350–900 nm and 12–77 cm depth collected at a site in the western Greenland ablation zone. The acquired spectral irradiance measurements are used to calculate flux attenuation coefficients using an exponential decay Bouguer law model and are compared to values calculated from two-stream radiative transfer theory. Relative to asymptotic two-stream theory, our empirical attenuation coefficients are up to one order of magnitude larger in the range 350–530 nm, suggesting light absorbing particles embedded in ice enhance visible light absorption at our field site. The empirical coefficients accurately describe light attenuation in the ice interior but underestimate light attenuation near the ice surface. Consequently, Bouguer's law overestimates transmitted flux by up to 50% depending on wavelength. Refraction is unlikely to explain the discrepancy. Instead, vertical variation in the ice microstructure and the concentration of light absorbing particles appears to enhance near-surface attenuation at our field site. The magnitude of this near-surface attenuation implies that optical penetration depth is lower by up to 19 cm (28%) at wavelengths relevant to visible-wavelength lidar altimetry of ice surface elevation (e.g. 532 nm for the Ice, Cloud, and Land Elevation Satellite-2) than is suggested by e-folding depths inferred from two stream theory for optically pure glacier ice. This enhanced near-surface attenuation implies shallower light transmission and therefore lower subsurface light availability for subsurface radiative heating and bio-photochemical cycling. We recommend radiative transfer models applied to bare ice in the Greenland Ice Sheet ablation zone account for vertical variation in light attenuation due to the vertical distribution of light absorbing particles and ice microstructure, and we provide new values of flux attenuation, absorption, and scattering coefficients to support model validation and parameterization.

1 Introduction

Understanding the transmission, absorption, and scattering of light in ice is important for snow and ice energy balance modelling (Brandt and Warren, 1993), lidar remote sensing of snow surface elevation and grain size (Deems et al., 2013; Yang et al., 2017b), primary productivity beneath sea ice (Frey et al., 2011; Grenfell, 1979), bio-photochemical cycling in ice and snow (France et al., 2011), and theoretical predictions of "Snowball Earth" paleoclimates (Dadic et al., 2013; Warren et al., 2002). Each of these applications requires knowledge of the vertical distribution of light attenuation in ice, which for a medium (such as glacier ice) that both absorbs and scatters light is specified by the spectral flux attenuation coefficient:

$$k_{\mathrm{att}} = k_{\mathrm{abs}} + k_{\mathrm{scat}} \quad (1)$$

where k_{abs} [m^{-1}] is the spectral flux absorption coefficient, k_{scat} [m^{-1}] is the spectral flux scattering coefficient, and all are functions of wavelength, λ. This study reports on k_{att} of bare glacier ice in the Greenland Ice Sheet ablation zone, a critical parameter needed to calculate subsurface absorption and backscattering of transmitted radiation that to our knowledge has received no direct field study.

Measurements of k_{att} in snowpack and sea ice indicate three main sources of variation with relevance to geophysical applications. First, the magnitude of k_{att} is primarily controlled by ice microstructure via its control on k_{scat}, which for the range of air bubble and ice grain sizes observed in natural snow and ice is nearly independent of wavelength (Perovich, 1996). Spectrally, k_{att} is low in the near-ultraviolet and blue-green spectral region (~250–600 nm) where k_{abs} is extremely low ($<10^{-8}$), and progressively higher for wavelengths >600 nm, where k_{abs} rapidly increases up to its maximum value ($\sim10^{-2}$) at the far end of the solar spectrum (Warren and Brandt, 2008). Vertically, k_{att} is at a maximum at the incident boundary (the snow or ice surface) where a significant portion of upwelling radiation (i.e. transmitted flux reflected upwards) escapes the ice volume before re-reflection downward. Within this near-surface optical boundary layer (Bohren and Barkstrom, 1974), attenuation rates rapidly decrease with depth to an asymptotic value as multiple scattering establishes an isotropic (diffuse) radiation field (Briegleb and Light, 2007; Warren, 1982). For fine-grained dry snow, a few cm depth is typically sufficient to reach the

"diffuse" asymptotic regime where k_{att} is constant (Brandt and Warren, 1993). For sea ice the depth required is typically larger and can exceed >20 cm depending on near-surface ice microstructure and the vertical location of the refractive boundary if present (Grenfell, 1991; Grenfell and Maykut, 1977). Attenuation coefficients are also influenced by the horizontal distribution of ice type and surface cover (Frey et al., 2011) but this source of variation is not examined here.

In addition to experimental values obtained from measurements of light transmission in ice or snow, k_{att} is obtained analytically from optical theory (Bohren, 1987; Warren et al., 2006). Light attenuation in pure ice is specified analytically by the complex index of refraction $m(\lambda) = m_{\mathrm{re}} - \mathrm{i}\, m_{\mathrm{im}}$, where m_{re} is the real refractive index (~1.31 in the visible), m_{im} is the imaginary index, λ is wavelength, and $k_{\mathrm{abs,ice}} = 4\pi\lambda^{-1}m_{\mathrm{im}}$ is the absorption coefficient of pure ice (Warren et al., 2006; Warren and Brandt, 2008). Light attenuation in glacier ice differs from pure ice owing to compositional and structural factors that control scattering and absorption, such as the size, geometry, and vertical distribution of embedded light absorbing particles (LAPs) and light scattering air bubbles and ice grains of size > wavelength (Askebjer et al., 1997; Picard et al., 2016; Price and Bergström, 1997; Warren et al., 2006). Analytical methods typically assume ice and snowpack can be approximated as homogeneous plane-parallel slabs of spherical ice grains and/or air bubbles, for which Mie theory is used to calculate single-scattering properties and two-stream radiative transfer theory is used to calculate multiple scattering and bulk absorption in the ice volume. Such models have been used to calculate subsurface meltwater production caused by penetration of solar radiation in ice both in Greenland (van den Broeke et al., 2008; Kuipers Munneke et al., 2009) and Antarctica (Brandt and Warren, 1993; Hoffman et al., 2014; Liston et al., 1999a, 1999b; Liston and Winther, 2005). However, theoretical values for k_{att} used as input to such models are rarely validated experimentally, and to our knowledge no such experimental values exist for glacier ice.

In addition to ice surface energy balance, understanding light attenuation in ice is important for interpreting interactions between visible-wavelength light sources and ice surfaces, for example laser altimetry measurements of ice surface elevation (Deems et al., 2013; Gardner et al., 2015; Greeley et al.,

2017). The reciprocal of k_{att} is the attenuation length, or the average distance travelled by a photon before attenuation by absorption or scattering (Ackermann et al., 2006). In the context of altimetry, the attenuation length is sometimes referred to as the penetration depth, or the average depth to which the electromagnetic signal penetrates before it is backscattered to the atmosphere (Ridley and Partington, 1988; Rignot et al., 2001; Zebker and Weber Hoen, 2000). The laser altimeter onboard Ice, Cloud, and Land Elevation Satellite-1 (ICESat-1) transmitted 1064 nm laser pulses to measure the distance (range) between the satellite and ice sheet surfaces (Schutz et al., 2005). Photons with wavelength 1064 nm penetrate snowpack no more than a few centimeters (Brandt and Warren, 1993; Järvinen and Leppäranta, 2013). This length scale is smaller than typical laser altimetry surface elevation errors due to ice and snow surface roughness and geolocation uncertainty (Deems et al., 2013). In contrast, the laser altimeter onboard ICESat-2 transmits 532 nm laser pulses (Markus et al., 2017). Ice is ~10× more transparent at 532 nm than at 1064 nm (Warren and Brandt, 2008), and photons at 532 nm may penetrate many tens of centimeters into glacier ice. These subsurface scattered photons may introduce a range bias in ICESat-2 surface elevation retrievals over glacier ice, similar to radar penetration into snow (Brunt et al., 2016; Gardner et al., 2015; Greeley et al., 2017). To our knowledge no in situ observations of 532 nm optical penetration depth for bare glacier ice exist, thereby precluding field validation of penetration depth obtained from theoretical radiative transfer models.

The purpose of this investigation is to provide experimental values for k_{att} obtained from measurements of solar flux attenuation in bare ice in the Greenland Ice Sheet ablation zone, and to compare them with theoretical values for k_{att} obtained from the two-stream analytical solution (c.f. Equation 26 Bohren, 1987; Schuster, 1905). We benchmark our field estimates against the two-stream solution because of its wide use in surface energy balance models applied to snow and ice. In Section 2 we describe the field measurements and the optical theory used to interpret the solar flux attenuation. In Section 3 we report values for k_{att} and k_{abs} obtained from our measurements, compare them with values obtained from two-stream theory, and propose a simple empirical model that accounts for enhanced near-surface attenuation. In Section 4 we discuss how our k values differ from prior experimental values acquired in sea ice and

snowpack and from theoretical values, and the implication of these differences for modelling radiative transfer in bare glacier ice. To demonstrate the broader implications of our study, we suggest how our findings can be used to understand interactions between visible-light laser altimetry (e.g. ICESat-2) and bare glacial ice surfaces, and how they can be used to improve models for subsurface heating of ablating glacier ice.

2 Data and Methods

2.1 Spectral transmittance measurements

Ice transmittance was measured on 20 July 2018 in the Kangerlussuaq sector of the western Greenland Ice Sheet. The study site (67.15 ^{o}N, 50.02 ^{o}W) is located ~1 km from the ice sheet margin at 840 m a.s.l. Subsurface (in-ice) spectral irradiance was measured at 0.35 nm spectral resolution in the wavelength range 300–900 nm with an Ocean Optics® JAZ spectrometer calibrated for absolute irradiance. Light was guided from the ice interior to the spectrometer with a 3 mm diameter Kevlar-sheathed fiber optic cable fitted inside a 2 m long insulated white PVC tube (Figure 2-1). The fiber was affixed at one end to a Spectralon remote cosine receptor (RCR) diffuser via a 90^{o} collimating lens adapter. The RCR barrel was wrapped in white PTFE tape and set 2 mm out from the PVC tube exterior to act as a contact horizon between its diffusing element and the ice. The system was operated from a battery-powered computer running the Ocean Optics Ocean View software. The computer and spectrometer were placed on a tripod platform oriented 180^{o} away from the sun and 2.5 m horizontal distance from the measurement location.

To access the interior of the ice, holes were drilled horizontally into a 2-m high sidewall of a natural ice feature with a battery powered hand drill fitted with a 3 cm diameter Kovacs auger bit. Each hole was drilled 2 m deep into the ice. Starting at the lowest hole near the bottom of the sidewall, the auger was advanced into the sidewall approximately 20 cm, levelled horizontally with a digital spirit level, and the sequence repeated to 2 m horizontal depth. The PVC tube-fiber optic assembly was then inserted into the hole, RCR facing upward, and a 2 m long ruler was shimmed under the bottom of the PVC tube to ensure the RCR barrel preserved contact with the overlying ice thus minimizing stray light contamination into the

RCR field of view. Ice shavings were packed around the drill hole to prevent light reflection into the hole. Spectral irradiance was recorded at 1 Hz frequency using a 20-scan average and 44 Hz integration time for 30 seconds yielding 30 irradiance profiles, after which the tube was removed, the next hole was drilled, and the sequence was repeated working from the bottom toward the ice surface.

Background upwelling and downwelling spectral irradiance were measured continuously at 2 m height above the ice surface approximately 3 m away from the in-ice measurements using a dual-channel Ocean Optics JAZ spectrometer calibrated for absolute irradiance. These data were recorded at 1 min frequency using a 20-scan average and 92 Hz integration time. Light was guided to the spectrometer via two 3 m fiber optic cables attached to two RCRs mounted in upward-looking and downward-looking orientation on a 2 m long horizontally levelled boom attached to a vertical mast drilled into the ice. The measurements were completed between 13:45 and 14:35 local time (UTC -3), at solar zenith angles of ~48–51°. Solar noon at this time and location is ~13:26.

2.2 Experimental determination of asymptotic flux attenuation coefficients

Spectral asymptotic flux attenuation coefficients are estimated by fitting a Bouguer-law exponential decay model as per Grenfell and Maykut (1977) to the in-ice irradiance depth profiles:

$$\mathrm{I}(\mathrm{z},\lambda) = \mathrm{I}(\mathrm{z_o},\lambda)\mathrm{e}^{-k_{\mathrm{att}}(\lambda)(\mathrm{z}-\mathrm{z_o})} \quad (2)$$

where $k_{\mathrm{att}}(\lambda)$ is the asymptotic flux attenuation coefficient for wavelength λ, $\mathrm{I}(\mathrm{z})$ is in-ice spectral irradiance at depth z, $\mathrm{I}(\mathrm{z_o})$ is background downwelling spectral irradiance, $\mathrm{z_o}$ is the ice surface, and $T(\mathrm{z},\lambda) = \mathrm{I}(\mathrm{z},\lambda)/\mathrm{I}(\mathrm{z_o},\lambda)$ is spectral transmittance. The raw 0.35 nm spectra were interpolated to 1 nm using bilinear interpolation and smoothed with a centered moving mean filter with window size 3 nm. Estimates of $k_{\mathrm{att}}(\lambda)$ for each 1 nm band were estimated as the slope of the ordinary least-squares linear solution to $\ln T(\mathrm{z},\lambda)$ vs. $(\mathrm{z}-\mathrm{z_o})$.

The optical depth $\tau(\mathrm{z},\lambda)$ is a dimensionless path length that scales the physical thickness of a layer by its attenuation rate:

$$\tau(z,\lambda) = k_{att}(\lambda) \cdot z = -\ln T(z,\lambda) \quad (3)$$

The attenuation length $l(\lambda)$ is the inverse of $k_{att}(\lambda)$, and is referred to elsewhere as the photon mean free path (Ackermann et al., 2006). It is equivalent to the path length in ice required to attenuate irradiance to 37% ($1/e$) of its incident intensity, i.e. the path length at which $T = 1/e$ and $\tau = 1$:

$$l(\lambda) = \frac{1}{k_{att}(\lambda)} \quad (4)$$

Note that attenuation is expressed in terms of $l(\lambda)$ in Section 3.4 and 4.3 to describe its physical in-situ length-scale. Solid ice-equivalent values of $k_{att}(\lambda)$, $k_{abs}(\lambda)$, and $k_{scat}(\lambda)$ are provided in Appendix 1.

2.3 Theoretical determination of asymptotic flux attenuation coefficients

Theoretical values of $k_{att}(\lambda)$ are calculated using the solution given by the two-stream radiative transfer approximation (Schuster, 1905):

$$k_{att}(\lambda) = \frac{3}{4}\frac{\rho_i}{\rho_{ice}}\frac{Q_{ext}(\lambda)}{r_{eff}}\sqrt{(1-\omega(\lambda))(1-g\omega(\lambda))} \quad (5)$$

where ρ_i is ice sample density (kg m^{-3}), ρ_{ice} is pure ice density (917 kg m^{-3}), $Q_{ext}(\lambda)$ is the extinction efficiency, r_{eff} is the effective scattering particle radius (m), $g(\lambda)$ is the average cosine of the scattering angle, and $\omega(\lambda)$ is the single-scattering albedo. Equation (5) describes light attenuation by multiple scattering and absorption in a homogeneous plane-parallel slab of absorbing spheres. Its derivation is available in Bohren (1987).

To estimate r_{eff}, Equation (5) is iteratively solved for the value of r_{eff} that minimizes the difference between measured and calculated k_{att} at $\lambda = 600$ nm. This method assumes all absorption at 600 nm is due to ice (Warren et al., 2006). If absorption was influenced by LAPs r_{eff} would be over-estimated. Values for $Q_{ext}(\lambda)$, $g(\lambda)$, and $\omega(\lambda)$ are obtained from Mie scattering algorithms provided as MATLAB code by Mätzler (2002), $m(\lambda)$ is from Warren and Brandt (2008), and ρ_i is obtained from an ice core extracted at the measurement location with depth-weighted measured ice density 835 kg m^{-3}. The optimal r_{eff} value is 2.8 mm and this value is used in all subsequent calculations.

2.4 Flux absorption coefficients

Warren et al. (2006) developed a method to estimate $k_{\mathrm{abs,ice}}(\lambda)$ from measurements of flux attenuation in snow in Antarctica. The method relies on three assumptions: 1) the value of $k_{\mathrm{abs,ice}}$ at 600 nm is known accurately, 2) the value of k_{abs} at 600 nm is not affected by LAPs in the measured snow or ice, and 3) $\omega(\lambda)$ varies so little as to be effectively independent of wavelength in the spectral range considered (here the near-UV and visible). Warren et al. (2006) verified the validity of these assumptions for the spectral range 350–600 nm and obtained the following relation (Equation 15 of that paper) between flux attenuation and flux absorption:

$$\left[\frac{k_{\mathrm{att}}(\lambda)}{k_{\mathrm{att}}(\lambda_{\mathrm{o}})}\right]^2 \approx \left[\frac{k_{\mathrm{abs}}(\lambda)}{k_{\mathrm{abs}}(\lambda_{\mathrm{o}})}\right] \tag{6}$$

where $\lambda_{\mathrm{o}} = 600$ nm is the reference wavelength. Equation (6) was used by Warren et al. (2006) to estimate k_{abs} for pure ice (i.e. $k_{\mathrm{abs,ice}}$) from 350–600 nm.

Equation (6) requires that absorption at the reference wavelength (600 nm) is not affected by LAPs but the relation can be used to estimate k_{abs} at any other wavelength, including those where absorption is affected by LAPs. At those wavelengths, Equation (6) will predict values for k_{abs} higher than those for pure ice if LAPs are present in the measured snow or ice volume, due to the influence of LAPs on k_{att}. Consequently, although not developed for this purpose, Equation (6) provides a means to infer the influence of LAPs on measured flux attenuation by comparison with values of $k_{\mathrm{abs,ice}}$ provided by Warren et al. (2006), which are compiled in Brandt and Warren (2008). A similar approach was used to infer LAP absorption in snowpack (Tuzet et al., 2019). Here, we exploit this to interpret differences between our theoretical and experimental values of k_{att} on the basis of differences between $k_{\mathrm{abs,ice}}$ (Warren et al., 2006) and the k_{abs} values that we obtain for glacier ice from Equation (6).

2.5 Near surface effects

The $k_{\mathrm{att}}(\lambda)$ values calculated using Equation (2) are applicable at distances far enough from the incident boundary (here the ice surface) that the radiation field is diffuse and $k_{\mathrm{att}}(\lambda)$ is constant with depth. Near

the ice surface the radiation field is converted via multiple scattering from direct to diffuse flux, and attenuation is enhanced by transmission of upward reflected light out of the ice volume before re-reflection downward (Briegleb and Light, 2007). Attenuation may also be enhanced by specular reflection at the ice surface, depending on its roughness (Dadic et al., 2013; Mullen and Warren, 1988). To parameterize these near-surface effects, we introduce a modified form of Equation (2):

$$\mathrm{I}(\mathrm{z},\lambda) = (1-\chi)\,\mathrm{I}(\mathrm{z_o},\lambda)\mathrm{e}^{-k_{\mathrm{att}}(\lambda)(\mathrm{z}-\mathrm{z_o})} \tag{7}$$

where χ is the fraction of incident spectral irradiance attenuated in the near-surface boundary layer (inclusive of the surface) and all other terms are as previously defined. The χ parameter is analogous to the i_{o} parameter introduced by Grenfell and Maykut (1977) to partition the bulk (spectrally-integrated) net absorbed solar flux between the upper 10 cm of sea ice, which they termed the "Surface Scattering Layer" (SSL), and the ice interior, in which radiation is exponentially attenuated at a constant rate. The i_{o} parameter has been widely adopted in energy balance models of glaciers and sea ice where radiation penetration is important (Bintanja and Van Den Broeke, 1995; Hoffman et al., 2014; Holland et al., 2012). For example, the sea ice component of the Community Earth System Model (CESM) uses $i_{\mathrm{o}} = 30\%$ (Briegleb and Light, 2007). The important distinction is that i_{o} is a spectrally integrated value applicable to energy balance modelling whereas χ is applicable for comparison with measurements of downward spectral irradiance within ice.

3 Results

3.1 Spectral transmittance

Four spectra of in-ice irradiance were collected at 12 cm, 36 cm, 58 cm, and 77 cm depth below the ice surface (Figure 2-2a). These spectra are normalized by the coincident-in-time surface spectra to calculate spectral transmittance, T (Figure 2-2c). At all depths, T is maximum at 430 nm and maintains relatively stable and high values up to about 500 nm in the visible, beyond which T decreases into the red end of the visible spectrum where absorption by ice is higher. Maximum T values vary from 78% at 12 cm to 41% at 77 cm. For $\lambda > 500$ nm T rapidly decreases both with wavelength and with depth. Beyond about 800 nm

nearly all incident light is attenuated below 36 cm, with T<2% at 36 cm and <0.6% at 58 and 77 cm depth. In contrast, T at 12 cm decreases from 18% at 800 nm to 5% at 900 nm, suggesting substantial subsurface flux absorption in the 12–36 cm depth region (Figure 2-2c).

3.2 Experimental estimates of flux attenuation coefficients and albedo

Example log-linear fits to Equation (2) at $\lambda = 350, 450, 550, 650, \text{and } 700 \text{ nm}$ give k_{att} values ranging from 1.03 m^{-1} to 5.51 m^{-1} (Figure 2-3a). These values correspond to attenuation lengths of 0.97 m to 0.18 m, respectively. Measured values of in-ice irradiance at 58 cm and 77 cm depth were too low to calculate k_{att} beyond 700 nm (Figure 2-2 and Figure 2-3c). Although T is maximum at 430 nm, the minimum k_{att} value (0.96 m^{-1}) occurs at 396 nm. The coefficient of determination (r^2) ranged from 0.96–1.0 ($p<0.01$), with a median value of 0.98, suggesting the data are described appropriately by the Bouguer-law exponential decay model.

Albedo spectra correspond closely to patterns in transmittance and k_{att} spectra (Figure 2-3c). The near-UV and blue wavelengths that efficiently transmit into ice mostly re-emerge as reflected light, owing to the extremely low values of ice absorption coefficient in the wavelength range 350–500 nm where albedo is maximum (Warren et al., 2006). The maximum measured albedo value (0.83) occurs at 447 nm, suggesting a slight red shift relative to the location of the minimum k_{att} value (0.96 m^{-1}) at 396 nm, however albedo varies little in the region of minimum k_{att} and is 0.82 at 396 nm. Beyond about 500 nm, albedo decreases rapidly, and most transmitted light is absorbed, as indicated by the larger k_{att} values and the extremely low transmittance at depths below 36 cm.

3.3 Theoretical flux attenuation coefficients

Theoretical k_{att} values predicted by the two-stream solution are nearly one order of magnitude lower than field estimates of k_{att} for $\lambda < 500 \text{ nm}$ (blue circles vs orange line, Figure 2-4a). This discrepancy can be inferred to relate to the presence of LAPs embedded in the ice matrix that increase the effective absorption of the ice volume. For example, differences between the field-estimate of k_{abs} and $k_{\text{abs,ice}}$ (Figure 2-4b)

mirror those between the field-estimate and theoretical estimate of k_{att} (Figure 2-4a). Namely, k_{abs} is nearly one order of magnitude larger than $k_{\mathrm{abs,ice}}$ in the range 350–500 nm, where even very small concentrations of LAPs in the measured ice volume would dominate absorption (Warren et al., 2006). In contrast, the two-stream solution and theory converge at $\lambda > 530$ nm where absorption is dominated by grain-size effects.

To gain further insight into the mechanisms that drive differences between field estimates and two-stream theory, we compare our k_{att} values for glacier ice in Greenland to published values of k_{att} for clean, fine-grained snow in Antarctica ($k_{\mathrm{att,snow}}$) (Warren et al., 2006) (Figure 2-5). The values for $k_{\mathrm{att,snow}}$ reported by Warren et al (2006) were obtained by applying Equation 1 to measurements of flux transmission in a ~45 cm thick snow layer at ~90–135 cm depth near Dome C (75°S, 123°E, 3230 m), adjusted to remove the absorptive influence of ~0.3 ppb soot (the radiative forcing of 0.3 ppb soot is equivalent to a 4 um increase in r_{eff}). These values are therefore representative of flux attenuation in optically pure snow. We also calculate $k_{\mathrm{att,snow}}$ using Equation (5) with values for r_{eff} (135 um) and ρ_{i} (463 kg m^{-3}) as reported by Warren et al (2006).

Because scattering is a function of r_{eff} but independent of λ, the curves for $k_{\mathrm{att,snow}}$ and $k_{\mathrm{att,ice}}$ (blue circles vs purple squares, Figure 2-4a) have a constant offset proportional to the ratio $r_{\mathrm{eff,snow}}/r_{\mathrm{eff,ice}}$ (c.f. Equation 16 of Warren et al., 2006). This holds true when considering structural differences between snow and ice that control scattering (i.e. snow grains vs air bubbles) since $r_{\mathrm{eff}} \gg \lambda$ in either case. In contrast, field estimates for glacier ice clearly diverge from theoretical estimates with a wavelength-dependent offset in the spectral range 350–530 nm where LAPs dominate absorption (blue circles vs. orange line, Figure 2-4a). Finally, it is evident that scattering by fine-grained snow greatly enhances flux attenuation. This comparison provides a useful contrast between the flux attenuation properties of snow vs glacier ice that is discussed in Section 4.

3.4 Transmitted irradiance and near-surface attenuation

Near the ice surface irradiance is not attenuated exponentially and Bouguer's law does not hold, as confirmed by the y-intercepts of the straight lines in Figure 2-3b at values <100%. This suggests k_{att} values are higher in the 0–12 cm near-surface region where irradiance measurements were not obtained. Consequently, transmitted irradiance is overestimated by 5–50% if Bouguer's law is applied to the incident surface irradiance using k_{att} values from the 12–77 cm region, with median over-estimation 16% (Figure 2-5a). The value of χ Equation (7) that minimizes the root-mean-squared-difference between measured and predicted transmitted irradiance, weighted equally at all depths and all λ, is 15%. Transmitted irradiance spectra predicted using Equation (7) with $\chi = 15\%$ are shown in Figure 2-5c.

Expressed in terms of attenuation rate, effective k_{att} values for the 0–12 cm region estimated from a finite-difference solution to Equation (2) are ~1.5× higher than those in the 12–77 cm region for $\lambda > 570$ nm, and are up to 3.7× higher between 400–570 nm (Figure 2-6). This suggests attenuation enhancement by LAPs is higher in the 0–12 cm region than in the 12–77 cm region, consistent with the expectation that impurity concentration is higher near the ice surface. Stated in terms of attenuation length, l varies from 117 cm at 356 nm to 14 cm at 700 nm. These values are calculated by combining the effective k_{att} values for the 0–12 cm region with the k_{att} values for the 12–77 cm region and therefore correspond to effective penetration depths. Effective penetration depths are smaller than attenuation lengths inferred from k_{att} values for the 12–77 cm region (i.e. from Equation 4), owing to the higher attenuation in the 0–12 cm region. The effective penetration depth at 532 nm is 49 cm, or 15 cm lower than the 64 cm attenuation length implied by our empirical k_{att} values in the 12–77 cm region, and 19 cm lower than the 68 cm attenuation length implied by theoretical k_{att} values for optically pure glacier ice.

The enhanced near-surface attenuation found here is consistent with observations of enhanced attenuation in the granular and porous surface layer on sea ice (Grenfell and Maykut, 1977). The field measurements were collected following several days of light but persistent rainfall and cloud cover, conditions that inhibit development of granular near-surface ice (e.g. 'weathering crust') (Müller and

Keeler, 1969). Qualitatively, the ice surface was semi-granular to a depth of ~4 cm, below which the ice transitioned to solid bubbly ice (Figure 2-7). For example, the upper four centimeters of ice core could not be recovered owing to its granular structure. The recovered core was split into three segments corresponding to depths of 4–45 cm, 45–74 cm, and 74–122 cm below the ice surface. The density of these segments was 801 kg m^{-3}, 884 kg m^{-3}, and 888 kg m^{-3}, respectively. An ice screw was used to recover an ice sample from the upper 8 cm. The density of this ice was 699 kg m^{-3}, confirming the presence of low-density granular near-surface ice.

For smooth ice surfaces, attenuation may be enhanced by refraction at the ice-air interface (Mullen and Warren, 1988). If present, a refractive boundary would enhance near-surface attenuation via external specular reflection, and possibly via enhanced near-surface absorption of the internally reflected downward flux. Following Briegleb and Light (2007), we calculate the external diffuse specular reflectivity for a flat ice surface to be 0.063, meaning specular reflection could enhance attenuation by up to 6.3%. This value is smaller than the 10–25% surface attenuation implied by the y-intercepts in Figure 2-3c, suggesting specular reflection alone cannot explain the discrepancy. Instead, we suggest that enhanced scattering by the granular near-surface ice microstructure, together with absorptive impurities, enhanced near-surface light attenuation at our field site.

3.5 Uncertainty analysis

We repeated the entire analysis reported in Section 3 using $\rho_{\mathrm{i}} = 801$ kg m^{-3} and $\rho_{\mathrm{i}} = 884$ kg m^{-3}, values that bracket the range of ice density measured in the ice interior. The optimal r_{eff} values were 2.5 mm and 3.2 mm, respectively. However, the single-scattering properties varied so little (max difference 0.2% for $\omega > 800$ nm) that all reported results were identical. The ice-equivalent k_{att} values given in Appendix 1 are referenced to the depth-weighted ice density measured in the 4–74 cm region (835 kg m^{-3}). The reader is advised that ice density varied from 801–884 kg m^{-3} between 4–122 cm depth; however, this analysis reports on measurements collected between 12–77 cm depth, for which ice density varied from 801–842 kg m^{-3}.

Two separate observers made ten independent measurements of the vertical distance between the in-ice irradiance collections. The mean error ($\pm$ one standard deviation) was 0.9 ± 1.2 cm. During the period 19–22 July one of these observers measured the height of an ablation stake using the same ruler that was used to measure the vertical distance between the in-ice irradiance collections. Two measurements were taken each time, for 41 total replicates. The mean error ($\pm$ one standard deviation) was 0.2 ± 1.2 cm. This suggests 1.2 cm is a reasonable approximation for vertical measurement uncertainty, and is represented as horizontal uncertainty bars on the in-ice transmittance values in Figure 2-3b and as shaded uncertainty bounds on the near-surface attenuation rates in Figure 2-6.

4 Discussion

4.1 Comparison with attenuation spectra for sea ice and snowpack

We report spectral measurements of near-UV and visible light transmission in bare ablating glacier ice. These measurements are used to estimate asymptotic flux attenuation coefficients k_{att} for the spectral range 350–700 nm. Prior studies quantified k_{att} for sea ice (c.f. Frey et al., 2011; Grenfell and Maykut, 1977; Light et al., 2008; Pegau and Zaneveld, 2000), snowpack (Fisher et al., 2005; Gerland et al., 2000; Järvinen and Leppäranta, 2013; King and Simpson, 2001; Meirold-Mautner and Lehning, 2004; Picard et al., 2016; Tuzet et al., 2019; Warren et al., 2006), and for compressed glacial ice at 800–2350 m depth in the Antarctic Ice Sheet for which optical scattering is not representative of near-surface ablating glacier ice (Ackermann et al., 2006; Askebjer et al., 1995, 1997).

Light attenuation in glacier ice differs from sea ice and snowpack in several important ways. Figure 2-8 compares the k_{att} spectra for glacier ice measured here to seven previously published k_{att} spectra for snowpack and sea ice. Light attenuation in sea ice is controlled by its unique vertical composition, including brine inclusions, air pockets, solid salts, sea ice algae, dissolved organic matter, and radiative interactions between the ice and underlying ocean (Perovich, 1996). Relative to prior measurements in sea ice (Grenfell et al., 2006; Grenfell and Maykut, 1977), our results suggest light attenuation by glacial ice is lower at blue-green wavelengths and higher at orange-red wavelengths, likely reflecting differences in the absorption

spectra of light absorbing material found in sea ice relative to that found in glacier ice (Figure 2-8). Relative to prior measurements made in snow near Summit, Greenland (Meirold-Mautner and Lehning, 2004), our results suggest attenuation by glacial ice has a similar spectral shape but lower attenuation at all wavelengths, likely due to enhanced scattering from the fine-grained structure of polar snow. Snow near Dome-C in Antarctica has lower attenuation at blue-green wavelengths than snow near Summit, Greenland, but is nearly identical at longer wavelengths, suggesting visible-light attenuation at Summit is enhanced by higher LAP concentration. Attenuation within the surface scattering layer (SSL) of sea ice is higher still, and attenuation at 5 cm depth in snow near Summit is highest of all, likely due to direct scattering of light out of the near-surface optical boundary layer. The comparison demonstrates the tremendous variation in k_{att} values caused by differences in ice structure and composition, and the importance of site-specific studies such as ours for characterization of ice optical properties.

4.2 Relevance to surface energy balance modelling and subsurface meltwater production

Our field estimates of k_{att} are up to one order of magnitude larger in the spectral range 350–530 nm than those obtained from two-stream theory for optically clean ice. This is important because visible light transmission provides an energy source for subsurface heating and internal melting of glacier ice in the ablation zones of glaciers and ice sheets (Cooper et al., 2018; Hoffman et al., 2014; Liston and Winther, 2005; Schuster, 2001). Prior estimates of subsurface meltwater production in bare ice used two-stream theory forced by values of $m(\lambda)$ for pure ice to calculate k_{att} and the absorbed solar flux as a function of depth below the ice surface in both Greenland and Antarctica (van den Broeke et al., 2008; Hoffman et al., 2014; Kuipers Munneke et al., 2009; Liston and Winther, 2005). Comparison with the spectral absorption coefficient of pure ice (Figure 2-4c) suggests the discrepancy we find is likely due to LAPs present in the measured ice volume, which appear to disproportionately enhance energy absorption near the ice surface.

Examples of LAPs found in near-surface glacier ice include dust, black carbon, and microorganisms such as cyanobacteria and algae, each of which absorb light at wavelengths < ~600 nm (Bøggild et al., 2010; Ryan et al., 2018; Stibal et al., 2017; Takeuchi, 2002; Warren et al., 2006; Yallop et

al., 2012). To our knowledge, the influence of LAPs on subsurface meltwater production has not been quantified and is beyond our scope here, but our results point to the potential for subsurface energy absorption enhancement by LAPs in ablating glacier ice. This is consistent with inferences made for surface melt rates caused by distributed LAPs on bare ice surfaces in Greenland (Bøggild et al., 1996; Goelles et al., 2015; Goelles and Bøggild, 2017), and for subsurface energy absorption in snowpack (Tuzet et al., 2019). Moreover, if present in higher concentration near the ice surface, LAPs would reduce light availability for subsurface heating at depth. This is supported by the enhanced attenuation rates found at wavelengths between 400–570 nm for the 0–12 cm region relative to those for the 12–77 cm interior ice region (Figure 2-6b).

4.3 Relevance of enhanced near-surface attenuation to ICESat-2

Our results suggest penetration depth of visible wavelength light into solid glacier ice is lower by up to 19 cm at wavelengths relevant to visible-wavelength lidar altimetry of ice surface elevation (e.g. 532 nm for the Ice, Cloud, and Land Elevation Satellite-2). Our asymptotic k_{att} values suggest e-folding penetration depth (the physical depth in units of ice thickness equivalent to one optical depth; equivalently, the physical depth required to attenuate incident irradiance to $1/e$ or ~37%) at 532 nm is 64 cm, in relatively close agreement with two-stream theory that predicts 68 cm. However, this path length is only relevant at depths within the ice volume where the light field is diffuse and attenuation rates are asymptotic (Briegleb and Light, 2007). Near the ice surface attenuation rates are enhanced and rapidly decrease to their asymptotic value. The net effect at our field site is to reduce 532 nm penetration depth to ~49 cm. This enhanced near-surface attenuation is expected, but its magnitude has not previously been measured in near-surface glacier ice. The optimal value $\chi = 15\%$, which parameterizes the magnitude of enhanced near-surface attenuation relative to the interior asymptotic attenuation rate, is one-half the canonical 30% value used in two-layer sea ice models (Briegleb and Light, 2007; Grenfell and Maykut, 1977). This lower value is consistent with our field observations of an anomalously thin (~4 cm) near-surface weathered ice layer (Figure 2-7), likely due to several days of persistent rain prior to our field measurements. This suggests penetration depths

could be reduced further over heavily weathered ice or impurity-laden ice (for which backscatter magnitude may also be reduced), conditions that are common in the Greenland Ice Sheet ablation zone (Cooper and Smith, 2019; Goelles and Bøggild, 2017; Ryan et al., 2018; Tedstone et al., 2017).

The following caveats are important for interpreting the relevance of this experiment to ICESat-2. This experiment quantified the in-ice attenuation of diffuse solar flux. The ICESat-2 instrument transmits and receives discrete laser pulses over finite timesteps at 0^{o} incidence and records the distribution of single-photon travel times returned through the intervening atmosphere (Markus et al., 2017). The penetration depth values given here are therefore not estimates of ICESat-2 laser penetration depth in glacier ice but provide validation data for radiative transfer models specific to the ICESat-2 measurement problem.

4.4 Suggestions for further work

Our results suggest that existing methods for sea ice radiative transfer modelling are readily applicable to ablating glacier ice (Holland et al., 2012; Light et al., 2004). Observations of non-exponential attenuation in sea ice due to enhanced near-surface scattering and vertical variations in ice microstructure motivated adoption of two-layer and then multi-layer models with vertically-varying inherent optical properties, providing a ready template for the enhanced near-surface attenuation we describe here (Briegleb and Light, 2007; Grenfell, 1991; Grenfell and Maykut, 1977; Light et al., 2003). The simple empirical model we demonstrate (Figure 2-5) suggests the need for a two-layer approach to modelling light attenuation in glacier ice. Vertical variation in ice microstructure and/or scattering geometry can be approximated by treating g and ω as free parameters (Meirold-Mautner and Lehning, 2004), or by using a similarity approach that infers optimal scattering and absorption coefficient values from co-located observations of albedo and transmittance (Light et al., 2004). The values we report provide a possible first step toward using this approach to diagnose structural controls on albedo and radiative transfer in ablating glacier ice. Finally, the k_{abs} values we report provide new insight into the magnitude of this fundamental but uncertain optical property, and provide support for the lower bound pure ice estimate from Warren et al. (2006) (Figure 2-9).

5 Conclusion

We report first in-situ spectral measurements of near-UV and visible light attenuation coefficients k_{att} for near-surface bare glacial ice, collected in the Greenland Ice Sheet ablation zone during July 2018. In general, our empirical k_{att} values are nearly one order of magnitude larger in the range 350–530 nm than predicted by asymptotic two-stream radiative transfer theory using canonical values for the complex index of refraction of pure ice (Warren and Brandt, 2008). This suggests light absorbing particles enhance visible light absorption and reduce optical penetration depth at our field site. The simple Bouguer exponential decay model accurately describes light attenuation in the ice interior but underestimates light attenuation near the ice surface. Consequently, light transmission is overestimated by 5–50% depending on wavelength. This enhanced near-surface attenuation is consistent with observations of enhanced scattering from the semi-granular near-surface ice layer on sea ice and appears to be further enhanced at our field site by light absorbing particles concentrated near the ice surface. The magnitude of this near-surface attenuation suggests that visible-light penetration depth at wavelengths relevant to ice surface laser altimetry (e.g. 532 nm for Ice, Cloud, and Land Elevation Satellite-2) is lower by 19 cm than would be inferred from two stream theory for optically pure glacier ice. This enhanced near-surface attenuation implies shallower light transmission and therefore lower light availability for bio-photochemical cycling and subsurface energy absorption in glacier ice. Further work should quantify the sensitivity of light attenuation to vertical variations in ice microstructure and absorptive impurity concentrations representative of near-surface ice in the Greenland Ice Sheet ablation zone, and we provide new values of flux attenuation, absorption, and scattering coefficients to support model parameterization and validation.

6 Figures

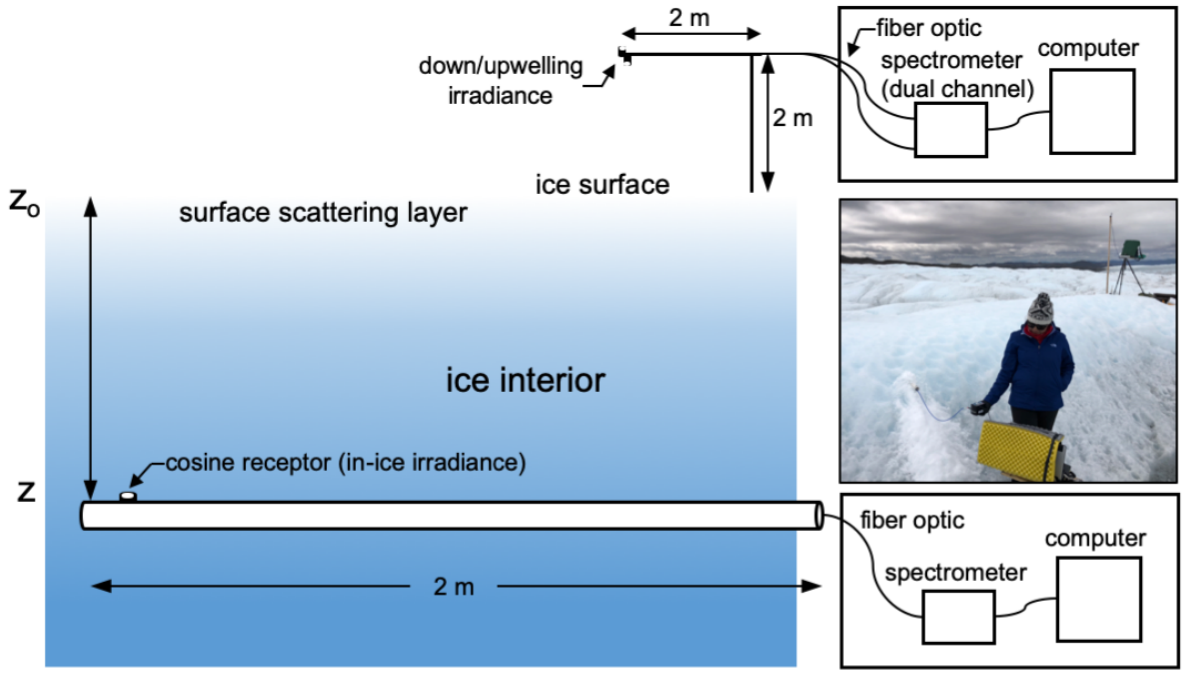

Figure 2-1. Experimental setup schematic. The horizontal cylindrical rod is an insulated white PVC tube of 2 m length. Holes are drilled level and horizontal into the ice, the tube is inserted, and drill shavings are packed around the hole to prevent stray reflections, working from the bottom toward the top. Inside the tube is a fiber optic cable attached to a remote cosine receptor with a Spectralon diffusing element oriented parallel to the rod (normal to the vertical), set approximately 2 mm out from the tube exterior and in contact with the overlying ice. The cosine receptor collects the downwelling light, guides it to the fiber optic cable that transmits the light to an Ocean Optics JAZ spectrometer, and a computer running the Ocean Optics Ocean View software records the spectra. Background upwelling and downwelling surface spectra are recorded on a 2 m mast drilled into the ice approximately 3 m to the northwest of the in-ice measurement location (visible in the photo). After all measurements are complete, a 2 m ruler is inserted into each hole, two at a time, and the distance between the holes is recorded to determine their depth relative to each other and to the surface.

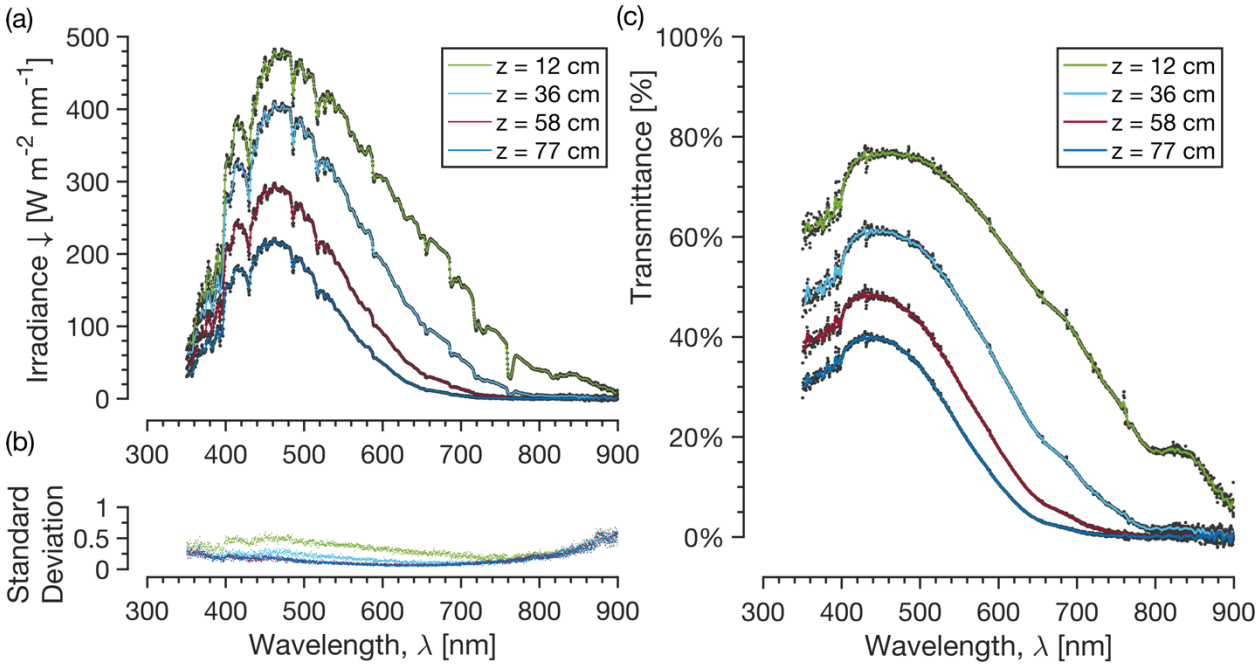

Figure 2-2. (a) Field spectra of in-ice irradiance at four depths below the ice surface collected on 20 July 2018 between 13:45 and 14:35 local time in the western Greenland Ice Sheet ablation zone (67.15 ºN, 50.02 ºW). Raw data were recorded at 1 Hz frequency for 30 seconds, yielding 30 irradiance profiles at each depth. Shown here are 30-second averages at ~0.35 nm spectral resolution for each depth (black dots), and 1-nm interpolated values smoothed with a 3-nm centered moving mean filter for clarity (continuous lines). (b) Standard deviation of the 1 Hz raw data (N=30 for each value) is <1 W m^{-2} nm^{-1} at all wavelengths and measured depths. (c) Relative irradiance (in-ice irradiance divided by surface downwelling irradiance) at each depth, with 30-second averages (black dots) and 1-nm interpolated values (continuous lines) as in (a).

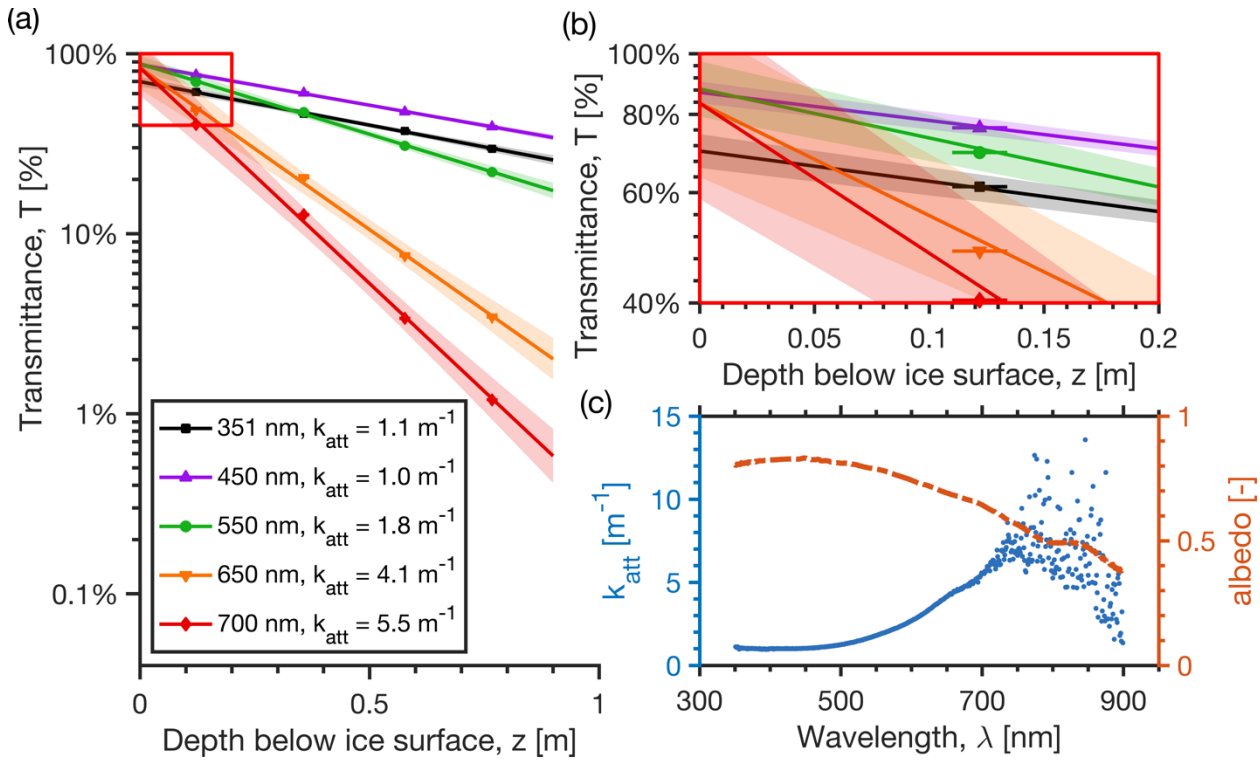

Figure 2-3. (a) Sample least-squares regressions between measured transmittance (indicated by solid symbols) and depth for five representative wavelengths spanning the measured spectral range. The slope of each line is the attenuation coefficient k_{att} (k_{att} values are indicated in the legend). Shaded bounds are one standard error in the linear regression estimate. (b) Red box inset in (a) shows the y-axis intercept of each regression is less than 100%, indicating the magnitude of deviation from Bouguer's law. Horizontal lines through each symbol represent $\pm$1.2 cm vertical measurement uncertainty. (c) Spectral k_{att} (blue dots; left axis) and spectral albedo (red dashed line; right axis). Beyond ~700 nm, in-ice transmitted irradiance is too low to reliably estimate k_{att} (see Figure 3-2a and 3-2c), as indicated by the increased scatter in k_{att} values. The minimum k_{att} value within the range 350–700 nm is 0.96 m^{-1} (0.87 m^{-1} in solid ice-equivalent units) and occurs at 396 nm. The maximum albedo value is 0.83 and occurs at 447 nm.

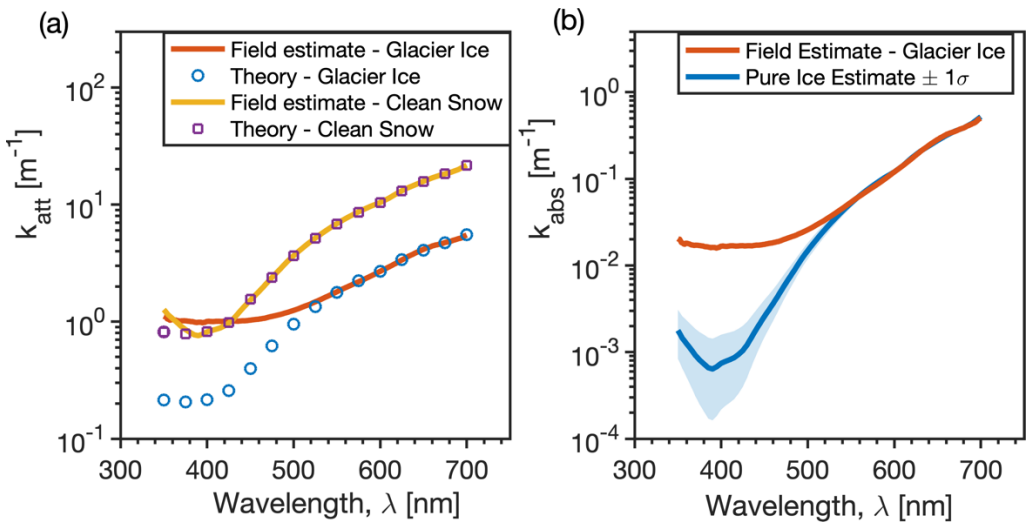

Figure 2-4. (a) Values of the flux attenuation coefficient k_{att} as determined from field measurements of flux transmission in glacier ice (this study), theoretical values for glacier ice using two-stream theory, field measurements in clean snow (Warren et al., 2006), and theoretical values for snow using two-stream theory. The theoretical k_{att} values for ice and snow differ by a constant offset proportional to the ratio of their optical grain sizes, whereas the field-estimate for glacier ice diverges from theory in the region 350–525 nm. (b) Flux absorption coefficient, k_{abs} estimated from the field-estimated k_{att} values using the method of Warren et al (2006) compared to flux absorption coefficient for pure ice, $k_{\mathrm{abs,ice}}$ obtained from field measurements in clean snow in Antarctica by Warren et al (2006). Uncertainty ($\pm$ one standard error in the linear regression coefficient) are shown for both estimates but are imperceptible for glacier ice. As with k_{att}, the k_{abs} values are up to one order of magnitude larger at $\lambda < 525$ nm for glacier ice than pure ice, suggesting light absorbing particles enhance flux absorption at our field site.

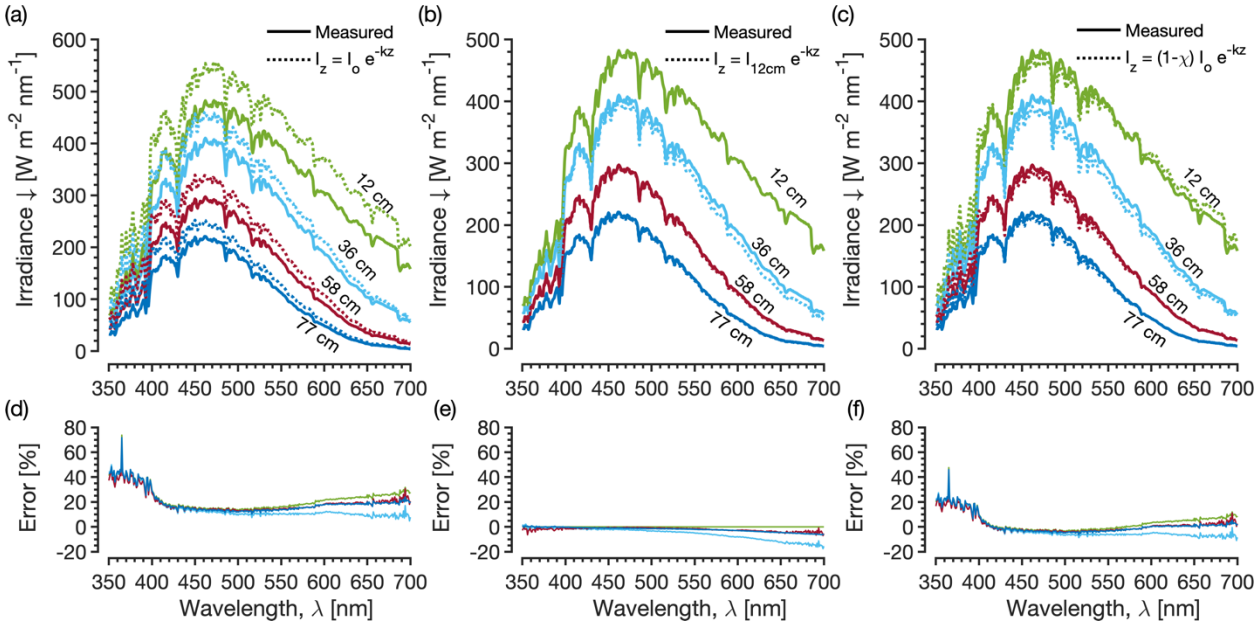

Figure 2-5. Measured in-ice irradiance compared with three empirical models of in-ice irradiance: (a) Bouguer's law (Equation 2) with no modification, (b) Bouguer's law (Equation 2) with $I(z_o) = I(z_{12cm})$, which effectively removes errors due to attenuation in the 0–12 cm near-surface region and isolates the accuracy of Bouguer's law within the ice interior, and (c) the modified Bouguer law (Equation 7) with $\chi = 15\%$. The error structure (d–f) provides insight into the attenuation processes in the 0–12 cm region: (d) relative errors (%) are positive (model under-predicts attenuation) at all wavelengths but are highest in the near-UV, lowest in the blue, and increase monotonically into the red end of the visible spectrum. The spectral dependence suggests a contribution of absorption to near-surface attenuation enhancement; (e) errors are negative (model over-predicts attenuation) and generally decrease monotonically with increasing wavelength from the near-UV through the blue-green; (f) as in (d) the spectral pattern of error due to near-surface attenuation is preserved, but errors are much lower due to the χ parameter. Taken together, near-surface attenuation enhancement is on the order 5–50% but has less relative influence in the blue-green spectrum and more relative influence in the red-orange and near-UV and violet regions of the visible spectrum.

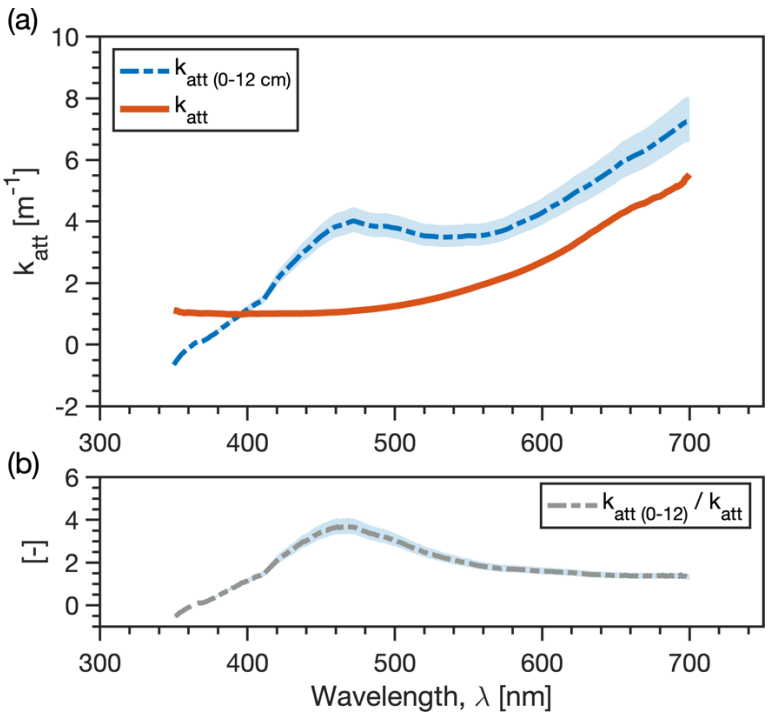

Figure 2-6. (a) Effective attenuation coefficient k_{att} for the near-surface 0–12 cm region estimated with a finite-difference solution to Equation (1) compared to k_{att} values estimated for the interior 12–77 cm region. The shaded bounds represent $\pm$1.2 cm vertical measurement uncertainty. (b) Effective k_{att} values are ~1.6× higher at wavelengths larger than about 600 nm but are ~3.7× higher between 400–600 nm. The shaded bounds represent $\pm$1.2 cm vertical measurement uncertainty. The spectral dependence suggests higher influence of absorptive impurities on attenuation enhancement near the ice surface than in the ice interior. In contrast, the relatively constant attenuation enhancement beyond about 600 nm suggests near-surface ice microstructure, for example the size, shape, and orientation of weathered ice grains or air bubbles, contributes to enhanced near-surface attenuation.

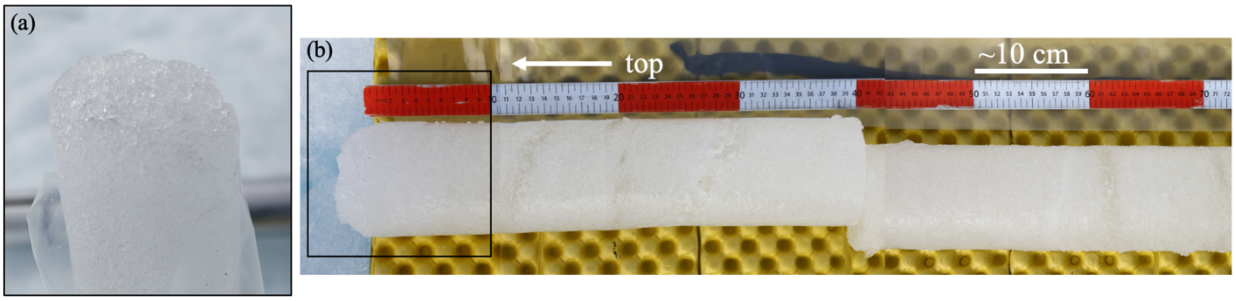

Figure 2-7. Photographs of an ice core collected at the field site. (a) The upper few centimeters of ice is semi-granular. (b) The 122 cm ice core was broken into three segments corresponding to depths of 4–45 cm, 45–74 cm, and 74–122 cm below the ice surface (the far right of the image in (b) is at 74 cm). The density of these segments is 801 kg m^{-3}, 884 kg m^{-3}, and 888 kg m^{-3}, respectively. Black box in (b) is approximately the image area in (a).

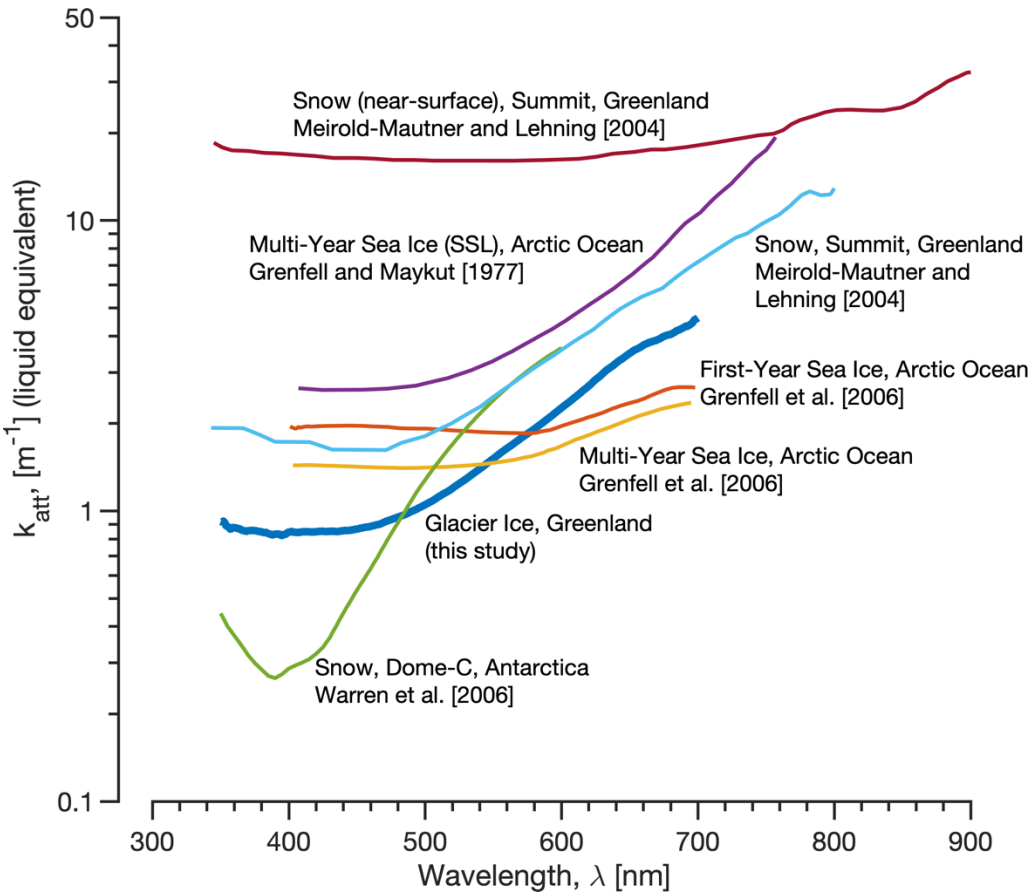

Figure 2-8. Attenuation coefficient spectra for seven distinct ice structures: interior of clean, dry, fine-grained snowpack in Antarctica (Warren et al., 2006), interior of ablating glacier ice in Greenland (this study), interior of multi-year sea ice in the Arctic Ocean (Grenfell et al., 2006), interior of first-year sea ice in the Arctic Ocean (Grenfell et al., 2006), interior of dry, fine-grained snow near Summit, Greenland (Meirold-Mautner and Lehning, 2004), surface scattering layer (SSL) of multi-year sea ice in the Arctic Ocean (Grenfell and Maykut, 1977), and near-surface (5 cm depth) dry, fine-grained snow near Summit, Greenland (analogous to SSL) (Meirold-Mautner and Lehning, 2004). Differences in attenuation magnitude at each wavelength are mostly controlled by structural differences that control scattering, whereas spectral differences are mostly controlled by differences in type and concentration of absorbing impurities. In general, glacial ice attenuates light less efficiently than all other examples shown, with the exception of clean snow near Dome-C in Antarctica for $\lambda < 450$ nm, and multi-year and first-year sea ice for $\lambda > 600$ nm.

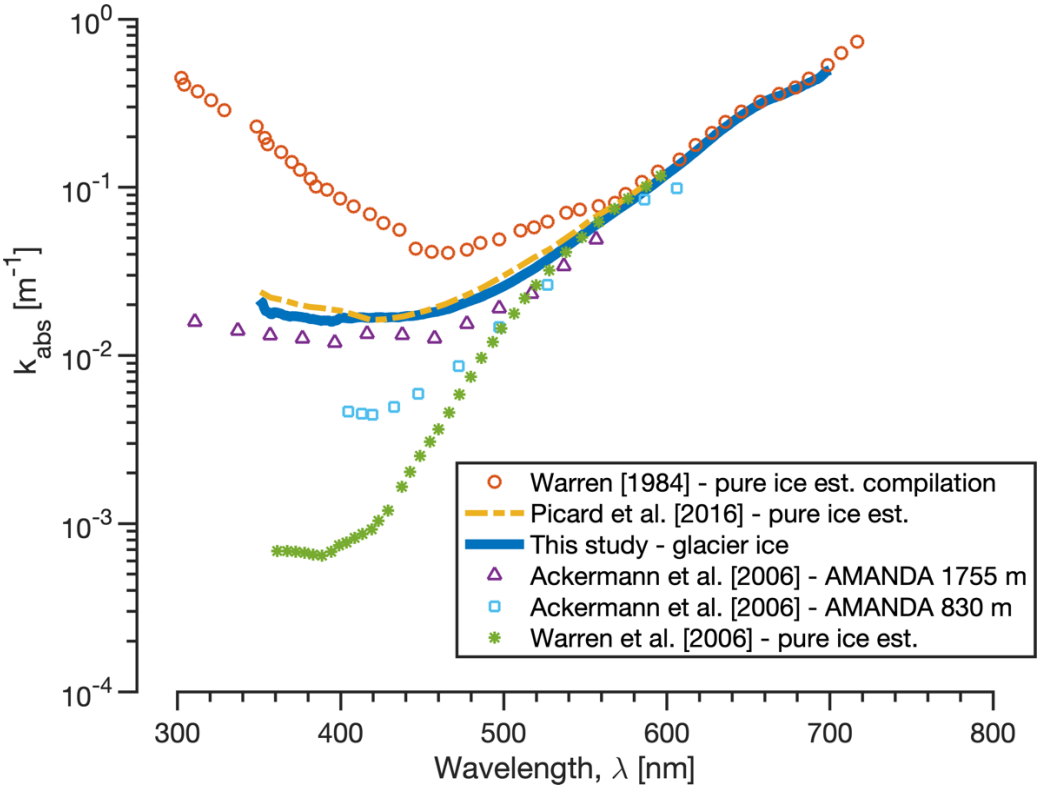

Figure 2-9. Estimates of ice absorption coefficient k_{abs}, obtained from five distinct sources: laboratory-grown pure ice (Grenfell and Perovich, 1981; Perovich and Govoni, 1991), as compiled in Warren (1984), snow in Antarctica, with the effect of light absorbing particles (LAPs) removed (pure ice estimate) (Picard et al., 2016), glacial ice in Greenland with unknown concentration of LAPs (this study), compressed glacier ice at 1755 m depth and 830 m depth in the Antarctic Ice Sheet contaminated by dust deposited during the late Pleistocene and Early Holocene, respectively (Ackermann et al., 2006), and snow in Antarctica with the effect of LAPs removed (pure ice estimate) (Warren et al., 2006). The Picard et al (2016) pure ice estimate is higher at some wavelengths than our glacier ice estimate, which was undoubtedly influenced by LAPs, providing support for the pure ice estimate from Warren et al (2006).

3 Meltwater storage in low-density near-surface bare ice in the Greenland Ice Sheet ablation zone

Abstract. We document the density and hydrologic properties of bare, ablating ice in a mid-elevation (1215 m a.s.l.) supraglacial internally drained catchment in the Kangerlussuaq sector of the western Greenland Ice Sheet. We find low-density (0.43–0.91 g cm^{-3}, μ=0.69 g cm^{-3}) ice to at least 1.1 m depth below the ice sheet surface. This near-surface, low-density ice consists of alternating layers of water-saturated, porous ice and clear solid ice lenses, overlain by a thin (<0.5 m), even lower density (0.33–0.56 g cm^{-3}, μ=0.45 g cm^{-3}) unsaturated weathering crust. Ice density data from 10 shallow (0.9–1.1 m) ice cores along an 800 m transect suggest an average 14–18 cm of specific meltwater storage within this low-density ice. Water saturation of this ice is confirmed through measurable water levels (1–29 cm above hole bottoms, μ=10 cm) in 84% of cryoconite holes and rapid refilling of 83% of 1m drilled holes sampled along the transect. These findings are consistent with descriptions of shallow, depth-limited aquifers on the weathered surface of glaciers worldwide and confirm the potential for substantial transient meltwater storage within porous low-density ice on the Greenland Ice Sheet ablation zone surface. A conservative estimate for the ~63 km^2 supraglacial catchment yields 0.009–0.012 km3 of liquid meltwater storage in near-surface, porous ice. Further work is required to determine if these findings are representative of broader areas of the Greenland Ice Sheet ablation zone, and to assess the implications for sub-seasonal mass balance processes, surface lowering observations from airborne and satellite altimetry, and supraglacial runoff processes.

1 Introduction

Each summer a vast hydrologic network of lakes and rivers forms on the surface of the western Greenland Ice Sheet ablation zone in response to surface melting (Chu, 2014b; Smith et al., 2015). Evidence suggests that most or all of this water is efficiently delivered via supraglacial rivers to moulins, crevasses, and, ultimately, to proglacial rivers and surrounding oceans (van As et al., 2017; Colgan et al., 2011; Lindbäck et al., 2015; Rennermalm et al., 2013a; Smith et al., 2015). The assumption of efficient meltwater delivery

is reflected in regional climate and surface mass balance models for Greenland that instantaneously credit ablation zone surface runoff to the ocean with no physical representation of hydrologic processes taking place on the bare ice surface (Smith et al., 2017). Field studies and satellite remote sensing, however, have found evidence of substantial meltwater runoff delays on daily to monthly timescales in the Greenland Ice Sheet ablation zone (van As et al., 2017; Karlstrom and Yang, 2016; Koenig et al., 2015; Lindbäck et al., 2015; Overeem et al., 2015; Rennermalm et al., 2013a; Smith et al., 2017). Similar runoff delays are observed on valley glaciers elsewhere (Karlstrom et al., 2014; Munro, 1990), inferred to relate to the presence of a degraded, porous "weathering crust" (Müller and Keeler, 1969) on the bare ice surface of glaciers and ice sheets that stores meltwater, delaying its delivery to supraglacial channels via porous subsurface flow (Irvine-Fynn et al., 2011; Karlstrom et al., 2014; Munro, 2011). The porous weathering crust may also provide a locus for internal and/or surficial refreezing of meltwater (Hoffman et al., 2014; Paterson, 1972; Willis et al., 2002). Together, hydrologic processes in the weathering crust are similar to those of meltwater transport, storage, and refreezing in snow and firn (Cox et al., 2015; Forster et al., 2014; Harper et al., 2012; Machguth et al., 2016). The presence of weathering crust in Greenland, however, has gone largely undocumented, and little is known about its effect on hydrologic processes in the bare ice ablation zone, where >85% of ice sheet surface meltwater runoff is generated (Machguth et al., 2016).

Weathering crusts are fractured, disintegrated, or "rotten" ice layers that form during the melt season on the thermally transient surface of ablating glaciers (Fountain and Walder, 1998; Irvine-Fynn et al., 2011; Müller and Keeler, 1969). In temperate ice, liquid water exists within an interconnected network of meltwater veins (Lliboutry, 1996; Mader, 1992; Nye and Frank, 1973). When glacier ice is exposed to water, these veins coarsen to the order of tenths of a millimeter in diameter, a process referred to as "rotting" (Nye, 1991). On bare ice surfaces exposed to solar radiation, this action is intensified by the transmission and absorption of solar radiation through the upper few meters of ice (Cook et al., 2016; Fountain and Walder, 1998; Irvine-Fynn and Edwards, 2014). Subsurface radiative heating enhances melting along ice

grain edges, further coarsening vein networks and disaggregating ice crystals, creating a layer of porous ice typically <2 m thick (Figure 3-1).

Weathering crust formation reflects a balance between the vertical depth of subsurface melting and the rate of ice surface lowering. This balance evolves in response to spatio-temporal changes in the surface energy balance during the melt season (Müller and Keeler, 1969). During clear-sky conditions, solar radiative heating promotes development and deepening of the weathering crust. The depth of subsurface melting is typically limited to <2 m by the exponential attenuation of radiative heating with depth (Brandt and Warren, 1993). Conversely, during exceptionally warm, windy, or cloudy conditions when surface melt rates are enhanced relative to subsurface melting, the weathering crust may decay or be rapidly removed (Müller and Keeler, 1969). As the weathering crust develops, a shallow, depth-limited aquifer may establish in the near-surface porous ice (Figure 3-1) (Irvine-Fynn and Edwards, 2014). At vertical depths where meltwater drains through the permeable weathering crust to seeps and supraglacial channels, the near-surface ice density is reduced with no detectable change in glacier surface height (Hoffman et al., 2014; Müller and Keeler, 1969). Consequently, weathering crust ice density exhibits a characteristic non-linear increase from a very low-density (<0.5 g cm^{-3}) surface layer to a higher density (~0.90 g cm^{-3}) impermeable substrate (Figure 3-1) (Cook et al., 2016; LaChapelle, 1959). As such, mass change during periods of weathering crust development or removal cannot be resolved solely from ice surface elevation changes, but also requires knowledge of the subsurface depth-density profile (Braithwaite et al., 1998; LaChapelle, 1959; Müller and Keeler, 1969; Munro, 1990).

Weathering crust is often enhanced by cryoconite, the biologically active dark sediment that preferentially absorbs solar radiation, locally enhancing melt in quasi-cylindrical holes that deepen into the weathering crust and brighten the ice surface relative to dispersed or uniform debris-covered ice (Bøggild et al., 2010). Cryoconite holes are coupled to the weathering crust via porous subsurface water exchange (Cook et al., 2016) and surface flow that redistributes sediments, nutrients, and microbial cells between holes and the ice surface, potentially controlling their distribution and ecological structure (Edwards et al.,

2011; Hodson et al., 2007; Hotaling et al., 2017; Takeuchi et al., 2000). Weathering crust hydrology, therefore, exerts a dynamic control on the "photic zone" where solar radiation, liquid water, nutrients, and air provide habitat for a rich microbial community within the upper few meters of an ablating glacier (Figure 3-1) (Irvine-Fynn and Edwards, 2014). Physical controls on these ecohydrologic interactions, however, have only recently been explored and remain poorly understood, especially the seasonal evolution of depth-variable ice density, permeability, water storage, and microbial mobility (Cook et al., 2016; Irvine-Fynn et al., 2012; Stevens et al., 2018).

Despite the hydrological and ecological implications of weathering crust for supraglacial processes, no studies have described the physical structure or documented subsurface meltwater storage for the Greenland Ice Sheet weathering crust. When present, the weathering crust could provide a temporary storage reservoir, thus modulating meltwater delivery to supraglacial channels, crevasses, and englacial hydrologic systems (Karlstrom et al., 2014). In addition, because mass may be removed from the weathering crust without detectable change in glacier surface height, the growth and decay of the crust may confound estimates of sub-seasonal surface mass balance made from ice surface elevation change or surface energy balance models that neglect its presence (van den Broeke et al., 2008; Munro, 1990). Weathering crust structure and hydrologic storage is therefore an important but understudied component of the Greenland Ice Sheet bare ice ablation zone. The purpose of this study is to describe the physical structure and hydrologic storage of the weathering crust in a mid-elevation Greenland Ice Sheet supraglacial catchment. We provide an initial set of measurements of near-surface ice density, porosity, water saturation, and water table height, and use these data to estimate meltwater storage within the weathering crust. To illustrate the implications of our findings, we extrapolate this storage estimate across the study catchment for comparison with proglacial meltwater runoff volumes. Finally, we discuss broader implications of the findings for ablation zone hydrology and surface mass balance processes to guide future work.

2 Data and methods

The data presented in this study were collected during a 6–14 July 2016 field campaign in the middle ablation zone (67.049° N, 49.022° W, 1215 m a.s.l.), in the Kangerlussuaq sector of the Greenland Ice Sheet. We measured near-surface ice density, effective porosity, presence/absence of subsurface water saturation, cryoconite hole depth, cryoconite hole water levels, and ice surface topography. Measurements were made along an 800 m transect in a 63.1 km^2 moulin-terminating supraglacial river catchment in the bare ice ablation zone (Figure 3-2). We supplement these transect measurements with daily records of meteorological variables recorded by the nearby PROMICE/GAP KAN-M automatic weather station (AWS) (www.promice.org) (van As et al., 2017). KAN-M is located ~8.3 km ENE of our field site at ~1270 m a.s.l. and is the closest AWS to our study site (Figure 3-2).

2.1 Density and stratigraphy of near-surface ice

At 80 m intervals along the 800 m transect (Figure 3-2), shallow ice cores 0.9–1.1 m deep were collected with a 7.25 cm diameter Kovacs Mark III coring system (www.kovacsicedrillingequipment.com). Cores were collected and processed adjacent to the core sites on 11 July (#4–10; Figure 3-2) and 12 July (#1–3; Figure 3-2) between 14:00 and 21:00 local time. Core stratigraphy observations recorded in field notes include the presence of liquid water, ice lenses, and air bubbles. Natural breaks were used to separate the cores into individual segments. Each segment's length and diameter were measured to the nearest 0.1 cm with a caliper and weighed to the nearest 0.1 g on an Acculab digital scale to determine the ice density of each segment. The natural break segmentation yielded a 13 ± 6 cm mean sampling interval. Individual segments ranged from 3 to 40 cm in length.

At six sites (core #1, 2, 4, 5, 9, and 10), the upper 14–30 cm of ice lacked sufficient cohesion for intact removal with the coring system. To obtain density measurements for this material, ice samples were removed adjacent to the core sites with a Snowmetrics© (www.snowmetrics.com) 1000 cm^3 wedge-type steel snow density sampler (Figure 3-3). In typical usage, the snow density sampler is inserted horizontally into the sidewall of a snow pit to obtain undisturbed snow samples. For this study, ice samples were obtained

by inserting the 20 cm sampler vertically downward into the ice. To our knowledge, this instrument has not been used for ice density studies on weathering crust but was highly effective for our purposes. These measurements provide bulk density estimates for the upper 20 cm for the six aforementioned sites; however, the density measurements may be more representative of the uppermost ~6 cm of ice because of the shape of the sampler (see Figure 3-3). Missing data between 20–30 cm depth for cores #1, 4, 5, and 9 were gap filled with linear interpolation. Together, the shallow ice core and density sampler measurements provide depth-density profiles to depths ranging from 0.9–1.1 m. The nominal 1 m coring depth was selected based on the expectation that weathered ice would not extend below the 1 m depth of the drill barrel. For additional context, two 1.8 m cores were extracted but ice density measurements were not undertaken, these cores are described further in Section 3.3.

Density measurement uncertainty cannot be quantified with known accuracy as each ice core segment was unique in size and shape. Based on visual inspection, we consider 1.5 cm (~10%) uncertainty in ice core segment length to be conservative. This 10% measurement uncertainty primarily accounts for loss of material at the irregular ends of the ice core segments, which would tend to result in overestimated volume and underestimated ice density. Additionally, it is possible some interstitial meltwater remained in the ice cores when weighed, resulting in overestimated mass and ice density. The cores were held vertically and drained when extracted, and drainage continued prior to analysis and weighing adjacent to the core sites. Nevertheless, some interstitial meltwater likely remained. Estimates of depth-dependent glacier ice water content range from 0–9% though 15 of 18 independent estimates range from 0% to less than <3.4% (Pettersson et al., 2004). Such water retention errors would tend to cancel with overestimated volume errors, though to an unknown extent. We consider both sources of error to be poorly constrained within the ±10% limits, which we consider sufficiently conservative without giving undue confidence to either the measurements or the error estimate. This uncertainty is incorporated into calculations of density and porosity, propagating into ±14% specific water storage uncertainty (see Section 2.2 and Section 2.4).

2.2 Effective porosity of near-surface ice

The porosity of the near-surface ice was examined to determine the liquid meltwater storage capacity of the study area weathering crust. In theory, the total porosity of a solid material is the ratio of pore space volume to total volume and is calculated from the ratio of measured density to pure material density (Dingman, 2002):

$$\phi_{\mathrm{T}} = 1 - \frac{\rho_{\mathrm{M}}}{\rho_{\mathrm{T}}} \geq \phi_{\mathrm{eff}} \quad (1)$$

where ϕ_{T} (-) is total porosity, ρ_{M} (g cm^{-3}) is measured density, ρ_{T} is solid material density (0.917 g cm^{-3} for pure ice), and ϕ_{eff} (-) is effective porosity, or the porosity effectively available for water storage. Because glacier ice contains closed air bubbles that are unavailable for water storage, the ϕ_{eff} can be less, but not greater than ϕ_{T}, and cannot be calculated directly from ice density. Instead, ϕ_{eff} must be estimated by measuring the ratio of interconnected pore volume to total ice volume.

To measure ϕ_{eff} we used the 1000 cm^3 weathering crust ice samples extracted with the snow sampler described above. Twenty-four samples were collected in total, one at each core site and fourteen additional sites at random along the transect Samples were immediately weighed to determine ρ_{M}. Liquid water sourced from nearby flowing rills was then applied to the levelled ice-filled sampler until the water level was coincident with the ice surface (i.e., until the interconnected pore space was filled with water). ϕ_{eff} was computed as the ratio of the water volume required to fill the sample to the 1000 cm^3 ice sample volume. We restricted our measurements of ϕ_{eff} to ice sampled from assumed dry weathering crust, but it was not possible to control for the effect of residual liquid water content. Air bubbles and ice crystals were observed for signs of melt and none were observed.

To estimate ϕ_{eff} throughout the shallow ice core samples (where ϕ_{eff} was not measured) an "error-in-variables" (EIV) linear model (York, 1968) was computed between coincident point measurements of ϕ_{eff} and ρ_{M} obtained with the snow sampler. EIV refers to a general class of methods for fitting a straight line to experimental data when measurement errors are present in both the independent and dependent variables. The method has been widely applied in geophysical research when measurement errors are

considered important (Brutsaert and Lopez, 1998; York, 1968). The important feature is that EIV regression accounts for error in both the independent and dependent variables when determining the slope and intercept of the straight line. The model is identical in form to a standard ordinary least squares regression but contains additional error terms:

$$\hat{\phi}^{*}_{\mathrm{eff}} = \alpha + \beta \cdot (\rho^{*} + \eta) + \varepsilon \quad (2)$$

where ϕ^{*}_{eff} and ρ^{*} are the 'true' but unobserved effective porosity and ice density, $\hat{\phi}^{*}_{\mathrm{eff}}$ is the EIV estimate of effective porosity, η and ε are the measurement errors (10%), and α and β are the intercept and slope, respectively. The exact solution procedure is described in (York et al., 2004). The α and β estimates are then applied to the shallow ice core ρ_{M} to estimate ϕ_{eff} for each shallow ice core segment.

2.3 Depth to liquid water saturation

At 8 m intervals along the 800 m transect, the presence/absence of liquid water saturation within the weathering crust, the depth of cryoconite holes, and the depth to water within cryoconite holes were measured with respect to the ice sheet surface. First, the presence/absence of liquid water saturation was assessed by drilling a 1 m deep hole into the weathering crust with a 5 cm diameter Kovacs auger. The drilled holes were monitored for liquid water refilling within 30 minutes as an indication of subsurface water saturation. Second, the nearest cryoconite hole within a 1 m radius of each measurement interval was identified and the total depth of each hole and the depth to water in each hole below the surface were measured. The height of water in each hole is calculated as the difference between the depth of the hole and the depth to water. The depth to water in the holes is used as an estimate of the depth to liquid water saturation (i.e. the water table height). Absence of cryoconite holes was noted if none were present within a 1 m radius of the 8 m measurement interval.

As an additional qualitative check on the weathering crust structure, a Snowmetrics© steel pointed depth probe was forced downward adjacent to each 1 m drilled hole until impenetrable ice was encountered. The expectation was that these measurements would approximate the depth to the shoulder of the subsurface density profile, roughly corresponding to the depth of rotten unsaturated ice as per Figure (1) in (Müller

and Keeler, 1969). Initial field observations confirmed the upper few tens of centimeters of ice was composed of weakly-bonded, coarse-grained ice that was easily removed with a flat bladed shovel and penetrated with the depth probe. The depth probe measurements are used as a qualitative description of the weathering crust structure in Section 3.3.

2.4 Estimating water storage in the weathering crust

The total volumetric water storage S in the weathering crust is defined as:

$$S = S_{\mathrm{P}} + S_{\mathrm{CH}} + S_{\mathrm{cap}} \tag{3}$$

where S_{P} is free-draining liquid water storage within the weathering crust ice matrix, S_{CH} is liquid water storage in cryoconite holes, and S_{cap} is irreducible liquid water held under capillary tension within the weathering crust. The focus of this work is S_{P}, which we estimate with the following relationship:

$$S_{\mathrm{P}} = \phi_{\mathrm{eff}} \cdot D_{\mathrm{P}} \tag{4}$$

where ϕ_{eff} is the effective porosity of the saturated porous ice within the weathering crust and D_{P} is the thickness of saturated porous ice. Equation (4) is applied to each segment of porous ice in the extracted ice cores, where ϕ_{eff} is calculated from the segment's ρ_{M} (Equation 2), and D_{P} is the measured thickness of each segment. We exclude the thickness of unsaturated ice in each core, as estimated by the average depth to water in cryoconite holes measured adjacent to the core sites, which we show is relatively constant along the transect (Section 3.3). The ±10% measurement uncertainty for D_{P} and ϕ_{eff} (η and ε, Equation 2) propagate into ±14% uncertainty for S_P:

$$\Delta S_{\mathrm{P}} = \sqrt{\eta^2 + \varepsilon^2} = 14\% \tag{5}$$

The segment S_{P} ($\pm\Delta S_{\mathrm{P}}$) values are then summed across each core and reported as lower and upper values for specific storage (cm).

Finally, for illustrative purposes we scale our S_{P} estimate to the study catchment by multiplying the lower and upper values for S_{P} estimated from the shallow ice cores by the bare ice surface area of the study catchment (63.1 km^2). In terms of total water storage, this calculation is conservative since it assumes

there is no water storage below the ~1 m depth measured with our field equipment and excludes storage within cryoconite holes and unsaturated storage. However, it also assumes the ice density, porosity, and saturation conditions measured along the transect are representative of conditions across the entire catchment. Recognizing this uncertainty, we caution that it is meant for illustrative purposes.

3 Results

3.1 Density and stratigraphy of near-surface ice

Throughout the study area, the ice sheet surface was characterized by a layer of coarse-grained, weakly-bonded ice, a few tens of centimeters thick (Figure 3-3). Bulk ρ_{M} of this material measured to 20 cm depth with the snow sampler is 0.45 ± 0.05 g cm^{-3}, and ranges from 0.33–0.56 g cm^{-3}. This is much lower than typical glacier ice densities of 0.83–0.90 g cm^{-3} (Cuffey and Paterson, 2010), but is consistent with previous findings of ice densities <0.50 g cm^{-3} in the upper few tens of centimeters of weathering crust (Müller and Keeler, 1969; Schuster, 2001). Suggestive of its weak bonding, this material was easily removed with a flat bladed shovel, penetrated with the depth probe, and often deformed or collapsed slightly underfoot. Free draining liquid water was not observed in the extracted ice samples and there was no subsurface water table observed within this upper weathering crust layer, for example when penetrated with the depth probe or when the material was removed with the shovel.

Subsurface ρ_{M} averaged across the ~1 m depth from the shallow ice cores is 0.69 ± 0.10 g cm^{-3}, and ranges from 0.43–0.91 g cm^{-3}. In most cores, ρ_{M} steadily increased with depth but remained less than solid ice density across the entire depth profile, suggesting substantial subsurface ablation across the ~1 m depth sampled by the cores (Figure 3-4). Sampling resolution limited our ability to resolve the depth-density profile in the upper few tens of centimeters, but the observed profiles are generally consistent with the expected non-linear increase in weathering crust ice density from the upper few tens of centimeters to unweathered glacier ice across the upper 1–2 m (Figure 3-1). However, densities less than <0.50 g cm^{-3} were found at depths of 50 cm, 40 cm, and 92 cm at core sites 2, 5, and 8, respectively, and density

variability was twice as large across the depth of the shallow ice cores than the upper 20 cm (0.10 g cm^{-3} and 0.05 g cm^{-3}, respectively).

The source of this density variability likely corresponds to core stratigraphy. While coring, alternating weak and resistant layers were qualitatively observed based on the resistance to downward motion. This structure was confirmed by the presence of alternating layers of coarse-grained (>1 cm), weathered ice and clear, solid ice lenses in all cores. The ice lenses were readily identified in the core stratigraphy and removed intact from the granular, friable ice between lenses (Figure 3-5). The ice lenses contained visible closed air bubbles trapped in clear solid ice. Subtle evidence of internal melting along coarse grain edges was visible in some ice lenses, but most were solid with minimal or no apparent evidence of weathering. Densities of these lenses were not measured in the field but based on their solid structure are estimated to be in the range of typical glacier ice densities (e.g. 0.83–0.90 g cm^{-3}) (Cuffey and Paterson, 2010).

Previous analyses of weathering crusts have not reported ice structure, therefore the pattern we find of alternating coarse-grained, weathered ice and clear, solid ice cannot be compared to previous studies (Hoffman et al., 2014; Müller and Keeler, 1969; Schuster, 2001). Though refrozen meltwater lenses are found in firn at elevations above the study area (Cox et al., 2015; Machguth et al., 2016), refrozen meltwater lenses are unlikely in a bare ice, ablating weathering crust (Schuster, 2001). Rather, the observed stratigraphy likely reflects differential weathering of the underlying structural ice fabric (Hudleston, 2015). Surface expression of differential weathering is visible as contrasting dark and light areas along the transect (Figure 3-2), similar to kilometer-scale foliated bands associated with outcropping of stratified impurities in the study region (Wientjes et al., 2012). At the scale of the shallow ice cores, stratified distributions of crystal size and shape, bubble elongation and distribution, and impurity content with depth could each influence rates of subsurface radiative heating (Brandt and Warren, 1993; Liston et al., 1999a) and hence could promote differential weathering of centimeter-scale foliated ice layers at depth (Hudleston, 2015). Meltwater advection along micro-seams and cracks, or along foliated planes with enhanced permeability

(Wakahama et al., 1973) could provide an additional differential heat source at depth, either via enhanced rotting of temperate ice (Nye, 1991) or, if transported to cold ice, via meltwater refreezing. The ice lenses, then, may represent structural resistance to weathering, and/or result from heterogeneity in subsurface flow paths that promote differential weathering of subsurface ice. We would thus expect lenses to be localized features, which helps explain the lack of consistent stratigraphy among cores. Mechanism aside, the ρ_{M} values reported in Figure 3-4 were calculated from the mass of each ice core segment measured prior to removing the ice lenses, and therefore represent the bulk density of each segment (i.e. weathered ice + lens ice). These features are discussed further in Section 4.

3.2 Measured and estimated effective porosity

Effective porosity ϕ_{eff} measured with the snow sampler is 0.44 ± 0.05 and ranges from 0.33–0.56. Measured values were generally smaller than the theoretical upper bound total porosity (ϕ_{T}) calculated from ρ_{M} (Figure 3-6), likely owing to observed closed air bubbles in the porous ice grains that decrease the density without increasing the porosity. This result suggests our measurement technique was accurate, as data points above the dashed line would be physically implausible. A significant linear relationship was found ($\phi_{\mathrm{eff}} = -0.97\rho_{\mathrm{M}} + 0.89$; r2 = 0.53, RMSE = 0.03), and was used to predict ϕ_{eff} from the shallow ice core ρ_{M} (Figure 3-4, top axis). Predicted ϕ_{eff} averaged across all core segments is 0.22 ± 0.11 and ranges from 0.002–0.47. Though lower on average (and more variable) than the range of ϕ_{eff} measured with the snow sampler in the upper 20 cm of crust, this range suggests substantial porosity across the ~1 m depth sampled with the shallow ice corer. However, the narrow range of ρ_{M}, and structural differences in the ice sampled with the corer, are sources of uncertainty when extrapolating outside of the measurement range (i.e. $\phi_{\mathrm{eff}} < 0.35$ and $\phi_{\mathrm{eff}} > 0.55$ have greater uncertainty).

3.3 Evidence of saturation from drilled holes and cryoconite holes

The ice surface topography along the study transect was highly variable across short spatial scales (<10 m) (Figure 3-7). Qualitatively, the surface was characterized by hummocks and hollows separated by shallow

rills (often flowing) and pitted cryoconite deposits. Water-filled cryoconite holes were ubiquitous across the study area surface, though variability in cryoconite hole water levels and spatial coverage was observed. For example, at 14 of the 100 measurement locations no cryoconite holes were present within the nominal 1 m observation radius and at 9 locations all cryoconite holes within the 1 m radius were dry at the time of observation. At the remaining 77 locations cryoconite holes contained measurable water levels. Cryoconite holes were 25.2 ± 11.4 cm deep and water levels were 15.5 ± 7.8 cm below the ice sheet surface, equivalent to water heights of 9.7 ± 7.8 cm above hole bottoms (Figure 3-7b). The height of water in these holes likely varied diurnally and could have steadily drained or filled during the study period (Cook et al., 2016), thus the 15.5 cm average depth to water likely represents a snapshot of the transient water table surface. As such, the presence/absence of water in cryoconite holes may have also varied during the study period. With respect to distance along the transect, there was a trend toward shallower holes (-0.012 cm m-1, $p<0.005$) but no trend in depth to water below the ice sheet surface. Rather, cryoconite hole water levels generally mirrored the 8 m scale topographic variability (Figure 3-7b). We measured the water level in a single hole at each 8 m interval and thus cannot quantify sub-8 m scale water table height variability, but these measurements suggest the subsurface water table drains to seeps and supraglacial channels at <8 m spatial scale.

In 83 of 100 drilled 1 m holes, water from surrounding ice refilled the hole within the nominal 30-minute post-drilling observation period. Refilling rates were not systematically measured but were observed to vary from nearly instantaneous refilling before the auger was removed, to relatively slow (and incomplete) refilling over the 30-minute observation period, suggesting substantial variability over short spatial scales. In addition to this rapid refilling and the widespread presence of water-filled cryoconite holes, all but one of the ten shallow ice core boreholes were observed filling with water during the post-drilling period, though the equilibrium height of water in these holes was not measured. Collectively, these measurements suggest the ice was saturated across the entire 800 m transect to a depth of at least 1 m, albeit with substantial spatial variability in refilling rates.

Based on these observations, we characterize the near-surface ice as composed of two continuous layers with varying thicknesses. The upper layer consisted of low-density (0.33–0.56 g cm^{-3}), unsaturated weathering crust ice with relatively uniform crystal structure and no marked stratigraphy. This ice was readily probed, easily removed with a shovel, and often deformed or collapsed under foot. This layer was penetrated to 11.3 ± 5.8 cm (maximum 49 cm) with the depth probe. Beneath this layer was a higher density (0.43–0.91 g cm^{-3}), saturated ice layer that we could not excavate with the shovel nor penetrate with the depth probe. The transition between layers was marked by a distinct increase in material strength across a short (~4 cm) distance below which the shovel and depth probe could not penetrate. Though inferred from the shovel and depth probe, this transition likely marks the non-linear increase in density on the shoulder of the theoretical depth-density curve (Figure 3-1). The transition roughly coincides with the 15.5 cm average depth to water measured in cryoconite holes, suggesting a possible link between ice density and water table height.

The vertical structure of the higher density, saturated ice was highly variable, consisting of alternating layers of coarse-grained, porous ice and clear, solid ice lenses. The thickness of the saturated ice layer could not be definitively determined with the drilling equipment. However, at two locations shallow ice cores 1.8 m deep were extracted. The densities of these cores were not measured, but at both sites the ice cores consisted of coarse-grained, porous ice alternating with clear, solid ice lenses across their entire depth. There were no qualitative differences between the ice in these cores and the ice presented in Figure 3-4 and Figure 3-5. At one of these two sites, weathered ice persisted to 1.8 m depth. At the other site, a 20 cm thick segment of solid ice was found between 1.6 and 1.8 m, possibly marking the transition to cold, solid, impermeable ice at this location.

3.4 Meltwater storage in the near-surface ice and the seasonal context

Averaged across the 94 cm mean depth of the 10 shallow ice cores, S_P is 14–18 cm (Table 3-1). The average ρ_M and ϕ_{eff} are 0.69 g cm^{-3} and 0.22, respectively. As each ice core was unique in terms of sampling interval, the ρ_M and ϕ_{eff} are depth-weighted mean values whereas S_P is summed across each core. S_P is

lower in cores 1–3 owing to higher subsurface ρ_{M} and hence lower ϕ_{eff} below ~50–60 cm depth, whereas S_{P} in cores 4–10 consistently ranges between 14 and 21 cm, owing to lower ρ_{M} across their entire depth. While these estimates suggest substantial S_{P} at the time of observation, they should be considered minimum bounds (within ±14% uncertainty) as they do not include the potential for additional liquid meltwater storage below the measured ice core depths. The methods used in this study did not yield a definitive bound on the thickness of the saturated ice layer, nor the variation in porosity with depth below the range of the shallow boreholes, and thus deeper water storage cannot be ruled out.

Given the transient nature of the weathering crust, it is important to place these findings in a seasonal context. Antecedent meteorology such as the timing of snowmelt, rainfall, and prevalence of shortwave radiation, would each influence weathering crust growth and decay. Albedo data recorded at the KAN-M automatic weather station (AWS) indicate the spring snow cover melted out on ~8 June, followed by two ephemeral snowfall events on ~16 June and ~25 June (Figure 3-8, vertical grey bars). These dates correspond closely to the ~21 June snow disappearance date reported for the Kangerlussuaq region in Tedstone et al. (2017), based on data from the Modèle Atmosphérique Régional (MAR) regional climate model (Fettweis et al., 2017). AWS data indicate the ice surface was actively melting prior to 12 July in response to positive air temperatures (>0°C) and positive net shortwave radiation (Figure 3-8). Ice surface ablation rates averaged 1.85 cm d^{-1} during this period but were relatively low compared to the peak daily ablation rates (>5 cm d^{-1}) recorded between 15 July and 01 August, suggesting conditions were favorable for weathering crust development. AWS data indicate ~74 cm of cumulative ice surface ablation occurred prior to collection of the shallow ice cores on 11–12 July, equivalent to 66.6 cm water equivalent assuming solid ice density of ~0.90 g cm^{-3}. The inferred 14–18 cm S_P is therefore equivalent to ~21–27% of the cumulative seasonal ice surface ablation recorded prior to 12 July, or ~11–14% of the ~1.25 m average annual surface ablation at KAN-M (van As et al., 2017).

Further, MAR data suggests conditions during summer 2016 favored weathering crust growth in the study region. These include below average cloud cover and rainfall, and above average downward

shortwave radiation (e.g. compare to 2000–2016 period, Figure 1–4 in Tedstone et al., 2017). These meteorological conditions suggest that the presence of a well-developed weathering crust in the study area at the time of observation is not surprising, though inferring a likely thickness is not possible without a physical model for weathering crust development. The AWS data presented in Figure 3-8 provide context for our study, but a detailed investigation of weathering crust formation is well beyond our scope here. Nevertheless, the >1.6 m thickness of weathered ice we find is perhaps surprising given the ephemeral snow cover and ~26 June snow disappearance date suggested by the AWS albedo data. These data suggest the conditions we document developed over a relatively short period of exposure to solar radiation, or persisted during the previous winter, further suggesting structural controls unrelated to penetration of shortwave radiation may underlie the observed weathering crust structure.

4 Discussion

We have presented measurements of near-surface ice density which, to our knowledge, provides the first characterization of the structure and hydrologic storage of a bare ice weathering crust in the Greenland Ice Sheet ablation zone. These data suggest 14–18 cm of liquid meltwater was stored within porous, low-density ice at the time of observation, and that substantial subsurface melting may occur in the Greenland Ice Sheet bare ice ablation zone. Together, these findings suggest hydrologic processes in the bare ice ablation zone are affected by porous ice, and that surface lowering measurements may not accurately quantify total mass loss during periods of weathering crust growth and decay in the Greenland Ice Sheet ablation zone.

4.1 Weathering crust structure and hydrologic storage

Water storage in the weathering crust has been reported (Irvine-Fynn et al., 2011; Larson, 1978) but is generally not considered a significant component of water storage in supraglacial environments, owing to its transient nature (Fountain and Walder, 1998; Jansson et al., 2003; Müller and Keeler, 1969). While more work is required to determine the spatial extent and seasonal evolution of the conditions found in this

investigation, our documentation of a saturated weathering crust storing up to 18 cm of liquid meltwater supports the possibility of a substantial transient reservoir in Greenland's bare ice ablation zone, consistent with observations of weathering crust for supraglacial environments worldwide (Irvine-Fynn, 2008; Larson, 1978; Munro, 1990). Though a snapshot characterization, the weathering crust structure presented in Figure 3-7 is consistent with conceptual models of the near-surface weathering crust-cryoconite hole hydrologic system (e.g. Figure 3-1) (Irvine-Fynn and Edwards, 2014; Müller and Keeler, 1969) and confirms this system is present in the Greenland Ice Sheet ablation zone. The ubiquity of water-filled cryoconite holes, the rapid refilling of drilled holes with liquid water, and the excavation of saturated ice cores to depths >1.6 m suggests the study area weathering crust acts as a depth-limited aquifer (Irvine-Fynn et al., 2011), storing meltwater in the seasonally-temperate near-surface ice and likely delaying the delivery of meltwater to supraglacial streams and rivers via saturated subsurface flow (Irvine-Fynn et al., 2011; Karlstrom et al., 2014; Munro, 2011).

In addition to meltwater storage, we describe the structure of the weathering crust. We find a pattern of porous, granular ice alternating with solid ice lenses in the upper 1-2 m of weathering crust in the study area, rather than a homogeneous rotten near-surface ice layer (Müller and Keeler, 1969). Given the rapidly ablating ice surface prior to the study, we posit the solid ice lenses are emergent structural features, as refrozen meltwater is unlikely in an ablating weathering crust (Schuster, 2001). Though beyond the scope of the data collected in this study, we hypothesize two mechanisms to explain the observed stratigraphy. First, stratified distributions of crystal size and shape, bubble elongation and distribution, and impurity content with depth could influence rates of subsurface radiative heating (Brandt and Warren, 1993; Liston et al., 1999a). The ice lenses may then represent optically transparent ice layers with larger crystal size, lower air bubble content, or lower impurity content. The optical properties of these layers may reduce absorption of shortwave radiation, substantially reducing internal melting relative to optically opaque layers. Second, meltwater advection along micro seams, cracks, or foliated ice layers with enhanced permeability may promote differential melting via sensible and frictional heat transfer (Hambrey, 1977;

Hambrey and Lawson, 2000; Wakahama et al., 1973). Therefore, underlying structural features such as foliation, cracks, and fractures caused by thermal expansion (Sanderson, 1978) may be accentuated by differential radiative heating, enhanced "rotting" by meltwater along preferential flow paths, or heating due to meltwater refreezing. Together, these suggest weathering crust formation in the study area may be more complicated than previous descriptions of a process driven solely by solar radiative heating (Hoffman et al., 2014; Müller and Keeler, 1969), and suggest meltwater dynamics and ice structure may be important controls on weathering crust development.

Though we interpret the lenses as structural features, there is evidence that internal refreezing of meltwater occurs in weathering crust on the Dry Valley glaciers in Antarctica (Hoffman et al., 2014). Although the climatic context is different, this raises the possibility of meltwater refreezing within the weathering crust ice matrix in Greenland. If so, refreezing would represent a heat source within near-surface ice, and a possible sink for meltwater retention (Pfeffer et al., 1991). Though detailed energy balance studies suggest internal refreezing is negligible in near-surface porous ice on alpine glaciers in the Canadian Rockies (Paterson, 1972; Schuster, 2001), such analyses have not been performed for the Greenland Ice Sheet ablation zone. Regardless of internal refreezing at depth, we frequently observed night-time refreezing of meltwater at the surface of cryoconite holes and water tracks in the study area (Figure 3-9), though the magnitude of this refreezing was not studied. In addition to careful observation of subsurface ice structure, future work should determine if internally refrozen meltwater occurs within weathering crust in the Greenland Ice Sheet ablation zone, especially during seasonal transitions from temperate to cold near-surface ice.

4.2 Estimating meltwater storage of the study catchment weathering crust

While extrapolating these local scale findings to broader areas of the Greenland Ice Sheet is not justified presently, it is illustrative to consider the potential meltwater storage volume of the weathering crust in our study catchment. For example, if we assume our shallow ice core data are broadly representative of conditions across its 63 km^2 area, multiplying the lower and upper estimate of S_P (Table 3-1) by the bare

ice surface area of the study catchment yields 0.009–0.012 km3 of meltwater storage. To put these numbers in perspective, one hour of peak discharge measured at the Watson River in Kangerlussuaq during the July 2012 record melt event (Nghiem et al., 2012) was equivalent to 0.0115 km3 (van As et al., 2017). Our study catchment is equivalent to ~2% of the ~2800 km^2 ablation zone contributing area draining to the Watson River (Lindbäck et al., 2015). Thus, while our 800 m shallow ice core survey may not be representative of ice density or porosity more widely over the Greenland Ice Sheet ablation zone, even relatively small areas of weathering crust have the potential to buffer large volumes of supraglacial meltwater, potentially delaying its delivery to en-, sub- and proglacial systems. Future work should seek to identify the underlying meteorological controls on weathering crust development in the Greenland Ice Sheet ablation zone to determine the likely spatial extent of the conditions we document.

4.3 Implications of weathering crust for surface mass balance processes

Our findings of low-density, saturated weathering crust in the Greenland Ice Sheet ablation zone have at least three implications for Greenland Ice Sheet surface mass balance (SMB). First, subsurface meltwater generation within the weathering crust does not materially lower the ice surface (Braithwaite et al., 1998; Müller and Keeler, 1969; Munro, 2011). Lateral drainage of internal meltwater through the permeable weathering crust to supraglacial channels reduces weathering crust density, by removing mass with no detectable change in surface height. As a result, mass change during periods of weathering crust development may be underpredicted, or, during periods of weathering crust removal, overpredicted, if determined solely from ice surface elevation changes (Braithwaite et al., 1998; LaChapelle, 1959; Müller and Keeler, 1969). In the Kangerlussuaq region of the southwest Greenland Ice Sheet ablation zone, penetration of shortwave radiation into near-surface ice is estimated to generate 20–30% of total summertime melt, suggesting ice surface elevation change measurements may not be reliable for short-term model validation in this region unless subsurface melt is accounted for (van den Broeke et al., 2008; Munro, 1990).

Second, the timing, magnitude, and location of meltwater delivery to the englacial system is powerfully altered by surface hydrologic processes operating on the Greenland Ice Sheet bare ice surface (Smith et al., 2017). In addition to catchment size and shape, transient water storage in the weathering crust has been inferred to attenuate the timing of meltwater delivery to englacial and proglacial hydrologic systems (Karlstrom et al., 2014; Munro, 2011). Typical flow velocities of 0.4–2.6 m s^{-1} in supraglacial meltwater channels on the Greenland Ice Sheet surface are 3–5 orders of magnitude greater than hydraulic conductivity estimates for permeable ice (Cook et al., 2016; Gleason et al., 2016; Karlstrom et al., 2014; Wakahama et al., 1973). Thus, porous subsurface meltwater flow may modulate delivery of surface meltwater to supraglacial channels, which in turn deliver meltwater to englacial and subglacial systems. Yet, the Greenland Ice Sheet weathering crust hydraulic conductivity has only recently been investigated (Stevens et al., 2018) and its effect on meltwater delivery to the en-, sub-, and proglacial hydrologic system is poorly understood (Munro, 1990, 2011; Smith et al., 2017).

Finally, the weathering crust provides a substrate for retention of impurities, cryoconite, and microbial communities that influence the Greenland Ice Sheet ablation zone surface albedo (Bøggild et al., 2010; Lutz et al., 2014; Ryan et al., 2017a; Yallop et al., 2012). Cryoconite deposits locally enhance melt, forming quasi-cylindrical melt holes that deepen into the weathering crust (Gribbon, 1979), likely reducing their direct effect on mesoscale ice albedo patterns in southwest Greenland (Ryan et al., 2016; Tedstone et al., 2017). Conversely, interstitial water within the weathering crust, such as that documented in this study, provides abundant habitat for microalgae and cyanobacteria (Irvine-Fynn and Edwards, 2014), which reduce ice surface albedo (Yallop et al., 2012). Subsurface water exchange may further redistribute soluble impurities and microbes between the permeable weathering crust and cryoconite holes (Cook et al., 2016), while channel invasion of cryoconite holes during periods of weathering crust removal may disperse cryoconite sediments and microbes across the ice surface (Hodson et al., 2007; Takeuchi et al., 2000). Thus, while it has not been confirmed, weathering crust hydrology, in addition to its growth and removal, could

modulate the distribution of impurities and microbial communities on the Greenland Ice Sheet ablation zone surface, and hence could influence surface albedo patterns.

Underpinning each of these implications of weathering crust, however, is the transient nature of its growth and decay. Our study provides a snapshot characterization of what appears to be a deeply developed weathering crust, approximately midway through a summer characterized by below average cloud cover, albedo, rainfall, and spring snow depth, earlier than average snow disappearance, and above average downward shortwave radiation (e.g. compare to Figures 1–4 in Tedstone et al., 2017). These conditions suggest abundant time for weathering crust development, and lack of conditions conducive to its removal or decay. Interannual variability in these conditions is substantial, and the conditions we document may not be representative of normal conditions. The net seasonal effect of weathering crust processes on Greenland Ice Sheet ablation zone hydrology and mass balance remains poorly understood and should form the basis for future work.

5 Conclusion

This study suggests presence of a water-saturated weathering crust at least 1 m thick on the bare ice surface of the Greenland Ice Sheet ablation zone. The observed characteristics of this weathering crust are similar to those described for supraglacial environments worldwide (Cook et al., 2016; Hoffman et al., 2014; Irvine-Fynn and Edwards, 2014; Karlstrom et al., 2014; Larson, 1978; Müller and Keeler, 1969; Munro, 2011). Namely, the weathering crust acts as a depth-limited aquifer (Irvine-Fynn et al., 2011), storing liquid meltwater and likely slowing its transport to supraglacial streams via porous subsurface flow (Cook et al., 2016; Karlstrom et al., 2014). Our empirical relationship ($\phi_{\mathrm{eff}} = -0.97\rho_{\mathrm{M}} + 0.89$) between measured ice density and measured ice porosity at the study field site suggests 14–18 cm of meltwater storage within weathering crust at our study site. If these findings are representative of broader areas of the Greenland Ice Sheet ablation zone, they suggest the potential for substantial sub-seasonal meltwater storage within porous low-density ice on the Greenland Ice Sheet ablation zone bare ice surface. Future work should examine how spatio-temporal changes in the surface energy balance and underlying ice structure control weathering

crust development, and quantify potential errors in sub-seasonal mass balance and surface elevation change estimates derived from surface energy balance models and altimetry, as most currently neglect removal of mass due to subsurface melting in the bare ice ablation zone.

6 Tables

Table 3-1. Shallow ice core depth, mean core density, mean core porosity, and specific water storage depth (S_P), for each shallow ice core.

Core	Ice Core Depth	Mean Core Density	Mean Core Porosity	S_P
	(cm)	(g cm^{-3})	(-)	(cm)
1	100	0.72	0.19	12 – 16
2	100	0.72	0.19	11 – 15
3	100	0.76	0.15	10 – 13
4	90	0.63	0.28	15 – 21
5	89	0.63	0.27	16 – 21
6	97	0.74	0.17	15 – 20
7	90	0.65	0.26	15 – 20
8	102	0.72	0.19	15 – 20
9	90	0.64	0.26	16 – 21
10	82	0.64	0.27	14 – 18
Average:	**94**	**0.69**	**0.22**	**14 – 18**

7 Figures

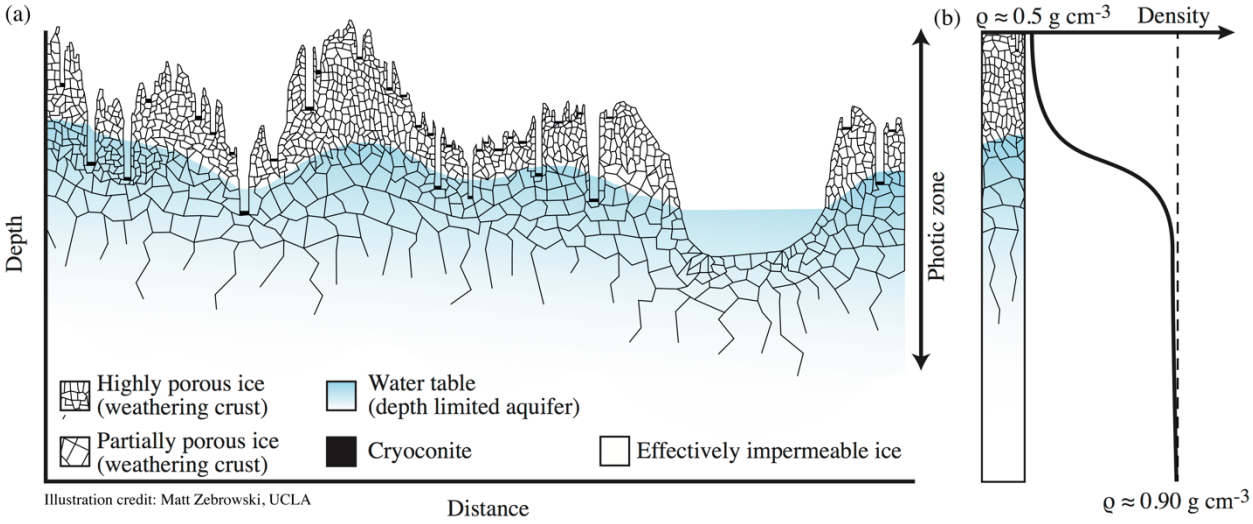

Figure 3-1. (a) Conceptual diagram of weathering crust structure, highlighting the porous ice layers, cryoconite holes, and saturated water table adapted from Irvine-Fynn and Edwards (2014) and Müller and Keeler (1969). (b) Theoretical subsurface depth-density profile showing the non-linear increase in ice density from the highly porous, low density near-surface ice to higher-density, unweathered glacier ice adapted from LaChapelle (1959). Illustration credit: Matt Zebrowski, UCLA.

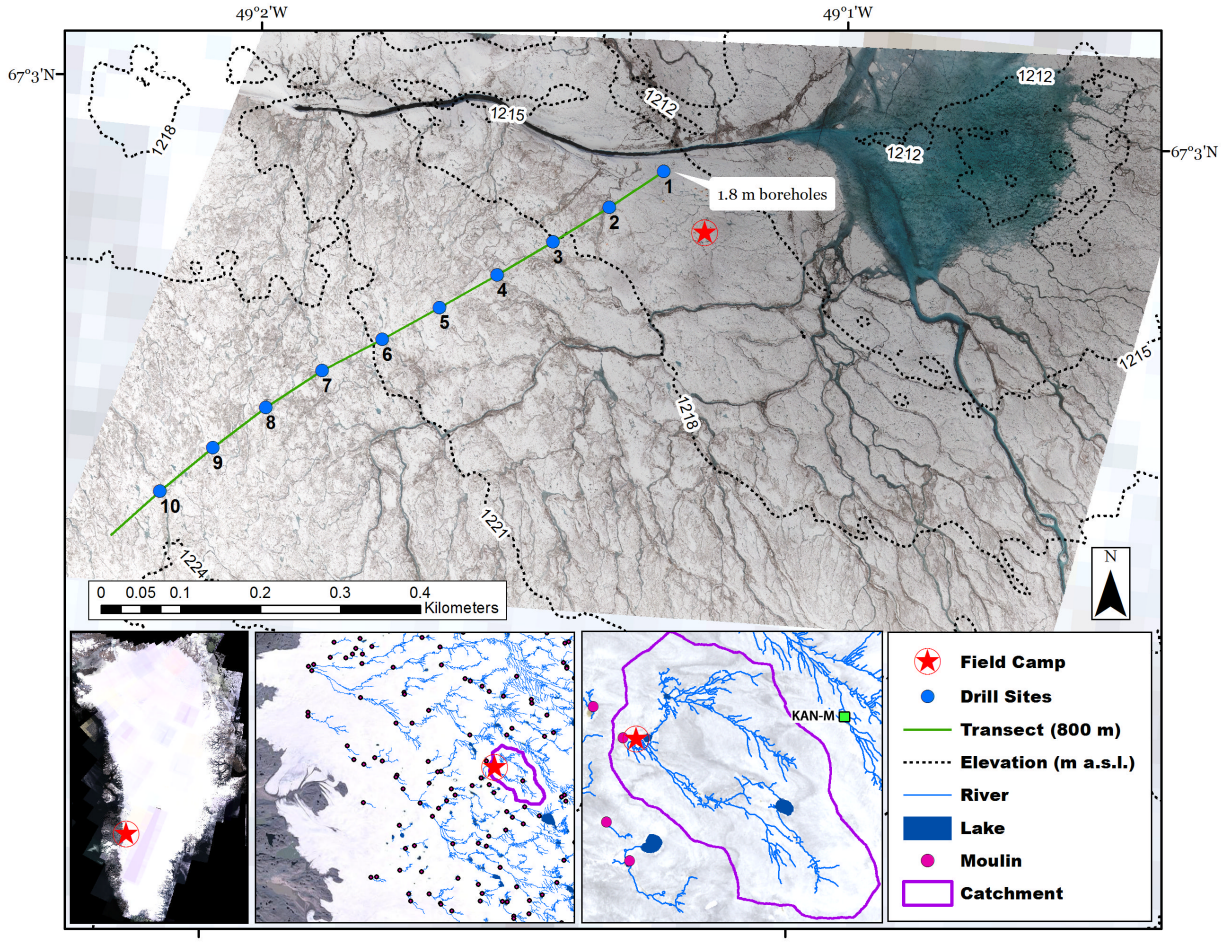

Figure 3-2. Ortho-rectified image mosaic of the study area at 6 cm ground resolution from RGB camera imagery collected 10 July 2016 on board a quad-copter drone. Background 30 m Landsat image collected same day. Shallow ice cores extracted at 80 m intervals (blue circles) along the 800 m transect provide ice density measurements to depths of 1.1 m, with two additional shallow ice cores extracted to 1.8 m depth at interval 1. Insets (below) show the 63.1 km^2 supraglacial catchment extent (magenta outline), as delineated from WorldView satellite stereo-photogrammetric digital elevation model topography, and supraglacial river and moulin locations derived from Landsat 8 imagery (Yang and Smith, 2016).

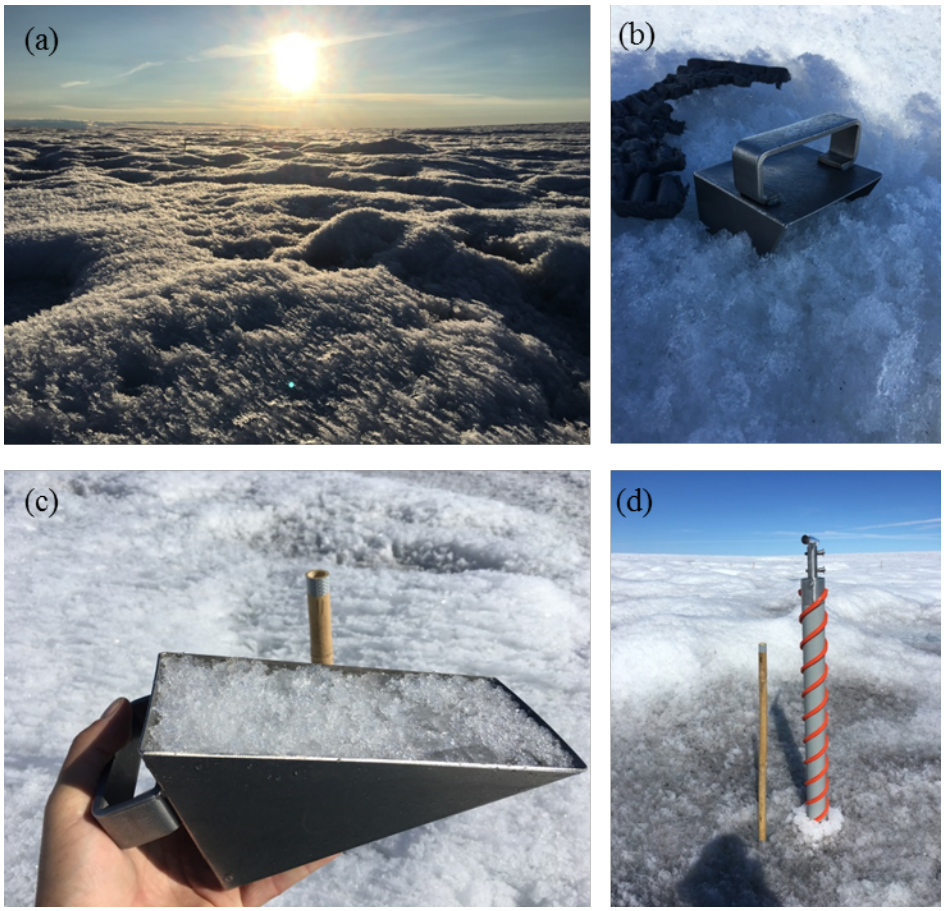

Figure 3-3. (a) A surface weathering crust was pervasive throughout the study area, characterized by small scale topographic variability and cryoconite holes. (b-c) A 1000 cm^3 steel snow density sampler was vertically inserted into the upper 20 cm weathered ice. (d) A shallow ice corer was used to obtain ice samples to depths of 1.8 m.

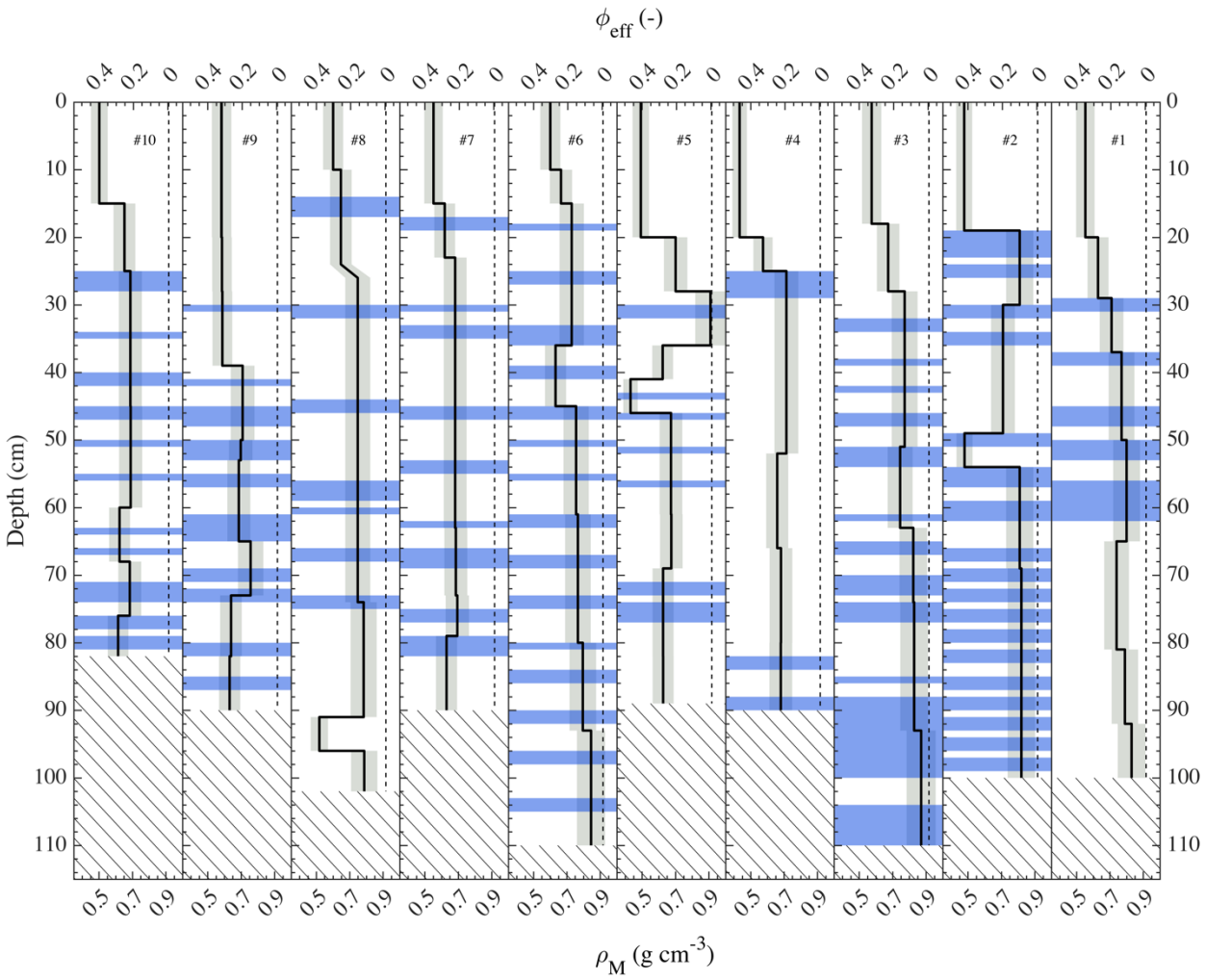

Figure 3-4. Subsurface measured ice density (ρ_M) and corresponding calculated effective porosity (ϕ_{eff}), and stratigraphy profiles from 10 shallow ice cores (#10-1, left to right) extracted at 80 m intervals along the study transect (see Figure 2-2 for ice core locations). Horizontal blue shading represents solid ice layers. Vertical dashed line at solid ice density 0.917 g cm^{-3}. Assumed ±10% measurement uncertainty represented by shaded grey bars. Hatched areas are no data.

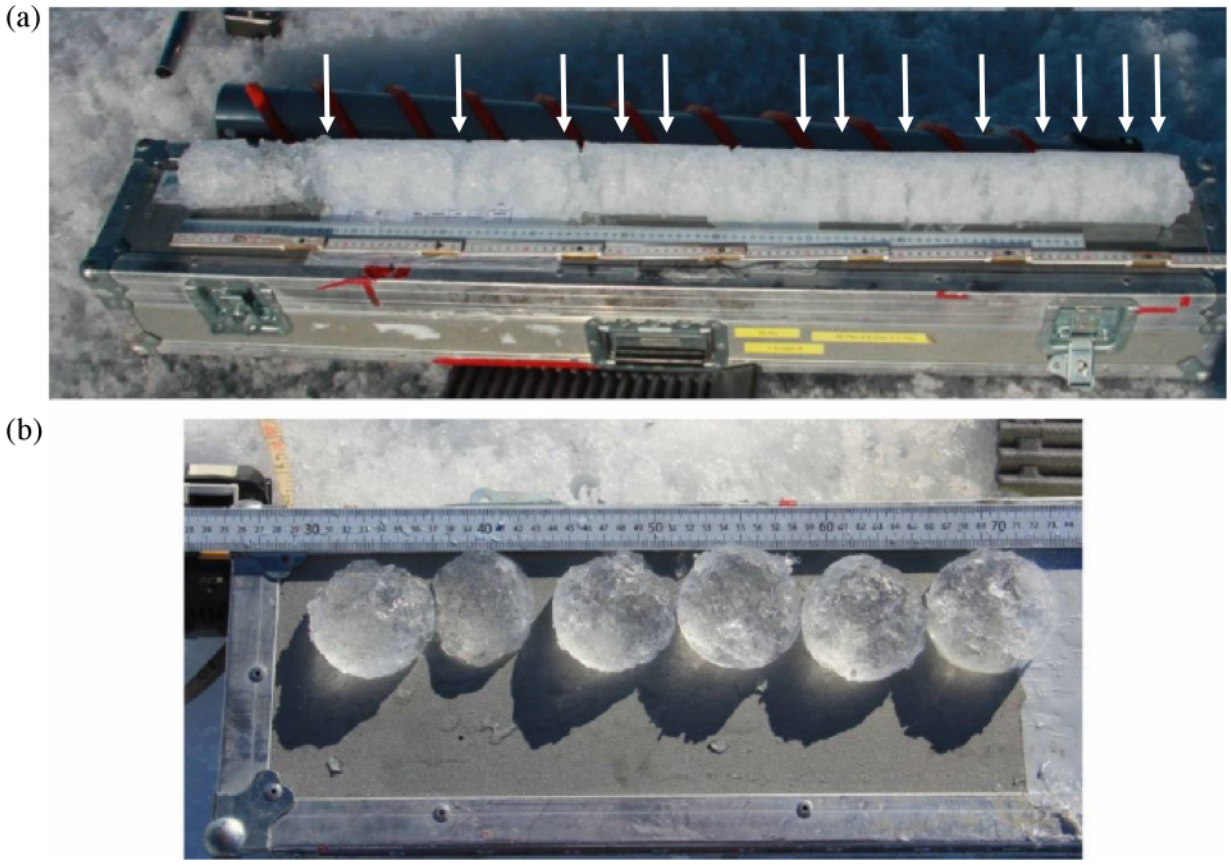

Figure 3-5. (a) Typical near-surface shallow ice core (core #6) prior to in situ analysis of density and stratigraphy. Clear, solid ice lenses alternate with granular, fractured ice. Approximate locations of ice lenses noted with white arrows (not all lenses are clearly visible). (b) Ice lenses removed and confirmed after completed core analysis (core #1).

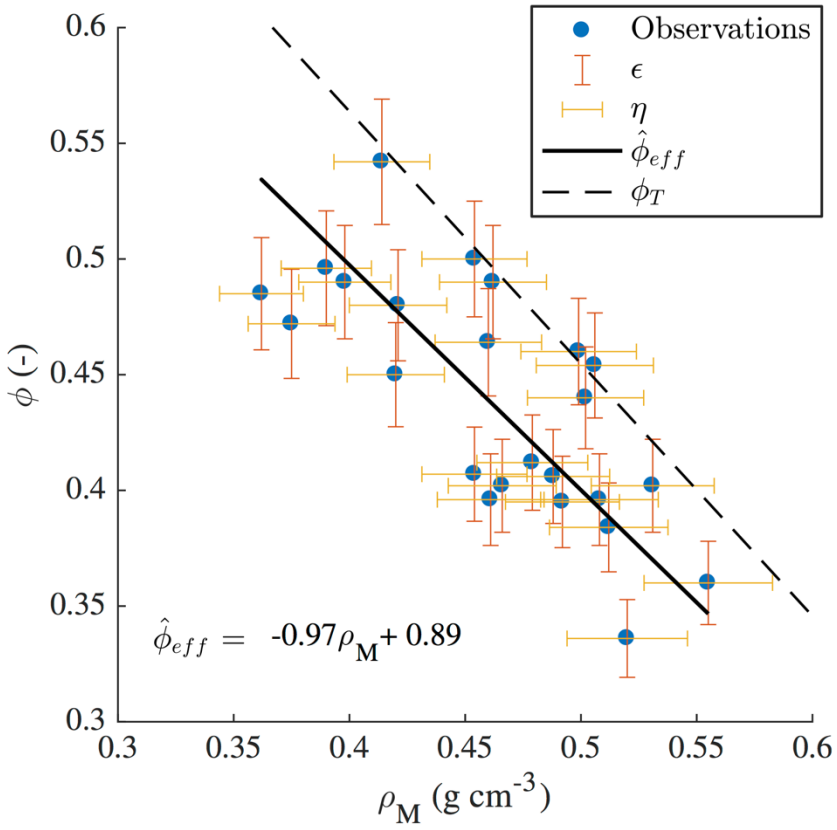

Figure 3-6. Linear relationship ($\hat{\phi}_{eff}$, solid line) between measured ice density (ρ_M) and effective porosity (ϕ_{eff}) and assumed ±10% measurement error (whiskers). Dashed line is theoretical upper limit where effective porosity equals total porosity (i.e. $\phi_T = \rho_M/\rho_T$).

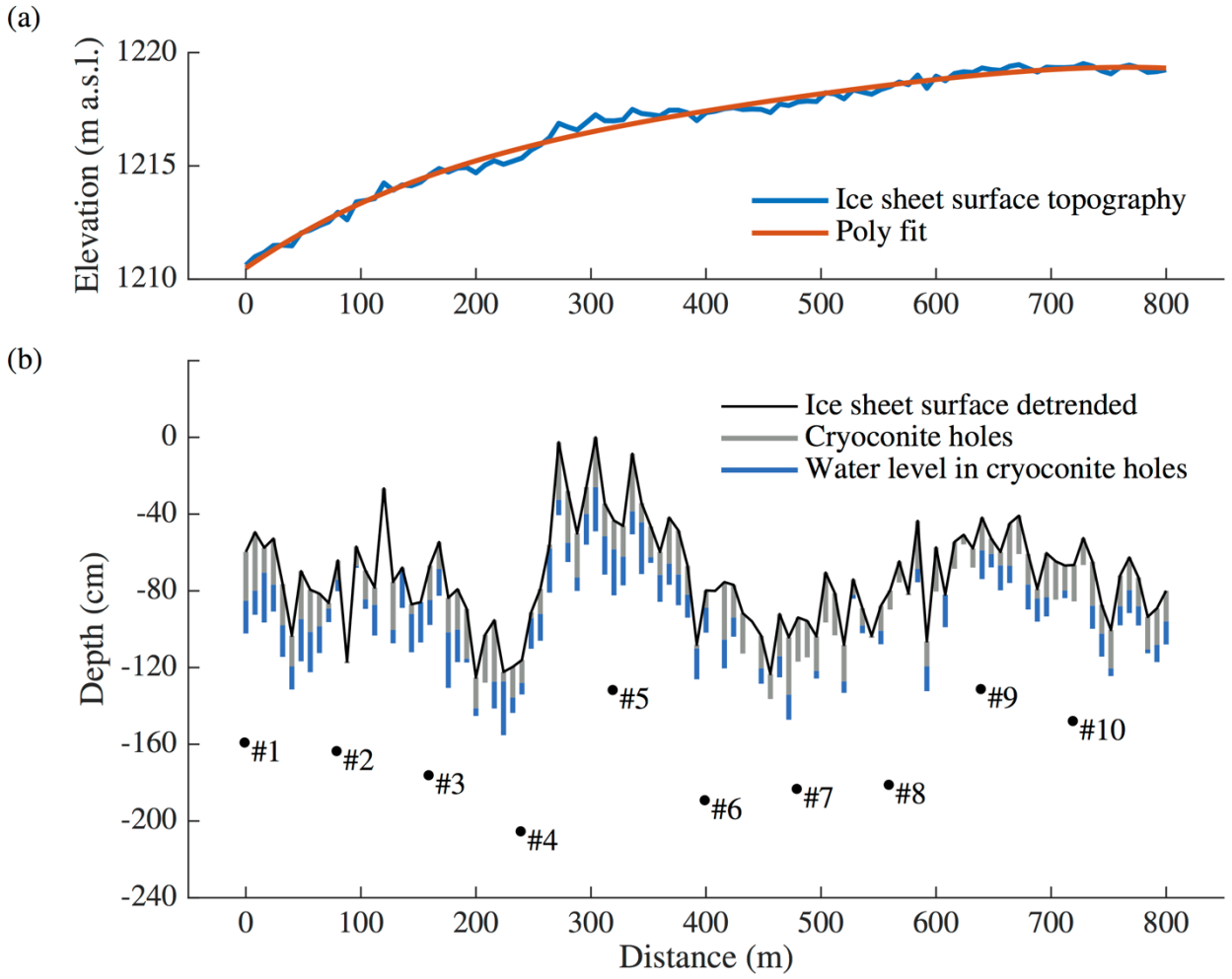

Figure 3-7. (a) Ice sheet surface topography along the 800 m study transect extracted from a 6 cm resolution stereo-photogrammetric digital elevation model derived from RGB imagery collected 10 July 2016 from a quad-copter drone and the 2nd-order polynomial best fit. (b) Ice sheet surface topography detrended with the polynomial best fit, cryoconite hole depths (vertical grey bars), and cryoconite hole water levels (vertical blue bars) sampled along the 800 m study transect, adjusted to a common vertical reference. Locations of the 10 shallow boreholes and their depth relative to the detrended surface are labelled #1-10.

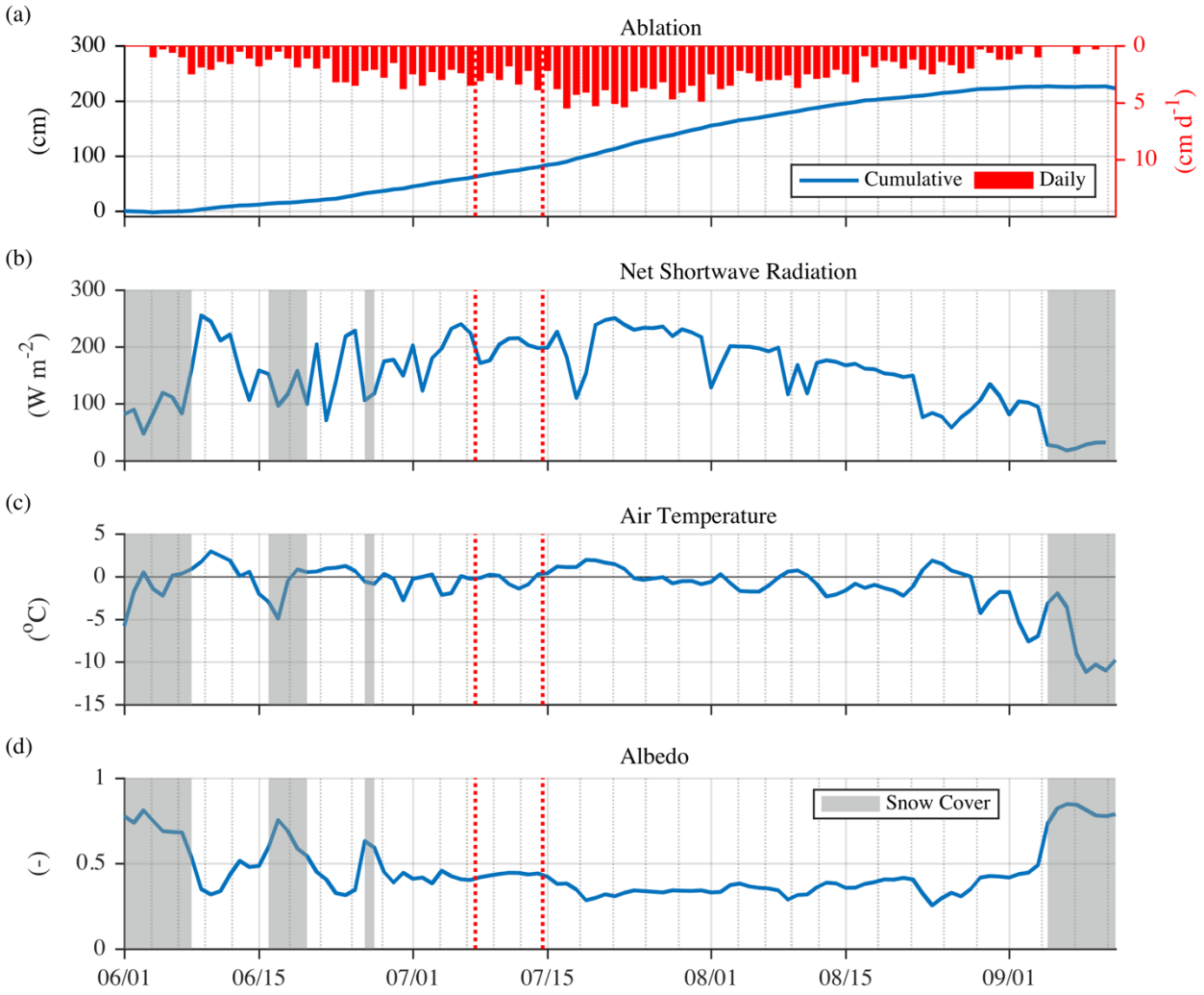

Figure 3-8. Meteorological records of (a) daily and cumulative ice surface ablation, (b) net shortwave radiation, (c) 2 m air temperature, and (d) albedo, for the period 01 June 2016 – 15 September 2016. Data were collected by the PROMICE/GAP KAN-M automatic weather station (see Figure 2-2 for location). Vertical grey shaded bars indicate time periods when albedo was greater than >0.5, indicating snow cover was likely present. Albedo is calculated from the ratio of outgoing solar radiation to incoming solar radiation measured ~2 m above the ice sheet surface at the KAN-M station (www.promice.org).

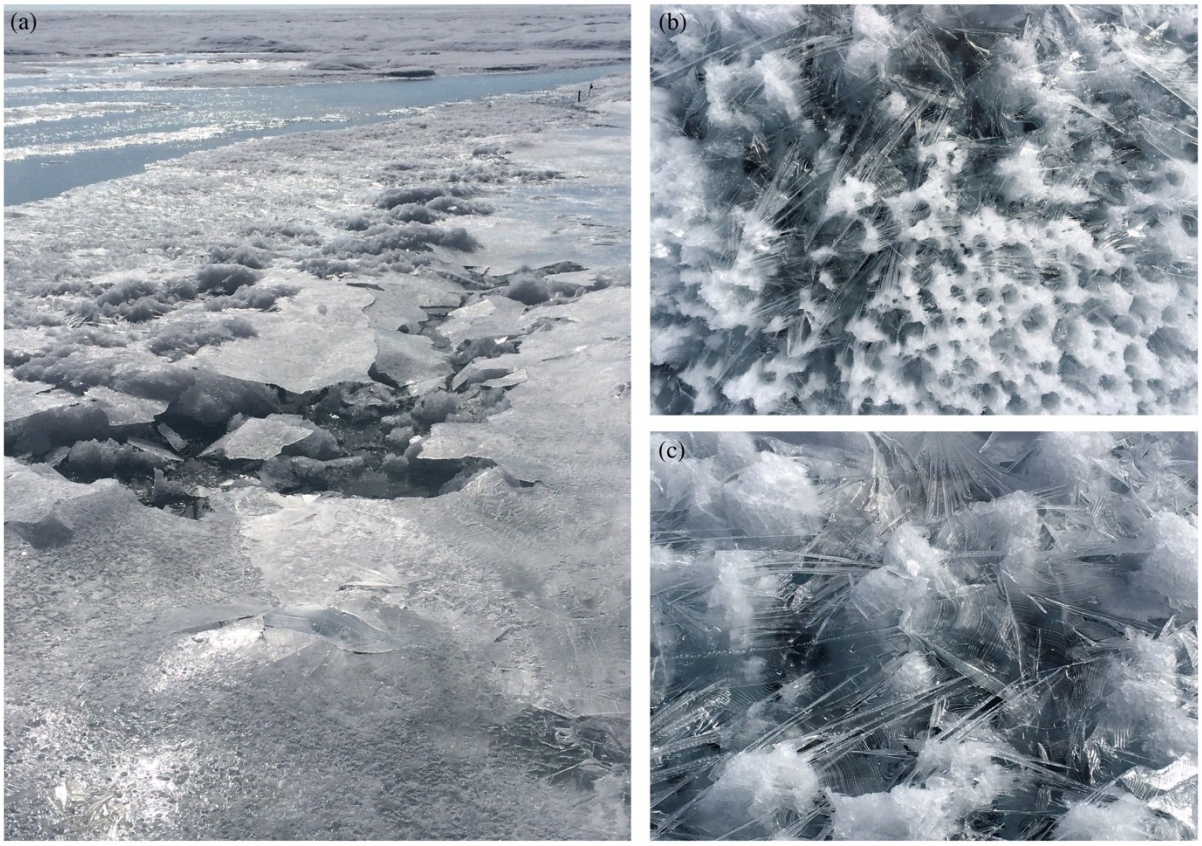

Figure 3-9. Night-time refreezing of meltwater at the surface of (a) water tracks (~10 m length scale), and (b) cryoconite holes (~0.1–1 m length scale) was frequently observed during the field study. Photos were collected by the first author during the 6 July – 12 July 2016 field campaign between 04:00 and 07:00 local time.

4 Reduced meltwater runoff from the Greenland Ice Sheet attributed to refreezing in the bare-ice ablation zone

Abstract. Greenland's contribution to sea level rise is dominated by meltwater runoff from the bare-ice ablation zone, but there is growing evidence that climate models overestimate runoff from this area of the ice sheet. Presently, climate models assume that all bare-ice runoff escapes to the global ocean, in contrast to snow-covered areas of the ice sheet where a fraction of runoff is retained and/or refrozen in porous firn. Here we use in situ measurements of ice sheet meltwater runoff, climate model output, and numerical modeling to show that nocturnal refreezing of liquid meltwater produced by subsurface penetration of solar radiation in bare ice retains a non-trivial fraction of surface runoff on Greenland's ablation zone. Climate models that neglect nocturnal refreezing in bare ice overpredict meltwater runoff by up to +56%. Counterintuitively, these errors are exacerbated when realistic satellite observations of ice albedo are used as model forcing. Incorporating representation of liquid meltwater refreezing in bare glacial ice reconciles model predictions with mass loss observations. Meltwater that refreezes must melt a second time before it contributes to runoff, and climate models that neglect this process will overestimate Greenland's contribution to sea level rise.

1 Introduction

The Greenland Ice Sheet is a major source of global sea level rise with recent mass loss dominated by melting of bare ice in the ablation zone (Bevis et al., 2019; van den Broeke et al., 2016; Ryan et al., 2019; Trusel et al., 2018). Within this critically important zone, winter snowpack melts entirely each summer exposing dark, bare glacier ice that absorbs up to three times as much sunlight as bright snow (Gardner and Sharp, 2010; Warren, 1982). Warming temperatures and reduced summer snowfall have exposed larger areas of bare ice in recent decades, driving enhanced surface melt on the Greenland ablation zone (Bevis et al., 2019; Noël et al., 2019; Ryan et al., 2019). As a consequence, Greenland's mass loss is now controlled by melting bare ice more so than solid ice discharge (Bevis et al., 2019; van den Broeke et al., 2016;

Mouginot et al., 2019). Understanding the fate of meltwater from Greenland's growing bare-ice zone is therefore critical for accurate sea level predictions (MacFerrin et al., 2019).

Meltwater runoff generated on bare ice surfaces is thought to contribute in its entirety to sea level (Smith et al., 2015). Climate models currently treat any snow-free area of the ice sheet as impervious, high-density ice with zero porosity and no capacity to store water (Reijmer et al., 2012). In contrast, some portion of meltwater produced on snow and firn is refrozen or stored as liquid in firn aquifers (Forster et al., 2014; Harper et al., 2012). Less than <20% of Greenland's meltwater runoff is produced on snow and firn (Steger et al., 2017), yet firn meltwater retention may delay centennial-scale sea level rise by ~1–5 cm as its pore space progressively fills with refrozen meltwater (Harper et al., 2012; MacFerrin et al., 2019; Machguth et al., 2016; Pfeffer et al., 1991).

Meltwater retention in the bare ice zone is considered negligible, despite growing field evidence to the contrary (Chu et al., 2016; Cooper et al., 2018; Kendrick et al., 2018; Koenig et al., 2015; Lüthi et al., 2015). River discharges measured at the ice sheet periphery show up to 30% less annual meltwater release from the ice sheet to the ocean than climate model calculations (Mernild et al., 2018; Overeem et al., 2015; Rennermalm et al., 2013a; Smith et al., 2015). Similarly, supraglacial lakes that form on the melt-intensive southwest ablation zone bare-ice surface fill at slower rates than indicated by climate model meltwater runoff (Yang et al., 2019b), and direct measurements of supraglacial runoff suggest +21 to +58% overestimation by climate models (Smith et al., 2017). In this same region, climate models overestimate ice sheet surface lowering by up to 40% relative to satellite measurements (Sutterley et al., 2018), and ice sheet mass changes from the GRACE satellite suggest climate models overestimate mass loss unless statistical corrections are applied (Sasgen et al., 2012a; Xu et al., 2016).

Reconciling climate model calculations with mass loss observations is difficult because direct measurements of meltwater runoff on the bare-ice surface prior to its release from the ice sheet are extremely rare (Rennermalm et al., 2013a; Smith et al., 2015). To address this problem, we pair numerical surface mass balance modeling with in situ measurements of meltwater runoff (Smith et al., 2017) from a

well-studied surface catchment on the southwest Greenland bare-ice ablation zone, where the majority of this ice sheet's surface mass loss originates (Bevis et al., 2019; Ryan et al., 2019).

2 Results

2.1 Climate models overestimate meltwater runoff in the bare-ice ablation zone

Rio Behar is a supraglacial river contained within Greenland's southwest ablation zone that drains approximately ~60–63 km^2 of upstream catchment area, depending on year (Smith et al., 2017; Yang et al., 2018, 2019b) (Figure S4-5). As noted above, our prior field measurements of meltwater runoff discharges in the main stem Rio Behar during July 2015 found that regional and global climate models overpredicted observed ice sheet runoff. Shallow ice cores collected at the same site in July 2016 revealed that the bare ice surface was porous and saturated with meltwater, with an average bare-ice density of 690 kg m^{-3} within the upper one meter of ice (Cooper et al., 2018). During the July 2016 field experiment we revisited the site to collect a seven day record of hourly discharges in the Rio Behar (Smith et al., 2020) and concurrent three-hourly ice surface lowering measurements at a network of ablation stakes installed near the gauging site (see Methods). Here, we investigate these measured discharges (hereafter 'runoff') and surface lowering rates through comparisons with simulated runoff and meltwater production from regional climate models, a global climate reanalysis model, and a one-dimensional model of spectral radiation and thermodynamic heat transfer (Liston et al., 1999a) (see Methods). The climate models include the polar version of the Regional Atmospheric Climate Model version 2.3 (RACMO2.3) (Noël et al., 2018), the Modèle Atmosphérique Régional version 3.11 (MAR3.11) (Fettweis et al., 2017), and the global climate reanalysis Modern-Era Retrospective Analysis for Research and Applications, version 2 (MERRA-2) (Gelaro et al., 2017) (Figure S4-7).

Consistent with previous studies (Smith et al., 2017; Yang et al., 2019b), we find that modeled values of bare-ice runoff overestimate measured meltwater runoff (Figure 4-1). By the end of the 6–13 July 2016 field experiment, climate model runoff ranges from -13% lower (MERRA-2) to +53% higher (RACMO2.3) than observed runoff, with all but MERRA-2 exceeding observed runoff values (Figure 4-1).

Among the climate models examined here, RACMO2.3 most closely reproduces observed albedo and net turbulent and radiative heat fluxes (Figure S4-8 and Figure S4-9), yet severely overpredicts runoff despite good representation of these critical surface energy balance components.

To explain these observations and why climate models cannot reproduce them, we developed a numerical model of ice sheet meltwater runoff that we call 'SkinModel' (see Methods and SI). SkinModel represents the ice surface as an infinitely thin, impermeable 'skin' layer of high-density (900 kg m^{-3}) ice with zero heat capacity, emulating the ice surface energy balance used in climate models (see Methods Equation 1) (Reijmer et al., 2012). When SkinModel is forced with values of albedo output from each climate model, its predictions are virtually identical to climate model predictions (Figure 4-1; dashed lines vs solid lines). Note that all model forcings except albedo are consistent across the emulator simulations, signifying that differences in assumed ice surface albedo alone drive virtually all differences between climate model predictions of runoff shown in Figure 4-1.

SkinModel forcings are obtained with an hourly time step by the PROMICE/GAP KAN-M surface-based automatic weather station proximal to the Rio Behar catchment (Figure S5-1) (Fausto and van As, 2019). When SkinModel is forced with realistic values of albedo recorded at the KAN-M automatic weather station, modeled runoff is +43% higher than measured runoff, much like the other models (Figure 4-1; green solid line). Even greater runoff overprediction is simulated if MODIS satellite albedo values are used (Figure S4-8). These results are mirrored when the same models are tested using the same methods against our earlier measurements from 2015 (Smith et al., 2017) (Figure S4-11). Albedo, therefore, does not explain the runoff overestimation by climate models documented here.

2.2 Attributing climate model overestimation of meltwater runoff to refreezing in bare ice

We developed a second numerical model of ice sheet meltwater runoff that we call 'IceModel' (see Methods and SI). IceModel updates an earlier model of spectral radiation and thermodynamic heat transfer in glacier ice (Liston et al., 1999a) with a field-calibrated constraint on shortwave radiation absorption enhancement by dark impurities present within Greenland's ablating ice (Cooper et al., 2020). In contrast to SkinModel,

IceModel simulates an ice column with time-varying ice, air, vapor, and liquid water content (see Methods Equation 2), informed by measurements of ice sheet surface properties collected during a multi-year field campaign in the Greenland Ice Sheet ablation zone (Cooper et al., 2018, 2020; Pitcher and Smith, 2019; Rennermalm et al., 2013a; Smith et al., 2015, 2017; Yang et al., 2018). A critical feature of IceModel is that it allows sunlight to penetrate bare ice, providing heat that produces meltwater within the ice subsurface, rather than restricting all energy expenditure on an infinitely thin 'skin' layer.

IceModel reproduces observed cumulative runoff to within 3%, well within catchment boundary uncertainty (Figure 4-1, solid blue line with shaded uncertainty bounds). This suggests that the observed reduction in runoff relative to climate model simulations is explained by nocturnal refreezing of liquid meltwater within the upper decimeters of the weathered ice matrix (Figure 4-2a). During daylight hours, penetration of shortwave radiation produces an isothermal ice column nearly 1.5 m thick that stores latent heat in the form of liquid meltwater, a phenomenon independently validated by our field observations of saturated bare ice extending at least 1.2 m below the ice surface (Cooper et al., 2018). Lateral transport of meltwater generated within isothermal bare ice is constrained by its low horizontal hydraulic conductivity (order 10^{-4} m h^{-1}) (Karlstrom et al., 2014; Stevens et al., 2018) and impermeable lower boundary. At night, the cold polar boundary layer cools the ice surface to -5°C on average during July at this location, as indicated by modeled and observed surface temperatures (Figure 4-2b). This cold surface drives refreezing of subsurface liquid meltwater at rates approaching 0.002 m hr^{-1} between 02:00–04:00 local time, when the ice surface temperature drops as low as -6°C (Figure 4-2).

As the nocturnal cold front propagates downward from the surface into the upper active layer of ice, liquid water refreezes, and volume expansion displaces air. The simultaneous increase in ice content and reduction in air and water content increases the modeled effective thermal conductivity of the near surface ice (Figure 4-2a), promoting efficient heat loss and development of cold content that inhibits melting when daytime heating commences. These simulations are consistent with observed refreezing of open water stored in surface depressions at night and into the early morning when low sun angles and cold

air kept surface temperatures below freezing (Figure 4-2). Together with the recycling of melt energy required to melt ice a second time, this thermal cooling reduces modeled runoff by nearly ~6 cm cumulative over our seven-day field experiment during peak summer melt conditions in the southwest sector, where the majority of Greenland's surface mass loss originates.

Patterns of climate model mass loss overprediction obtained from the catchment-scale runoff comparison are mirrored in measurements of ice surface lowering at our network of ablation stakes and at the KAN-M AWS (Figure 4-3a). Unlike SkinModel and the climate models it emulates, IceModel detects internal mass loss below the ice surface (Figure 4-3b). Modeled values of ice density vary from <300 kg m^{-3} in the upper decimeter of ice to 900 kg m^{-3} below ~1.2 m, with a column-averaged modeled ice density within 2% of measured ice density (Figure 4-3b). These measurements reveal that substantial melting occurs beneath the ice surface, where meltwater is retained within porous bare ice, undetected by climate model simulations of the 'skin' energy balance, and available for nocturnal refreezing.

3 Discussion

Like previous studies (Overeem et al., 2015; Rennermalm et al., 2013a; Smith et al., 2015, 2017) our comparison of in situ meltwater runoff measurements on Greenland's ablating bare ice surface with runoff predictions from a suite of regional and global climate models finds that they overestimate runoff, here by up to +53%. Two models that do estimate runoff realistically (MERRA-2, MAR3.11) do so only incidentally, by overestimating albedo. This apparent over-prediction of runoff by ice sheet runoff models can only be explained by nocturnal refreezing of meltwater generated in the bare-ice ablation zone, a process observed on mountain glaciers (Ambach, 1955; Hastenrath, 1983) that has eluded detection in Greenland and is not included in climate model mass loss predictions (Reijmer et al., 2012).

Unlike the slow thermal response of firn (Harper et al., 2012), bare ice responds rapidly to nocturnal cooling of the ice surface, producing numerous small but frequent melt-freeze cycles that accumulate into non-trivial reductions in runoff leaving the ice sheet surface. A simple extrapolation of the physical process reported here to just 10% of the Greenland bare-ice ablation zone (173,694 km^2) (Ryan et al. 2019) would

yield a 5 Gt runoff reduction after thirty consecutive nights of nocturnal refreezing. This mass loss reduction is commensurate with 10% of the annual refreezing in snow and firn predicted by regional climate models for this sector of the ice sheet (Steger et al., 2017). Longer periods of below-freezing air temperatures and seasonal transitions from melt to freeze-up similarly consume melt energy, potentially reducing realized runoff export from bare ice by up to 32% annually, as indicated by a 21-year simulation of meltwater runoff from the Rio Behar catchment (Figure 4-4).

Regional climate models are the primary tools used to predict the amount of runoff exported from Greenland's ablation zone to the global ocean, but these models currently lack representation of the nocturnal refreezing process described here. Refreezing in snow and firn has potential to reduce centennial-scale sea level rise by ~1–5 cm (Harper et al., 2012; Pfeffer et al., 1991), yet refreezing in bare ice is currently set to zero in regional climate models (Reijmer et al., 2012). With nearly all (85–93%) of Greenland's meltwater currently sourced from bare ice, this seemingly innocuous process accumulates into a large reduction in runoff. In addition to snow and firn processes, characterizing mechanisms of meltwater retention within Greenland's bare-ice ablation zone is necessary to accurately inform future sea level rise predictions, as climate models that neglect refreezing on bare ice will overestimate mass loss.

4 Figures

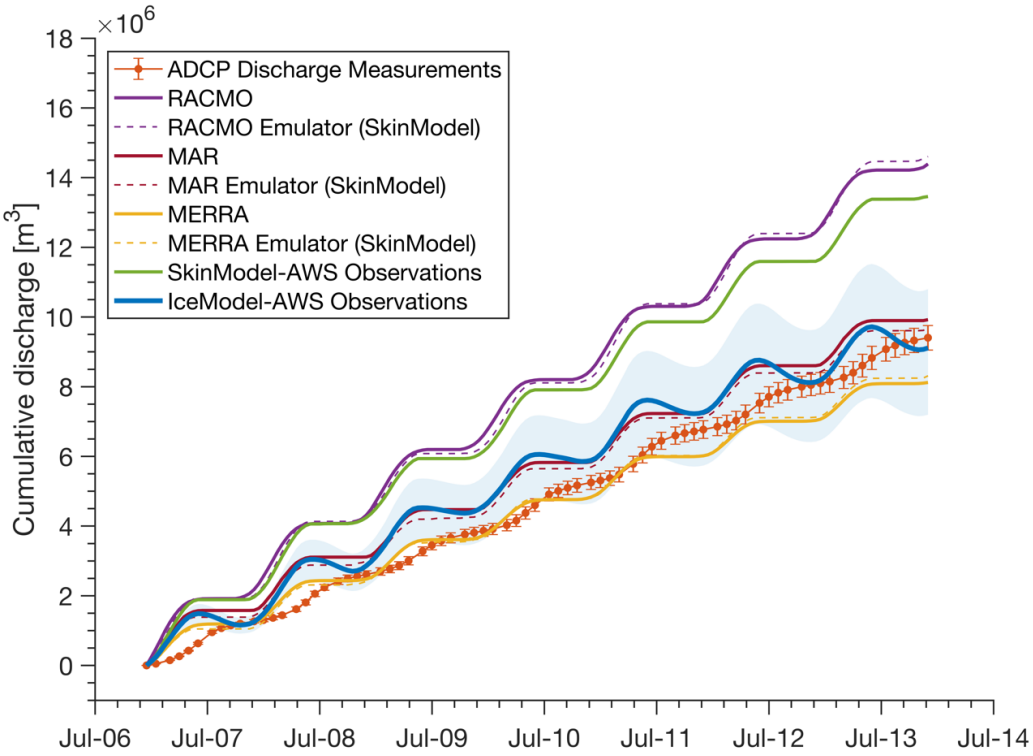

Figure 4-1. Climate model cumulative runoff predictions at the end of the 06–13 July 2016 field experiment are -13% lower to +53% higher than observed values of ice sheet surface meltwater runoff (ADCP discharge measurements). These climate model predictions are reproduced with 'SkinModel', our zero-dimensional surface energy balance model designed to emulate the 'skin' representation of the ice sheet surface used by climate models. When SkinModel is deliberately forced with albedo output from each climate model, its predictions are virtually identical with those of each model (dashed lines vs solid lines). When SkinModel is forced with observed albedo values recorded by automatic weather station (AWS) proximate to our experimental site, modeled runoff is overpredicted by +43% (green solid line), demonstrating that misrepresented albedo does not explain climate model runoff overestimation at this time and location. In contrast, meltwater runoff is closely reproduced by our numerical mass and heat transfer model 'IceModel', which accounts for subsurface meltwater produced by solar radiation penetration into bare ice and nocturnal refreezing of this meltwater. Solid and dashed lines represent volumetric runoff from upstream catchment area (60.04 km^2). Shaded uncertainty bounds represent highly conservative lower (48.4 km^2) and upper (71.3 km^2) bounds on catchment area (see Methods).

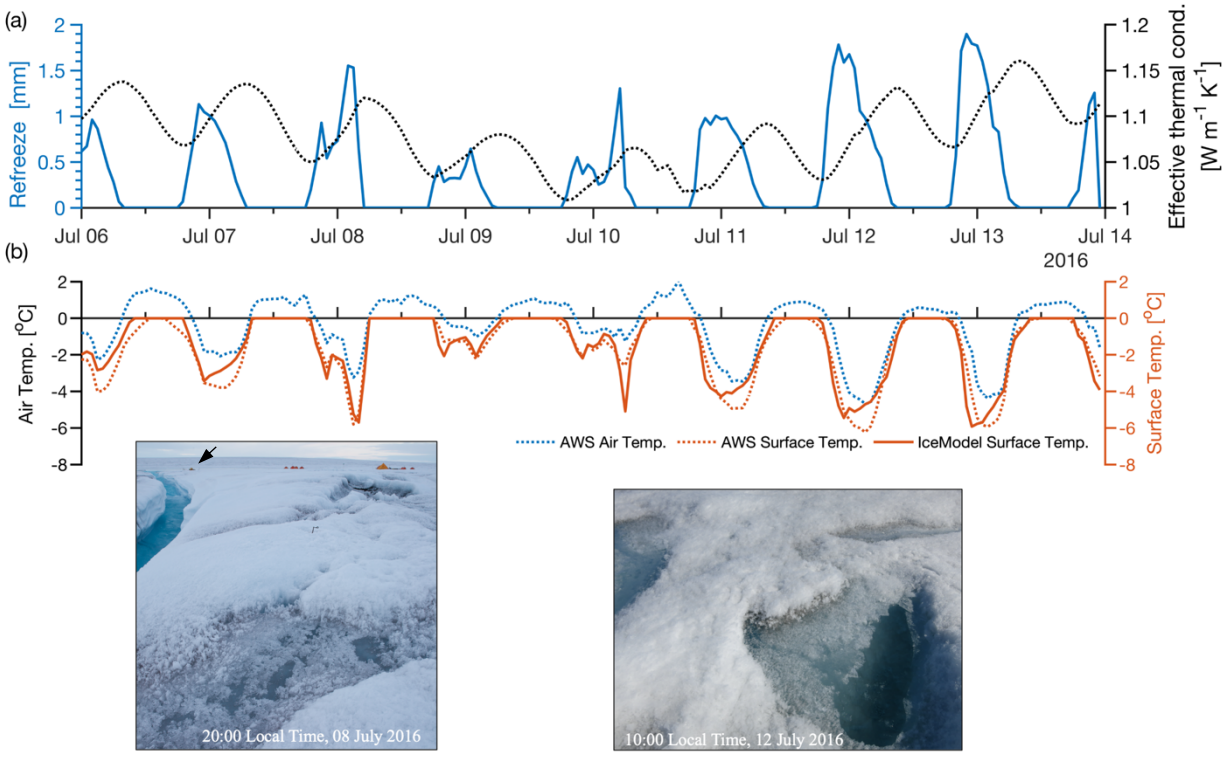

Figure 4-2. (a) Modeled values of refreezing during the seven day field experiment closely track the diurnal variation of (b) observed air temperature and ice surface temperature, which is closely reproduced by IceModel simulations of ice surface temperature (compare solid red line to dotted red line). As liquid meltwater within the ice matrix freezes, the effective thermal conductivity (black dotted line) of the upper decimeters of ice matrix increases because ice has ~4 times higher thermal conductivity than liquid water. The increase in thermal conductivity during nocturnal freeze enhances heat loss to the atmosphere and cold content development that inhibits runoff generation when daytime solar heating commences. Main tick marks in (a) and (b) are at 00:00 local time (UTC-3), minor tick marks are 12:00. Photographs taken during the field experiment show refreezing of meltwater entrained on the weathered bare ice surface at night and into the early morning when low sun angles and cold air kept surface temperatures below freezing. Photograph at right shows surficial refrozen meltwater persisting to 10:00 local time on 12 July 2016 following the coldest night during the seven day field experiment. The approximate location of the discharge gaging station is indicated by arrow in photo at left. All photos were taken by the first author.

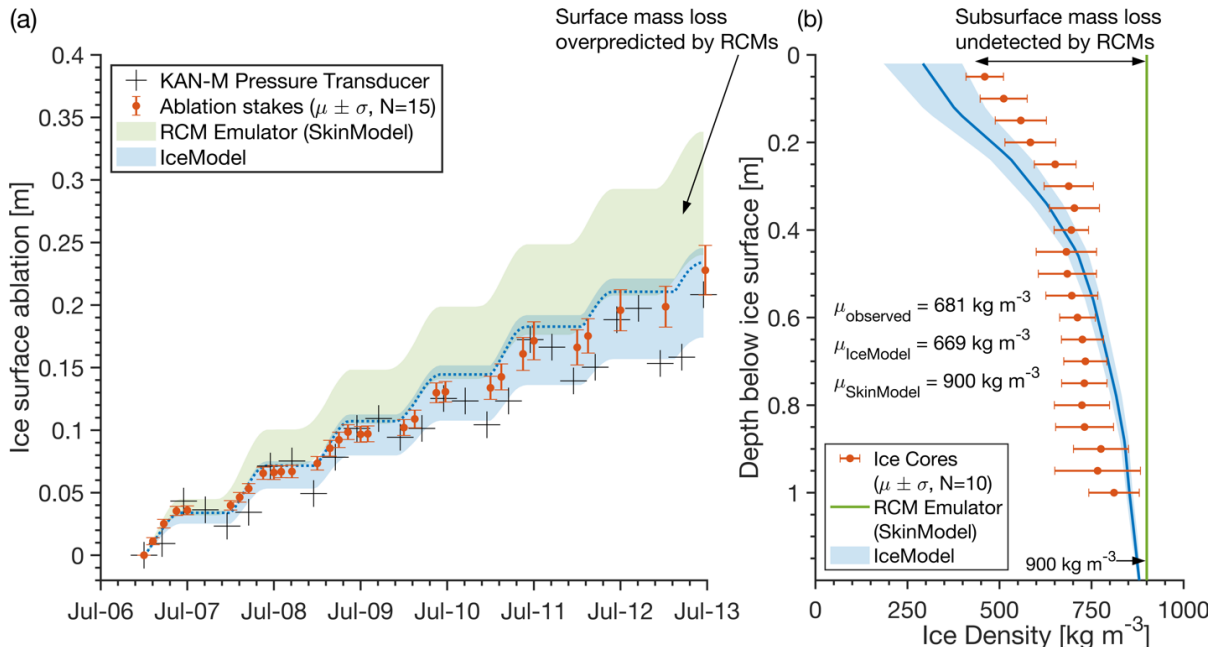

Figure 4-3. Observed values of ice surface mass loss during the 06–13 July 2016 field experiment are closely reproduced by our one-dimensional ice column mass and heat transfer model 'IceModel' but are overpredicted by our climate model emulator 'SkinModel'. Climate models used to estimate mass loss from the Greenland Ice Sheet currently treat the bare ice ablation zone as a solid impermeable ice surface with no mass or heat retention capacity. (a) Ice surface ablation values recorded by the KAN-M automatic weather station (black crosses proportional to ±1 cm instrument uncertainty) and measured values from a network of ablation stakes in the Rio Behar experimental catchment (red error bars ±1 standard deviation). The green and blue envelopes are SkinModel and IceModel meltwater converted to ice thickness using a lower (600 kg m^{-3}) and upper (900 kg m^{-3}) assumed ice density. The dotted blue line is IceModel thickness change computed directly from the modeled vertical column ice density, shown as the blue line in (b) with shaded envelope representing ±1 standard deviation in modeled ice density during 06–13 July 2016. The column-averaged modeled ice density (μ = 669 kg m^{-3}) is within 2% of measured ice density (μ = 681 kg m^{-3}) from 10 shallow ice cores collected in the Rio Behar catchment on 11–12 July 2016 (Cooper et al., 2018).

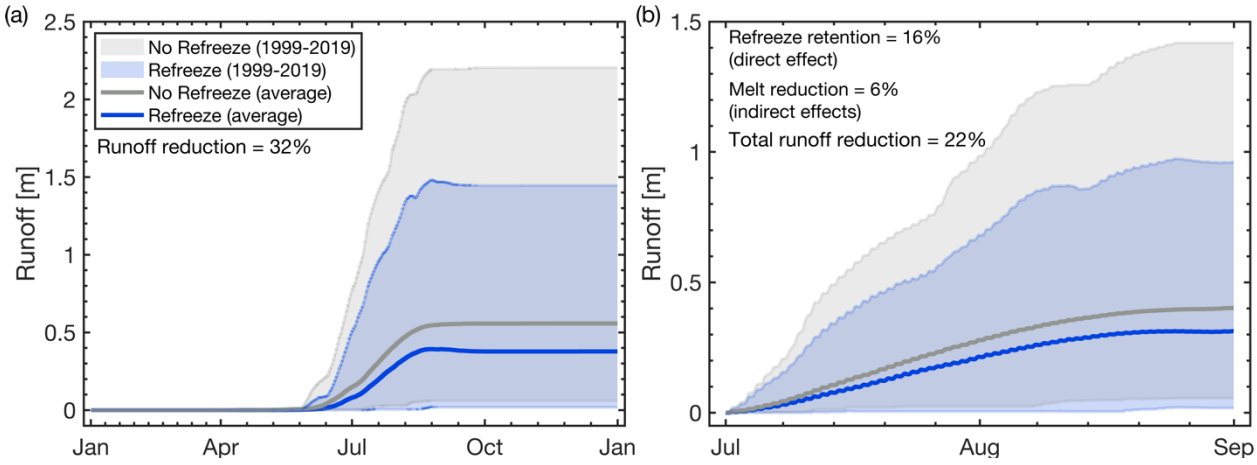

Figure 4-4. (a) An idealized 21-year simulation that disallows meltwater refreezing within the ice column. Meltwater that refreezes must melt again before it contributes to runoff, here directly reducing bare ice runoff by 32% relative to our baseline simulation with refreezing. (b) Same as (a) but restricted to the peak melt period July–August when bare ice exposure is maximum in this region (Ryan et al., 2019). Refreezing increases the ice effective thermal conductivity (Figure 4-2a), enhancing the ice column's capacity to cool during night and during seasonal transitions between melting and freeze-up. This enhances ice cold content development, which reduces meltwater production by 6% on average during July–August, adding to the 16% reduction in runoff due to the direct effect of re-melting ice. Note that condensation, rainfall, and snow accumulation are not included in these idealized simulations designed to isolate bare ice melt/refreeze processes, and therefore the second-order effects of cold content development are not evaluated for the annual period shown in (a). Shaded areas represent the range of modeled runoff during the 1999–2019 simulation period. Solid lines are the 21-year average runoff.

5 Data and Methods

5.1 Field datasets

Hourly catchment discharges were measured during two field campaigns (20–23 July 2015 and 06–13 July 2016) (Smith et al., 2017, 2020) with a SonTek RiverSurveyor M9 Acoustic Doppler Current Profiler (ADCP) mounted on a SonTek HydroBoard II. The M9 was escorted across the Rio Behar main-stem channel with a bank-operated modified Tyrolean system. The M9 system transmits channel geometry and flow velocity measurements in real time to a bank-operated computer running the RiverSurveyor software. During each measurement hour, from 3–9 sub-hourly measurements and associated quality measures were recorded. These raw data are converted to channel flow rate [m^3 s^{-1}] in post-processing following data quality assurance and control workflows optimized for the supraglacial environment (Smith et al., 2020). The sub-hourly measurements are used to estimate ± 15 m^3 s^{-1} measurement uncertainty (error bars in Figure 4-1).

Measurements of ice surface elevation change are recorded by pressure transducer installed on the PROMICE/GAP KAN-M automated weather station (van As et al., 2017) and by a network of bamboo ablation stakes we installed at our field camp (67.049º N, 49.022º W) (Figure S4-13). Twelve stakes were installed within an area covering ~0.5 km^2. Stake locations were selected by generating twelve random distance-direction pairs from a common center. Following their installation on 4 July 2016 and a 24-hour freeze-in period, ablation stake measurements were recorded at 3-hour intervals continuously from 12:00 on 06 July 2016 to 21:00 on 12 July 2016. The ablation stakes were drilled 3 m deep into the ice. Freeze-in was confirmed prior to each measurement to infer potential vertical displacement of these stakes due to melt-out at their base (none occurred). Prior to each measurement, an 8×8 inch wooden ablation board was placed at the base of the stake and oriented to magnetic north. This board operated as a datum from which the stake height was measured. Cumulative changes in stake height are converted directly to ice surface elevation change for comparison with simulated melt rates. Field datasets of ice density from shallow ice

cores, ice porosity, ice saturation, and water table height within cryoconite holes and within excavated boreholes used to supplement this analysis are described in Cooper et al. (2018).

5.2 Satellite and airborne datasets

Catchment-scale topography and surface classification is provided by true color images of the ice sheet surface collected with an uncrewed aerial vehicle (Ryan et al., 2015) (Figure S4-6). These images are used to reconstruct the ice sheet surface topography using Agisoft PhotoScan Pro stereophotogrammetry software. Surface types of snow, water, and bare ice are classified with a k-Nearest Neighbors algorithm yielding 2.7% snow cover during the 06–13 July 2016 field experiment, and 6.5% for the 2015 experiment (Smith et al., 2017) (Figure S4-6). WorldView-1 and WorldView-2 satellite imagery and associated high resolution stereo-photogrammetric digital elevation models are used to delineate the Rio Behar contributing catchment area following methods in Smith et al. (2017). Briefly, digital elevation based methods are supplemented with manual delineation of surface stream networks, flow direction, and channel heads following Yang et al. (2017a). Interior channel heads (initiation points of channels that drain into the catchment) yield a minimum estimate of catchment area. Areas of internal drainage to moulins and crevasses that exist within the catchment boundary areas are removed from this lower catchment area estimate. Outer channel heads (initiation points of channels that drain away from the catchment) yields an upper maximum estimate of catchment area. The optimal "best guess" catchment area is delineated by tracing the inner and outer channel heads in the high resolution WorldView imagery and adding back areas that undoubtedly flow into the catchment and subtracting areas that undoubtedly flow out of the catchment. This approach yields contributing catchment area independent from error-prone digital elevation model-based methods (Yang et al., 2015).

5.3 Climate model data

We use climate model output from the polar version of the Regional Atmospheric Climate Model version 2.3 (RACMO2.3) (Noël et al., 2018), the Modèle Atmosphérique Régional version 3.11 (MAR3.11)

(Fettweis et al., 2017), and the global climate model Modern-Era Retrospective analysis for Research and Applications, version 2 (MERRA-2) (Gelaro et al., 2017). MAR3.11 data are provided at 15 km horizontal resolution and hourly timestep forced by European Centre for Medium-Range Weather Forecasts (ECMWF) ERA5 reanalysis (Delhasse et al., 2020). RACMO2.3 data are provided at 11 km horizontal resolution and 3-hourly timestep forced with ECMWF ERA-Interim reanalysis (Dee et al., 2011). MERRA-2 data are provided on a global 0.5°×0.625° latitude-longitude grid at 3-hourly timestep.

Hourly catchment runoff volumes for each model are extracted by intersecting the climate model horizontal grids with a bounding box that surrounds the Rio Behar catchment boundary ±0.06° in latitude and ±0.04° in longitude (Figure S4-7). These latitude and longitude coordinates are projected onto the National Snow and Ice Data Center Equal-Area Scalable Earth (EASE) version 2.0 (Brodzik et al., 2012) coordinate system onto which the gridded climate model hourly runoff values are resampled at 100 m horizontal grid spacing using Delaunay triangulation and nearest neighbor interpolation. These 100 m gridded values are then intersected with the lower, upper, and best guess catchment boundaries and converted to volumetric quantities using the catchment-scale area weighted average of the 100 m gridded values to minimize edge effects. This procedure is repeated for all other climate model output used in this study.

5.4 SkinModel Description

SkinModel solves a zero-dimensional surface energy balance of the form (Hoffman et al., 2014):

$$\chi Q_{\mathrm{si}}(1-\alpha) + Q_{\mathrm{li}} - \epsilon\sigma T_{\mathrm{sfc}}^4 + Q_{\mathrm{h}} + Q_{\mathrm{e}} + Q_{\mathrm{c}} = Q_{\mathrm{m}} \quad (1)$$

where χ [-] allocates the incoming shortwave solar radiation Q_{si} [W m^{-2}] into a 'skin' surface component and a subsurface component, α [-] is ice surface albedo, Q_{li} [W m^{-2}] is incoming longwave radiation, $\epsilon\sigma T_{\mathrm{sfc}}^4$ [W m^{-2}] is longwave radiation emitted by the ice surface, ϵ [-] is the ice surface emissivity, σ [W m^{-2} K^{-4}] is the Stefan-Boltzmann constant, T_{sfc} [K] is the ice surface temperature, Q_{h} [W m^{-2}] is the sensible heat flux, Q_{e} [W m^{-2}] is the latent heat flux, Q_{c} [W m^{-2}] is the conductive heat flux, and Q_{m} [W m^{-2}] is energy available for meltwater production. For SkinModel simulations $\chi = 0.0$ meaning all shortwave solar

radiation is absorbed at the skin. Monin-Obukhov similarity theory is used to obtain Q_{h} and Q_{e} as described in Liston et al. (1999a). Values for near-surface air temperature, relative humidity, and Q_{si} and Q_{li} required to solve Equation 1 are provided by the KAN-M automatic weather station on an hourly timestep. A complete description of the model is given in the Supplementary Material.

5.5 IceModel description

IceModel solves the one-dimensional thermodynamic equation (Liston et al., 1999a):

$$C_{\mathrm{v}}\frac{\partial T_{\mathrm{i}}}{\partial t} - \rho_{\mathrm{i}}L_{\mathrm{f}}\frac{\partial \theta_{\mathrm{i}}}{\partial t} = \frac{\partial}{\partial z}\left[(k_{\mathrm{i}} + k_{\mathrm{v}})\frac{\partial T_{\mathrm{i}}}{\partial z}\right] - \frac{\partial \mathrm{q}}{\partial z} - C_{\mathrm{v}}v_{\mathrm{i}}\frac{\partial T_{\mathrm{i}}}{\partial z} \quad (2)$$

where ρ_{i} [kg m^{-3}] is ice density, C_{v} [J m^{-3} K^{-1}] is volumetric specific heat capacity, T_{i} [K] is ice temperature, L_{f} [J kg^{-1}] is the latent heat of fusion of ice, θ_{i} [m^3 m^{-3}] is volumetric ice content, k_{i} is ice thermal conductivity, k_{v} is the vapor diffusion coefficient for the ice matrix air passages, v_{i} [m s^{-1}] is the ice surface ablation rate, and z [m] is the vertical coordinate. The model updates an earlier version (Liston et al., 1999a) with new values for the spectral absorption coefficient of ice (Warren and Brandt, 2008) and a deforming numerical grid that permits inclusion of the ice advection term v_{i} following Jordan (1991). The upper boundary condition for Equation 2 is the ice surface temperature T_{sfc}, which is initially unknown. To estimate it, Equation 1 is cast in a form where T_{sfc} is the only unknown and the Newton-Raphson method is used to estimate T_{sfc}.

The net solar flux $\partial \mathrm{q}/\partial \mathrm{z}$ [W m^{-3}] is evaluated with a two-stream radiative transfer model with 118 spectral bands (Brandt and Warren, 1993; Liston et al., 1999a; Schlatter, 1972). A key input to this model is the solar radiation extinction coefficient, κ, which controls the vertical distribution of absorbed solar radiation within ice. We constrain κ with our direct measurements of $\partial \mathrm{q}/\partial \mathrm{z}$ in Greenland's ablating ice, and thereby capture the melt-enhancing effect of dark impurities present within the ice (Cooper et al., 2020). The melt enhancing effect of dark impurities is further constrained by albedo observations from the PROMICE/GAP KAN-M automatic weather station (AWS) (Figure S4-5) used as the upper boundary

condition on the two-stream model (see Methods). A complete description of the model is given in the Supplementary Material.

6 Supplementary Material

6.1 Supplementary Figures

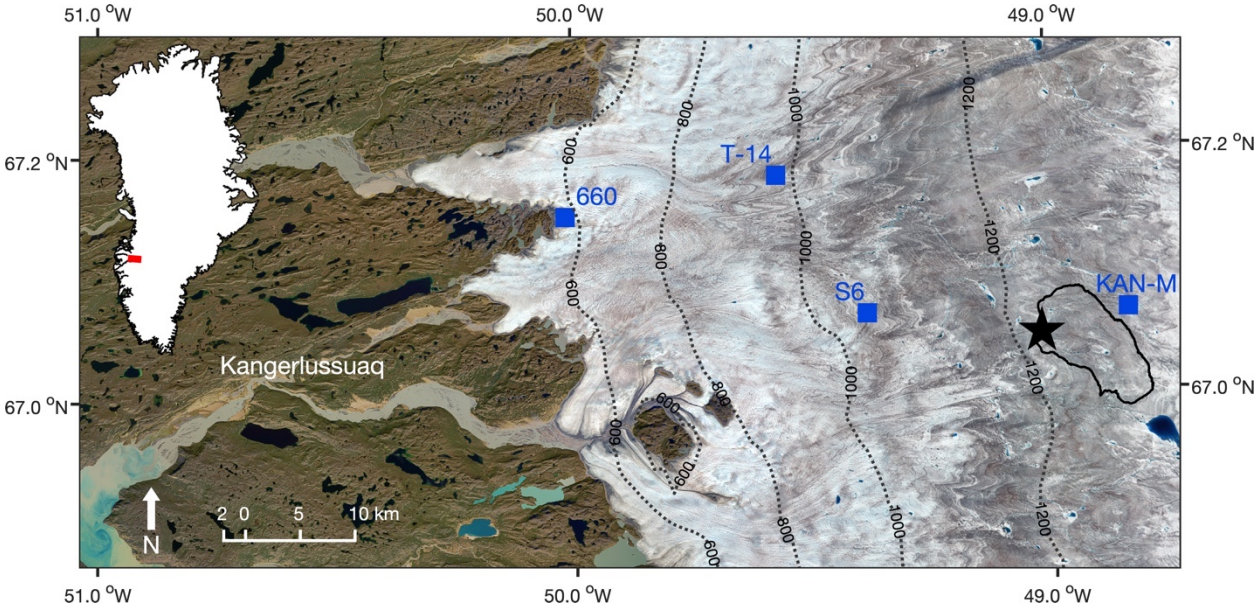

Figure S4-5. Map of southwest Greenland study area showing the location of Rio Behar catchment (black star indicates discharge gage site location, black outline is catchment boundary) (67.05°N, -49.02°W; 1215 m. a.s.l.) in relation to site S6, where we collected ice density data in 2018, site T-14 where an unrelated team collected ice temperature thermistor data in 2015 and 2016 (Hills et al., 2018), site 660, where we collected ice density data in 2018 and where we measured in-ice solar irradiance to estimate $\partial q / \partial z$ in Equation 1 (see Methods) (Cooper et al., 2020).

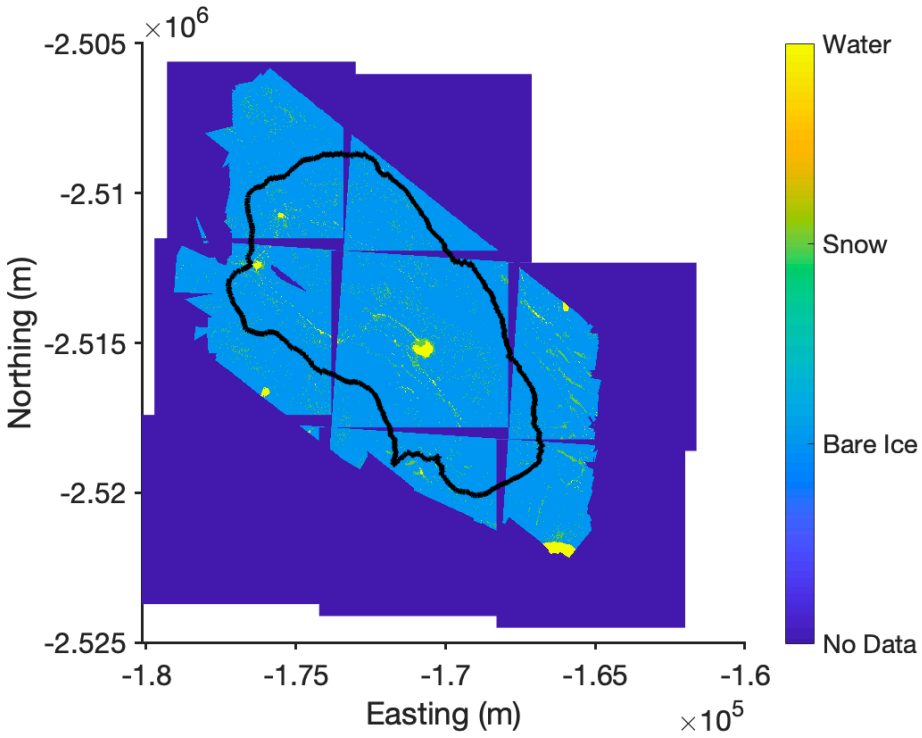

Figure S4-6. The 60.04 km^2 Rio Behar catchment (black outline) was surveyed with an uncrewed aerial vehicle carrying an RGB camera during the 06–13 July 2016 field experiment. Aerial photographs were stitched using Agisoft PhotoScan Pro stereophotogrammetry software. The catchment surface is classified as snow, water, and bare ice with a k-Nearest Neighbors algorithm that yields 3.1% snow cover, 1.2% water, and 95.7% bare ice during the 6–13 July 2016 field experiment (snow cover was 6.5% for the 2015 experiment) (Smith et al., 2017). The low snow cover suggests meltwater refreezing in snow was minimal. Field notes and meteorological observations indicate that clouds were nearly absent, supported by modeled values of absorbed shortwave radiation that accounts for 87% of melt energy. Together these observations indicate meltwater runoff within the Rio Behar was dominated by solar radiation-driven bare ice meltwater production.

Figure S4-7. Example of processing stream applied to RACMO2.3 climate model output used in this study. (a) The native climate model output is provided at ~7.5 km grid spacing. (b) The catchment boundary for 2015 shown here contains internal areas drained by crevasse fields. The native climate model grid is projected onto the National Snow and Ice Data Center Equal-Area Scalable Earth (EASE) and the climate model data is resampled at 100 m horizontal grid spacing using Delaunay triangulation and nearest neighbor interpolation. (c) These 100 m gridded values are then intersected with the lower, upper, and best guess catchment boundaries and converted to volumetric quantities using the catchment-scale area weighted average of the 100 m grid cells at right.

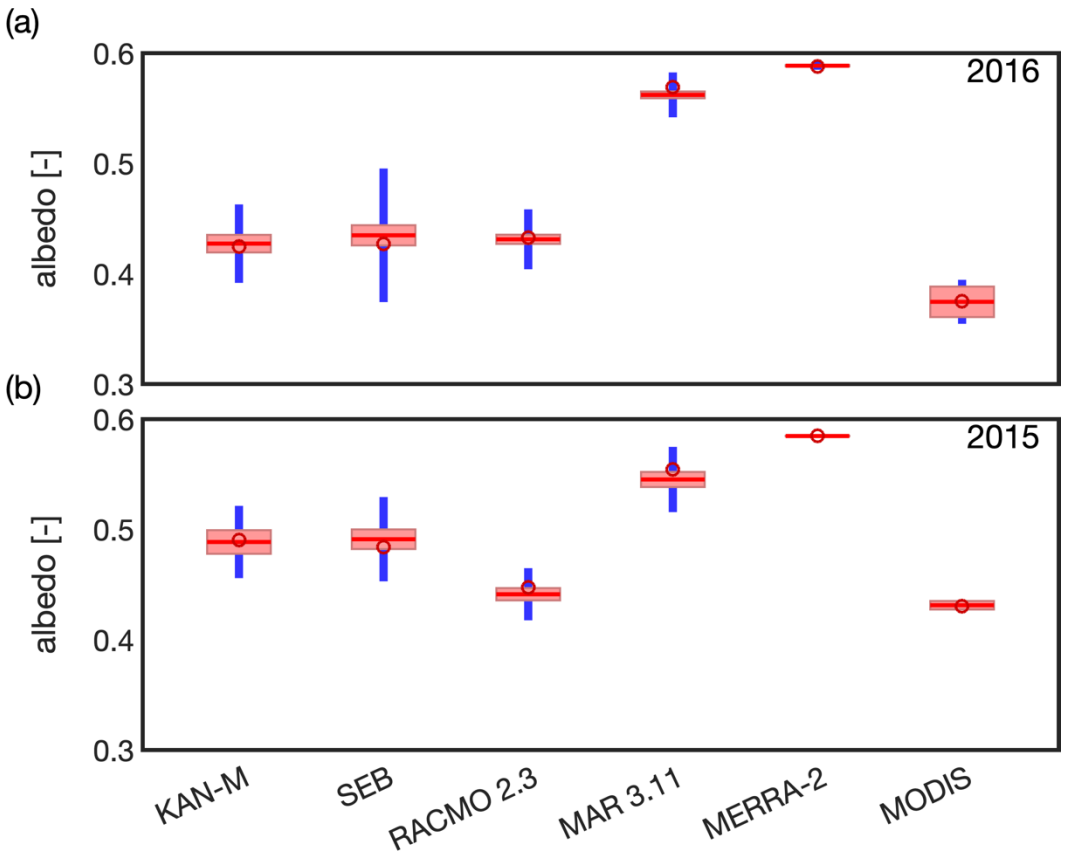

Figure S4-8. Comparison of observed hourly albedo from the KAN-M automatic weather station with albedo output from the offline ice surface energy balance model (SEB), two regional climate models (RACMO2.3 and MAR3.11), one global climate model (MERRA-2), and daily albedo from the MODIS satellite during the (a) 6–13 July 2016 field experiment, and (b) 20–23 July 2015 field experiment. Among the climate models examined, RACMO2.3 most closely reproduces observed albedo values. Consequently, RACMO2.3 most closely reproduces energy available for meltwater production, but overestimates meltwater runoff. The MODIS satellite time of overflight at this location is 10:30 for Terra and 13:30 for Aqua. This may explain the lower MODIS albedo values, as they are collected when the ice surface is rapidly melting. Note that model simulations presented in this study labeled 'AWS Observations', and also the SEB model, are forced with KAN-M albedo observations.

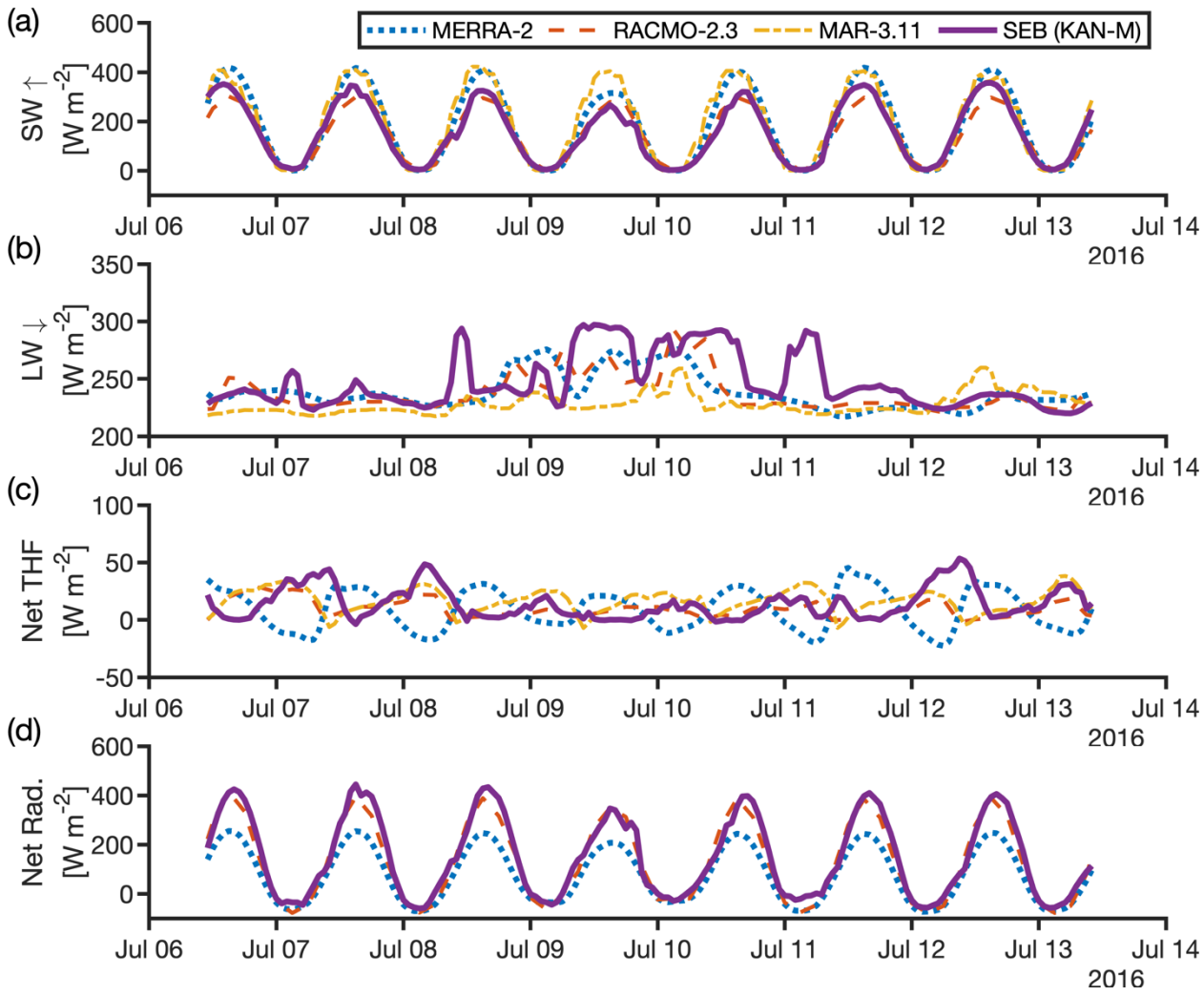

Figure S4-9. Hourly values of (a) reflected shortwave radiation, (b) incoming longwave radiation, (c) net turbulent heat flux, and (d) net radiation from MERRA-2, RACMO2.3, MAR3.11, and the SEB model during the 06–13 July 2016 field campaign. Consistent with the July 2015 field experiment, among these models, RACMO2.3 most closely reproduces net radiation and turbulent energy fluxes but overestimates meltwater runoff. Note that SEB is forced with KAN-M automatic weather station observations and therefore is proxy for observed values.

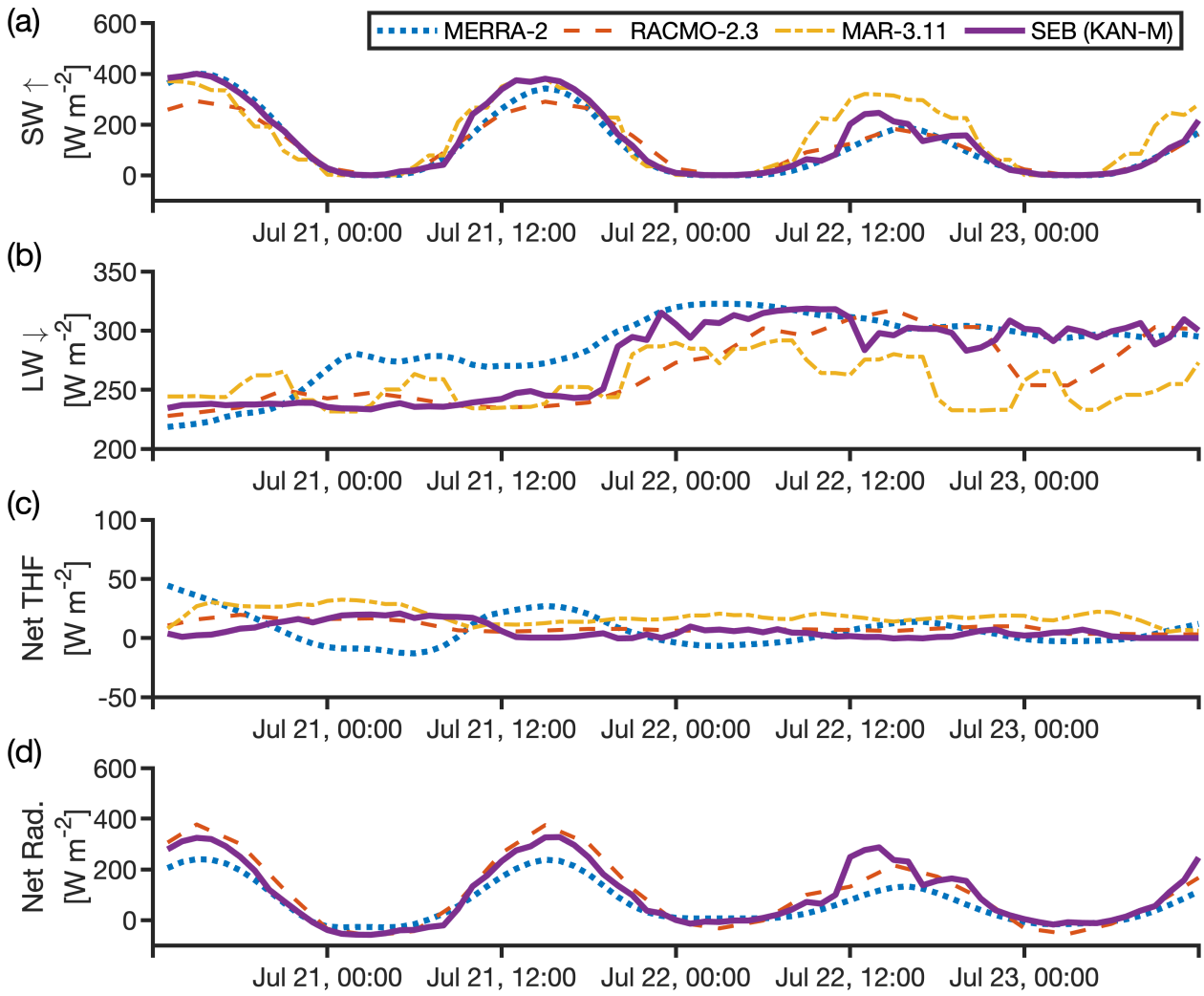

Figure S4-10. Hourly values of (a) reflected shortwave radiation, (b) incoming longwave radiation, (c) net turbulent heat flux, and (d) net radiation from MERRA-2, RACMO2.3, MAR3.11, and the SEB model forced with KAN-M automatic weather station observations during the 20–23 July 2015 field campaign. Among these models, RACMO2.3 most closely reproduces net radiation and turbulent energy fluxes but overestimates meltwater runoff.

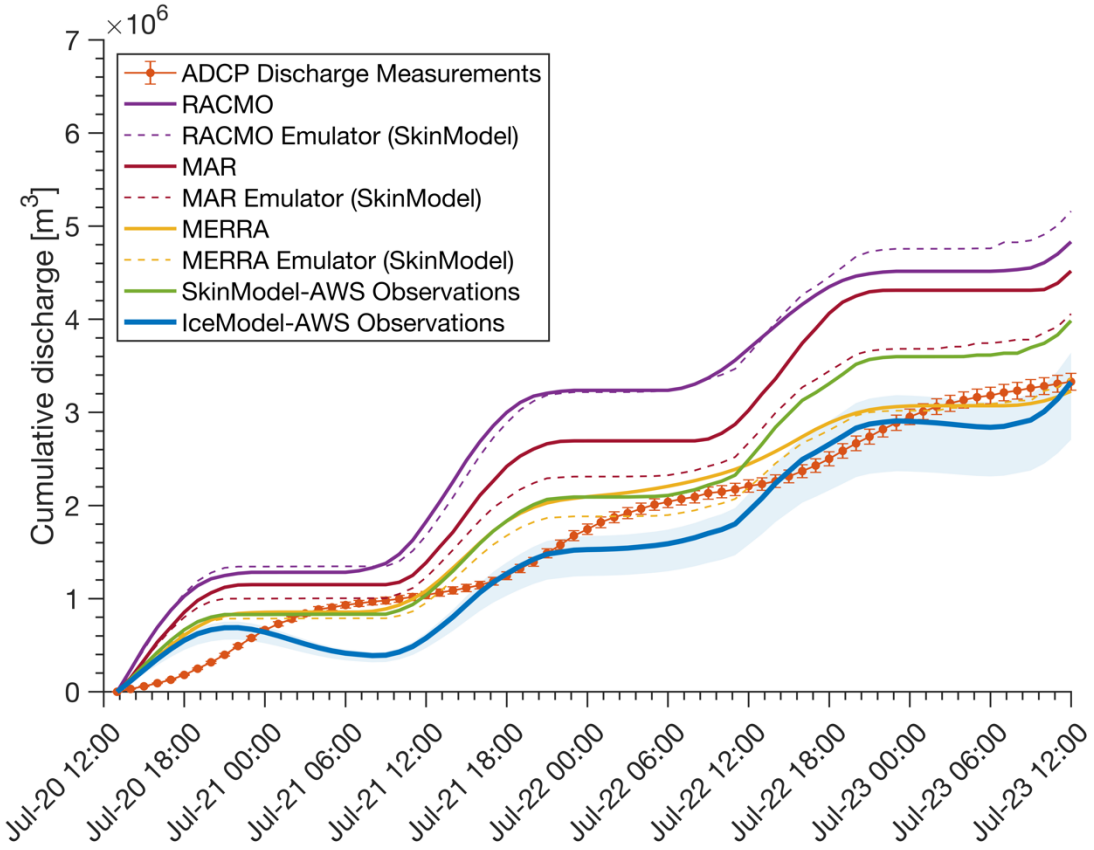

Figure S4-11. Model simulations of ice sheet surface meltwater runoff compared with direct measurements of ice sheet catchment discharge collected during the 20–23 July 2015 field experiment (Smith et al., 2017). During this field experiment, heavy cloud cover was present during the final ~24 h. The radiative effect of cloud cover contributes to enhanced spread between climate model simulations and the climate model emulator "SkinModel" which is forced with hourly meteorological variables recorded at the KAN-M automatic weather station. Regardless of these slight discrepancies, the one-dimensional ice column model IceModel reproduces observed discharge to within 1% cumulative, whereas two of three climate models overestimate runoff for this time and location. As with our 2016 experimental findings, MERRA-2 simulates lower runoff incidentally due to its low albedo (Figure S4-8).

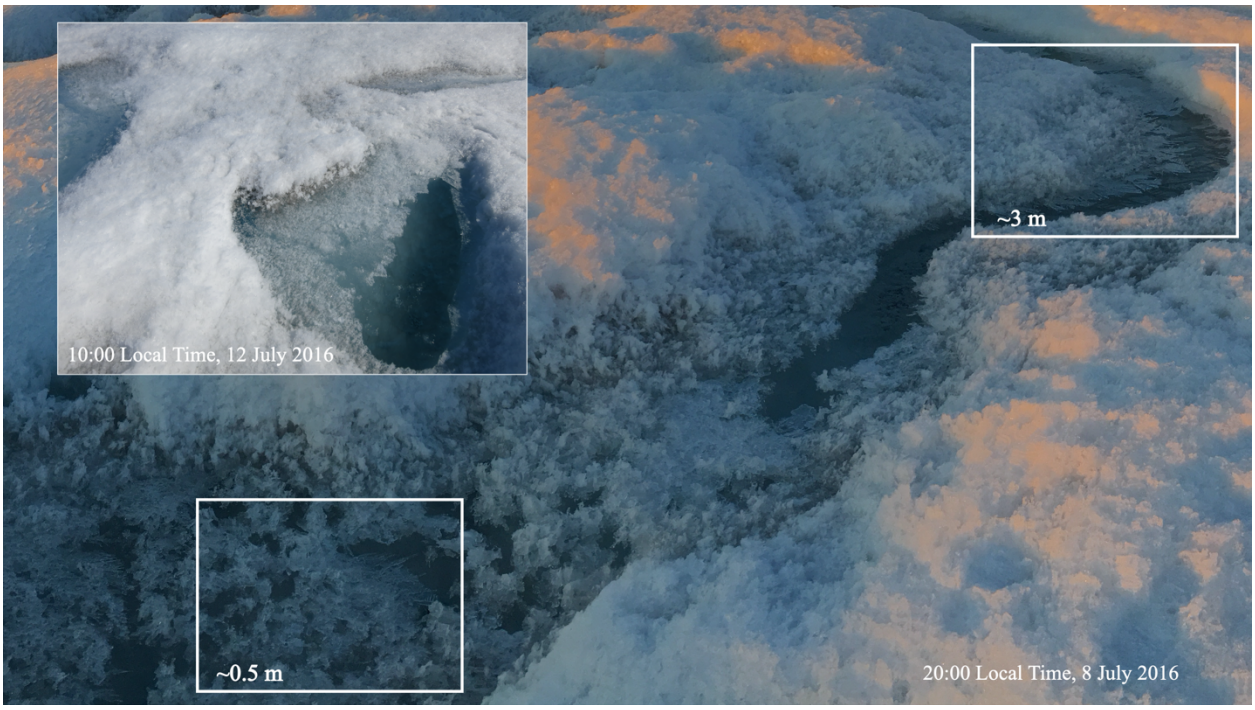

Figure S4-12. Photographs taken during the 06–13 July 2016 field experiment show refreezing of meltwater entrained on the weathered bare ice surface. Surficial meltwater refreezing of open water stored in surface depressions was observed at our field site at night and into the early morning when low sun angles and cold air kept surface temperatures below freezing. Photograph in upper left shows surficial refrozen meltwater persisting to ~10:00 local time on 12 July 2016 following the coldest night during the seven day field experiment as indicated by automatic weather station observations of air temperature (see Figure 4-2 in Main). Approximate scale is indicated by white boxes. Background photograph taken at ~20:00 local time on 08 July 2016. All photos were taken by the first author.

Figure S4-13. A network of twelve bamboo ablation stakes were randomly distributed across an ~0.5 km^2 area within the study catchment. The distance from the 8x8 inch wooden datum to the top of each stake was measured on a three-hourly schedule from 12:00 on 06 July 2016 to 21:00 on 12 July 2016. The board was oriented true north and 2–4 measurements were made from a line printed on the board to the number printed on top of each stake (visible in images at center and at right) to minimize local ablation rate variability. These distances are converted to cumulative surface lowering for comparison with simulated melt rates. Bright, white ice (center image) contrasts with dark ice (right image). White boxes show stake locations faintly visible in image background.

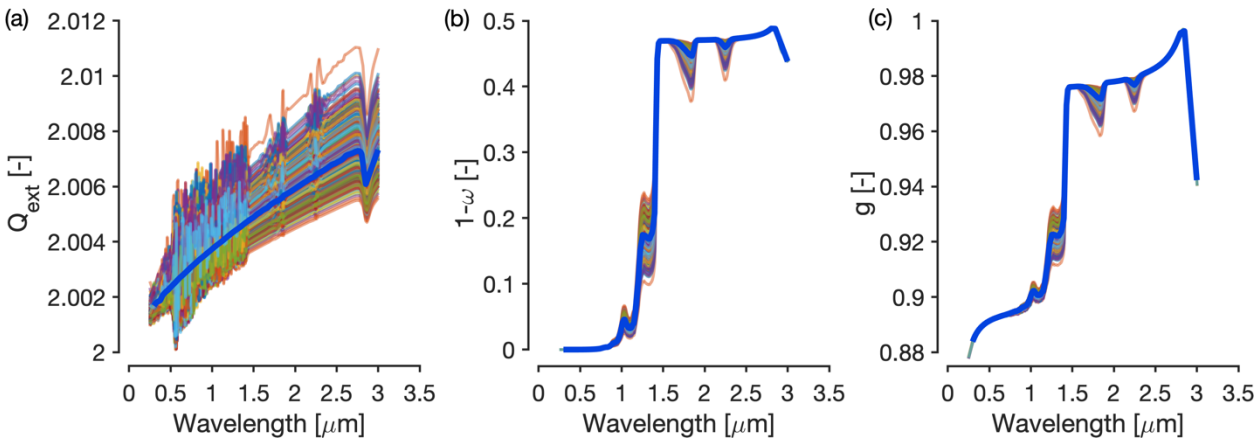

Figure S4-14. Values of (a) single-scattering extinction coefficient Q_{ext}, (b) single-scattering co-albedo $1 - \omega$, and (c) asymmetry parameter g, calculated with Mie scattering algorithms for an ensemble of grain sizes (N=1000) randomly drawn from a normal distribution with mean value 2.0 mm and standard deviation 0.3 mm. These single-scattering properties describe the extinction of shortwave radiation by individual spherical particles (here ice grains) due to absorption and scattering. The mean values of each ensemble (thick blue lines) at 118 spectral bands that span the solar spectrum (here 0.3–3.03 μm) are used to calculate spectral flux extinction coefficients (Equation S13), which describe the extinction by absorption and scattering of shortwave radiation by a volume of ice grains having an effective optical radius equivalent to the grain radius used for the Mie scattering calculations.

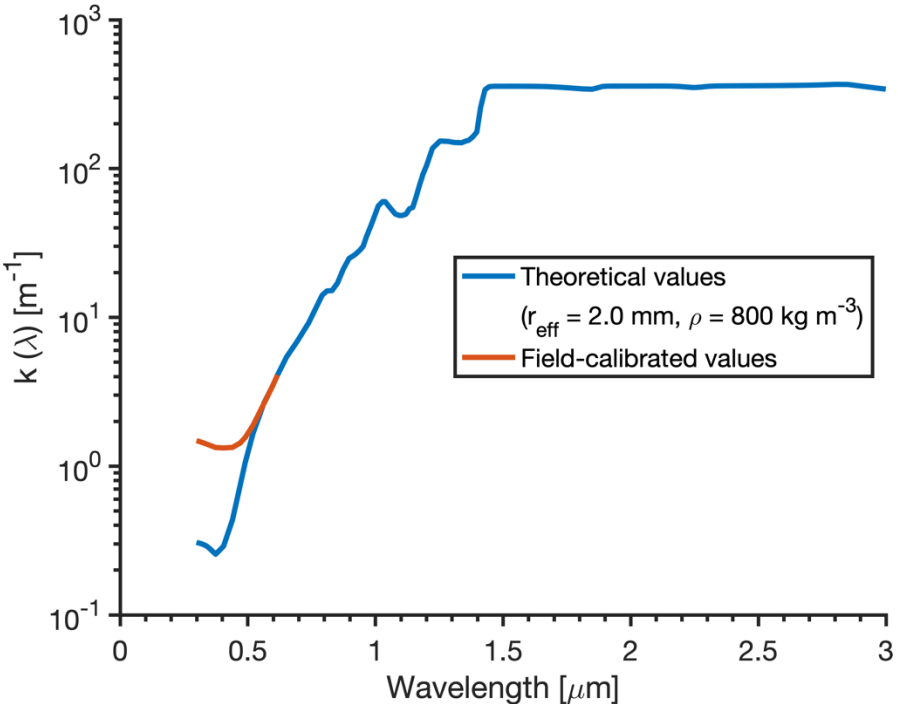

Figure S4-15. Values of spectral flux extinction coefficient, $k(\lambda)$, for an ice volume with effective optical grain radius $r_{\text{eff}} = 2.0 \pm 0.3$ mm and bulk density $\rho = 800$ kg m^{-3}, calculated with Equation S13 (theoretical values) using the single scattering properties in Figure S4-14, and field-calibrated values calculated with Equation S14 using ice absorption coefficient values obtained from measurements of solar flux attenuation in glacier ice in the Greenland Ice Sheet ablation zone (Cooper et al., 2020). The higher values in the spectral region 0.3–0.7 μm are caused by dark impurities present within the ice column in the Greenland Ice Sheet ablation zone.

6.2 Supplementary Methods

6.2.1 Description of IceModel numerical model

Ice temperature, meltwater production, and refreezing are calculated using a one-dimensional coupled model of mass and heat transport:

$$C_{\mathrm{v}} \frac{\partial T_{\mathrm{i}}}{\partial t} - \rho_{\mathrm{i}} L_{\mathrm{f}} \frac{\partial \theta_{\mathrm{i}}}{\partial t} = \frac{\partial}{\partial z}\left[(k_{\mathrm{i}} + k_{\mathrm{v}}) \frac{\partial T_{\mathrm{i}}}{\partial z}\right] - \frac{\partial q}{\partial z} - v_{\mathrm{i}} C_{\mathrm{p}} \frac{\partial T_{\mathrm{i}}}{\partial z} \quad \text{(S1)}$$

where ρ_{i} [kg m^{-3}] is solid ice density, C_{v} [J m^{-3} K^{-1}] is volumetric specific heat capacity, T_{i} [K] is ice temperature, L_{f} [J kg^{-1}] is the latent heat of fusion of ice, θ_{i} [m^3 m^{-3}] is volumetric ice content, z [m] is distance in the vertical dimension, $\partial \mathrm{q} / \partial \mathrm{z}$ [W m^{-3}] is the net solar flux divergence, and v_{i} [m s^{-1}] is the ice surface ablation rate. The model updates an earlier version (Liston et al., 1999a) with new values for the spectral absorption coefficient of ice (Warren and Brandt, 2008) and a deforming numerical grid that permits inclusion of the advection term v_{i} following Jordan (1991).

Changes in enthalpy associated with heat gained or lost by melting and refreezing of liquid water are governed by changes in ice content, where a decrease in ice content is equivalent to an increase in water content:

$$\frac{\partial \theta_{\mathrm{w}}}{\partial t} = -\frac{\partial \theta_{\mathrm{i}}}{\partial t} \quad \text{(S2)}$$

and an increase in air content θ_{a} [m^3 m^{-3}] is equivalent to a decrease in ice content scaled by volume expansion:

$$\frac{\partial \theta_{\mathrm{a}}}{\partial t} = -\frac{\partial \theta_{\mathrm{i}}}{\partial t} \frac{\rho_{\mathrm{w}}}{\rho_{\mathrm{i}}}. \quad \text{(S3)}$$

The ice thermal conductivity, k_{i} [W m^{-1} K^{-1}], is given by Calonne et al. (2019):

$$k_{\mathrm{i}} = 2.107 + 0.003618(\rho - \rho_{\mathrm{i}}) \quad \text{(S4)}$$

where the volumetric ice density ρ and solid ice density ρ_{i} are in units of kg m^{-3}. The latent heat flux coefficient, k_{v}, accounts for water vapor diffusion within the ice matrix air passages, and is defined by:

$$k_{\mathrm{v}} = \frac{D_{\mathrm{e}} L_{\mathrm{s}}}{R_{\mathrm{v}} T_{\mathrm{i}}} \frac{de_{\mathrm{si}}}{dT_{\mathrm{i}}} \quad \text{(S5)}$$

where L_s [J kg^{-1}] is the latent heat of sublimation, R_v [J kg^{-1} K^{-1}] is the gas constant for water vapor, the water vapor diffusivity, D_e [m^2 s^{-1}] is given by Anderson, (1976):

$$D_e = 9.0 \times 10^{-5} \left(\frac{T_i}{273.16}\right)^{14} \tag{S6}$$

and the saturation vapor pressure over ice e_{si} (Pa) is defined according to Murray (1967):

$$e_{si} = 610.78 \exp\left[\frac{21.875(T_i - 273.16)}{T_i - 7.66}\right] \tag{S7}$$

where T_i is in [K].

When meltwater is contained within the ice matrix, k_i is replaced with k_{iw}:

$$k_{iw} = \theta_i k_i + \theta_w k_w \tag{S8}$$

and $C_v = C_s/\rho_s$ is updated according to:

$$C_s = \theta_i C_i + \theta_w C_w + \theta_a C_a \tag{S9}$$

where C_i, C_w, and C_a [J kg^{-1} K^{-1}] are the specific heat capacities of pure ice, water, and air, respectively, and ρ_s [kg m^{-3}] is the ice matrix bulk density:

$$\rho_s = \theta_i \rho_i + \theta_w \rho_w + \theta_a \rho_a. \tag{S10}$$

The residual liquid water content of the ice matrix is set to 2% following Pettersson et al. (2004).

6.2.2 Treatment of subsurface absorbed solar radiation

The solar radiation source term $\partial q/\partial z$ is evaluated using the two-stream radiative transfer model described by Schlatter (1972). During model setup, spectral flux extinction coefficients are computed for 118 spectral bands using a prescribed grain size of 2.0 ± 0.3 mm. The single-scattering extinction coefficient Q_{ext}, single-scattering co-albedo $1 - \omega$, and asymmetry parameter g, are computed as functions of grain size using Mie scattering algorithms provided as MATLAB code by Mätzler (2002) and the complex index of refraction of pure ice from Warren and Brandt (2008). These single-scattering properties are estimated as mean values of an ensemble constructed from N=1000 random draws from a normal distribution representing the grain size of glacier ice ($\mu = 2.0 \pm 0.3$ mm) (Figure S4-14). This procedure accounts for

random variations in grain size within the ice matrix and smooths numerical oscillations associated with Bessel functions used in the Mie solution algorithms (Bohren and Huffman, 2007). The entire N=1000 distribution set and mean values identical to those used in this study are publicly available (https://github.com/mguycooper/ice_optics).

To solve the two-stream model, the spectral flux extinction coefficients are applied to a downwelling solar irradiance profile for an Arctic mid-winter atmosphere that is interpolated to the 118 spectral bands. At the start of each model timestep, the two-stream model is solved using the observed broadband albedo as an upper boundary condition. The spectral flux extinction coefficients are combined with the modeled ice and liquid water fraction of each vertical layer to compute an effective bulk extinction coefficient:

$$K(z) = \Theta_{\mathrm{m}}(z) \times \eta(z) \tag{S11}$$

where $\Theta_{\mathrm{m}} = \theta_{\mathrm{w}} + \theta_{\mathrm{i}} \times \rho_{\mathrm{i}}/\rho_{\mathrm{w}}$ is the total equivalent liquid water content of the layer. The bulk extinction coefficient, $\eta(z)$, is calculated following Brandt and Warren, (1993):

$$\eta(z) = -\frac{1}{\Delta z} ln\left[\frac{\int Q_{\lambda}^{\downarrow}(0)\, \exp[-k_{\lambda}(z+dz)]\, d\lambda}{\int Q_{\lambda}^{\downarrow}(0)\, \exp[-k_{\lambda}(z)]\, d\lambda}\right] \tag{S12}$$

where $Q_{\lambda}^{\downarrow}(0)$ is the incoming spectral irradiance at the ice surface and k_{λ} is the spectral flux extinction coefficient for wavelength λ:

$$k(\lambda) = \frac{3}{4}\frac{Q_{\mathrm{ext}}(\lambda)}{r_{\mathrm{eff}}}\sqrt{\big(1-\omega(\lambda)\big)\big(1-g(\lambda)\omega(\lambda)\big)}. \tag{S13}$$

An additional model option allows the $k(\lambda)$ values from Equation S13 to be scaled by a user-defined absorption coefficient profile following Equation 15 of Warren et al. (2006):

$$k(\lambda) = k(\lambda_o)\sqrt{\frac{k_{\mathrm{abs}}(\lambda)}{k_{\mathrm{abs}}(\lambda_o)}}, \qquad 300 < \lambda < 700 \tag{S14}$$

where $\lambda_{\mathrm{o}} = 600$ nm is a reference wavelength at which absorption is dominated by ice, rather than organic or inorganic material within the ice. The relation is valid within the stated spectral range, wherein $\omega(\lambda)$ varies so little as to be effectively independent of wavelength (see Figure S4-14b). When Equation S14 is

applied to $k_{\mathrm{abs}}(\lambda)$ values that include the effect of absorption by impurities, the values of $k(\lambda)$ provided by Equation S13 will be appropriately scaled to represent the enhanced absorption. Impurities found on Greenland's ablating ice surface such as algae, cyanobacteria, and black carbon affect absorption within this spectral region.

In this study, values for $k_{\mathrm{abs}}(\lambda)$ used as input to Equation S14 were obtained from measurements of flux attenuation ($\partial \mathrm{q}/\,\partial \mathrm{z}$) within glacier ice in Greenland's ablation zone (Cooper et al., 2020). These values therefore capture the net effect of impurities present within Greenland's ablating bare ice. An example spectral extinction coefficient profile for an ice volume having an effective optical grain radius $r_{\mathrm{eff}} = 2.0$ mm and bulk volumetric ice density of 800 kg m^{-3}, calculated with Equation S13 and Equation S14 is shown in Figure S4-15. The enhanced absorption of visible-wavelength light due to organic and inorganic light absorbing particles present in Greenland's melting glacier ice is demonstrated by the higher values of $k(\lambda)$ from 0.3–0.6 um.

The key aspects of our methodology are summarized as follows. First, the total shortwave radiation absorbed by the ice is prescribed by observed values of broadband albedo and incoming shortwave radiation recorded by the KAN-M automatic weather station. These values are recorded on an hourly schedule, which dictates the model timestep. Variability in albedo caused by solar zenith angle is therefore captured. Second, the vertical distribution of absorbed shortwave radiation within the ice column is calculated using the two-stream radiative transfer model. As input to this model, the spectral variation in both incoming shortwave radiation and the spectral absorption properties of the ice column are specified by the single scattering properties (Figure S4-14) and by Equation S13. The spectrally-dependent enhancement of energy absorption by dark impurities within the ice is further constrained by Equation S14. The output of this procedure is a field-calibrated spectral extinction coefficient profile for glacier ice (Figure S4-15), which is then converted to a bulk (depth-dependent, spectrally-integrated) extinction coefficient using Equation S12, which is further coupled to the evolving ice and liquid water fractions of the ice column with Equation S11.

6.2.3 Numerical implementation

The general numerical solution uses one-dimensional finite volume discretization, fully implicit time stepping, and a fixed grid with enthalpy and mass-conserving thin-layer refinement at the upper boundary (Jordan, 1991). The spectral model is discretized at 1 mm vertical grid resolution to 12 m depth. The two-stream solution follows Appendix 1 of Schlatter (1972). A tri-diagonal matrix solver is used to obtain values for $\partial \mathrm{q} / \partial \mathrm{z}$ at each 1 mm layer. These values are interpolated to the thermal grid, which is discretized at 2 cm vertical grid resolution to 20 m depth.

The thermal model is solved using the finite control volume method (Patankar, 1980). Changes in heat capacity associated with the evolving ice, air, and liquid water fractions and their impact on the effective thermal conductivity ($k_\mathrm{i} + k_\mathrm{v}$; Equation S1) are updated at the end of each timestep. As with the spectral model, a tri-diagonal matrix solver is used to obtain values for T_i.

The upper boundary condition for Equation S1 is the ice surface temperature T_sfc, which is initially unknown. To estimate it, a surface energy budget is constructed that takes the following form:

$$\chi(1-\alpha)Q_\mathrm{si} + Q_\mathrm{li} - \epsilon\sigma T_\mathrm{sfc}^4 + Q_\mathrm{h} + Q_\mathrm{e} + Q_\mathrm{c} = Q_\mathrm{m} \tag{S15}$$

where χ [-] allocates the incoming shortwave solar radiation Q_si [W m^{-2}] into its surface component and its subsurface component, α [-] is ice surface albedo, Q_li [W m^{-2}] is incoming longwave radiation, $\epsilon\sigma T_\mathrm{sfc}^4$ [W m^{-2}] is longwave radiation emitted by the ice surface, ϵ [-] is the ice surface emissivity, σ [W m^{-2} K^{-4}] is the Stefan-Boltzmann constant, T_sfc [K] is the ice surface temperature, Q_h [W m^{-2}] is the sensible heat flux, Q_e [W m^{-2}] is the latent heat flux, Q_c [W m^{-2}] is the conductive heat flux, and Q_m [W m^{-2}] is energy available for meltwater production. The standard bulk aerodynamic methods used to obtain Q_h and Q_e are described in Liston et al. (1999a).

The bottom boundary condition for Equation S1 is:

$$\left.\frac{dT_\mathrm{i}}{dz}\right|_{z_\mathrm{max}} = 0.0 \tag{S16}$$

where $z_{\max}$ is taken to be 20.0 m and the model is initialized with $T_{\mathrm{i}}(z_{\max}) = -8.0°\mathrm{C}$ based on observations of ice temperature at site T-14 (Figure S4-5) (Hills et al., 2018).

To solve Equation S15, each term is cast in a form that leaves T_{sfc} as the only unknown, and the Newton-Raphson method is used to find the value of T_{sfc} that minimizes Q_{m}. If the resulting value for T_{sfc} is greater than 0°C, then its value is converted to melt energy, T_{sfc} is set to 0.0, and the flux terms that have T_{sfc} as input are evaluated. If T_{sfc} is less than 0°C, then the energy deficit available to freeze liquid water is computed.

As part of the numerical grid refinement process, if the ice thickness of the topmost layer is less than 1 mm it is combined with the layer below. The two layers are combined by adding their ice and liquid water mass and updating the bulk density and thermodynamic properties using the combination formulas in Jordan et al. (1991) (Equations 136–139).

Operator splitting is used to sequentially obtain solutions to the coupled radiative, thermodynamic, and hydrologic conservation equations (Clark et al., 2015). Within a timestep, the surface energy balance is computed, followed by the numerical thermodynamic equation, the melt and freeze calculations, and the hydraulic redistribution. The ice, air, and liquid volumetric fractions are then updated based on phase change and hydraulic redistribution, and a new enthalpy profile is computed to account for release and consumption of latent heat, followed by new profiles of specific heat capacity, thermal conductivity, and vapor diffusivity, which are used in the following time step.

The model uses mixture theory (Jordan, 1991), where the mass fraction of each individual control volume is composed of partial fractions of ice, liquid water, and air:

$$\gamma_{\mathrm{k}} = \theta_{\mathrm{k}} \rho_{\mathrm{k}} \tag{S17}$$

where θ_{k} [$\mathrm{m^3\,m^{-3}}$], γ_{k} [$\mathrm{kg\,m^{-3}}$] and ρ_{k} [$\mathrm{kg\,m^{-3}}$] are respectively the partial volume fraction, partial density, and intrinsic density of constituent k.

The sum of the volume fractions is unity:

$$\sum_{k} \theta_{\mathrm{k}} = 1 \tag{S18}$$

and the sum of the bulk densities is the total density:

$$\rho_{\mathrm{t}} = \sum_{\mathrm{k}} \theta_{\mathrm{k}} \rho_{\mathrm{k}} = \sum_{\mathrm{k}} \gamma_{\mathrm{k}} \,. \tag{S19}$$

The snow density ρ_{s} is the combined liquid water and ice bulk densities i.e. $\rho_{\mathrm{s}} \cong \gamma_{\mathrm{l}} + \gamma_{\mathrm{i}}$.

Porosity is the ratio of pore volume to total volume [$\mathrm{m^3\,m^{-3}}$]:

$$\phi = 1 - \theta_{\mathrm{i}} = 1 - \frac{\gamma_{\mathrm{i}}}{\rho_{\mathrm{i}}} \tag{S20}$$

The volume fractions can also be expressed in terms of the porosity and the liquid saturation s, or the volume of liquid water per unit volume of voids [$\mathrm{m^3\,m^{-3}}$]:

$$\theta_{\mathrm{i}} = 1 - \phi \tag{S21}$$

$$\theta_{\mathrm{l}} = s\phi$$

$$\theta_{\mathrm{a}} = \phi - s\phi$$

The liquid saturation s is set equal to the residual liquid water holding capacity 2% following Pettersson et al. (2004) for the upper layer. Below this layer, liquid water that exceeds ϕ is drained into the layer below. If a sub-freezing layer is encountered, the liquid water is instantaneously drained from the ice column. Note that volume expansion due to freezing reduces ϕ and therefore expels liquid water.

Appendix A

Table A-1. Estimates of attenuation coefficient, absorption coefficient, and scattering coefficient obtained from solar flux transmission measurements in glacier ice (Cooper et al., 2020). Coefficient values are in units of solid ice-equivalent referenced to in-situ measured ice density 835 kg m^3. Also given are values for one standard error in the linear regression coefficient and the coefficient of determination (r^2) for k_{att}, and one standard error in the k_{abs} estimate.

wavelength	k_{att}	standard error (k_{att})	r^2	k_{abs}	standard error (k_{abs})	k_{sca}
(nm)	(m^{-1})	(m^{-1})	(-)	(m^{-1})	(m^{-1})	(m^{-1})
350	1.049	0.043	0.998	0.0222	-0.00064	1.036
351	1.013	0.028	0.999	0.0204	-0.00059	0.992
352	0.978	0.013	1.000	0.0186	-0.00054	0.947
353	0.979	0.043	0.997	0.0191	-0.00055	0.960
354	1.022	0.041	0.997	0.0202	-0.00059	0.987
355	0.936	0.027	0.999	0.0181	-0.00052	0.935
356	0.892	0.085	0.985	0.0159	-0.00046	0.878
357	0.959	0.037	0.998	0.0179	-0.00052	0.930
358	0.937	0.030	0.998	0.0178	-0.00052	0.928
359	0.960	0.010	1.000	0.0184	-0.00053	0.943
360	0.948	0.046	0.996	0.0179	-0.00052	0.930
361	0.938	0.056	0.994	0.0183	-0.00053	0.941
362	0.946	0.030	0.998	0.0179	-0.00052	0.929
363	0.943	0.029	0.998	0.0175	-0.00051	0.921
364	0.940	0.022	0.999	0.0175	-0.00051	0.921
365	0.937	0.024	0.999	0.0175	-0.00051	0.920
366	0.934	0.025	0.999	0.0175	-0.00051	0.919
367	0.908	0.011	1.000	0.0167	-0.00048	0.899
368	0.921	0.031	0.998	0.0169	-0.00049	0.906
369	0.934	0.011	1.000	0.0175	-0.00051	0.920
370	0.916	0.024	0.999	0.0169	-0.00049	0.904
371	0.922	0.011	1.000	0.0170	-0.00049	0.908
372	0.931	0.027	0.999	0.0174	-0.00050	0.916
373	0.925	0.018	0.999	0.0169	-0.00049	0.904
374	0.935	0.017	0.999	0.0174	-0.00050	0.918
375	0.921	0.018	0.999	0.0167	-0.00048	0.900
376	0.921	0.023	0.999	0.0167	-0.00048	0.900

377	0.924	0.022	0.999	0.0170	-0.00049	0.908
378	0.919	0.022	0.999	0.0168	-0.00049	0.902
379	0.923	0.025	0.999	0.0169	-0.00049	0.905
380	0.910	0.017	0.999	0.0165	-0.00048	0.893
381	0.918	0.018	0.999	0.0167	-0.00048	0.900
382	0.914	0.013	1.000	0.0162	-0.00047	0.885
383	0.900	0.011	1.000	0.0162	-0.00047	0.887
384	0.912	0.020	0.999	0.0164	-0.00048	0.892
385	0.921	0.022	0.999	0.0169	-0.00049	0.905
386	0.893	0.030	0.998	0.0160	-0.00046	0.881
387	0.894	0.040	0.997	0.0160	-0.00046	0.881
388	0.880	0.033	0.998	0.0157	-0.00045	0.872
389	0.905	0.020	0.999	0.0163	-0.00047	0.889
390	0.897	0.013	1.000	0.0161	-0.00047	0.883
391	0.914	0.014	1.000	0.0166	-0.00048	0.897
392	0.904	0.024	0.999	0.0160	-0.00046	0.881
393	0.882	0.016	0.999	0.0155	-0.00045	0.867
394	0.906	0.015	1.000	0.0165	-0.00048	0.893
395	0.895	0.012	1.000	0.0160	-0.00046	0.880
396	0.876	0.032	0.998	0.0153	-0.00044	0.862
397	0.893	0.012	1.000	0.0161	-0.00047	0.882
398	0.915	0.004	1.000	0.0167	-0.00048	0.900
399	0.904	0.012	1.000	0.0164	-0.00047	0.890
400	0.919	0.016	0.999	0.0167	-0.00048	0.900
401	0.923	0.015	1.000	0.0171	-0.00049	0.909
402	0.911	0.015	1.000	0.0166	-0.00048	0.895
403	0.920	0.015	1.000	0.0168	-0.00049	0.902
404	0.926	0.017	0.999	0.0169	-0.00049	0.903
405	0.896	0.012	1.000	0.0162	-0.00047	0.885
406	0.917	0.016	1.000	0.0168	-0.00049	0.901
407	0.909	0.016	0.999	0.0164	-0.00048	0.892
408	0.914	0.016	0.999	0.0167	-0.00048	0.899
409	0.920	0.019	0.999	0.0169	-0.00049	0.905
410	0.911	0.016	0.999	0.0167	-0.00048	0.898
411	0.918	0.009	1.000	0.0169	-0.00049	0.904
412	0.924	0.018	0.999	0.0170	-0.00049	0.908
413	0.915	0.011	1.000	0.0167	-0.00048	0.900
414	0.918	0.006	1.000	0.0170	-0.00049	0.908
415	0.914	0.011	1.000	0.0167	-0.00048	0.898
416	0.919	0.013	1.000	0.0169	-0.00049	0.904

417	0.914	0.016	1.000	0.0166	-0.00048	0.896
418	0.915	0.016	0.999	0.0167	-0.00048	0.900
419	0.913	0.015	1.000	0.0166	-0.00048	0.898
420	0.919	0.013	1.000	0.0169	-0.00049	0.905
421	0.921	0.017	0.999	0.0169	-0.00049	0.904
422	0.916	0.013	1.000	0.0167	-0.00048	0.900
423	0.924	0.010	1.000	0.0170	-0.00049	0.906
424	0.922	0.016	1.000	0.0170	-0.00049	0.907
425	0.917	0.024	0.999	0.0167	-0.00049	0.900
426	0.925	0.017	0.999	0.0171	-0.00049	0.909
427	0.917	0.016	1.000	0.0167	-0.00048	0.899
428	0.917	0.014	1.000	0.0167	-0.00048	0.899
429	0.914	0.015	1.000	0.0167	-0.00048	0.899
430	0.920	0.021	0.999	0.0169	-0.00049	0.903
431	0.929	0.011	1.000	0.0172	-0.00050	0.912
432	0.921	0.014	1.000	0.0169	-0.00049	0.904
433	0.918	0.012	1.000	0.0168	-0.00049	0.902
434	0.917	0.009	1.000	0.0167	-0.00048	0.900
435	0.918	0.017	0.999	0.0168	-0.00049	0.903
436	0.924	0.017	0.999	0.0171	-0.00049	0.909
437	0.916	0.020	0.999	0.0167	-0.00049	0.900
438	0.916	0.021	0.999	0.0169	-0.00049	0.904
439	0.930	0.013	1.000	0.0173	-0.00050	0.914
440	0.926	0.017	0.999	0.0171	-0.00050	0.910
441	0.929	0.014	1.000	0.0173	-0.00050	0.914
442	0.926	0.021	0.999	0.0171	-0.00050	0.910
443	0.923	0.015	1.000	0.0170	-0.00049	0.908
444	0.928	0.016	0.999	0.0172	-0.00050	0.911
445	0.924	0.020	0.999	0.0172	-0.00050	0.913
446	0.933	0.015	1.000	0.0174	-0.00050	0.917
447	0.932	0.015	1.000	0.0174	-0.00050	0.917
448	0.933	0.018	0.999	0.0173	-0.00050	0.915
449	0.932	0.018	0.999	0.0174	-0.00050	0.917
450	0.942	0.018	0.999	0.0177	-0.00051	0.925
451	0.941	0.019	0.999	0.0176	-0.00051	0.923
452	0.939	0.020	0.999	0.0175	-0.00051	0.921
453	0.941	0.017	0.999	0.0177	-0.00051	0.926
454	0.951	0.019	0.999	0.0181	-0.00052	0.934
455	0.948	0.021	0.999	0.0179	-0.00052	0.931
456	0.951	0.022	0.999	0.0180	-0.00052	0.933

457	0.950	0.015	1.000	0.0181	-0.00052	0.935
458	0.951	0.017	0.999	0.0181	-0.00052	0.935
459	0.958	0.017	0.999	0.0183	-0.00053	0.942
460	0.956	0.016	1.000	0.0183	-0.00053	0.940
461	0.952	0.018	0.999	0.0181	-0.00053	0.936
462	0.968	0.018	0.999	0.0187	-0.00054	0.951
463	0.968	0.018	0.999	0.0187	-0.00054	0.949
464	0.964	0.019	0.999	0.0186	-0.00054	0.948
465	0.971	0.019	0.999	0.0188	-0.00055	0.954
466	0.971	0.021	0.999	0.0188	-0.00055	0.954
467	0.979	0.018	0.999	0.0191	-0.00055	0.959
468	0.975	0.022	0.999	0.0190	-0.00055	0.959
469	0.982	0.023	0.999	0.0193	-0.00056	0.965
470	0.993	0.020	0.999	0.0196	-0.00057	0.973
471	0.996	0.021	0.999	0.0196	-0.00057	0.974
472	1.001	0.018	0.999	0.0199	-0.00058	0.981
473	1.001	0.020	0.999	0.0200	-0.00058	0.983
474	1.005	0.024	0.999	0.0202	-0.00058	0.987
475	1.011	0.023	0.999	0.0204	-0.00059	0.991
476	1.012	0.022	0.999	0.0205	-0.00059	0.993
477	1.019	0.024	0.999	0.0207	-0.00060	1.000
478	1.023	0.025	0.999	0.0209	-0.00061	1.004
479	1.027	0.024	0.999	0.0212	-0.00061	1.010
480	1.029	0.023	0.999	0.0211	-0.00061	1.010
481	1.030	0.024	0.999	0.0212	-0.00061	1.011
482	1.041	0.027	0.999	0.0216	-0.00063	1.021
483	1.042	0.024	0.999	0.0218	-0.00063	1.025
484	1.048	0.028	0.999	0.0220	-0.00064	1.029
485	1.049	0.027	0.999	0.0220	-0.00064	1.029
486	1.051	0.022	0.999	0.0220	-0.00064	1.030
487	1.061	0.024	0.999	0.0225	-0.00065	1.040
488	1.069	0.026	0.999	0.0228	-0.00066	1.048
489	1.072	0.027	0.999	0.0229	-0.00066	1.051
490	1.079	0.026	0.999	0.0233	-0.00067	1.058
491	1.087	0.029	0.999	0.0235	-0.00068	1.064
492	1.083	0.026	0.999	0.0235	-0.00068	1.064
493	1.093	0.026	0.999	0.0239	-0.00069	1.072
494	1.102	0.030	0.999	0.0243	-0.00070	1.080
495	1.100	0.035	0.998	0.0243	-0.00070	1.081
496	1.115	0.032	0.999	0.0248	-0.00072	1.091

497	1.119	0.032	0.999	0.0250	-0.00072	1.096
498	1.122	0.032	0.999	0.0251	-0.00073	1.099
499	1.132	0.032	0.999	0.0255	-0.00074	1.107
500	1.134	0.034	0.998	0.0257	-0.00075	1.112
501	1.142	0.030	0.999	0.0261	-0.00076	1.119
502	1.154	0.030	0.999	0.0266	-0.00077	1.130
503	1.157	0.032	0.999	0.0267	-0.00077	1.131
504	1.161	0.032	0.999	0.0271	-0.00078	1.139
505	1.171	0.032	0.999	0.0274	-0.00079	1.147
506	1.175	0.034	0.999	0.0276	-0.00080	1.150
507	1.186	0.035	0.999	0.0281	-0.00081	1.160
508	1.197	0.030	0.999	0.0287	-0.00083	1.172
509	1.204	0.034	0.999	0.0289	-0.00084	1.177
510	1.209	0.035	0.999	0.0292	-0.00085	1.182
511	1.223	0.036	0.999	0.0298	-0.00086	1.195
512	1.226	0.036	0.999	0.0299	-0.00087	1.197
513	1.235	0.032	0.999	0.0305	-0.00088	1.207
514	1.245	0.036	0.999	0.0310	-0.00090	1.217
515	1.255	0.036	0.999	0.0314	-0.00091	1.226
516	1.258	0.039	0.998	0.0316	-0.00092	1.229
517	1.264	0.030	0.999	0.0321	-0.00093	1.239
518	1.270	0.032	0.999	0.0323	-0.00094	1.243
519	1.286	0.038	0.999	0.0331	-0.00096	1.256
520	1.297	0.035	0.999	0.0336	-0.00097	1.266
521	1.304	0.034	0.999	0.0340	-0.00098	1.273
522	1.314	0.035	0.999	0.0345	-0.00100	1.283
523	1.327	0.036	0.999	0.0352	-0.00102	1.295
524	1.337	0.042	0.998	0.0357	-0.00103	1.304
525	1.346	0.036	0.999	0.0361	-0.00105	1.312
526	1.348	0.038	0.999	0.0363	-0.00105	1.314
527	1.366	0.034	0.999	0.0373	-0.00108	1.332
528	1.376	0.041	0.999	0.0379	-0.00110	1.342
529	1.383	0.041	0.999	0.0382	-0.00111	1.348
530	1.393	0.040	0.999	0.0388	-0.00112	1.358
531	1.402	0.040	0.999	0.0394	-0.00114	1.369
532	1.419	0.039	0.999	0.0402	-0.00117	1.382
533	1.428	0.037	0.999	0.0408	-0.00118	1.391
534	1.440	0.040	0.999	0.0414	-0.00120	1.402
535	1.453	0.039	0.999	0.0422	-0.00122	1.415
536	1.461	0.041	0.999	0.0426	-0.00124	1.422

537	1.475	0.038	0.999	0.0435	-0.00126	1.436
538	1.486	0.041	0.999	0.0441	-0.00128	1.446
539	1.501	0.041	0.999	0.0450	-0.00130	1.459
540	1.507	0.042	0.999	0.0454	-0.00131	1.466
541	1.519	0.040	0.999	0.0462	-0.00134	1.478
542	1.533	0.045	0.999	0.0470	-0.00136	1.491
543	1.545	0.044	0.999	0.0477	-0.00138	1.501
544	1.560	0.041	0.999	0.0486	-0.00141	1.516
545	1.576	0.043	0.999	0.0495	-0.00143	1.528
546	1.586	0.044	0.999	0.0502	-0.00146	1.540
547	1.600	0.044	0.999	0.0512	-0.00148	1.554
548	1.614	0.043	0.999	0.0520	-0.00151	1.567
549	1.623	0.046	0.999	0.0526	-0.00152	1.575
550	1.641	0.046	0.999	0.0537	-0.00156	1.591
551	1.649	0.049	0.999	0.0546	-0.00158	1.604
552	1.664	0.048	0.999	0.0554	-0.00161	1.615
553	1.679	0.047	0.999	0.0564	-0.00163	1.628
554	1.699	0.050	0.999	0.0576	-0.00167	1.645
555	1.709	0.051	0.999	0.0583	-0.00169	1.655
556	1.720	0.050	0.999	0.0591	-0.00171	1.667
557	1.742	0.049	0.999	0.0604	-0.00175	1.684
558	1.749	0.050	0.999	0.0611	-0.00177	1.693
559	1.763	0.053	0.999	0.0621	-0.00180	1.706
560	1.776	0.054	0.998	0.0629	-0.00182	1.717
561	1.793	0.055	0.998	0.0641	-0.00186	1.734
562	1.802	0.053	0.999	0.0649	-0.00188	1.743
563	1.816	0.053	0.999	0.0660	-0.00191	1.757
564	1.831	0.051	0.999	0.0670	-0.00194	1.770
565	1.850	0.054	0.999	0.0684	-0.00198	1.787
566	1.861	0.055	0.999	0.0691	-0.00200	1.796
567	1.874	0.053	0.999	0.0703	-0.00203	1.811
568	1.891	0.058	0.998	0.0715	-0.00207	1.827
569	1.904	0.055	0.999	0.0725	-0.00210	1.839
570	1.925	0.059	0.998	0.0740	-0.00214	1.857
571	1.934	0.061	0.998	0.0746	-0.00216	1.865
572	1.958	0.058	0.999	0.0763	-0.00221	1.884
573	1.960	0.059	0.999	0.0769	-0.00223	1.892
574	1.981	0.060	0.998	0.0785	-0.00227	1.910
575	1.992	0.061	0.998	0.0793	-0.00230	1.920
576	2.013	0.062	0.998	0.0809	-0.00234	1.939

577	2.024	0.065	0.998	0.0817	-0.00237	1.948
578	2.042	0.065	0.998	0.0830	-0.00240	1.963
579	2.055	0.067	0.998	0.0848	-0.00246	1.983
580	2.068	0.068	0.998	0.0856	-0.00248	1.992
581	2.086	0.063	0.998	0.0869	-0.00252	2.007
582	2.106	0.063	0.999	0.0886	-0.00257	2.025
583	2.126	0.066	0.998	0.0900	-0.00261	2.041
584	2.140	0.069	0.998	0.0911	-0.00264	2.052
585	2.154	0.069	0.998	0.0928	-0.00269	2.071
586	2.175	0.066	0.998	0.0946	-0.00274	2.090
587	2.193	0.071	0.998	0.0961	-0.00278	2.106
588	2.208	0.070	0.998	0.0973	-0.00282	2.119
589	2.230	0.074	0.998	0.0991	-0.00287	2.137
590	2.252	0.077	0.998	0.1008	-0.00292	2.155
591	2.262	0.075	0.998	0.1026	-0.00297	2.173
592	2.286	0.077	0.998	0.1043	-0.00302	2.190
593	2.303	0.078	0.998	0.1061	-0.00307	2.208
594	2.322	0.075	0.998	0.1077	-0.00312	2.224
595	2.348	0.076	0.998	0.1101	-0.00319	2.247
596	2.366	0.078	0.998	0.1115	-0.00323	2.261
597	2.393	0.081	0.998	0.1143	-0.00331	2.288
598	2.403	0.078	0.998	0.1157	-0.00335	2.301
599	2.428	0.078	0.998	0.1179	-0.00341	2.322
600	2.451	0.076	0.998	0.1200	-0.00348	2.342
601	2.471	0.081	0.998	0.1219	-0.00353	2.359
602	2.485	0.077	0.998	0.1233	-0.00357	2.372
603	2.519	0.078	0.998	0.1264	-0.00366	2.400
604	2.538	0.082	0.998	0.1283	-0.00372	2.417
605	2.549	0.080	0.998	0.1300	-0.00377	2.433
606	2.571	0.078	0.998	0.1322	-0.00383	2.452
607	2.595	0.081	0.998	0.1346	-0.00390	2.473
608	2.622	0.084	0.998	0.1372	-0.00398	2.496
609	2.649	0.082	0.998	0.1399	-0.00405	2.519
610	2.667	0.083	0.998	0.1417	-0.00410	2.534
611	2.695	0.087	0.998	0.1441	-0.00417	2.554
612	2.703	0.083	0.998	0.1465	-0.00424	2.575
613	2.735	0.086	0.998	0.1497	-0.00434	2.601
614	2.771	0.088	0.998	0.1534	-0.00444	2.631
615	2.789	0.087	0.998	0.1554	-0.00450	2.647
616	2.812	0.092	0.998	0.1579	-0.00457	2.667

617	2.841	0.087	0.998	0.1608	-0.00466	2.690
618	2.872	0.091	0.998	0.1646	-0.00477	2.721
619	2.878	0.092	0.998	0.1666	-0.00483	2.736
620	2.909	0.094	0.998	0.1702	-0.00493	2.764
621	2.939	0.093	0.998	0.1726	-0.00500	2.782
622	2.983	0.099	0.998	0.1778	-0.00515	2.821
623	2.998	0.097	0.998	0.1795	-0.00520	2.834
624	3.046	0.098	0.998	0.1850	-0.00536	2.875
625	3.066	0.099	0.998	0.1870	-0.00542	2.889
626	3.102	0.096	0.998	0.1913	-0.00554	2.920
627	3.105	0.097	0.998	0.1929	-0.00559	2.932
628	3.142	0.102	0.998	0.1986	-0.00575	2.972
629	3.173	0.102	0.998	0.2013	-0.00583	2.991
630	3.201	0.104	0.998	0.2048	-0.00593	3.015
631	3.243	0.105	0.998	0.2101	-0.00608	3.051
632	3.287	0.106	0.998	0.2154	-0.00624	3.088
633	3.291	0.108	0.998	0.2155	-0.00624	3.088
634	3.335	0.106	0.998	0.2217	-0.00642	3.129
635	3.365	0.110	0.998	0.2244	-0.00650	3.147
636	3.365	0.105	0.998	0.2271	-0.00658	3.165
637	3.405	0.111	0.998	0.2320	-0.00672	3.197
638	3.432	0.114	0.998	0.2356	-0.00682	3.220
639	3.457	0.109	0.998	0.2387	-0.00692	3.240
640	3.481	0.109	0.998	0.2422	-0.00701	3.261
641	3.551	0.113	0.998	0.2511	-0.00727	3.317
642	3.547	0.113	0.998	0.2519	-0.00730	3.322
643	3.585	0.113	0.998	0.2566	-0.00743	3.350
644	3.604	0.108	0.999	0.2595	-0.00752	3.368
645	3.624	0.117	0.998	0.2636	-0.00763	3.392
646	3.643	0.115	0.998	0.2652	-0.00768	3.402
647	3.697	0.121	0.998	0.2727	-0.00790	3.447
648	3.736	0.125	0.998	0.2787	-0.00807	3.482
649	3.746	0.120	0.998	0.2803	-0.00812	3.491
650	3.767	0.123	0.998	0.2833	-0.00821	3.508
651	3.797	0.121	0.998	0.2874	-0.00832	3.531
652	3.830	0.128	0.998	0.2916	-0.00845	3.555
653	3.865	0.129	0.998	0.2969	-0.00860	3.584
654	3.886	0.131	0.998	0.2996	-0.00868	3.600
655	3.939	0.138	0.998	0.3098	-0.00897	3.656
656	3.897	0.126	0.998	0.3046	-0.00882	3.627

657	3.908	0.117	0.999	0.3087	-0.00894	3.650
658	3.972	0.127	0.998	0.3148	-0.00912	3.683
659	4.001	0.129	0.998	0.3198	-0.00926	3.710
660	4.064	0.140	0.998	0.3298	-0.00955	3.763
661	4.027	0.128	0.998	0.3238	-0.00938	3.731
662	4.072	0.134	0.998	0.3309	-0.00958	3.768
663	4.092	0.132	0.998	0.3345	-0.00969	3.788
664	4.076	0.128	0.998	0.3331	-0.00965	3.780
665	4.163	0.140	0.998	0.3432	-0.00994	3.832
666	4.157	0.135	0.998	0.3437	-0.00996	3.835
667	4.123	0.128	0.998	0.3423	-0.00992	3.828
668	4.147	0.129	0.998	0.3446	-0.00998	3.839
669	4.181	0.131	0.998	0.3503	-0.01015	3.869
670	4.229	0.142	0.998	0.3565	-0.01033	3.900
671	4.177	0.122	0.999	0.3494	-0.01012	3.864
672	4.257	0.139	0.998	0.3620	-0.01049	3.927
673	4.240	0.130	0.998	0.3591	-0.01040	3.913
674	4.293	0.138	0.998	0.3679	-0.01066	3.956
675	4.345	0.148	0.998	0.3749	-0.01086	3.991
676	4.338	0.140	0.998	0.3740	-0.01083	3.986
677	4.353	0.141	0.998	0.3756	-0.01088	3.994
678	4.364	0.137	0.998	0.3828	-0.01109	4.029
679	4.340	0.135	0.998	0.3798	-0.01100	4.014
680	4.436	0.147	0.998	0.3914	-0.01134	4.070
681	4.391	0.140	0.998	0.3884	-0.01125	4.056
682	4.366	0.132	0.998	0.3815	-0.01105	4.023
683	4.540	0.159	0.998	0.4107	-0.01190	4.160
684	4.454	0.143	0.998	0.3986	-0.01155	4.104
685	4.559	0.151	0.998	0.4167	-0.01207	4.188
686	4.599	0.160	0.998	0.4212	-0.01220	4.208
687	4.475	0.137	0.998	0.4008	-0.01161	4.114
688	4.596	0.148	0.998	0.4216	-0.01221	4.210
689	4.626	0.146	0.998	0.4278	-0.01239	4.238
690	4.650	0.151	0.998	0.4344	-0.01258	4.268
691	4.729	0.165	0.998	0.4412	-0.01278	4.297
692	4.611	0.136	0.999	0.4306	-0.01247	4.250
693	4.790	0.168	0.998	0.4542	-0.01316	4.355
694	4.558	0.123	0.999	0.4288	-0.01242	4.241
695	4.832	0.162	0.998	0.4683	-0.01357	4.415
696	4.837	0.149	0.998	0.4714	-0.01366	4.428

697	4.850	0.156	0.998	0.4791	-0.01388	4.461
698	4.922	0.157	0.998	0.4951	-0.01434	4.527
699	5.060	0.182	0.998	0.4996	-0.01447	4.545
700	5.021	0.159	0.998	0.5027	-0.01456	4.559

Bibliography

Abdalati, W. and Steffen, K.: Passive microwave-derived snow melt regions on the Greenland Ice Sheet, Geophys. Res. Lett., 22(7), 787–790, doi:10.1029/95GL00433, 1995.

Abdalati, W. and Steffen, K.: The apparent effects of the Mt. Pinatubo Eruption on the Greenland Ice Sheet melt extent, Geophys. Res. Lett., 24(14), 1795–1797, doi:10.1029/97GL01706, 1997.

Abdalati, W. and Steffen, K.: Greenland Ice Sheet melt extent: 1979–1999, J. Geophys. Res. Atmospheres, 106(D24), 33983–33988, doi:10.1029/2001JD900181, 2001.

Abdalati, W., Zwally, H. J., Bindschadler, R., Csatho, B., Farrell, S. L., Fricker, H. A., Harding, D., Kwok, R., Lefsky, M., Markus, T., Marshak, A., Neumann, T., Palm, S., Schutz, B., Smith, B., Spinhirne, J. and Webb, C.: The ICESat-2 Laser Altimetry Mission, Proc. IEEE, 98(5), 735–751, doi:10.1109/JPROC.2009.2034765, 2010.

Abshire, J. B., Sun, X., Riris, H., Sirota, J. M., McGarry, J. F., Palm, S., Yi, D. and Liiva, P.: Geoscience Laser Altimeter System (GLAS) on the ICESat Mission: On-orbit measurement performance, Geophys. Res. Lett., 32(21), L21S02, doi:10.1029/2005GL024028, 2005.

Ackermann, M., Ahrens, J., Bai, X., Bartelt, M., Barwick, S. W., Bay, R. C., Becka, T., Becker, J. K., Becker, K.-H., Berghaus, P., Bernardini, E., Bertrand, D., Boersma, D. J., Böser, S., Botner, O., Bouchta, A., Bouhali, O., Burgess, C., Burgess, T., Castermans, T., Chirkin, D., Collin, B., Conrad, J., Cooley, J., Cowen, D. F., Davour, A., Clercq, C. D., Heros, C. P. de los, Desiati, P., DeYoung, T., Ekström, P., Feser, T., Gaisser, T. K., Ganugapati, R., Geenen, H., Gerhardt, L., Goldschmidt, A., Groß, A., Hallgren, A., Halzen, F., Hanson, K., Hardtke, D. H., Harenberg, T., Hauschildt, T., Helbing, K., Hellwig, M., Herquet, P., Hill, G. C., Hodges, J., Hubert, D., Hughey, B., Hulth, P. O., Hultqvist, K., Hundertmark, S., Jacobsen, J., Kampert, K. H., Karle, A., Kestel, M., Kohnen, G., Köpke, L., Kowalski, M., Kuehn, K., Lang, R., Leich, H., Leuthold, M., Liubarsky, I., Lundberg, J., Madsen, J., Marciniewski, P., Matis, H. S., McParland, C. P., Messarius, T., Minaeva, Y., Miočinović, P., Morse, R., Münich, K., Nahnhauer, R., Nam, J. W., Neunhöffer, T., Niessen, P., Nygren, D. R., Olbrechts, P., Pohl, A. C., Porrata, R., Price, P. B., Przybylski, G. T., Rawlins, K., Resconi, E., Rhode, W., Ribordy, M., Richter, S., Martino, J. R., Sander, H.-G., Schlenstedt, S., Schneider, D., Schwarz, R., Silvestri, A., Solarz, M., Spiczak, G. M., et al.: Optical properties of deep glacial ice at the South Pole, J. Geophys. Res. Atmospheres, 111(D13), doi:10.1029/2005JD006687, 2006.

Alberti, M. and Biscaro, D.: Height variation detection in polar regions from ICESat satellite altimetry, Comput. Geosci., 36(1), 1–9, doi:10.1016/j.cageo.2009.07.002, 2010.

Alexander, P. M., Tedesco, M., Fettweis, X., van de Wal, R. S. W., Smeets, C. J. P. P. and van den Broeke, M. R.: Assessing spatio-temporal variability and trends in modelled and measured Greenland Ice Sheet albedo (2000–2013), The Cryosphere, 8(6), 2293–2312, doi:https://doi.org/10.5194/tc-8-2293-2014, 2014.

Alley, R. B.: Ice-Sheet and Sea-Level Changes, Science, 310(5747), 456–460, doi:10.1126/science.1114613, 2005.

Alley, R. B., Spencer, M. K. and Anandakrishnan, S.: Ice-sheet mass balance: assessment, attribution and prognosis, Ann. Glaciol., 46, 1–7, doi:10.3189/172756407782871738, 2007.

Ambach, W.: Über den nächtlichen Wärmeumsatz der gefrorenen Gletscheroberfläche, Arch. Für Meteorol. Geophys. Bioklimatol. Ser. A, 8(4), 411–426, doi:10.1007/BF02247097, 1955.

Andersen, J. K., Hansen, K., Box, J. E., Andersen, S. B., Ahlstrøm, A. P., van As, D., Citterio, M., Colgan, W., Karlsson, N. B., Kjeldsen, K. K., Korsgaard, N. J., Larsen, S. H., Mankoff, K. D., Pedersen, A. Ø., Shields, C. L., Solgaard, A. and Vandecrux, B.: Update of annual calving front lines for 47 marine terminating outlet glaciers in Greenland (1999–2018), Geol. Surv. Den. Greenl. Bull., 43, e2019430202, doi:10.34194/GEUSB-201943-02-02, 2019.

Andersen, M. L., Stenseng, L., Skourup, H., Colgan, W., Khan, S. A., Kristensen, S. S., Andersen, S. B., Box, J. E., Ahlstrøm, A. P., Fettweis, X. and Forsberg, R.: Basin-scale partitioning of Greenland ice sheet mass balance components (2007–2011), Earth Planet. Sci. Lett., 409, 89–95, doi:10.1016/j.epsl.2014.10.015, 2015.

Anderson, E. A.: A point energy and mass balance model of a snow cover, edited by N. W. S. United States, [online] Available from: https://repository.library.noaa.gov/view/noaa/6392, 1976.

van Angelen, J. H., Lenaerts, J. T. M., Lhermitte, S., Fettweis, X., Kuipers Munneke, P., van den Broeke, M. R., Meijgaard, E. van and Smeets, C. J. P. P.: Sensitivity of Greenland Ice Sheet surface mass balance to surface albedo parameterization: a study with a regional climate model, The Cryosphere, 6(5), 1175–1186, doi:https://doi.org/10.5194/tc-6-1175-2012, 2012.

van Angelen, J. H., van den Broeke, M. R., Wouters, B. and Lenaerts, J. T. M.: Contemporary (1960–2012) Evolution of the Climate and Surface Mass Balance of the Greenland Ice Sheet, Surv. Geophys., 35(5), 1155–1174, doi:10.1007/s10712-013-9261-z, 2014.

Arnold, N. S., Banwell, A. F. and Willis, I. C.: High-resolution modelling of the seasonal evolution of surface water storage on the Greenland Ice Sheet, The Cryosphere, 8(4), 1149–1160, doi:10.5194/tc-8-1149-2014, 2014.

Arthern, R. J., Wingham, D. J. and Ridout, A. L.: Controls on ERS altimeter measurements over ice sheets: Footprint-scale topography, backscatter fluctuations, and the dependence of microwave penetration depth on satellite orientation, J. Geophys. Res. Atmospheres, 106(D24), 33471–33484, doi:10.1029/2001JD000498, 2001.

van As, D., Box, J. E. and Fausto, R. S.: Challenges of Quantifying Meltwater Retention in Snow and Firn: An Expert Elicitation, Front. Earth Sci., 4, 101, doi:10.3389/feart.2016.00101, 2016.

van As, D., Bech Mikkelsen, A., Holtegaard Nielsen, M., Box, J. E., Claesson Liljedahl, L., Lindbäck, K., Pitcher, L. and Hasholt, B.: Hypsometric amplification and routing moderation of Greenland ice sheet meltwater release, The Cryosphere, 11(3), 1371–1386, doi:10.5194/tc-11-1371-2017, 2017.

Ashcraft, I. S. and Long, D. G.: Comparison of methods for melt detection over Greenland using active and passive microwave measurements, Int. J. Remote Sens., 27(12), 2469–2488, doi:10.1080/01431160500534465, 2006.

Askebjer, P., Barwick, S. W., Bergström, L., Bouchta, A., Carius, S., Coulthard, A., Engel, K., Erlandsson, B., Goobar, A., Gray, L., Hallgren, A., Halzen, F., Hulth, P. O., Jacobsen, J., Johansson, S., Kandhadai, V., Liubarsky, I., Lowder, D., Miller, T., Mock, P. C., Morse, R., Porrata, R., Price, P. B., Richards, A., Rubinstein, H., Schneider, E., Sun, Q., Tilav, S., Walck, C. and Yodh, G.: Optical Properties of the South Pole Ice at Depths Between 0.8 and 1 Kilometer, Science, 267(5201), 1147–1150, doi:10.1126/science.267.5201.1147, 1995.

Askebjer, P., Barwick, S. W., Bergström, L., Bouchta, A., Carius, S., Dalberg, E., Erlandsson, B., Goobar, A., Gray, L., Hallgren, A., Halzen, F., Heukenkamp, H., Hulth, P. O., Hundertmark, S., Jacobsen, J., Kandhadai, V., Karle, A., Liubarsky, I., Lowder, D., Miller, T., Mock, P., Morse, R., Porrata, R., Price, P. B., Richards, A., Rubinstein, H., Schneider, E., Spiering, C., Streicher, O., Sun, Q., Thon, T., Tilav, S., Wischnewski, R., Walck, C. and Yodh, G.: UV and optical light transmission properties in deep ice at the South Pole, Geophys. Res. Lett., 24(11), 1355–1358, doi:10.1029/97GL01246, 1997.

Bader, H.: The Greenland ice sheet, Cold Regions Research and Engineering Lab, Hanover, NH. [online] Available from: https://erdc-library.erdc.dren.mil/xmlui/handle/11681/2674 (Accessed 26 July 2019), 1961.

Bamber, J. L. and Rivera, A.: A review of remote sensing methods for glacier mass balance determination, Glob. Planet. Change, 59(1), 138–148, doi:10.1016/j.gloplacha.2006.11.031, 2007.

Bamber, J. L., Ekholm, S. and Krabill, W.: The accuracy of satellite radar altimeter data over the Greenland Ice Sheet determined from airborne laser data, Geophys. Res. Lett., 25(16), 3177–3180, doi:10.1029/98GL01594, 1998.

Bamber, J. L., Ekholm, S. and Krabill, W. B.: A new, high-resolution digital elevation model of Greenland fully validated with airborne laser altimeter data, J. Geophys. Res. Solid Earth, 106(B4), 6733–6745, doi:10.1029/2000JB900365, 2001.

Bamber, J. L., Griggs, J. A., Hurkmans, R. T. W. L., Dowdeswell, J. A., Gogineni, S. P., Howat, I., Mouginot, J., Paden, J., Palmer, S., Rignot, E. and Steinhage, D.: A new bed elevation dataset for Greenland, The Cryosphere, 7(2), 499–510, doi:https://doi.org/10.5194/tc-7-499-2013, 2013.

Bamber, J. L., Westaway, R. M., Marzeion, B. and Wouters, B.: The land ice contribution to sea level during the satellite era, Environ. Res. Lett., 13(6), 063008, doi:10.1088/1748-9326/aac2f0, 2018.

Barletta, V. R., Sabadini, R. and Bordoni, A.: Isolating the PGR signal in the GRACE data: impact on mass balance estimates in Antarctica and Greenland, Geophys. J. Int., 172(1), 18–30, doi:10.1111/j.1365-246X.2007.03630.x, 2008.

Bell, R. E.: The role of subglacial water in ice-sheet mass balance, Nat. Geosci., 1(5), 297–304, doi:10.1038/ngeo186, 2008.

Benning, L. G., Anesio, A. M., Lutz, S. and Tranter, M.: Biological impact on Greenland's albedo, Nat. Geosci., 7(10), 691–691, doi:10.1038/ngeo2260, 2014.

Benson, C. S.: Stratigraphic studies in the snow and firn of the Greenland Ice Sheet, Cold Regions Research and Engineering Lab, Hanover, NH. [online] Available from: http://www.dtic.mil/docs/citations/AD0288219 (Accessed 16 August 2018), 1962.

Bevis, M., Harig, C., Khan, S. A., Brown, A., Simons, F. J., Willis, M., Fettweis, X., Broeke, M. R. van den, Madsen, F. B., Kendrick, E., Caccamise, D. J., Dam, T. van, Knudsen, P. and Nylen, T.: Accelerating changes in ice mass within Greenland, and the ice sheet's sensitivity to atmospheric forcing, Proc. Natl. Acad. Sci., 116(6), 1934–1939, doi:10.1073/pnas.1806562116, 2019.

Bhardwaj, A., Sam, L., Akanksha, Martín-Torres, F. J. and Kumar, R.: UAVs as remote sensing platform in glaciology: Present applications and future prospects, Remote Sens. Environ., 175, 196–204, doi:10.1016/j.rse.2015.12.029, 2016.

Bhattacharya, I., Jezek, K. C., Wang, L. and Liu, H.: Surface melt area variability of the Greenland ice sheet: 1979–2008, Geophys. Res. Lett., 36(20), L20502, doi:10.1029/2009GL039798, 2009.

Bindschadler, R.: Monitoring ice sheet behavior from space, Rev. Geophys., 36(1), 79–104, doi:10.1029/97RG02669, 1998.

Bindschadler, R., Dowdeswell, J., Hall, D. and Winther, J.-G.: Glaciological applications with Landsat-7 imagery: Early assessments, Remote Sens. Environ., 78(1), 163–179, doi:10.1016/S0034-4257(01)00257-7, 2001.

Bindschadler, R. A. and Scambos, T. A.: Satellite-Image-Derived Velocity Field of an Antarctic Ice Stream, Science, 252(5003), 242–246, doi:10.1126/science.252.5003.242, 1991.

Bintanja, R. and Van Den Broeke, M. R.: The Surface Energy Balance of Antarctic Snow and Blue Ice, J. Appl. Meteorol., 34(4), 902–926, doi:10.1175/1520-0450(1995)034<0902:TSEBOA>2.0.CO;2, 1995.

Bjørk, A. A., Kjær, K. H., Korsgaard, N. J., Khan, S. A., Kjeldsen, K. K., Andresen, C. S., Box, J. E., Larsen, N. K. and Funder, S.: An aerial view of 80 years of climate-related glacier fluctuations in southeast Greenland, Nat. Geosci., 5(6), 427–432, doi:10.1038/ngeo1481, 2012.

Bøggild, C. E., Oerter, H. and Tukiainen, T.: Increased ablation of Wisconsin ice in eastern north Greenland: observations and modelling, Ann. Glaciol., 23, 144–148, doi:10.3189/S0260305500013367, 1996.

Bøggild, C. E., Brandt, R. E., Brown, K. J. and Warren, S. G.: The ablation zone in northeast Greenland: ice types, albedos and impurities, J. Glaciol., 56(195), 101–113, doi:10.3189/002214310791190776, 2010.

Bohren, C. F.: Multiple scattering of light and some of its observable consequences, Am. J. Phys., 55(6), 524–533, doi:10.1119/1.15109, 1987.

Bohren, C. F. and Barkstrom, B. R.: Theory of the optical properties of snow, J. Geophys. Res., 79(30), 4527–4535, doi:10.1029/JC079i030p04527, 1974.

Bohren, C. F. and Huffman, D. R.: Absorption and Scattering of Light by Small Particles, John Wiley & Sons, Ltd., 2007.

Boisvert, L. N., Lee, J. N., Lenaerts, J. T. M., Noël, B., Broeke, M. R. and Nolin, A. W.: Using remotely sensed data from AIRS to estimate the vapor flux on the Greenland ice sheet: Comparisons with observations and a regional climate model, J. Geophys. Res. Atmospheres, 122(1), 202–229, doi:10.1002/2016JD025674, 2017.

Bolch, T., Sørensen, L. S., Simonsen, S. B., Mölg, N., Machguth, H., Rastner, P. and Paul, F.: Mass loss of Greenland's glaciers and ice caps 2003–2008 revealed from ICESat laser altimetry data, Geophys. Res. Lett., 40(5), 875–881, doi:10.1002/grl.50270, 2013.

Borsa, A. A., Moholdt, G., Fricker, H. A. and Brunt, K. M.: A range correction for ICESat and its potential impact on ice-sheet mass balance studies, The Cryosphere, 8(2), 345–357, doi:10.5194/tc-8-345-2014, 2014.

Box, J. E. and Steffen, K.: Sublimation on the Greenland Ice Sheet from automated weather station observations, J. Geophys. Res. Atmospheres, 106(D24), 33965–33981, doi:10.1029/2001JD900219, 2001.

Box, J. E., Bromwich, D. H., Veenhuis, B. A., Bai, L.-S., Stroeve, J. C., Rogers, J. C., Steffen, K., Haran, T. and Wang, S.-H.: Greenland Ice Sheet Surface Mass Balance Variability (1988–2004) from Calibrated Polar MM5 Output, J. Clim., 19(12), 2783–2800, doi:10.1175/JCLI3738.1, 2006.

Box, J. E., Fettweis, X., Stroeve, J. C., Tedesco, M., Hall, D. K. and Steffen, K.: Greenland ice sheet albedo feedback: thermodynamics and atmospheric drivers, The Cryosphere, 6(4), 821–839, doi:10.5194/tc-6-821-2012, 2012.

Braithwaite, R. J., Konzelmann, T., Marty, C. and Olesen, O. B.: Errors in daily ablation measurements in northern Greenland, 1993-94, and their implications for glacier climate studies, J. Glaciol., 44(148), 583–588, doi:10.3189/S0022143000002094, 1998.

Brandt, R. E. and Warren, S. G.: Solar-heating rates and temperature profiles in Antarctic snow and ice, J. Glaciol., 39(131), 99–110, doi:10.3189/S0022143000015756, 1993.

Brenner, A. C., Bindschadler, R. A., Thomas, R. H. and Zwally, H. J.: Slope-induced errors in radar altimetry over continental ice sheets, J. Geophys. Res. Oceans, 88(C3), 1617–1623, doi:10.1029/JC088iC03p01617, 1983.

Brenner, A. C., DiMarzio, J. P. and Zwally, H. J.: Precision and Accuracy of Satellite Radar and Laser Altimeter Data Over the Continental Ice Sheets, IEEE Trans. Geosci. Remote Sens., 45(2), 321–331, doi:10.1109/TGRS.2006.887172, 2007.

Brenner, A. C., Zwally, H. J., Bentley, C. R., Csatho, B. M., Harding, D. J., Hofton, M. A., Minster, J.-B., Roberts, L., Saba, J. L., Thomas, R. H. and Yi, D.: The Algorithm Theoretical Basis Document for the Derivation of Range and Range Distributions from Laser Pulse Waveform Analysis for Surface Elevations, Roughness, Slope, and Vegetation Heights, Technical Memorandum, Goddard Space Flight Center, Greenbelt, Maryland., 2012.

Briegleb, B. P. and Light, B.: A Delta-Eddington Mutiple Scattering Parameterization for Solar Radiation in the Sea Ice Component of the Community Climate System Model, Technical Note, National Center for Atmospheric Research, Boulder, Colorado. [online] Available from: http://dx.doi.org/10.5065/D6B27S71 (Accessed 18 February 2019), 2007.

Brodzik, M. J., Billingsley, B., Haran, T., Raup, B. and Savoie, M. H.: EASE-Grid 2.0: Incremental but Significant Improvements for Earth-Gridded Data Sets, ISPRS Int. J. Geo-Inf., 1(1), 32–45, doi:10.3390/ijgi1010032, 2012.

van den Broeke, M. R., Smeets, P., Ettema, J., van der Veen, C., van de Wal, R. and Oerlemans, J.: Partitioning of melt energy and meltwater fluxes in the ablation zone of the west Greenland ice sheet, The Cryosphere, 2(2), 179–189, doi:10.5194/tc-2-179-2008, 2008.

van den Broeke, M. R., Bamber, J., Ettema, J., Rignot, E., Schrama, E., Berg, W. J. van de, Meijgaard, E. van, Velicogna, I. and Wouters, B.: Partitioning Recent Greenland Mass Loss, Science, 326(5955), 984–986, doi:10.1126/science.1178176, 2009.

van den Broeke, M. R., Enderlin, E. M., Howat, I. M., Kuipers Munneke, P., Noël, B. P. Y., van de Berg, W. J., van Meijgaard, E. and Wouters, B.: On the recent contribution of the Greenland ice sheet to sea level change, The Cryosphere, 10(5), 1933–1946, doi:10.5194/tc-10-1933-2016, 2016.

van den Broeke, M. R., Box, J., Fettweis, X., Hanna, E., Noël, B., Tedesco, M., van As, D., van de Berg, W. J. and van Kampenhout, L.: Greenland Ice Sheet Surface Mass Loss: Recent Developments in Observation and Modeling, Curr. Clim. Change Rep., 3(4), 345–356, doi:10.1007/s40641-017-0084-8, 2017.

Brooks, R. L., Campbell, W. J., Ramseier, R. O., Stanley, H. R. and Zwally, H. J.: Ice sheet topography by satellite altimetry, Nature, 274(5671), 539–543, doi:10.1038/274539a0, 1978.

Brunt, K. M., Neumann, T. A., Walsh, K. M. and Markus, T.: Determination of Local Slope on the Greenland Ice Sheet Using a Multibeam Photon-Counting Lidar in Preparation for the ICESat-2 Mission, IEEE Geosci. Remote Sens. Lett., 11(5), 935–939, doi:10.1109/LGRS.2013.2282217, 2014.

Brunt, K. M., Neumann, T. A., Amundson, J. M., Kavanaugh, J. L., Moussavi, M. S., Walsh, K. M., Cook, W. B. and Markus, T.: MABEL photon-counting laser altimetry data in Alaska for ICESat-2 simulations and development, The Cryosphere, 10(4), 1707–1719, doi:10.5194/tc-10-1707-2016, 2016.

Brunt, K. M., Hawley, R. L., Lutz, E. R., Studinger, M., Sonntag, J. G., Hofton, M. A., Andrews, L. C. and Neumann, T. A.: Assessment of NASA airborne laser altimetry data using ground-based GPS data near Summit Station, Greenland, The Cryosphere, 11(2), 681–692, doi:https://doi.org/10.5194/tc-11-681-2017, 2017.

Brutsaert, W. and Lopez, J. P.: Basin-scale geohydrologic drought flow features of riparian aquifers in the Southern Great Plains, Water Resour. Res., 34(2), 233–240, doi:10.1029/97WR03068, 1998.

Calonne, N., Milliancourt, L., Burr, A., Philip, A., Martin, C. L., Flin, F. and Geindreau, C.: Thermal Conductivity of Snow, Firn, and Porous Ice From 3-D Image-Based Computations, Geophys. Res. Lett., 2019GL085228, doi:10.1029/2019GL085228, 2019.

Carsey, F.: Remote sensing of ice and snow: review and status, Int. J. Remote Sens., 13(1), 5–11, doi:10.1080/01431169208904021, 1992.

Chander, S., Mishra, S. K., Chauhan, P. and Ajai: Ice Height and Backscattering Coefficient Variability over Greenland Ice Sheets Using SARAL Radar Altimeter, Mar. Geod., 38(sup1), 466–476, doi:10.1080/01490419.2014.990590, 2015.

Chandler, D. M., Alcock, J. D., Wadham, J. L., Mackie, S. L. and Telling, J.: Seasonal changes of ice surface characteristics and productivity in the ablation zone of the Greenland Ice Sheet, The Cryosphere, 9(2), 487–504, doi:10.5194/tc-9-487-2015, 2015.

Chang, T. C., Gloersen, P., Schmugge, T., Wilheit, T. T. and Zwally, H. J.: Microwave Emission From Snow and Glacier Ice, J. Glaciol., 16(74), 23–39, doi:10.3189/S0022143000031415, 1976.

Chu, V. W.: Greenland ice sheet hydrology: A review, Prog. Phys. Geogr. Earth Environ., 38(1), 19–54, doi:10.1177/0309133313507075, 2014a.

Chu, V. W.: Greenland ice sheet hydrology A review, Prog. Phys. Geogr., 38(1), 19–54, doi:10.1177/0309133313507075, 2014b.

Chu, V. W., Smith, L. C., Rennermalm, A. K., Forster, R. R., Box, J. E. and Reeh, N.: Sediment plume response to surface melting and supraglacial lake drainages on the Greenland ice sheet, J. Glaciol., 55(194), 1072–1082, doi:10.3189/002214309790794904, 2009.

Chu, W., Schroeder, D. M., Seroussi, H., Creyts, T. T., Palmer, S. J. and Bell, R. E.: Extensive winter subglacial water storage beneath the Greenland Ice Sheet, Geophys. Res. Lett., 43(24), 2016GL071538, doi:10.1002/2016GL071538, 2016.

Clark, M., Nijssen, B., Lundquist, J., Kavetski, D., Rupp, D., Woods, R., Freer, J., Gutmann, E., Wood, A., Brekke, L., Arnold, J., Gochis, D., Rasmussen, R., Tarboton, D., Mahat, V., Flerchinger, G. and Marks, D.: The structure for unifying multiple modeling alternatives (SUMMA), Version 1.0: Technical Description, UCAR/NCAR., 2015.

Colgan, W., Steffen, K., McLamb, W. S., Abdalati, W., Rajaram, H., Motyka, R., Phillips, T. and Anderson, R.: An increase in crevasse extent, West Greenland: Hydrologic implications, Geophys. Res. Lett., 38(18), L18502, doi:10.1029/2011GL048491, 2011.

Cook, J. M., Hodson, A. J. and Irvine-Fynn, T. D. L.: Supraglacial weathering crust dynamics inferred from cryoconite hole hydrology, Hydrol. Process., 30(3), 433–446, doi:10.1002/hyp.10602, 2016.

Cook, J. M., Hodson, A. J., Taggart, A. J., Mernild, S. H. and Tranter, M.: A predictive model for the spectral “bioalbedo” of snow, J. Geophys. Res. Earth Surf., 122(1), 434–454, doi:10.1002/2016JF003932, 2017a.

Cook, J. M., Hodson, A. J., Gardner, A. S., Flanner, M., Tedstone, A. J., Williamson, C., Irvine-Fynn, T. D. L., Nilsson, J., Bryant, R. and Tranter, M.: Quantifying bioalbedo: a new physically based model and discussion of empirical methods for characterising biological influence on ice and snow albedo, The Cryosphere, 11(6), 2611–2632, doi:10.5194/tc-11-2611-2017, 2017b.

Cooley, S. W. and Christoffersen, P.: Observation Bias Correction Reveals More Rapidly Draining Lakes on the Greenland Ice Sheet, J. Geophys. Res. Earth Surf., 122(10), 1867–1881, doi:10.1002/2017JF004255, 2017.

Cooper, M. G. and Smith, L. C.: Satellite Remote Sensing of the Greenland Ice Sheet Ablation Zone: A Review, Remote Sens., 11(20), 2405, doi:10.3390/rs11202405, 2019.

Cooper, M. G., Smith, L. C., Rennermalm, A. K., Miège, C., Pitcher, L. H., Ryan, J. C., Yang, K. and Cooley, S. W.: Meltwater storage in low-density near-surface bare ice in the Greenland ice sheet ablation zone, The Cryosphere, 12(3), 955–970, doi:10.5194/tc-12-955-2018, 2018.

Cooper, M. G., Smith, L. C., Rennermalm, A. K., Tedesco, M., Muthyala, R., Leidman, S. Z., Moustafa, S. E. and Fayne, J. V.: First spectral measurements of light attenuation in Greenland Ice Sheet bare ice suggest shallower subsurface radiative heating and ICESat-2 penetration depth in the ablation zone, Cryosphere Discuss., doi:10.5194/tc-2020-53, 2020.

Cox, C., Humphrey, N. and Harper, J.: Quantifying meltwater refreezing along a transect of sites on the Greenland ice sheet, The Cryosphere, 9(2), 691–701, doi:10.5194/tc-9-691-2015, 2015.

Csatho, B. M., Schenk, A. F., Veen, C. J. van der, Babonis, G., Duncan, K., Rezvanbehbahani, S., Broeke, M. R. van den, Simonsen, S. B., Nagarajan, S. and Angelen, J. H. van: Laser altimetry reveals complex pattern of Greenland Ice Sheet dynamics, Proc. Natl. Acad. Sci., 111(52), 18478–18483, doi:10.1073/pnas.1411680112, 2014.

Cuffey, K. and Paterson, W. S. B.: The Physics of Glaciers, 4th ed., Butterworth-Heinemann/Elsevier, Burlington, MA., 2010.

Dadic, R., Mullen, P. C., Schneebeli, M., Brandt, R. E. and Warren, S. G.: Effects of bubbles, cracks, and volcanic tephra on the spectral albedo of bare ice near the Transantarctic Mountains: Implications for sea glaciers on Snowball Earth, J. Geophys. Res. Earth Surf., 118(3), 1658–1676, doi:10.1002/jgrf.20098, 2013.

Davis, C. H.: A surface and volume scattering retracking algorithm for ice sheet satellite altimetry, IEEE Trans. Geosci. Remote Sens., 31(4), 811–818, doi:10.1109/36.239903, 1993a.

Davis, C. H.: The effect of sub-surface volume scattering on the accuracy of ice-sheet altimeter retracking algorithms, in Proceedings of IGARSS '93 - IEEE International Geoscience and Remote Sensing Symposium, pp. 1053–1057 vol.3., 1993b.

Davis, C. H.: Growth of the Greenland ice sheet: a performance assessment of altimeter retracking algorithms, IEEE Trans. Geosci. Remote Sens., 33(5), 1108–1116, doi:10.1109/36.469474, 1995.

Davis, C. H.: Temporal change in the extinction coefficient of snow on the Greenland ice sheet from an analysis of Seasat and Geosat altimeter data, IEEE Trans. Geosci. Remote Sens., 34(5), 1066–1073, doi:10.1109/36.536522, 1996.

Davis, C. H.: A robust threshold retracking algorithm for measuring ice-sheet surface elevation change from satellite radar altimeters, IEEE Trans. Geosci. Remote Sens., 35(4), 974–979, doi:10.1109/36.602540, 1997.

Davis, C. H. and Zwally, H. J.: Geographic and seasonal variations in the surface properties of the ice sheets by satellite-radar altimetry, J. Glaciol., 39(133), 687–697, doi:10.3189/S0022143000016580, 1993.

Davis, C. H., Kluever, C. A. and Haines, B. J.: Elevation Change of the Southern Greenland Ice Sheet, Science, 279(5359), 2086–2088, doi:10.1126/science.279.5359.2086, 1998.

Davis, C. H., Kluever, C. A., Haines, B. J., Perez, C. and Yoon, Y. T.: Improved elevation-change measurement of the southern Greenland ice sheet from satellite radar altimetry, IEEE Trans. Geosci. Remote Sens., 38(3), 1367–1378, doi:10.1109/36.843031, 2000.

Dee, D. P., Uppala, S. M., Simmons, A. J., Berrisford, P., Poli, P., Kobayashi, S., Andrae, U., Balmaseda, M. A., Balsamo, G., Bauer, P., Bechtold, P., Beljaars, A. C. M., van de Berg, L., Bidlot, J., Bormann, N., Delsol, C., Dragani, R., Fuentes, M., Geer, A. J., Haimberger, L., Healy, S. B., Hersbach, H., Hólm, E. V., Isaksen, L., Kållberg, P., Köhler, M., Matricardi, M., McNally, A. P., Monge-Sanz, B. M., Morcrette, J.-J., Park, B.-K., Peubey, C., de Rosnay, P., Tavolato, C., Thépaut, J.-N. and Vitart, F.: The ERA-Interim reanalysis: configuration and performance of the data assimilation system, Q. J. R. Meteorol. Soc., 137(656), 553–597, doi:10.1002/qj.828, 2011.

Deems, J. S., Painter, T. H. and Finnegan, D. C.: Lidar measurement of snow depth: a review, J. Glaciol., 59(215), 467–479, doi:10.3189/2013JoG12J154, 2013.

Delhasse, A., Kittel, C., Amory, C., Hofer, S., van As, D., S. Fausto, R. and Fettweis, X.: Brief communication: Evaluation of the near-surface climate in ERA5 over the Greenland Ice Sheet, The Cryosphere, 14(3), 957–965, doi:10.5194/tc-14-957-2020, 2020.

Di Girolamo, L.: Generalizing the definition of the bi-directional reflectance distribution function, Remote Sens. Environ., 88(4), 479–482, doi:10.1016/j.rse.2003.07.004, 2003.

Dietz, A. J., Kuenzer, C., Gessner, U. and Dech, S.: Remote sensing of snow – a review of available methods, Int. J. Remote Sens., 33(13), 4094–4134, doi:10.1080/01431161.2011.640964, 2012.

DiMarzio, J. P.: GLAS/ICESat 1 km Laser Altimetry Digital Elevation Model of Greenland, Version 1. NSIDC: National Snow and Ice Data Center., [online] Available from: https://doi.org/10.5067/FYMKT3GJE0TM, 2007.

Dingman, S. L.: Physical hydrology, Prentice Hall, Upper Saddle River, N.J., 2002.

Dozier, J. and Painter, T. H.: Multispectral and Hyperspectral Remote Sensing of Alpine Snow Properties, Annu. Rev. Earth Planet. Sci., 32(1), 465–494, doi:10.1146/annurev.earth.32.101802.120404, 2004.

Drinkwater, M. R., Francis, R., Ratier, G. and Wingham, D. J.: The European Space Agency's Earth Explorer Mission CryoSat: measuring variability in the cryosphere, Ann. Glaciol., 39, 313–320, doi:10.3189/172756404781814663, 2004.

Early, D. S. and Long, D. G.: Image reconstruction and enhanced resolution imaging from irregular samples, IEEE Trans. Geosci. Remote Sens., 39(2), 291–302, doi:10.1109/36.905237, 2001.

Edwards, A., Anesio, A. M., Rassner, S. M., Sattler, B., Hubbard, B., Perkins, W. T., Young, M. and Griffith, G. W.: Possible interactions between bacterial diversity, microbial activity and supraglacial hydrology of cryoconite holes in Svalbard, ISME J., 5(1), 150–160, doi:10.1038/ismej.2010.100, 2011.

Ekholm, S.: A full coverage, high-resolution, topographic model of Greenland computed from a variety of digital elevation data, J. Geophys. Res. Solid Earth, 101(B10), 21961–21972, doi:10.1029/96JB01912, 1996.

Ekholm, S., Forsberg, R. and Brozena, J. M.: Accuracy of satellite altimeter elevations over the Greenland Ice Sheet, J. Geophys. Res. Oceans, 100(C2), 2687–2696, doi:10.1029/94JC03042, 1995.

Enderlin, E. M., Howat, I. M., Jeong, S., Noh, M.-J., van Angelen, J. H. and van den Broeke, M. R.: An improved mass budget for the Greenland ice sheet, Geophys. Res. Lett., 41(3), 2013GL059010, doi:10.1002/2013GL059010, 2014.

Ettema, J., van den Broeke, M. R., van Meijgaard, E., van de Berg, W. J., Bamber, J. L., Box, J. E. and Bales, R. C.: Higher surface mass balance of the Greenland ice sheet revealed by high-resolution climate modeling, Geophys. Res. Lett., 36(12), L12501, doi:10.1029/2009GL038110, 2009.

Ewert, H., Popov, S. V., Richter, A., Schwabe, J., Scheinert, M. and Dietrich, R.: Precise analysis of ICESat altimetry data and assessment of the hydrostatic equilibrium for subglacial Lake Vostok, East Antarctica, Geophys. J. Int., 191(2), 557–568, doi:10.1111/j.1365-246X.2012.05649.x, 2012a.

Ewert, H., Groh, A. and Dietrich, R.: Volume and mass changes of the Greenland ice sheet inferred from ICESat and GRACE, J. Geodyn., 59–60, 111–123, doi:10.1016/j.jog.2011.06.003, 2012b.

Fahnestock, M., Bindschadler, R., Kwok, R. and Jezek, K.: Greenland Ice Sheet Surface Properties and Ice Dynamics from ERS-1 SAR Imagery, Science, 262(5139), 1530–1534, doi:10.1126/science.262.5139.1530, 1993.

Fahnestock, M., Abdalati, W., Joughin, I., Brozena, J. and Gogineni, P.: High Geothermal Heat Flow, Basal Melt, and the Origin of Rapid Ice Flow in Central Greenland, Science, 294(5550), 2338–2342, doi:10.1126/science.1065370, 2001.

Fahnestock, M., Scambos, T., Moon, T., Gardner, A., Haran, T. and Klinger, M.: Rapid large-area mapping of ice flow using Landsat 8, Remote Sens. Environ., 185, 84–94, doi:10.1016/j.rse.2015.11.023, 2016.

Farrell, S. L., Markus, T., Kwok, R. and Connor, L.: Laser altimetry sampling strategies over sea ice, Ann. Glaciol., 52(57), 69–76, doi:10.3189/172756411795931660, 2011.

Fausto, R. S. and van As, D.: Programme for monitoring of the Greenland ice sheet (PROMICE): Automatic weather station data, , doi:10.22008/PROMICE/DATA/AWS, 2019.

Felikson, D., Urban, T. J., Gunter, B. C., Pie, N., Pritchard, H. D., Harpold, R. and Schutz, B. E.: Comparison of Elevation Change Detection Methods From ICESat Altimetry Over the Greenland Ice Sheet, IEEE Trans. Geosci. Remote Sens., 55(10), 5494–5505, doi:10.1109/TGRS.2017.2709303, 2017.

Fettweis, X., Tedesco, M., van den Broeke, M. and Ettema, J.: Melting trends over the Greenland ice sheet (1958–2009) from spaceborne microwave data and regional climate models, The Cryosphere, 5(2), 359–375, doi:10.5194/tc-5-359-2011, 2011.

Fettweis, X., Hanna, E., Lang, C., Belleflamme, A., Erpicum, M. and Gallée, H.: Brief communication: important role of the mid-tropospheric atmospheric circulation in the recent surface melt increase over the Greenland ice sheet, The Cryosphere, 7(1), 241–248, doi:10.5194/tc-7-241-2013, 2013.

Fettweis, X., Box, J. E., Agosta, C., Amory, C., Kittel, C., Lang, C., van As, D., Machguth, H. and Gallée, H.: Reconstructions of the 1900–2015 Greenland ice sheet surface mass balance using the regional climate MAR model, The Cryosphere, 11(2), 1015–1033, doi:10.5194/tc-11-1015-2017, 2017.

Fisher, F. N., King, M. D. and Lee-Taylor, J.: Extinction of UV-visible radiation in wet midlatitude (maritime) snow: Implications for increased NOx emission, J. Geophys. Res. Atmospheres, 110(D21), D21301, doi:10.1029/2005JD005963, 2005.

Flechtner, F., Morton, P., Watkins, M. and Webb, F.: Status of the GRACE Follow-On Mission, in Gravity, Geoid and Height Systems, edited by U. Marti, pp. 117–121, Springer International Publishing., 2014.

Flechtner, F., Neumayer, K.-H., Dahle, C., Dobslaw, H., Fagiolini, E., Raimondo, J.-C. and Güntner, A.: What Can be Expected from the GRACE-FO Laser Ranging Interferometer for Earth Science Applications?, in Remote Sensing and Water Resources, edited by A. Cazenave, N. Champollion, J. Benveniste, and J. Chen, pp. 263–280, Springer International Publishing, Cham., 2016.

Forster, R. R., Isacks, B. L. and Das, S. B.: Shuttle imaging radar (SIR-C/X-SAR) reveals near-surface properties of the South Patagonian Icefield, J. Geophys. Res. Planets, 101(E10), 23169–23180, doi:10.1029/96JE01950, 1996.

Forster, R. R., Box, J. E., van den Broeke, M. R., Miège, C., Burgess, E. W., van Angelen, J. H., Lenaerts, J. T. M., Koenig, L. S., Paden, J., Lewis, C., Gogineni, S. P., Leuschen, C. and McConnell, J. R.: Extensive liquid meltwater storage in firn within the Greenland ice sheet, Nat. Geosci., 7(2), 95–98, doi:10.1038/ngeo2043, 2014.

Fountain, A. G. and Walder, J. S.: Water flow through temperate glaciers, Rev. Geophys., 36(3), 299–328, doi:10.1029/97RG03579, 1998.

France, J. L., King, M. D., Frey, M. M., Erbland, J., Picard, G., Preunkert, S., MacArthur, A. and Savarino, J.: Snow optical properties at Dome C (Concordia), Antarctica; implications for snow emissions and snow chemistry of reactive nitrogen, Atmospheric Chem. Phys., 11(18), 9787–9801, doi:https://doi.org/10.5194/acp-11-9787-2011, 2011.

Franco, B., Fettweis, X. and Erpicum, M.: Future projections of the Greenland ice sheet energy balance driving the surface melt, The Cryosphere, 7(1), 1–18, doi:https://doi.org/10.5194/tc-7-1-2013, 2013.

Freden, S. C. M.: Significant Results Obtained from the Earth Resources Technology Satellite-1. Volume 1: Technical presentations, sections A and B, in Symposium on Significant Results Obtained from the Earth Resources Technology Satellite-1, New Carrollton, MD. [online] Available from: https://ntrs.nasa.gov/search.jsp?R=19730019475 (Accessed 19 July 2019), 1973.

Frei, A., Tedesco, M., Lee, S., Foster, J., Hall, D. K., Kelly, R. and Robinson, D. A.: A review of global satellite-derived snow products, Adv. Space Res., 50(8), 1007–1029, doi:10.1016/j.asr.2011.12.021, 2012.

Frey, K. E., Perovich, D. K. and Light, B.: The spatial distribution of solar radiation under a melting Arctic sea ice cover, Geophys. Res. Lett., 38(22), doi:10.1029/2011GL049421, 2011.

Fricker, H. A., Borsa, A., Minster, B., Carabajal, C., Quinn, K. and Bills, B.: Assessment of ICESat performance at the salar de Uyuni, Bolivia, Geophys. Res. Lett., 32(21), L21S06, doi:10.1029/2005GL023423, 2005.

Fürst, J. J., Goelzer, H. and Huybrechts, P.: Ice-dynamic projections of the Greenland ice sheet in response to atmospheric and oceanic warming, The Cryosphere, 9(3), 1039–1062, doi:https://doi.org/10.5194/tc-9-1039-2015, 2015.

Gallaher, D., Campbell, G. G., Meier, W., Moses, J. and Wingo, D.: The process of bringing dark data to light: The rescue of the early Nimbus satellite data, GeoResJ, 6, 124–134, doi:10.1016/j.grj.2015.02.013, 2015.

Gardner, A. S. and Sharp, M. J.: A review of snow and ice albedo and the development of a new physically based broadband albedo parameterization, J. Geophys. Res. Earth Surf., 115(F1), F01009, doi:10.1029/2009JF001444, 2010.

Gardner, A. S., Smith, B. E., Brunt, K. M., Harding, D. J., Neumann, T. and Walsh, K.: ICESat2 subsurface-scattering biases estimated based on the 2015 SIMPL/AVRIS campaign, in AGU Fall Meeting Abstracts, vol. 41, pp. C41C-0710. [online] Available from: http://adsabs.harvard.edu/abs/2015AGUFM.C41C0710G (Accessed 25 January 2019), 2015.

Gelaro, R., McCarty, W., Suárez, M. J., Todling, R., Molod, A., Takacs, L., Randles, C. A., Darmenov, A., Bosilovich, M. G., Reichle, R., Wargan, K., Coy, L., Cullather, R., Draper, C., Akella, S., Buchard, V., Conaty, A., da Silva, A. M., Gu, W., Kim, G.-K., Koster, R., Lucchesi, R., Merkova, D., Nielsen, J. E., Partyka, G., Pawson, S., Putman, W., Rienecker, M., Schubert, S. D., Sienkiewicz, M. and Zhao, B.: The Modern-Era Retrospective Analysis for Research and Applications, Version 2 (MERRA-2), J. Clim., 30(14), 5419–5454, doi:10.1175/JCLI-D-16-0758.1, 2017.

Georgiou, S., Shepherd, A., McMillan, M. and Nienow, P.: Seasonal evolution of supraglacial lake volume from ASTER imagery, Ann. Glaciol., 50(52), 95–100, doi:10.3189/172756409789624328, 2009.

Gerland, S., Liston, G. E., Winther, J.-G., Ørbæk, J. B. and Ivanov, B. V.: Attenuation of solar radiation in Arctic snow: field observations and modelling, Ann. Glaciol., 31, 364–368, doi:10.3189/172756400781820444, 2000.

Gleason, C. J., Smith, L. C., Chu, V. W., Legleiter, C. J., Pitcher, L. H., Overstreet, B. T., Rennermalm, A. K., Forster, R. R. and Yang, K.: Characterizing supraglacial meltwater channel hydraulics on the Greenland Ice Sheet from in situ observations, Earth Surf. Process. Landf., 41(14), 2111–2122, doi:10.1002/esp.3977, 2016.

Gledhill, L. A. and Williamson, A. G.: Inland advance of supraglacial lakes in north-west Greenland under recent climatic warming, Ann. Glaciol., 59(76pt1), 66–82, doi:10.1017/aog.2017.31, 2018.

Goelles, T. and Bøggild, C. E.: Albedo reduction of ice caused by dust and black carbon accumulation: a model applied to the K-transect, West Greenland, J. Glaciol., 63(242), 1063–1076, doi:10.1017/jog.2017.74, 2017.

Goelles, T., Bøggild, C. E. and Greve, R.: Ice sheet mass loss caused by dust and black carbon accumulation, The Cryosphere, 9(5), 1845–1856, doi:10.5194/tc-9-1845-2015, 2015.

Gogineni, P. and Yan, J.-B.: Remote sensing of ice thickness and surface velocity, in Remote Sensing of the Cryosphere, pp. 187–230, Wiley-Blackwell., 2014.

Gogineni, S., Tammana, D., Braaten, D., Leuschen, C., Akins, T., Legarsky, J., Kanagaratnam, P., Stiles, J., Allen, C. and Jezek, K.: Coherent radar ice thickness measurements over the Greenland ice sheet, J. Geophys. Res. Atmospheres, 106(D24), 33761–33772, doi:10.1029/2001JD900183, 2001.

Gourmelen, N., Escorihuela, M. J., Shepherd, A., Foresta, L., Muir, A., Garcia-Mondéjar, A., Roca, M., Baker, S. G. and Drinkwater, M. R.: CryoSat-2 swath interferometric altimetry for mapping ice elevation and elevation change, Adv. Space Res., 62(6), 1226–1242, doi:10.1016/j.asr.2017.11.014, 2018.

Gray, L., Burgess, D., Copland, L., Cullen, R., Galin, N., Hawley, R. and Helm, V.: Interferometric swath processing of Cryosat data for glacial ice topography, The Cryosphere, 7(6), 1857–1867, doi:https://doi.org/10.5194/tc-7-1857-2013, 2013.

Gray, L., Burgess, D., Copland, L., Demuth, M. N., Dunse, T., Langley, K. and Schuler, T. V.: CryoSat-2 delivers monthly and inter-annual surface elevation change for Arctic ice caps, The Cryosphere, 9(5), 1895–1913, doi:https://doi.org/10.5194/tc-9-1895-2015, 2015.

Gray, L., Burgess, D., Copland, L., Dunse, T., Langley, K. and Moholdt, G.: A revised calibration of the interferometric mode of the CryoSat-2 radar altimeter improves ice height and height change measurements in western Greenland, The Cryosphere, 11(3), 1041–1058, doi:10.5194/tc-11-1041-2017, 2017.

Greeley, A., Kurtz, N. T., Neumann, T. and Markus, T.: Estimating Surface Elevation Bias Due to Subsurface Scattered Photons from Visible Wavelength Laser Altimeters, in AGU Fall Meeting Abstracts, vol. 51. [online] Available from: http://adsabs.harvard.edu/abs/2017AGUFM.C51A0961G (Accessed 25 January 2019), 2017.

Greicius, T.: GRACE-FO Resumes Data Collection, NASA [online] Available from: http://www.nasa.gov/feature/jpl/grace-fo-resumes-data-collection (Accessed 15 January 2019), 2018.

Grenfell, T. C.: The Effects of Ice Thickness on the Exchange of Solar Radiation Over the Polar Oceans, J. Glaciol., 22(87), 305–320, doi:10.3189/S0022143000014295, 1979.

Grenfell, T. C.: A radiative transfer model for sea ice with vertical structure variations, J. Geophys. Res. Oceans, 96(C9), 16991–17001, doi:10.1029/91JC01595, 1991.

Grenfell, T. C. and Maykut, G. A.: The Optical Properties of Ice and Snow in the Arctic Basin*, J. Glaciol., 18(80), 445–463, doi:10.3189/S0022143000021122, 1977.

Grenfell, T. C. and Perovich, D. K.: Radiation absorption coefficients of polycrystalline ice from 400–1400 nm, J. Geophys. Res. Oceans, 86(C8), 7447–7450, doi:10.1029/JC086iC08p07447, 1981.

Grenfell, T. C., Light, B. and Perovich, D. K.: Spectral transmission and implications for the partitioning of shortwave radiation in arctic sea ice, Ann. Glaciol., 44, 1–6, doi:10.3189/172756406781811763, 2006.

Greuell, W. and Knap, W. H.: Remote sensing of the albedo and detection of the slush line on the Greenland ice sheet, J. Geophys. Res. Atmospheres, 105(D12), 15567–15576, doi:10.1029/1999JD901162, 2000.

Greuell, W. and Oerlemans, J.: Narrowband-to-broadband albedo conversion for glacier ice and snow: equations based on modeling and ranges of validity of the equations, Remote Sens. Environ., 89(1), 95–105, doi:10.1016/j.rse.2003.10.010, 2004.

Gribbon, P. W. F.: Cryoconite Holes on Sermikavsak, West Greenland, J. Glaciol., 22(86), 177–181, doi:10.3189/S0022143000014167, 1979.

Guerreiro, K., Fleury, S., Zakharova, E., Rémy, F. and Kouraev, A.: Potential for estimation of snow depth on Arctic sea ice from CryoSat-2 and SARAL/AltiKa missions, Remote Sens. Environ., 186, 339–349, doi:10.1016/j.rse.2016.07.013, 2016.

Hale, G. M. and Querry, M. R.: Optical Constants of Water in the 200-nm to 200-μm Wavelength Region, Appl. Opt., 12(3), 555–563, doi:10.1364/AO.12.000555, 1973.

Hall, D. K.: Assessment of polar climate change using satellite technology, Rev. Geophys., 26(1), 26–39, doi:10.1029/RG026i001p00026, 1988.

Hall, D. K., Ormsby, J. P., Bindschadler, R. A. and Siddalingaiah, H.: Characterization of Snow and Ice Reflectance Zones On Glaciers Using Landsat Thematic Mapper Data, Ann. Glaciol., 9, 104–108, doi:10.3189/S0260305500000471, 1987.

Hall, D. K., Williams, R. S., Casey, K. A., DiGirolamo, N. E. and Wan, Z.: Satellite-derived, melt-season surface temperature of the Greenland Ice Sheet (2000–2005) and its relationship to mass balance, Geophys. Res. Lett., 33(11), L11501, doi:10.1029/2006GL026444, 2006.

Hall, D. K., Box, J. E., Casey, K. A., Hook, S. J., Shuman, C. A. and Steffen, K.: Comparison of satellite-derived and in-situ observations of ice and snow surface temperatures over Greenland, Remote Sens. Environ., 112(10), 3739–3749, doi:10.1016/j.rse.2008.05.007, 2008a.

Hall, D. K., Williams, R. S., Luthcke, S. B. and Digirolamo, N. E.: Greenland ice sheet surface temperature, melt and mass loss: 2000–06, J. Glaciol., 54(184), 81–93, doi:10.3189/002214308784409170, 2008b.

Hall, D. K., Nghiem, S. V., Schaaf, C. B., DiGirolamo, N. E. and Neumann, G.: Evaluation of surface and near-surface melt characteristics on the Greenland ice sheet using MODIS and QuikSCAT data, J. Geophys. Res. Earth Surf., 114(F4), F04006, doi:10.1029/2009JF001287, 2009.

Hall, D. K., Comiso, J. C., DiGirolamo, N. E., Shuman, C. A., Key, J. R. and Koenig, L. S.: A Satellite-Derived Climate-Quality Data Record of the Clear-Sky Surface Temperature of the Greenland Ice Sheet, J. Clim., 25(14), 4785–4798, doi:10.1175/JCLI-D-11-00365.1, 2012.

Hall, D. K., Comiso, J. C., DiGirolamo, N. E., Shuman, C. A., Box, J. E. and Koenig, L. S.: Variability in the surface temperature and melt extent of the Greenland ice sheet from MODIS, Geophys. Res. Lett., 40(10), 2114–2120, doi:10.1002/grl.50240, 2013.

Hambrey, M. J.: Foliation, minor folds and strain in glacier ice, Tectonophysics, 39(1), 397–416, doi:10.1016/0040-1951(77)90106-8, 1977.

Hambrey, M. J. and Lawson, W.: Structural styles and deformation fields in glaciers: a review, Geol. Soc. Lond. Spec. Publ., 176(1), 59, doi:10.1144/GSL.SP.2000.176.01.06, 2000.

Hanna, E., Huybrechts, P., Steffen, K., Cappelen, J., Huff, R., Shuman, C., Irvine-Fynn, T., Wise, S. and Griffiths, M.: Increased Runoff from Melt from the Greenland Ice Sheet: A Response to Global Warming, J. Clim., 21(2), 331–341, doi:10.1175/2007JCLI1964.1, 2008.

Hanna, E., Navarro, F. J., Pattyn, F., Domingues, C. M., Fettweis, X., Ivins, E. R., Nicholls, R. J., Ritz, C., Smith, B., Tulaczyk, S., Whitehouse, P. L. and Zwally, H. J.: Ice-sheet mass balance and climate change, Nature, 498(7452), 51–59, doi:10.1038/nature12238, 2013.

Hanna, E., Cropper, T. E., Hall, R. J. and Cappelen, J.: Greenland Blocking Index 1851–2015: a regional climate change signal, Int. J. Climatol., 36(15), 4847–4861, doi:10.1002/joc.4673, 2016.

Harig, C. and Simons, F. J.: Mapping Greenland's mass loss in space and time, Proc. Natl. Acad. Sci., 109(49), 19934–19937, doi:10.1073/pnas.1206785109, 2012.

Harig, C. and Simons, F. J.: Ice mass loss in Greenland, the Gulf of Alaska, and the Canadian Archipelago: Seasonal cycles and decadal trends, Geophys. Res. Lett., 43(7), 3150–3159, doi:10.1002/2016GL067759, 2016.

Harper, J., Humphrey, N., Pfeffer, W. T., Brown, J. and Fettweis, X.: Greenland ice-sheet contribution to sea-level rise buffered by meltwater storage in firn, Nature, 491(7423), 240–243, doi:10.1038/nature11566, 2012.

Hastenrath, S.: Diurnal thermal forcing and hydrological response of Lewis Glacier, Mount Kenya, Arch. Meteorol. Geophys. Bioclimatol. Ser. A, 32(4), 361–373, doi:10.1007/BF02266975, 1983.

He, T., Liang, S., Yu, Y., Wang, D., Gao, F. and Liu, Q.: Greenland surface albedo changes in July 1981–2012 from satellite observations, Environ. Res. Lett., 8(4), 044043, doi:10.1088/1748-9326/8/4/044043, 2013.

Helm, V., Humbert, A. and Miller, H.: Elevation and elevation change of Greenland and Antarctica derived from CryoSat-2, The Cryosphere, 8(4), 1539–1559, doi:10.5194/tc-8-1539-2014, 2014a.

Helm, V., Humbert, A. and Miller, H.: Elevation Models of Antarctica and Greenland derived from CryoSat-2 in the period 2011 to 2013, Suppl. Helm V Al 2014 Elev. Elev. Change Greenl. Antarct. Deriv. CryoSat-2 Cryosphere 84 1539-1559 Httpsdoiorg105194tc-8-1539-2014, doi:https://doi.org/10.1594/PANGAEA.831394, 2014b.

Hicks, B. R. and Long, D. G.: Inferring Greenland melt and refreeze severity from SeaWinds scatterometer data, Int. J. Remote Sens., 32(23), 8053–8080, doi:10.1080/01431161.2010.532174, 2011.

Hills, B. H., Harper, J. T., Meierbachtol, T. W., Johnson, J. V., Humphrey, N. F. and Wright, P. J.: Processes influencing heat transfer in the near-surface ice of Greenland's ablation zone, The Cryosphere, 12(10), 3215–3227, doi:https://doi.org/10.5194/tc-12-3215-2018, 2018.

Hodson, A., Anesio, A. M., Ng, F., Watson, R., Quirk, J., Irvine-Fynn, T., Dye, A., Clark, C., McCloy, P., Kohler, J. and Sattler, B.: A glacier respires: Quantifying the distribution and respiration CO2 flux of cryoconite across an entire Arctic supraglacial ecosystem, J. Geophys. Res. Biogeosciences, 112(G4), G04S36, doi:10.1029/2007JG000452, 2007.

Hodson, A., Bøggild, C., Hanna, E., Huybrechts, P., Langford, H., Cameron, K. and Houldsworth, A.: The cryoconite ecosystem on the Greenland ice sheet, Ann. Glaciol., 51(56), 123–129, doi:10.3189/172756411795931985, 2010.

Hofer, S., Tedstone, A. J., Fettweis, X. and Bamber, J. L.: Decreasing cloud cover drives the recent mass loss on the Greenland Ice Sheet, Sci. Adv., 3(6), e1700584, doi:10.1126/sciadv.1700584, 2017.

Hoffman, M. J., Fountain, A. G. and Liston, G. E.: Near-surface internal melting: a substantial mass loss on Antarctic Dry Valley glaciers, J. Glaciol., 60(220), 361–374, doi:10.3189/2014JoG13J095, 2014.

Hoffman, M. J., Perego, M., Andrews, L. C., Price, S. F., Neumann, T. A., Johnson, J. V., Catania, G. and Lüthi, M. P.: Widespread Moulin Formation During Supraglacial Lake Drainages in Greenland, Geophys. Res. Lett., 45(2), 778–788, doi:10.1002/2017GL075659, 2018.

Hofton, M. A., Blair, J. B., Luthcke, S. B. and Rabine, D. L.: Assessing the performance of 20–25 m footprint waveform lidar data collected in ICESat data corridors in Greenland, Geophys. Res. Lett., 35(24), L24501, doi:10.1029/2008GL035774, 2008.

Holland, M. M., Bailey, D. A., Briegleb, B. P., Light, B. and Hunke, E.: Improved Sea Ice Shortwave Radiation Physics in CCSM4: The Impact of Melt Ponds and Aerosols on Arctic Sea Ice*, J. Clim., 25(5), 1413–1430, doi:10.1175/JCLI-D-11-00078.1, 2012.

Hori, M., Aoki, T., Stamnes, K. and Li, W.: ADEOS-II/GLI snow/ice products — Part III: Retrieved results, Remote Sens. Environ., 111(2), 291–336, doi:10.1016/j.rse.2007.01.025, 2007.

Hotaling, S., Hood, E. and Hamilton, T. L.: Microbial ecology of mountain glacier ecosystems: biodiversity, ecological connections and implications of a warming climate, Environ. Microbiol., 19(8), 2935–2948, doi:10.1111/1462-2920.13766, 2017.

Howat, I. M., Smith, B. E., Joughin, I. and Scambos, T. A.: Rates of southeast Greenland ice volume loss from combined ICESat and ASTER observations, Geophys. Res. Lett., 35(17), L17505, doi:10.1029/2008GL034496, 2008.

Howat, I. M., Ahn, Y., Joughin, I., van den Broeke, M. R., Lenaerts, J. T. M. and Smith, B.: Mass balance of Greenland's three largest outlet glaciers, 2000–2010, Geophys. Res. Lett., 38(12), L12501, doi:10.1029/2011GL047565, 2011.

Howat, I. M., Negrete, A. and Smith, B. E.: The Greenland Ice Mapping Project (GIMP) land classification and surface elevation data sets, The Cryosphere, 8(4), 1509–1518, doi:10.5194/tc-8-1509-2014, 2014.

Hudleston, P. J.: Structures and fabrics in glacial ice: A review, J. Struct. Geol., 81, 1–27, doi:10.1016/j.jsg.2015.09.003, 2015.

Irvine-Fynn, T.: Modelling runoff from the maritime arctic cryopshere: Water storage and routing at Midtree Lovenbreen, Ph.D., University of Sheffield. [online] Available from: http://ethos.bl.uk/OrderDetails.do?uin=uk.bl.ethos.489371 (Accessed 18 January 2017), 2008.

Irvine-Fynn, T. D. L. and Edwards, A.: A frozen asset: The potential of flow cytometry in constraining the glacial biome, Cytometry A, 85(1), 3–7, doi:10.1002/cyto.a.22411, 2014.

Irvine-Fynn, T. D. L., Moorman, B. J., Williams, J. L. M. and Walter, F. S. A.: Seasonal changes in ground-penetrating radar signature observed at a polythermal glacier, Bylot Island, Canada, Earth Surf. Process. Landf., 31(7), 892–909, doi:10.1002/esp.1299, 2006.

Irvine-Fynn, T. D. L., Hodson, A. J., Moorman, B. J., Vatne, G. and Hubbard, A. L.: Polythermal Glacier Hydrology: A Review, Rev. Geophys., 49(4), RG4002, doi:10.1029/2010RG000350, 2011.

Irvine-Fynn, T. D. L., Edwards, A., Newton, S., Langford, H., Rassner, S. M., Telling, J., Anesio, A. M. and Hodson, A. J.: Microbial cell budgets of an Arctic glacier surface quantified using flow cytometry, Environ. Microbiol., 14(11), 2998–3012, doi:10.1111/j.1462-2920.2012.02876.x, 2012.

Jansson, P., Hock, R. and Schneider, T.: The concept of glacier storage: a review, J. Hydrol., 282(1–4), 116–129, doi:10.1016/S0022-1694(03)00258-0, 2003.

Järvinen, O. and Leppäranta, M.: Solar radiation transfer in the surface snow layer in Dronning Maud Land, Antarctica, Polar Sci., 7(1), 1–17, doi:10.1016/j.polar.2013.03.002, 2013.

Jezek, K. C., Gogineni, P. and Shanableh, M.: Radar measurements of melt zones on the Greenland Ice Sheet, Geophys. Res. Lett., 21(1), 33–36, doi:10.1029/93GL03377, 1994.

Johannessen, O. M., Khvorostovsky, K., Miles, M. W. and Bobylev, L. P.: Recent Ice-Sheet Growth in the Interior of Greenland, Science, 310(5750), 1013–1016, doi:10.1126/science.1115356, 2005.

Jordan, R.: A One-Dimensional Temperature Model for a Snow Cover, Special Report, Cold Regions Research and Engineering Laboratory, Hanover, NH. [online] Available from: https://hdl.handle.net/11681/11677 (Accessed 28 June 2020), 1991.

Joughin, I.: Ice-sheet velocity mapping: a combined interferometric and speckle-tracking approach, Ann. Glaciol., 34, 195–201, doi:10.3189/172756402781817978, 2002.

Joughin, I., Abdalati, W. and Fahnestock, M.: Large fluctuations in speed on Greenland's Jakobshavn Isbræ glacier, Nature, 432(7017), 608–610, doi:10.1038/nature03130, 2004.

Joughin, I., Howat, I. M., Fahnestock, M., Smith, B., Krabill, W., Alley, R. B., Stern, H. and Truffer, M.: Continued evolution of Jakobshavn Isbrae following its rapid speedup, J. Geophys. Res., 113(F4), F04006, doi:10.1029/2008JF001023, 2008.

Joughin, I., Smith, B. E. and Howat, I. M.: A complete map of Greenland ice velocity derived from satellite data collected over 20 years, J. Glaciol., 64(243), 1–11, doi:10.1017/jog.2017.73, 2018.

Joughin, I. R., Winebrenner, D. P. and Fahnestock, M. A.: Observations of ice-sheet motion in Greenland using satellite radar interferometry, Geophys. Res. Lett., 22(5), 571–574, doi:10.1029/95GL00264, 1995.

Joughin, I. R., Kwok, R. and Fahnestock, M. A.: Interferometric estimation of three-dimensional ice-flow using ascending and descending passes, IEEE Trans. Geosci. Remote Sens., 36(1), 25–37, doi:10.1109/36.655315, 1998.

Joughin, I. R., Fahnestock, M. A. and Bamber, J. L.: Ice flow in the northeast Greenland ice stream, Ann. Glaciol., 31, 141–146, doi:10.3189/172756400781820002, 2000.

Karlstrom, L. and Yang, K.: Fluvial supraglacial landscape evolution on the Greenland Ice Sheet, Geophys. Res. Lett., 2016GL067697, doi:10.1002/2016GL067697, 2016.

Karlstrom, L., Zok, A. and Manga, M.: Near-surface permeability in a supraglacial drainage basin on the Llewellyn Glacier, Juneau Icefield, British Columbia, The Cryosphere, 8(2), 537–546, doi:10.5194/tc-8-537-2014, 2014.

Kendrick, A. K., Schroeder, D. M., Chu, W., Young, T. J., Christoffersen, P., Todd, J., Doyle, S. H., Box, J. E., Hubbard, A., Hubbard, B., Brennan, P. V., Nicholls, K. W. and Lok, L. B.: Surface Meltwater Impounded by Seasonal Englacial Storage in West Greenland, Geophys. Res. Lett., 45(19), 10,474-10,481, doi:10.1029/2018GL079787, 2018.

Key, J., Wang, X. and Liu, Y.: NOAA Climate Data Record of AVHRR Polar Pathfinder Extended (APP-X), Version 1, NOAA Natl. Cent. Environ. Inf., doi:doi:10.7289/V5MK69W6, 2014.

Key, J., Wang, X., Liu, Y., Dworak, R. and Letterly, A.: The AVHRR Polar Pathfinder Climate Data Records, Remote Sens., 8(3), 167, doi:10.3390/rs8030167, 2016.

Khvorostovsky, K. S.: Merging and Analysis of Elevation Time Series Over Greenland Ice Sheet From Satellite Radar Altimetry, IEEE Trans. Geosci. Remote Sens., 50(1), 23–36, doi:10.1109/TGRS.2011.2160071, 2012.

Khvorostovsky, K. S. and Johannessen, O. M.: Merging of ERS-1, ERS-2 and Envisat altimeter data over the Greenland ice sheet, Technical Report, Nansen Environmental and Remote Sensing Center, Bergen, Norway. [online] Available from: https://www.nersc.no/sites/www.nersc.no/files/Report307_0.pdf, 2009.

King, M. D. and Simpson, W. R.: Extinction of UV radiation in Arctic snow at Alert, Canada (82°N), J. Geophys. Res. Atmospheres, 106(D12), 12499–12507, doi:10.1029/2001JD900006, 2001.

King, M. D., Howat, I. M., Jeong, S., Noh, M. J., Wouters, B., Noël, B. and van den Broeke, M. R.: Seasonal to decadal variability in ice discharge from the Greenland Ice Sheet, The Cryosphere, 12(12), 3813–3825, doi:10.5194/tc-12-3813-2018, 2018.

Kjeldsen, K. K., Khan, S. A., Wahr, J., Korsgaard, N. J., Kjær, K. H., Bjørk, A. A., Hurkmans, R., Broeke, M. R. van den, Bamber, J. L. and Angelen, J. H. van: Improved ice loss estimate of the northwestern Greenland ice sheet, J. Geophys. Res. Solid Earth, 118(2), 698–708, doi:10.1029/2012JB009684, 2013.

Kjeldsen, K. K., Korsgaard, N. J., Bjørk, A. A., Khan, S. A., Box, J. E., Funder, S., Larsen, N. K., Bamber, J. L., Colgan, W., Broeke, M. van den, Siggaard-Andersen, M.-L., Nuth, C., Schomacker, A., Andresen, C. S., Willerslev, E. and Kjær, K. H.: Spatial and temporal distribution of mass loss from the Greenland Ice Sheet since AD 1900, Nature, 528(7582), 396–400, doi:10.1038/nature16183, 2015.

Klein, A. G. and Stroeve, J.: Development and validation of a snow albedo algorithm for the MODIS instrument, Ann. Glaciol., 34, 45–52, doi:10.3189/172756402781817662, 2002.

Knap, W. H. and Oerlemans, J.: The surface albedo of the Greenland ice sheet: satellite-derived and in situ measurements in the Søndre Strømfjord area during the 1991 melt season, J. Glaciol., 42(141), 364–374, doi:10.3189/S0022143000004214, 1996.

Koenig, L. S. and Hall, D. K.: Comparison of satellite, thermochron and air temperatures at Summit, Greenland, during the winter of 2008/09, J. Glaciol., 56(198), 735–741, doi:10.3189/002214310793146269, 2010.

Koenig, L. S., Lampkin, D. J., Montgomery, L. N., Hamilton, S. L., Turrin, J. B., Joseph, C. A., Moutsafa, S. E., Panzer, B., Casey, K. A., Paden, J. D., Leuschen, C. and Gogineni, P.: Wintertime storage of water in buried supraglacial lakes across the Greenland Ice Sheet, The Cryosphere, 9(4), 1333–1342, doi:10.5194/tc-9-1333-2015, 2015.

König, M., Winther, J.-G. and Isaksson, E.: Measuring snow and glacier ice properties from satellite, Rev. Geophys., 39(1), 1–27, doi:10.1029/1999RG000076, 2001.

Korsgaard, N. J., Nuth, C., Khan, S. A., Kjeldsen, K. K., Bjørk, A. A., Schomacker, A. and Kjær, K. H.: Digital elevation model and orthophotographs of Greenland based on aerial photographs from 1978–1987, Sci. Data, 3, 160032, doi:10.1038/sdata.2016.32, 2016.

Kuipers Munneke, P., van den Broeke, M. R., Reijmer, C. H., Helsen, M. M., Boot, W., Schneebeli, M. and Steffen, K.: The role of radiation penetration in the energy budget of the snowpack at Summit, Greenland, The Cryosphere, 3(2), 155–165, doi:10.5194/tc-3-155-2009, 2009.

Kuipers Munneke, P., Ligtenberg, S. R. M., Noël, B. P. Y., Howat, I. M., Box, J. E., Mosley-Thompson, E., McConnell, J. R., Steffen, K., Harper, J. T., Das, S. B. and van den Broeke, M. R.: Elevation change of the Greenland Ice Sheet due to surface mass balance and firn processes, 1960–2014, The Cryosphere, 9(6), 2009–2025, doi:10.5194/tc-9-2009-2015, 2015.

LaChapelle, E.: Errors in Ablation Measurements from Settlement and Sub-Surface Melting*, J. Glaciol., 3(26), 458–467, doi:10.3198/1959JoG3-26-458-467, 1959.

Larour, E., Utke, J., Csatho, B., Schenk, A., Seroussi, H., Morlighem, M., Rignot, E., Schlegel, N. and Khazendar, A.: Inferred basal friction and surface mass balance of the Northeast Greenland Ice Stream using data assimilation of ICESat (Ice Cloud and land Elevation Satellite) surface altimetry and ISSM (Ice Sheet System Model), The Cryosphere, 8(6), 2335–2351, doi:10.5194/tc-8-2335-2014, 2014.

Larson, G. J.: Meltwater Storage in a Temperate Glacier Burroughs Glacier, Southeast Alaska, [online] Available from: http://hdl.handle.net/1811/48914 (Accessed 15 June 2016), 1978.

Legleiter, C. J., Tedesco, M., Smith, L. C., Behar, A. E. and Overstreet, B. T.: Mapping the bathymetry of supraglacial lakes and streams on the Greenland ice sheet using field measurements and high-resolution satellite images, The Cryosphere, 8(1), 215–228, doi:10.5194/tc-8-215-2014, 2014.

Lenaerts, J. T. M., Medley, B., Broeke, M. R. van den and Wouters, B.: Observing and Modeling Ice Sheet Surface Mass Balance, Rev. Geophys., 57, 376–420, doi:10.1029/2018RG000622, 2019.

Levinsen, J. F., Khvorostovsky, K., Ticconi, F., Shepherd, A., Forsberg, R., Sørensen, L. S., Muir, A., Pie, N., Felikson, D., Flament, T., Hurkmans, R., Moholdt, G., Gunter, B., Lindenbergh, R. C. and Kleinherenbrink, M.: ESA ice sheet CCI: derivation of the optimal method for surface elevation change detection of the Greenland ice sheet – round robin results, Int. J. Remote Sens., 36(2), 551–573, doi:10.1080/01431161.2014.999385, 2015.

Li, J. and Zwally, H. J.: Modeling of firn compaction for estimating ice-sheet mass change from observed ice-sheet elevation change, Ann. Glaciol., 52(59), 1–7, doi:10.3189/172756411799096321, 2011.

Li, X., Xu, K. and Xu, L.: Surface slope and roughness measurement using ICESat/GLAS elevation and laser waveform, Meas. Sci. Technol., 27(9), 095202, doi:10.1088/0957-0233/27/9/095202, 2016.

Li, X., Zhang, Y. and Liang, L.: Snowmelt detection on the Greenland ice sheet using microwave scatterometer measurements, Int. J. Remote Sens., 38(3), 796–807, doi:10.1080/01431161.2016.1271479, 2017.

Liang, S.: Narrowband to broadband conversions of land surface albedo I: Algorithms, Remote Sens. Environ., 76(2), 213–238, doi:10.1016/S0034-4257(00)00205-4, 2001.

Light, B., Maykut, G. A. and Grenfell, T. C.: A two-dimensional Monte Carlo model of radiative transfer in sea ice, J. Geophys. Res. Oceans, 108(C7), 3219, doi:10.1029/2002JC001513, 2003.

Light, B., Maykut, G. A. and Grenfell, T. C.: A temperature-dependent, structural-optical model of first-year sea ice, J. Geophys. Res., 109(C6), C06013, doi:10.1029/2003JC002164, 2004.

Light, B., Grenfell, T. C. and Perovich, D. K.: Transmission and absorption of solar radiation by Arctic sea ice during the melt season, J. Geophys. Res., 113(C3), C03023, doi:10.1029/2006JC003977, 2008.

Lim, Y.-K., Schubert, S. D., Nowicki, S. M. J., Lee, J. N., Molod, A. M., Cullather, R. I., Zhao, B. and Velicogna, I.: Atmospheric summer teleconnections and Greenland Ice Sheet surface mass variations: insights from MERRA-2, Environ. Res. Lett., 11(2), 024002, doi:10.1088/1748-9326/11/2/024002, 2016.

Lindbäck, K., Pettersson, R., Hubbard, A. L., Doyle, S. H., van As, D., Mikkelsen, A. B. and Fitzpatrick, A. A.: Subglacial water drainage, storage, and piracy beneath the Greenland ice sheet, Geophys. Res. Lett., 42(18), 2015GL065393, doi:10.1002/2015GL065393, 2015.

Liston, G. E. and Winther, J.-G.: Antarctic Surface and Subsurface Snow and Ice Melt Fluxes, J. Clim., 18(10), 1469–1481, doi:10.1175/JCLI3344.1, 2005.

Liston, G. E., Winther, J.-G., Bruland, O., Elvehøy, H. and Sand, K.: Below-surface ice melt on the coastal Antarctic ice sheet, J. Glaciol., 45(150), 273–285, doi:10.3189/S0022143000001775, 1999a.

Liston, G. E., Bruland, O., Winther, J.-G., Elvehøy, H. and Sand, K.: Meltwater production in Antarctic blue-ice areas: sensitivity to changes in atmospheric forcing, Polar Res., 18(2), 283–290, doi:10.1111/j.1751-8369.1999.tb00305.x, 1999b.

Lliboutry, L.: Temperate ice permeability, stability of water veins and percolation of internal meltwater, J. Glaciol., 42(141), 201–211, doi:10.3198/1996JoG42-141-201-211, 1996.

Long, D. G.: Polar Applications of Spaceborne Scatterometers, IEEE J. Sel. Top. Appl. Earth Obs. Remote Sens., 10(5), 2307–2320, doi:10.1109/JSTARS.2016.2629418, 2017.

Long, D. G. and Drinkwater, M. R.: Greenland ice-sheet surface properties observed by the Seasat-A scatterometer at enhanced resolution, J. Glaciol., 40(135), 213–230, doi:10.3189/S0022143000007310, 1994.

Long, D. G. and Hicks, B. R.: SeaWinds on QuikScat Enhanced Resolution Image Products (version 2), Brigham Young University, Provo, Utah, [online] Available from: https://www.scp.byu.edu/data/Quikscat/SIRv2/Quikscat_sirV2.html, 2005.

Lucchitta, B. K. and Ferguson, H. M.: Antarctica: Measuring Glacier Velocity from Satellite Images, Science, 234(4780), 1105–1108, doi:10.1126/science.234.4780.1105, 1986.

Luckman, A. and Murray, T.: Seasonal variation in velocity before retreat of Jakobshavn Isbræ, Greenland, Geophys. Res. Lett., 32(8), L08501, doi:10.1029/2005GL022519, 2005.

Luthcke, S. B., Rowlands, D. D., Williams, T. A. and Sirota, M.: Reduction of ICESat systematic geolocation errors and the impact on ice sheet elevation change detection, Geophys. Res. Lett., 32(21), L21S05, doi:10.1029/2005GL023689, 2005.

Lüthi, M. P., Ryser, C., Andrews, L. C., Catania, G. A., Funk, M., Hawley, R. L., Hoffman, M. J. and Neumann, T. A.: Heat sources within the Greenland Ice Sheet: dissipation, temperate paleo-firn and cryo-hydrologic warming, The Cryosphere, 9(1), 245–253, doi:10.5194/tc-9-245-2015, 2015.

Lutz, S., Anesio, A. M., Villar, J., E, S. and Benning, L. G.: Variations of algal communities cause darkening of a Greenland glacier, FEMS Microbiol. Ecol., 89(2), 402–414, doi:10.1111/1574-6941.12351, 2014.

MacFerrin, M., Machguth, H., As, D. van, Charalampidis, C., Stevens, C. M., Heilig, A., Vandecrux, B., Langen, P. L., Mottram, R., Fettweis, X., Broeke, M. R. van den, Pfeffer, W. T., Moussavi, M. S. and Abdalati, W.: Rapid expansion of Greenland's low-permeability ice slabs, Nature, 573(7774), 403–407, doi:10.1038/s41586-019-1550-3, 2019.

Machguth, H., MacFerrin, M., van As, D., Box, J. E., Charalampidis, C., Colgan, W., Fausto, R. S., Meijer, H. A. J., Mosley-Thompson, E. and van de Wal, R. S. W.: Greenland meltwater storage in firn limited by near-surface ice formation, Nat. Clim. Change, 6(4), 390–393, doi:10.1038/nclimate2899, 2016.

Mader, H. M.: Observations of the water-vein system in polycrystalline ice, J. Glaciol., 38(130), 333–347, doi:10.3189/S0022143000002227, 1992.

Mankoff, K. D., Colgan, W., Solgaard, A., Karlsson, N. B., Ahlstrøm, A. P., Van As, D., Box, J. E., Abbas Khan, S., Kjeldsen, K. K., Mouginot, J. and Fausto, R. S.: Greenland Ice Sheet solid ice discharge from 1986 through 2017, Earth Syst. Sci. Data, 11(2), 769–786, doi:10.5194/essd-11-769-2019, 2019.

Markus, T., Neumann, T., Martino, A., Abdalati, W., Brunt, K., Csatho, B., Farrell, S., Fricker, H., Gardner, A., Harding, D., Jasinski, M., Kwok, R., Magruder, L., Lubin, D., Luthcke, S., Morison, J., Nelson, R., Neuenschwander, A., Palm, S., Popescu, S., Shum, C., Schutz, B. E., Smith, B., Yang, Y. and Zwally, J.: The Ice, Cloud, and land Elevation Satellite-2 (ICESat-2): Science requirements, concept, and implementation, Remote Sens. Environ., 190, 260–273, doi:10.1016/j.rse.2016.12.029, 2017.

Martin, T. V., Zwally, H. J., Brenner, A. C. and Bindschadler, R. A.: Analysis and retracking of continental ice sheet radar altimeter waveforms, J. Geophys. Res. Oceans, 88(C3), 1608–1616, doi:10.1029/JC088iC03p01608, 1983.

Martonchik, J. V., Bruegge, C. J. and Strahler, A. H.: A review of reflectance nomenclature used in remote sensing, Remote Sens. Rev., 19(1–4), 9–20, doi:10.1080/02757250009532407, 2000.

Mätzler, C.: MATLAB Functions for Mie Scattering and Absorption Version 2, Research Report, Institut für Angewandte Physik, Bern, Switzerland. [online] Available from: http://www.atmo.arizona.edu/students/courselinks/spring09/atmo656b/maetzler_mie_v2.pdf, 2002.

Mätzler, C. and Wegmüller, U.: Dielectric properties of freshwater ice at microwave frequencies, J. Phys. Appl. Phys., 20(12), 1623–1630, doi:10.1088/0022-3727/20/12/013, 1987.

McMillan, M., Leeson, A., Shepherd, A., Briggs, K., Armitage, T. W. K., Hogg, A., Kuipers Munneke, P., Broeke, M., Noël, B., Berg, W. J., Ligtenberg, S., Horwath, M., Groh, A., Muir, A. and Gilbert, L.: A high-resolution record of Greenland mass balance, Geophys. Res. Lett., 43(13), 7002–7010, doi:10.1002/2016GL069666, 2016.

Meirold-Mautner, I. and Lehning, M.: Measurements and model calculations of the solar shortwave fluxes in snow on Summit, Greenland, Ann. Glaciol., 38, 279–284, doi:10.3189/172756404781814753, 2004.

Mernild, S. H., Liston, G. E., Hiemstra, C. A. and Christensen, J. H.: Greenland Ice Sheet Surface Mass-Balance Modeling in a 131-Yr Perspective, 1950–2080, J. Hydrometeorol., 11(1), 3–25, doi:10.1175/2009JHM1140.1, 2010.

Mernild, S. H., Mote, T. L. and Liston, G. E.: Greenland ice sheet surface melt extent and trends: 1960–2010, J. Glaciol., 57(204), 621–628, doi:10.3189/002214311797409712, 2011.

Mernild, S. H., Liston, G. E., van As, D., Hasholt, B. and Yde, J. C.: High-resolution ice sheet surface mass-balance and spatiotemporal runoff simulations: Kangerlussuaq, west Greenland, Arct. Antarct. Alp. Res., 50(1), S100008, doi:10.1080/15230430.2017.1415856, 2018.

Miles, K. E., Willis, I. C., Benedek, C. L., Williamson, A. G. and Tedesco, M.: Toward Monitoring Surface and Subsurface Lakes on the Greenland Ice Sheet Using Sentinel-1 SAR and Landsat-8 OLI Imagery, Front. Earth Sci., 5, 58, doi:10.3389/feart.2017.00058, 2017.

Millan, R., Rignot, E., Mouginot, J., Wood, M., Bjørk, A. A. and Morlighem, M.: Vulnerability of Southeast Greenland Glaciers to Warm Atlantic Water From Operation IceBridge and Ocean Melting Greenland Data: VULNERABILITY OF SOUTHEAST GREENLAND, Geophys. Res. Lett., 45(6), 2688–2696, doi:10.1002/2017GL076561, 2018.

Moon, T. and Joughin, I.: Changes in ice front position on Greenland's outlet glaciers from 1992 to 2007, J. Geophys. Res. Earth Surf., 113(F2), F02022, doi:10.1029/2007JF000927, 2008.

Morlighem, M. and Willis, J.: Improving Bed Topography Mapping of Greenland Glaciers Using NASA's Oceans Melting Greenland (OMG) Data, Oceanography, 29(4), 62–71, doi:10.5670/oceanog.2016.99, 2016.

Morlighem, M., Rignot, E., Seroussi, H., Larour, E., Dhia, H. B. and Aubry, D.: A mass conservation approach for mapping glacier ice thickness, Geophys. Res. Lett., 38(19), L19503, doi:10.1029/2011GL048659, 2011.

Morlighem, M., Williams, C. N., Rignot, E., An, L., Arndt, J. E., Bamber, J. L., Catania, G., Chauché, N., Dowdeswell, J. A., Dorschel, B., Fenty, I., Hogan, K., Howat, I., Hubbard, A., Jakobsson, M., Jordan, T. M., Kjeldsen, K. K., Millan, R., Mayer, L., Mouginot, J., Noël, B. P. Y., O'Cofaigh, C., Palmer, S., Rysgaard, S., Seroussi, H., Siegert, M. J., Slabon, P., Straneo, F., van den Broeke, M. R., Weinrebe, W., Wood, M. and Zinglersen, K. B.: BedMachine v3: Complete Bed Topography and Ocean Bathymetry Mapping of Greenland From Multibeam Echo Sounding Combined With Mass Conservation, Geophys. Res. Lett., 44(21), 11,051-11,061, doi:10.1002/2017GL074954, 2017.

Mote, T. L.: Greenland surface melt trends 1973–2007: Evidence of a large increase in 2007, Geophys. Res. Lett., 34(22), L22507, doi:10.1029/2007GL031976, 2007.

Mote, T. L.: MEaSUREs Greenland Surface Melt Daily 25km EASE-Grid 2.0, , doi:10.5067/measures/cryosphere/nsidc-0533.001, 2014.

Mote, T. L. and Anderson, M. R.: Variations in snowpack melt on the Greenland ice sheet based on passive-microwave measurements, J. Glaciol., 41(137), 51–60, doi:10.3189/S0022143000017755, 1995.

Mote, T. L., Anderson, M. R., Kuivinen, K. C. and Rowe, C. M.: Passive microwave-derived spatial and temporal variations of summer melt on the Greenland ice sheet, Ann. Glaciol., 17, 233–238, doi:10.1017/S0260305500012891, 1993.

Mouginot, J., Rignot, E., Scheuchl, B. and Millan, R.: Comprehensive Annual Ice Sheet Velocity Mapping Using Landsat-8, Sentinel-1, and RADARSAT-2 Data, Remote Sens., 9(4), 364, doi:10.3390/rs9040364, 2017.

Mouginot, J., Rignot, E., Bjørk, A. A., Broeke, M. van den, Millan, R., Morlighem, M., Noël, B., Scheuchl, B. and Wood, M.: Forty-six years of Greenland Ice Sheet mass balance from 1972 to 2018, Proc. Natl. Acad. Sci., 116(19), 9239–9244, doi:10.1073/pnas.1904242116, 2019.

Moustafa, S. E., Rennermalm, A. K., Smith, L. C., Miller, M. A., Mioduszewski, J. R., Koenig, L. S., Hom, M. G. and Shuman, C. A.: Multi-modal albedo distributions in the ablation area of the southwestern Greenland Ice Sheet, The Cryosphere, 9(3), 905–923, doi:10.5194/tc-9-905-2015, 2015.

Moustafa, S. E., Rennermalm, A. K., Román, M. O., Wang, Z., Schaaf, C. B., Smith, L. C., Koenig, L. S. and Erb, A.: Evaluation of satellite remote sensing albedo retrievals over the ablation area of the southwestern Greenland ice sheet, Remote Sens. Environ., 198, 115–125, doi:10.1016/j.rse.2017.05.030, 2017.

Mullen, P. C. and Warren, S. G.: Theory of the optical properties of lake ice, J. Geophys. Res. Atmospheres, 93(D7), 8403–8414, doi:10.1029/JD093iD07p08403, 1988.

Müller, F. and Keeler, C. M.: Errors in Short-Term Ablation Measurements on Melting Ice Surfaces, J. Glaciol., 8(52), 91–105, doi:10.3189/S0022143000020785, 1969.

Munro, D. S.: Comparison of Melt Energy Computations and Ablatometer Measurements on Melting Ice and Snow, Arct. Alp. Res., 22(2), 153–162, doi:10.2307/1551300, 1990.

Munro, S. D.: Delays of supraglacial runoff from differently defined microbasin areas on the Peyto Glacier, Hydrol. Process., 25(19), 2983–2994, doi:10.1002/hyp.8124, 2011.

Murray, F. W.: On the Computation of Saturation Vapor Pressure, J. Appl. Meteorol., 6(1), 203–204, doi:10.1175/1520-0450(1967)006<0203:OTCOSV>2.0.CO;2, 1967.

NASA/JPL-Caltech: GRACE-FO First Gravity Field Data Now Available, GRACE-FO [online] Available from: https://gracefo.jpl.nasa.gov/news/145/grace-fo-first-gravity-field-data-now-available (Accessed 2 July 2019), 2019.

Nghiem, S. V., Steffen, K., Kwok, R. and Tsai, W. Y.: Detection of snowmelt regions on the Greenland ice sheet using diurnal backscatter change, J. Glaciol., 47(159), 539–547, doi:10.3189/172756501781831738, 2001.

Nghiem, S. V., Steffen, K., Neumann, G. and Huff, R.: Mapping of ice layer extent and snow accumulation in the percolation zone of the Greenland ice sheet, J. Geophys. Res. Earth Surf., 110, F02017, doi:10.1029/2004JF000234, 2005.

Nghiem, S. V., Hall, D. K., Mote, T. L., Tedesco, M., Albert, M. R., Keegan, K., Shuman, C. A., DiGirolamo, N. E. and Neumann, G.: The extreme melt across the Greenland ice sheet in 2012, Geophys. Res. Lett., 39(20), L20502, doi:10.1029/2012GL053611, 2012.

Nicodemus, F. E., Richmond, J. C., Hsia, J. J., Ginsberg, I. W. and Limperis, T.: Geometrical considerations and nomenclature for reflectance, Monograph, National Bureau of Standards, Washington, D.C. [online] Available from: http://adsabs.harvard.edu/abs/1977nbs..reptR....N (Accessed 25 July 2019), 1977.

Nilsson, J., Vallelonga, P., Simonsen, S. B., Sørensen, L. S., Forsberg, R., Dahl-Jensen, D., Hirabayashi, M., Goto-Azuma, K., Hvidberg, C. S., Kjær, H. A. and Satow, K.: Greenland 2012 melt event effects on CryoSat-2 radar altimetry, Geophys. Res. Lett., 42(10), 3919–3926, doi:10.1002/2015GL063296, 2015.

Noël, B., Berg, W. J. van de, Wessem, J. M. van, Meijgaard, E. van, As, D. van, Lenaerts, J. T. M., Lhermitte, S., Kuipers Munneke, P., Smeets, C. J. P. P., Ulft, L. H. van, Wal, R. S. W. van de and Broeke, M. R. van den: Modelling the climate and surface mass balance of polar ice sheets using RACMO2 – Part 1: Greenland (1958–2016), The Cryosphere, 12(3), 811–831, doi:https://doi.org/10.5194/tc-12-811-2018, 2018.

Noël, B., van de Berg, W. J., Lhermitte, S. and van den Broeke, M. R.: Rapid ablation zone expansion amplifies north Greenland mass loss, Sci. Adv., 5(9), eaaw0123, doi:10.1126/sciadv.aaw0123, 2019.

Nolin, A. W.: Mapping snow grain size on the ice sheets with a laser altimeter, in IEEE International Geoscience and Remote Sensing (IGARSS '98) Symposium on Sensing and Managing the Environment, vol. 4, pp. 2264–2266., 1998.

Nolin, A. W.: Recent advances in remote sensing of seasonal snow, J. Glaciol., 56(200), 1141–1150, doi:10.3189/002214311796406077, 2010.

Nolin, A. W. and Mar, E.: Arctic Sea Ice Surface Roughness Estimated from Multi-Angular Reflectance Satellite Imagery, Remote Sens., 11(1), 50, doi:10.3390/rs11010050, 2019.

Nolin, A. W. and Payne, M. C.: Classification of glacier zones in western Greenland using albedo and surface roughness from the Multi-angle Imaging SpectroRadiometer (MISR), Remote Sens. Environ., 107(1), 264–275, doi:10.1016/j.rse.2006.11.004, 2007.

Nolin, A. W. and Stroeve, J.: The changing albedo of the Greenland ice sheet: implications for climate modeling, Ann. Glaciol., 25, 51–57, doi:10.1017/S0260305500013793, 1997.

Nolin, A. W., Fetterer, F. M. and Scambos, T. A.: Surface roughness characterizations of sea ice and ice sheets: case studies with MISR data, IEEE Trans. Geosci. Remote Sens., 40(7), 1605–1615, doi:10.1109/TGRS.2002.801581, 2002.

Nye, J. F.: The rotting of temperate ice, J. Cryst. Growth, 113(3), 465–476, doi:10.1016/0022-0248(91)90081-F, 1991.

Nye, J. F. and Frank, F. C.: Hydrology of the intergranular veins in a temperate glacier, in Symposium on the Hydrology of Glaciers, vol. 95, pp. 157–161, Citeseer, Cambridge England., 1973.

Overeem, I., Hudson, B., Welty, E., Mikkelsen, A., Bamber, J., Petersen, D., Lewinter, A. and Hasholt, B.: River inundation suggests ice-sheet runoff retention, J. Glaciol., 61(228), 776–788, doi:10.3189/2015JoG15J012, 2015.

Painter, T. H., Duval, B., Thomas, W. H., Mendez, M., Heintzelman, S. and Dozier, J.: Detection and Quantification of Snow Algae with an Airborne Imaging Spectrometer, Appl Env. Microbiol, 67(11), 5267–5272, doi:10.1128/AEM.67.11.5267-5272.2001, 2001.

Parrinello, T., Shepherd, A., Bouffard, J., Badessi, S., Casal, T., Davidson, M., Fornari, M., Maestroni, E. and Scagliola, M.: CryoSat: ESA's ice mission – Eight years in space, Adv. Space Res., 62(6), 1178–1190, doi:10.1016/j.asr.2018.04.014, 2018.

Partington, K. C.: Discrimination of glacier facies using multi-temporal SAR data, J. Glaciol., 44(146), 42–53, doi:10.3189/S0022143000002331, 1998.

Partington, K. C., Ridley, J. K., Rapley, C. G. and Zwally, H. J.: Observations of the Surface Properties of the Ice Sheets by Satellite Radar Altimetry, J. Glaciol., 35(120), 267–275, doi:10.3189/S0022143000004603, 1989.

Patankar, S. V.: Numerical Heat Transfer and Fluid Flow, Hemisphere Publishing Corporation., 1980.

Paterson, W. S. B.: Temperature Distribution in the Upper Layers of the Ablation Area of Athabasca Glacier, Alberta, Canada, J. Glaciol., 11(61), 31–41, doi:10.3198/1972JoG11-61-31-41, 1972.

Pattyn, F., Ritz, C., Hanna, E., Asay-Davis, X., DeConto, R., Durand, G., Favier, L., Fettweis, X., Goelzer, H., Golledge, N. R., Munneke, P. K., Lenaerts, J. T. M., Nowicki, S., Payne, A. J., Robinson, A., Seroussi, H., Trusel, L. D. and Broeke, M. van den: The Greenland and Antarctic ice sheets under 1.5 °C global warming, Nat. Clim. Change, 8(12), 1053–1061, doi:10.1038/s41558-018-0305-8, 2018.

Pegau, W. S. and Zaneveld, J. R. V.: Field measurements of in-ice radiance, Cold Reg. Sci. Technol., 31(1), 33–46, doi:10.1016/S0165-232X(00)00004-5, 2000.

Perovich, D. K.: The Optical Properties of Sea Ice., U.S. Army Cold Regions Research and Engineering Laboratory, Hanover, NH. [online] Available from: https://apps.dtic.mil/dtic/tr/fulltext/u2/a310586.pdf, 1996.

Perovich, D. K. and Govoni, J. W.: Absorption coefficients of ice from 250 to 400 nm, Geophys. Res. Lett., 18(7), 1233–1235, doi:10.1029/91GL01642, 1991.

Pettersson, R., Jansson, P. and Blatter, H.: Spatial variability in water content at the cold-temperate transition surface of the polythermal Storglaciären, Sweden, J. Geophys. Res. Earth Surf., 109(F2), F02009, doi:10.1029/2003JF000110, 2004.

Pfeffer, W. T., Meier, M. F. and Illangasekare, T. H.: Retention of Greenland runoff by refreezing: Implications for projected future sea level change, J. Geophys. Res. Oceans, 96(C12), 22117–22124, doi:10.1029/91JC02502, 1991.

Picard, G., Libois, Q. and Arnaud, L.: Refinement of the ice absorption spectrum in the visible using radiance profile measurements in Antarctic snow, The Cryosphere, 10(6), 2655–2672, doi:10.5194/tc-10-2655-2016, 2016.

Pitcher, L. H. and Smith, L. C.: Supraglacial Streams and Rivers, Annu. Rev. Earth Planet. Sci., 47(1), 421–452, doi:10.1146/annurev-earth-053018-060212, 2019.

Poinar, K., Joughin, I., Das, S. B., Behn, M. D., Lenaerts, J. T. M. and Broeke, M. R. van den: Limits to future expansion of surface-melt-enhanced ice flow into the interior of western Greenland, Geophys. Res. Lett., 42(6), 1800–1807, doi:10.1002/2015GL063192, 2015.

Pope, A., Scambos, T. A., Moussavi, M., Tedesco, M., Willis, M., Shean, D. and Grigsby, S.: Estimating supraglacial lake depth in West Greenland using Landsat 8 and comparison with other multispectral methods, The Cryosphere, 10(1), 15–27, doi:10.5194/tc-10-15-2016, 2016.

Pope, R. M. and Fry, E. S.: Absorption spectrum (380–700 nm) of pure water. II. Integrating cavity measurements, Appl. Opt., 36(33), 8710–8723, doi:10.1364/AO.36.008710, 1997.

Price, P. B. and Bergström, L.: Optical properties of deep ice at the South Pole: scattering, Appl. Opt., 36(18), 4181–4194, doi:10.1364/AO.36.004181, 1997.

Pritchard, H. D., Arthern, R. J., Vaughan, D. G. and Edwards, L. A.: Extensive dynamic thinning on the margins of the Greenland and Antarctic ice sheets, Nature, 461(7266), 971–975, doi:10.1038/nature08471, 2009.

Pritchard, H. D., Luthcke, S. B. and Fleming, A. H.: Understanding ice-sheet mass balance: progress in satellite altimetry and gravimetry, J. Glaciol., 56(200), 1151–1161, doi:10.3189/002214311796406194, 2011.

Quincey, D. J. and Luckman, A.: Progress in satellite remote sensing of ice sheets, Prog. Phys. Geogr., 33(4), 547–567, doi:10.1177/0309133309346883, 2009.

Racoviteanu, A. E., Williams, M. W. and Barry, R. G.: Optical Remote Sensing of Glacier Characteristics: A Review with Focus on the Himalaya, Sensors, 8(5), 3355–3383, doi:10.3390/s8053355, 2008.

Rajkumar, K. S., Maheshwari, M., Pallipad, J., Rajak, D. R., Kumar, R. and Oza, S. R.: Concurrent Use of OSCAT and AltiKa to Characterize Antarctic Ice Surface Features, Mar. Geod., 38(sup1), 497–509, doi:10.1080/01490419.2014.1001047, 2015.

Ramage, J. M. and Isacks, B. L.: Determination of melt-onset and refreeze timing on southeast Alaskan icefields using SSM/I diurnal amplitude variations, Ann. Glaciol., 34, 391–398, doi:10.3189/172756402781817761, 2002.

Ramillien, G., Lombard, A., Cazenave, A., Ivins, E. R., Llubes, M., Remy, F. and Biancale, R.: Interannual variations of the mass balance of the Antarctica and Greenland ice sheets from GRACE, Glob. Planet. Change, 53(3), 198–208, doi:10.1016/j.gloplacha.2006.06.003, 2006.

Ramillien, G., Famiglietti, J. S. and Wahr, J.: Detection of Continental Hydrology and Glaciology Signals from GRACE: A Review, Surv. Geophys., 29(4), 361–374, doi:10.1007/s10712-008-9048-9, 2008.

Reijmer, C. H., van den Broeke, M. R., Fettweis, X., Ettema, J. and Stap, L. B.: Refreezing on the Greenland ice sheet: a comparison of parameterizations, The Cryosphere, 6(4), 743–762, doi:10.5194/tc-6-743-2012, 2012.

Rémy, F. and Parouty, S.: Antarctic Ice Sheet and Radar Altimetry: A Review, Remote Sens., 1(4), 1212–1239, doi:10.3390/rs1041212, 2009.

Rémy, F., Flament, T., Michel, A. and Verron, J.: Ice sheet survey over Antarctica using satellite altimetry: ERS-2, Envisat, SARAL/AltiKa, the key importance of continuous observations along the same repeat orbit, Int. J. Remote Sens., 35(14), 5497–5512, doi:10.1080/01431161.2014.926419, 2014.

Rémy, F., Flament, T., Michel, A. and Blumstein, D.: Envisat and SARAL/AltiKa Observations of the Antarctic Ice Sheet: A Comparison Between the Ku-band and Ka-band, Mar. Geod., 38(sup1), 510–521, doi:10.1080/01490419.2014.985347, 2015.

Rennermalm, A. K., Smith, L. C., Chu, V. W., Box, J. E., Forster, R. R., Van den Broeke, M. R., Van As, D. and Moustafa, S. E.: Evidence of meltwater retention within the Greenland ice sheet, The Cryosphere, 7(5), 1433–1445, doi:10.5194/tc-7-1433-2013, 2013a.

Rennermalm, A. K., Moustafa, S. E., Mioduszewski, J., Chu, V. W., Forster, R. R., Hagedorn, B., Harper, J. T., Mote, T. L., Robinson, D. A., Shuman, C. A., Smith, L. C. and Tedesco, M.: Understanding Greenland ice sheet hydrology using an integrated multi-scale approach, Environ. Res. Lett., 8(1), 015017, doi:10.1088/1748-9326/8/1/015017, 2013b.

Richter-Menge, J. A., Colbeck, S. C. and Jezek, K. C.: Recent Progress in Snow and Ice Research, Rev. Geophys., 29(S1), 218–226, doi:10.1002/rog.1991.29.s1.218, 1991.

Ridley, J. K. and Partington, K. C.: A model of satellite radar altimeter return from ice sheets, Int. J. Remote Sens., 9(4), 601–624, doi:10.1080/01431168808954881, 1988.

Rignot, E. and Thomas, R. H.: Mass Balance of Polar Ice Sheets, Science, 297(5586), 1502–1506, doi:10.1126/science.1073888, 2002.

Rignot, E., Jezek, K. C. and Sohn, H. G.: Ice flow dynamics of the Greenland Ice Sheet from SAR interferometry, Geophys. Res. Lett., 22(5), 575–578, doi:10.1029/94GL03381, 1995.

Rignot, E., Echelmeyer, K. and Krabill, W.: Penetration depth of interferometric synthetic-aperture radar signals in snow and ice, Geophys. Res. Lett., 28(18), 3501–3504, doi:10.1029/2000GL012484, 2001.

Rignot, E., Braaten, D., Gogineni, S. P., Krabill, W. B. and McConnell, J. R.: Rapid ice discharge from southeast Greenland glaciers, Geophys. Res. Lett., 31(10), L10401, doi:10.1029/2004GL019474, 2004.

Rignot, E., Box, J. E., Burgess, E. and Hanna, E.: Mass balance of the Greenland ice sheet from 1958 to 2007, Geophys. Res. Lett., 35(20), L20502, doi:10.1029/2008GL035417, 2008.

Rignot, E., Velicogna, I., van den Broeke, M. R., Monaghan, A. and Lenaerts, J. T. M.: Acceleration of the contribution of the Greenland and Antarctic ice sheets to sea level rise, Geophys. Res. Lett., 38(5), L05503, doi:10.1029/2011GL046583, 2011.

Rosenau, R., Scheinert, M. and Dietrich, R.: A processing system to monitor Greenland outlet glacier velocity variations at decadal and seasonal time scales utilizing the Landsat imagery, Remote Sens. Environ., 169, 1–19, doi:10.1016/j.rse.2015.07.012, 2015.

Rott, H. and Mätzler, C.: Possibilities and Limits of Synthetic Aperture Radar for Snow and Glacier Surveying, Ann. Glaciol., 9, 195–199, doi:10.3189/S0260305500000604, 1987.

Ryan, J. C., Hubbard, A. L., Box, J. E., Todd, J., Christoffersen, P., Carr, J. R., Holt, T. O. and Snooke, N.: UAV photogrammetry and structure from motion to assess calving dynamics at Store Glacier, a large outlet draining the Greenland ice sheet, The Cryosphere, 9(1), 1–11, doi:10.5194/tc-9-1-2015, 2015.

Ryan, J. C., Hubbard, A., Stibal, M., Box, J. E. and team, T. D. S. P.: Attribution of Greenland's ablating ice surfaces on ice sheet albedo using unmanned aerial systems, Cryosphere Discuss, 2016, 1–23, doi:10.5194/tc-2016-204, 2016.

Ryan, J. C., Hubbard, A., Box, J. E., Brough, S., Cameron, K., Cook, J. M., Cooper, M., Doyle, S. H., Edwards, A., Holt, T., Irvine-Fynn, T., Jones, C., Pitcher, L. H., Rennermalm, A. K., Smith, L. C., Stibal, M. and Snooke, N.: Derivation of High Spatial Resolution Albedo from UAV Digital Imagery: Application over the Greenland Ice Sheet, Front. Earth Sci., 5, doi:10.3389/feart.2017.00040, 2017a.

Ryan, J. C., Hubbard, A. L., Irvine-Fynn, T. D., Doyle, S. H., Cook, J. M., Stibal, M. and Box, J. E.: How robust are in situ observations for validating satellite-derived albedo over the dark zone of the Greenland Ice Sheet?, Geophys. Res. Lett., 44(12), 6218–6225, doi:10.1002/2017GL073661, 2017b.

Ryan, J. C., Hubbard, A. L., Stibal, M., Irvine-Fynn, T. D., Cook, J., Smith, L. C., Cameron, K. and Box, J. E.: Dark zone of the Greenland Ice Sheet controlled by distributed biologically-active impurities, Nat. Commun., 9(1), 1065, doi:10.1038/s41467-018-03353-2, 2018.

Ryan, J. C., Smith, L. C., As, D. van, Cooley, S. W., Cooper, M. G., Pitcher, L. H. and Hubbard, A.: Greenland Ice Sheet surface melt amplified by snowline migration and bare ice exposure, Sci. Adv., 5(3), eaav3738, doi:10.1126/sciadv.aav3738, 2019.

Sanderson, T. J. O.: Thermal Stresses near the Surface of a Glacier, J. Glaciol., 20(83), 257–283, doi:10.3198/1978JoG20-83-257-283, 1978.

Sasgen, I., van den Broeke, M., Bamber, J. L., Rignot, E., Sørensen, L. S., Wouters, B., Martinec, Z., Velicogna, I. and Simonsen, S. B.: Timing and origin of recent regional ice-mass loss in Greenland, Earth Planet. Sci. Lett., 333–334, 293–303, doi:10.1016/j.epsl.2012.03.033, 2012a.

Sasgen, I., Klemann, V. and Martinec, Z.: Towards the inversion of GRACE gravity fields for present-day ice-mass changes and glacial-isostatic adjustment in North America and Greenland, J. Geodyn., 59–60, 49–63, doi:10.1016/j.jog.2012.03.004, 2012b.

Schaaf, C. B., Gao, F., Strahler, A. H., Lucht, W., Li, X., Tsang, T., Strugnell, N. C., Zhang, X., Jin, Y., Muller, J.-P., Lewis, P., Barnsley, M., Hobson, P., Disney, M., Roberts, G., Dunderdale, M., Doll, C., d'Entremont, R. P., Hu, B., Liang, S., Privette, J. L. and Roy, D.: First operational BRDF, albedo nadir reflectance products from MODIS, Remote Sens. Environ., 83(1), 135–148, doi:10.1016/S0034-4257(02)00091-3, 2002.

Schaaf, C. B., Wang, Z. and Strahler, A. H.: Commentary on Wang and Zender—MODIS snow albedo bias at high solar zenith angles relative to theory and to in situ observations in Greenland, Remote Sens. Environ., 115(5), 1296–1300, doi:10.1016/j.rse.2011.01.002, 2011.

Schaepman-Strub, G., Schaepman, M. E., Painter, T. H., Dangel, S. and Martonchik, J. V.: Reflectance quantities in optical remote sensing—definitions and case studies, Remote Sens. Environ., 103(1), 27–42, doi:10.1016/j.rse.2006.03.002, 2006.

Schenk, T. and Csatho, B.: A New Methodology for Detecting Ice Sheet Surface Elevation Changes From Laser Altimetry Data, IEEE Trans. Geosci. Remote Sens., 50(9), 3302–3316, doi:10.1109/TGRS.2011.2182357, 2012.

Schenk, T., Csatho, B., van der Veen, C. and McCormick, D.: Fusion of multi-sensor surface elevation data for improved characterization of rapidly changing outlet glaciers in Greenland, Remote Sens. Environ., 149, 239–251, doi:10.1016/j.rse.2014.04.005, 2014.

Schlatter, T. W.: The Local Surface Energy Balance and Subsurface Temperature Regime in Antarctica, J. Appl. Meteorol., 11(7), 1048–1062, doi:10.1175/1520-0450(1972)011<1048:TLSEBA>2.0.CO;2, 1972.

Schröder, L., Horwath, M., Dietrich, R., Helm, V., Broeke, M. R. van den and Ligtenberg, S. R. M.: Four decades of Antarctic surface elevation changes from multi-mission satellite altimetry, The Cryosphere, 13(2), 427–449, doi:https://doi.org/10.5194/tc-13-427-2019, 2019.

Schuster, A.: Radiation through a foggy atmosphere, Astrophys. J., XX1(1), 1–22, 1905.

Schuster, C.: Weathering crust processes on melting glacier ice (Alberta, Canada), Theses Diss. Compr. [online] Available from: http://scholars.wlu.ca/etd/489, 2001.

Schutz, B. E., Zwally, H. J., Shuman, C. A., Hancock, D. and DiMarzio, J. P.: Overview of the ICESat Mission, Geophys. Res. Lett., 32(21), L21S01, doi:10.1029/2005GL024009, 2005.

Scott, J. B. T., Nienow, P., Mair, D., Parry, V., Morris, E. and Wingham, D. J.: Importance of seasonal and annual layers in controlling backscatter to radar altimeters across the percolation zone of an ice sheet, Geophys. Res. Lett., 33, L24502, doi:10.1029/2006GL027974, 2006.

Shepherd, A., Ivins, E. R., A, G., Barletta, V. R., Bentley, M. J., Bettadpur, S., Briggs, K. H., Bromwich, D. H., Forsberg, R., Galin, N., Horwath, M., Jacobs, S., Joughin, I., King, M. A., Lenaerts, J. T. M., Li, J., Ligtenberg, S. R. M., Luckman, A., Luthcke, S. B., McMillan, M., Meister, R., Milne, G., Mouginot, J., Muir, A., Nicolas, J. P., Paden, J., Payne, A. J., Pritchard, H., Rignot, E., Rott, H., Sørensen, L. S., Scambos, T. A., Scheuchl, B., Schrama, E. J. O., Smith, B., Sundal, A. V., Angelen, J. H. van, Berg, W. J. van de, Broeke, M. R. van den, Vaughan, D. G., Velicogna, I., Wahr, J., Whitehouse, P. L., Wingham, D. J., Yi, D., Young, D. and Zwally, H. J.: A Reconciled Estimate of Ice-Sheet Mass Balance, Science, 338(6111), 1183–1189, doi:10.1126/science.1228102, 2012.

Shi, J. and Dozier, J.: Measurements of snow- and glacier-covered areas with single-polarization SAR, Ann. Glaciol., 17, 72–76, doi:10.3189/S0260305500012635, 1993.

Shimada, R., Takeuchi, N. and Aoki, T.: Inter-Annual and Geographical Variations in the Extent of Bare Ice and Dark Ice on the Greenland Ice Sheet Derived from MODIS Satellite Images, Front. Earth Sci., 4, doi:10.3389/feart.2016.00043, 2016.

Shuman, C. A., Zwally, H. J., Schutz, B. E., Brenner, A. C., DiMarzio, J. P., Suchdeo, V. P. and Fricker, H. A.: ICESat Antarctic elevation data: Preliminary precision and accuracy assessment, Geophys. Res. Lett., 33(7), L07501, doi:10.1029/2005GL025227, 2006.

Shuman, C. A., Hall, D. K., DiGirolamo, N. E., Mefford, T. K. and Schnaubelt, M. J.: Comparison of Near-Surface Air Temperatures and MODIS Ice-Surface Temperatures at Summit, Greenland (2008–13), J. Appl. Meteorol. Climatol., 53(9), 2171–2180, doi:10.1175/JAMC-D-14-0023.1, 2014.

Siegfried, M. R., Hawley, R. L. and Burkhart, J. F.: High-Resolution Ground-Based GPS Measurements Show Intercampaign Bias in ICESat Elevation Data Near Summit, Greenland, IEEE Trans. Geosci. Remote Sens., 49(9), 3393–3400, doi:10.1109/TGRS.2011.2127483, 2011.

Simonsen, S. B. and Sørensen, L. S.: Implications of changing scattering properties on Greenland ice sheet volume change from Cryosat-2 altimetry, Remote Sens. Environ., 190, 207–216, doi:10.1016/j.rse.2016.12.012, 2017.

Slobbe, D. C., Lindenbergh, R. C. and Ditmar, P.: Estimation of volume change rates of Greenland's ice sheet from ICESat data using overlapping footprints, Remote Sens. Environ., 112(12), 4204–4213, doi:10.1016/j.rse.2008.07.004, 2008.

Smith, B., Fricker, H. A., Gardner, A. S., Siegfried, M. R., Adusumilli, S., Csathó, B. M., Holschuh, N., Nilsson, J., Paolo, F. S. and ICESat-2 Science Team: ATLAS/ICESat-2 L3A Land Ice Height, Version 1, Boulder Colo. USA, NSIDC: National Snow and Ice Data Center, doi:https://doi.org/10.5067/ATLAS/ATL06.001, 2019.

Smith, L. C., Forster, R. R., Isacks, B. L. and Hall, D. K.: Seasonal climatic forcing of alpine glaciers revealed with orbital synthetic aperture radar, J. Glaciol., 43(145), 480–488, doi:10.3189/S0022143000035085, 1997.

Smith, L. C., Sheng, Y., Forster, R. R., Steffen, K., Frey, K. E. and Alsdorf, D. E.: Melting of small Arctic ice caps observed from ERS scatterometer time series, Geophys. Res. Lett., 30(20), 2034, doi:10.1029/2003GL017641, 2003.

Smith, L. C., Chu, V. W., Yang, K., Gleason, C. J., Pitcher, L. H., Rennermalm, A. K., Legleiter, C. J., Behar, A. E., Overstreet, B. T., Moustafa, S. E., Tedesco, M., Forster, R. R., LeWinter, A. L., Finnegan, D. C., Sheng, Y. and Balog, J.: Efficient meltwater drainage through supraglacial streams and rivers on the southwest Greenland ice sheet, Proc. Natl. Acad. Sci., 112(4), 1001–1006, doi:10.1073/pnas.1413024112, 2015.

Smith, L. C., Yang, K., Pitcher, L. H., Overstreet, B. T., Chu, V. W., Rennermalm, Å. K., Ryan, J. C., Cooper, M. G., Gleason, C. J., Tedesco, M., Jeyaratnam, J., As, D. van, Broeke, M. R. van den, Berg, W. J. van de, Noël, B., Langen, P. L., Cullather, R. I., Zhao, B., Willis, M. J., Hubbard, A., Box, J. E., Jenner, B. A. and Behar, A. E.: Direct measurements of meltwater runoff on the Greenland ice sheet surface, Proc. Natl. Acad. Sci., 114(50), E10622–E10631, doi:10.1073/pnas.1707743114, 2017.

Smith, L. C., Andrews, L. A., Pitcher, L. H., Overstreet, B. T., Cooper, M. G., Rennermalm, Å. K., Ryan, J., Miège, C., Kershner, C. and Simpson, C. E.: Supraglacial meltwater forcing of short-term subglacial water storage and ice sheet motion, Rev., 2020.

Snyder, W. C.: Definition and invariance properties of structured surface BRDF, IEEE Trans. Geosci. Remote Sens., 40(5), 1032–1037, doi:10.1109/TGRS.2002.1010890, 2002.

Sohn, H.-G. and Jezek, K. C.: Mapping ice sheet margins from ERS-1 SAR and SPOT imagery, Int. J. Remote Sens., 20(15–16), 3201–3216, doi:10.1080/014311699211705, 1999.

Sole, A., Payne, T., Bamber, J., Nienow, P. and Krabill, W.: Testing hypotheses of the cause of peripheral thinning of the Greenland Ice Sheet: is land-terminating ice thinning at anomalously high rates?, The Cryosphere, 2(2), 205–218, doi:10.5194/tc-2-205-2008, 2008.

Sørensen, L. S., Simonsen, S. B., Nielsen, K., Lucas-Picher, P., Spada, G., Adalgeirsdottir, G., Forsberg, R. and Hvidberg, C. S.: Mass balance of the Greenland ice sheet (2003–2008) from ICESat data – the impact of interpolation, sampling and firn density, The Cryosphere, 5(1), 173–186, doi:10.5194/tc-5-173-2011, 2011.

Sørensen, L. S., Simonsen, S. B., Meister, R., Forsberg, R., Levinsen, J. F. and Flament, T.: Envisat-derived elevation changes of the Greenland ice sheet, and a comparison with ICESat results in the accumulation area, Remote Sens. Environ., 160, 56–62, doi:10.1016/j.rse.2014.12.022, 2015.

Sørensen, L. S., Simonsen, S. B., Forsberg, R., Khvorostovsky, K., Meister, R. and Engdahl, M. E.: 25 years of elevation changes of the Greenland Ice Sheet from ERS, Envisat, and CryoSat-2 radar altimetry, Earth Planet. Sci. Lett., 495, 234–241, doi:10.1016/j.epsl.2018.05.015, 2018.

Steffen, K., Box, J. E. and Abdalati, W.: Greenland Climate Network: GC-Net, in Special Report 96-27 Glaciers, Ice Sheets and Volcanoes: A Tribute to Mark F. Meier, edited by Colbeck, Samuel C., pp. 98–103, CRREL., 1996.

Steger, C. R., Reijmer, C. H. and Broeke, M. R. van den: The modelled liquid water balance of the Greenland Ice Sheet, The Cryosphere, 11(6), 2507–2526, doi:https://doi.org/10.5194/tc-11-2507-2017, 2017.

Stevens, I. T., Irvine-Fynn, T. D. L., Porter, P. R., Cook, J. M., Edwards, A., Smart, M., Moorman, B. J., Hodson, A. J. and Mitchell, A. C.: Near-surface hydraulic conductivity of Northern Hemisphere glaciers, Hydrol. Process., 332, 850–865, doi:10.1002/hyp.11439, 2018.

Stibal, M., Box, J. E., Cameron, K. A., Langen, P. L., Yallop, M. L., Mottram, R. H., Khan, A. L., Molotch, N. P., Chrismas, N. A. M., Quaglia, F. C., Remias, D., Smeets, C. J. P. P., Broeke, M. R. van den, Ryan, J. C., Hubbard, A., Tranter, M., As, D. van and Ahlstrøm, A. P.: Algae Drive Enhanced Darkening of Bare Ice on the Greenland Ice Sheet, Geophys. Res. Lett., 44(22), 11,463-11,471, doi:10.1002/2017GL075958, 2017.

Stroeve, J.: Assessment of Greenland albedo variability from the advanced very high resolution radiometer Polar Pathfinder data set, J. Geophys. Res. Atmospheres, 106(D24), 33989–34006, doi:10.1029/2001JD900072, 2001.

Stroeve, J. and Steffen, K.: Variability of AVHRR-Derived Clear-Sky Surface Temperature over the Greenland Ice Sheet, J. Appl. Meteorol., 37(1), 23–31, doi:10.1175/1520-0450(1998)037<0023:VOADCS>2.0.CO;2, 1998.

Stroeve, J., Haefliger, M. and Steffen, K.: Surface Temperature from ERS-1 ATSR Infrared Thermal Satellite Data in Polar Regions, J. Appl. Meteorol., 35(8), 1231–1239, doi:10.1175/1520-0450(1996)035<1231:STFAIT>2.0.CO;2, 1996.

Stroeve, J., Box, J. E., Gao, F., Liang, S., Nolin, A. and Schaaf, C.: Accuracy assessment of the MODIS 16-day albedo product for snow: comparisons with Greenland in situ measurements, Remote Sens. Environ., 94(1), 46–60, doi:10.1016/j.rse.2004.09.001, 2005.

Stroeve, J., Box, J. E., Wang, Z., Schaaf, C. and Barrett, A.: Re-evaluation of MODIS MCD43 Greenland albedo accuracy and trends, Remote Sens. Environ., 138, 199–214, doi:10.1016/j.rse.2013.07.023, 2013.

Stroeve, J. C. and Nolin, A. W.: New methods to infer snow albedo from the MISR instrument with applications to the Greenland ice sheet, IEEE Trans. Geosci. Remote Sens., 40(7), 1616–1625, doi:10.1109/TGRS.2002.801144, 2002.

Stroeve, J. C., Box, J. E., Fowler, C., Haran, T. and Key, J.: Intercomparison between In Situ and AVHRR Polar Pathfinder-Derived Surface Albedo over Greenland, Remote Sens. Environ., 75(3), 360–374, doi:10.1016/S0034-4257(00)00179-6, 2001.

Stroeve, J. C., Box, J. E. and Haran, T.: Evaluation of the MODIS (MOD10A1) daily snow albedo product over the Greenland ice sheet, Remote Sens. Environ., 105(2), 155–171, doi:10.1016/j.rse.2006.06.009, 2006.

Su, X., Shum, C. K., Guo, J., Duan, J., Howat, I. and Yi, Y.: High resolution Greenland ice sheet inter-annual mass variations combining GRACE gravimetry and Envisat altimetry, Earth Planet. Sci. Lett., 422, 11–17, doi:10.1016/j.epsl.2015.04.016, 2015.

Su, X., Shum, C.-, Kuo, C. and Yi, Y.: Improved Envisat Altimetry Ice Sheet Elevation Change Data Processing Algorithms Using Repeat-Track Analysis, IEEE Geosci. Remote Sens. Lett., 13(8), 1099–1103, doi:10.1109/LGRS.2016.2567486, 2016.

Su, X., Luo, Z. and Zhou, Z.: Assessing backscatter change due to backscatter gradient over the Greenland ice sheet using Envisat and SARAL altimetry, J. Geodyn., 117, 41–48, doi:10.1016/j.jog.2018.03.007, 2018.

Suryawanshi, M. R., Chander, S., Oza, S. R. and Bahuguna, I. M.: Volume loss of the Greenland ice sheet revealed by SARAL/AltiKa repeat passes radar altimetry, J. Earth Syst. Sci., 128(7), 187, doi:10.1007/s12040-019-1209-3, 2019.

Sutterley, T. C., Velicogna, I., Fettweis, X., Rignot, E., Noël, B. and van den Broeke, M. R.: Evaluation of reconstructions of snow/ice melt in Greenland by regional atmospheric climate models using laser altimetry data., Geophys. Res. Lett., 45, 8324–8333, doi:10.1029/2018GL078645, 2018.

Swenson, S. and Wahr, J.: Post-processing removal of correlated errors in GRACE data, Geophys. Res. Lett., 33(8), L08402, doi:10.1029/2005GL025285, 2006.

Takeuchi, N.: Optical characteristics of cryoconite (surface dust) on glaciers: the relationship between light absorbency and the property of organic matter contained in the cryoconite, Ann. Glaciol., 34(1), 409–414, doi:10.3189/172756402781817743, 2002.

Takeuchi, N., Kohshima, S., Yoshimura, Y., Seko, K. and Fujita, K.: Characteristics of cryoconite holes on a Himalayan glacier, Yala Glacier Central Nepal, Bull. Glaciol. Res., 17, 51–59, 2000.

Takeuchi, N., Dial, R., Kohshima, S., Segawa, T. and Uetake, J.: Spatial distribution and abundance of red snow algae on the Harding Icefield, Alaska derived from a satellite image, Geophys. Res. Lett., 33(21), L21502, doi:10.1029/2006GL027819, 2006.

Tedesco, M.: Snowmelt detection over the Greenland ice sheet from SSM/I brightness temperature daily variations, Geophys. Res. Lett., 34(2), L02504, doi:10.1029/2006GL028466, 2007.

Tedesco, M., Ed.: Remote sensing of the cryosphere, Wiley Blackwell, Hoboken, NJ., 2015.

Tedesco, M., Fettweis, X., Broeke, M. R. van den, Wal, R. S. W. van de, Smeets, C. J. P. P., Berg, W. J. van de, Serreze, M. C. and Box, J. E.: The role of albedo and accumulation in the 2010 melting record in Greenland, Environ. Res. Lett., 6(1), 014005, doi:10.1088/1748-9326/6/1/014005, 2011.

Tedesco, M., Fettweis, X., Mote, T., Wahr, J., Alexander, P., Box, J. E. and Wouters, B.: Evidence and analysis of 2012 Greenland records from spaceborne observations, a regional climate model and reanalysis data, The Cryosphere, 7(2), 615–630, doi:10.5194/tc-7-615-2013, 2013.

Tedesco, M., Doherty, S., Warren, S. G., Tranter, M., Stroeve, J. C., Fettweis, X. and Alexander, P.: What Darkens the Greenland Ice Sheet?, Eos, 96, doi:10.1029/2015EO035773, 2015.

Tedesco, M., Doherty, S., Fettweis, X., Alexander, P., Jeyaratnam, J. and Stroeve, J.: The darkening of the Greenland ice sheet: trends, drivers, and projections (1981–2100), The Cryosphere, 10(2), 477–496, doi:10.5194/tc-10-477-2016, 2016.

Tedstone, A. J., Bamber, J. L., Cook, J. M., Williamson, C. J., Fettweis, X., Hodson, A. J. and Tranter, M.: Dark ice dynamics of the south-west Greenland Ice Sheet, The Cryosphere, 11(6), 2491–2506, doi:10.5194/tc-11-2491-2017, 2017.

Thomas, R., Frederick, E., Krabill, W., Manizade, S., Martin, C. and Mason, A.: Elevation changes on the Greenland ice sheet from comparison of aircraft and ICESat laser-altimeter data, Ann. Glaciol., 42, 77–82, doi:10.3189/172756405781813050, 2005.

Thomas, R., Frederick, E., Krabill, W., Manizade, S. and Martin, C.: Progressive increase in ice loss from Greenland, Geophys. Res. Lett., 33(10), L10503, doi:10.1029/2006GL026075, 2006.

Thomas, R., Davis, C., Frederick, E., Krabill, W., Li, Y., Manizade, S. and Martin, C.: A comparison of Greenland ice-sheet volume changes derived from altimetry measurements, J. Glaciol., 54(185), 203–212, doi:10.3189/002214308784886225, 2008.

Thomas, R. H., Martin, T. V. and Zwally, H. J.: Mapping Ice-Sheet Margins from Radar Altimetry Data, Ann. Glaciol., 4, 283–288, doi:10.3189/S0260305500005619, 1983.

Transon, J., d'Andrimont, R., Maugnard, A. and Defourny, P.: Survey of Hyperspectral Earth Observation Applications from Space in the Sentinel-2 Context, Remote Sens., 10(3), 157, doi:10.3390/rs10020157, 2018.

Trusel, L. D., Das, S. B., Osman, M. B., Evans, M. J., Smith, B. E., Fettweis, X., McConnell, J. R., Noël, B. P. Y. and van den Broeke, M. R.: Nonlinear rise in Greenland runoff in response to post-industrial Arctic warming, Nature, 564(7734), 104–108, doi:10.1038/s41586-018-0752-4, 2018.

Turyshev, S. G., Sazhin, M. V. and Toth, V. T.: General relativistic laser interferometric observables of the GRACE-Follow-On mission, Phys. Rev. D, 89(10), 105029, doi:10.1103/PhysRevD.89.105029, 2014.

Tuzet, F., Dumont, M., Arnaud, L., Voisin, D., Lamare, M., Larue, F., Revuelto, J. and Picard, G.: Influence of light-absorbing particles on snow spectral irradiance profiles, The Cryosphere, 13(8), 2169–2187, doi:10.5194/tc-13-2169-2019, 2019.

Uetake, J., Naganuma, T., Hebsgaard, M. B., Kanda, H. and Kohshima, S.: Communities of algae and cyanobacteria on glaciers in west Greenland, Polar Sci., 4(1), 71–80, doi:10.1016/j.polar.2010.03.002, 2010.

Välisuo, I., Vihma, T., Pirazzini, R. and Schäfer, M.: Interannual Variability of Atmospheric Conditions and Surface Melt in Greenland in 2000–2014, J. Geophys. Res. Atmospheres, 123(18), 10,443-10,463, doi:10.1029/2018JD028445, 2018.

Vandecrux, B., MacFerrin, M., Machguth, H., Colgan, W. T., As, D. van, Heilig, A., Stevens, C. M., Charalampidis, C., Fausto, R. S., Morris, E. M., Mosley-Thompson, E., Koenig, L., Montgomery, L. N., Miège, C., Simonsen, S. B., Ingeman-Nielsen, T. and Box, J. E.: Firn data compilation reveals widespread decrease of firn air content in western Greenland, The Cryosphere, 13(3), 845–859, doi:https://doi.org/10.5194/tc-13-845-2019, 2019.

van der Veen, C. J., Ahn, Y., Csatho, B. M., Mosley-Thompson, E. and Krabill, W. B.: Surface roughness over the northern half of the Greenland Ice Sheet from airborne laser altimetry, J. Geophys. Res. Earth Surf., 114(F1), F01001, doi:10.1029/2008JF001067, 2009.

Velicogna, I.: Increasing rates of ice mass loss from the Greenland and Antarctic ice sheets revealed by GRACE, Geophys. Res. Lett., 36(19), L19503, doi:10.1029/2009GL040222, 2009.

Velicogna, I. and Wahr, J.: Greenland mass balance from GRACE, Geophys. Res. Lett., 32(18), L18505, doi:10.1029/2005GL023955, 2005.

Velicogna, I. and Wahr, J.: Acceleration of Greenland ice mass loss in spring 2004, Nature, 443(7109), 329–331, doi:10.1038/nature05168, 2006.

Velicogna, I. and Wahr, J.: Time-variable gravity observations of ice sheet mass balance: Precision and limitations of the GRACE satellite data, Geophys. Res. Lett., 40(12), 3055–3063, doi:10.1002/grl.50527, 2013.

Verron, J., Sengenes, P., Lambin, J., Noubel, J., Steunou, N., Guillot, A., Picot, N., Coutin-Faye, S., Sharma, R., Gairola, R. M., Murthy, D. V. A. R., Richman, J. G., Griffin, D., Pascual, A., Rémy, F. and Gupta, P. K.: The SARAL/AltiKa Altimetry Satellite Mission, Mar. Geod., 38(sup1), 2–21, doi:10.1080/01490419.2014.1000471, 2015.

Vizcaíno, M., Mikolajewicz, U., Gröger, M., Maier-Reimer, E., Schurgers, G. and Winguth, A. M. E.: Long-term ice sheet–climate interactions under anthropogenic greenhouse forcing simulated with a complex Earth System Model, Clim. Dyn., 31(6), 665–690, doi:10.1007/s00382-008-0369-7, 2008.

Vizcaíno, M., Lipscomb, W. H., Sacks, W. J., van Angelen, J. H., Wouters, B. and van den Broeke, M. R.: Greenland Surface Mass Balance as Simulated by the Community Earth System Model. Part I: Model Evaluation and 1850–2005 Results, J. Clim., 26(20), 7793–7812, doi:10.1175/JCLI-D-12-00615.1, 2013a.

Vizcaíno, M., Lipscomb, W. H., Sacks, W. J. and van den Broeke, M.: Greenland Surface Mass Balance as Simulated by the Community Earth System Model. Part II: Twenty-First-Century Changes, J. Clim., 27(1), 215–226, doi:10.1175/JCLI-D-12-00588.1, 2013b.

Vizcaíno, M., Mikolajewicz, U., Ziemen, F., Rodehacke, C. B., Greve, R. and van den Broeke, M. R.: Coupled simulations of Greenland ice sheet and climate change up to AD 2300, Geophys. Res. Lett., 42, 3927–3935, doi:10.1002/2014GL061142, 2015.

Wahr, J., Swenson, S. and Velicogna, I.: Accuracy of GRACE mass estimates, Geophys. Res. Lett., 33(6), L06401, doi:10.1029/2005GL025305, 2006.

Wakahama, G., Kuroiwa, D., Kobayashi, D., Tanuma, K., Endo, Y., Mizuno, Y. and Kobayashi, S.: Observations of permeating water through a glacier body, Low Temp. Sci. A, 31, 217–219, 1973.

Wan, Z. and Dozier, J.: Land-surface temperature measurement from space: physical principles and inverse modeling, IEEE Trans. Geosci. Remote Sens., 27(3), 268–278, doi:10.1109/36.17668, 1989.

Wan, Z. and Li, Z.-L.: Radiance-based validation of the V5 MODIS land-surface temperature product, Int. J. Remote Sens., 29(17–18), 5373–5395, doi:10.1080/01431160802036565, 2008.

Wang, L., Sharp, M., Rivard, B. and Steffen, K.: Melt season duration and ice layer formation on the Greenland ice sheet, 2000–2004, J. Geophys. Res. Earth Surf., 112(F4), F04013, doi:10.1029/2007JF000760, 2007.

Wang, S., Tedesco, M., Xu, M. and Alexander, P. M.: Mapping Ice Algal Blooms in Southwest Greenland From Space, Geophys. Res. Lett., 45(21), 11,779-11,788, doi:10.1029/2018GL080455, 2018.

Wang, X. and Zender, C. S.: MODIS snow albedo bias at high solar zenith angles relative to theory and to in situ observations in Greenland, Remote Sens. Environ., 114(3), 563–575, doi:10.1016/j.rse.2009.10.014, 2010.

Warren, S. G.: Optical properties of snow, Rev. Geophys., 20(1), 67–89, doi:10.1029/RG020i001p00067, 1982.

Warren, S. G.: Optical constants of ice from the ultraviolet to the microwave, Appl. Opt., 23(8), 1206–1225, doi:10.1364/AO.23.001206, 1984.

Warren, S. G.: Can black carbon in snow be detected by remote sensing?, J. Geophys. Res. Atmospheres, 118(2), 779–786, doi:10.1029/2012JD018476, 2013.

Warren, S. G. and Brandt, R. E.: Optical constants of ice from the ultraviolet to the microwave: A revised compilation, J. Geophys. Res. Atmospheres, 113(D14), D14220, doi:10.1029/2007JD009744, 2008.

Warren, S. G., Brandt, R. E., Grenfell, T. C. and McKay, C. P.: Snowball Earth: Ice thickness on the tropical ocean, J. Geophys. Res. Oceans, 107(C10), 31-1-31–18, doi:10.1029/2001JC001123, 2002.

Warren, S. G., Brandt, R. E. and Grenfell, T. C.: Visible and near-ultraviolet absorption spectrum of ice from transmission of solar radiation into snow, Appl. Opt., 45(21), 5320–5334, doi:10.1364/AO.45.005320, 2006.

Watkins, M. M., Wiese, D. N., Yuan, D.-N., Boening, C. and Landerer, F. W.: Improved methods for observing Earth's time variable mass distribution with GRACE using spherical cap mascons, J. Geophys. Res. Solid Earth, 120(4), 2648–2671, doi:10.1002/2014JB011547, 2015.

Wientjes, I. G. M. and Oerlemans, J.: An explanation for the dark region in the western melt zone of the Greenland ice sheet, The Cryosphere, 4(3), 261–268, doi:10.5194/tc-4-261-2010, 2010.

Wientjes, I. G. M., Van de Wal, R. S. W., Reichart, G. J., Sluijs, A. and Oerlemans, J.: Dust from the dark region in the western ablation zone of the Greenland ice sheet, The Cryosphere, 5(3), 589–601, doi:10.5194/tc-5-589-2011, 2011.

Wientjes, I. G. M., De Van Wal, R. S. W., Schwikowski, M., Zapf, A., Fahrni, S. and Wacker, L.: Carbonaceous particles reveal that Late Holocene dust causes the dark region in the western ablation zone of the Greenland ice sheet, J. Glaciol., 58(210), 787–794, doi:10.3189/2012JoG11J165, 2012.

Willis, I. C., Arnold, N. S. and Brock, B. W.: Effect of snowpack removal on energy balance, melt and runoff in a small supraglacial catchment, Hydrol. Process., 16(14), 2721–2749, doi:10.1002/hyp.1067, 2002.

Wingham, D. J., Francis, C. R., Baker, S., Bouzinac, C., Brockley, D., Cullen, R., de Chateau-Thierry, P., Laxon, S. W., Mallow, U., Mavrocordatos, C., Phalippou, L., Ratier, G., Rey, L., Rostan, F., Viau, P. and Wallis, D. W.: CryoSat: A mission to determine the fluctuations in Earth's land and marine ice fields, Adv. Space Res., 37(4), 841–871, doi:10.1016/j.asr.2005.07.027, 2006.

Winker, D. M., Couch, R. H. and McCormick, M. P.: An overview of LITE: NASA's Lidar In-space Technology Experiment, Proc. IEEE, 84(2), 164–180, doi:10.1109/5.482227, 1996.

Wismann, V.: Monitoring of seasonal snowmelt on Greenland with ERS scatterometer data, IEEE Trans. Geosci. Remote Sens., 38(4), 1821–1826, doi:10.1109/36.851766, 2000.

Wouters, B., Chambers, D. and Schrama, E. J. O.: GRACE observes small-scale mass loss in Greenland, Geophys. Res. Lett., 35(20), L20501, doi:10.1029/2008GL034816, 2008.

Wouters, B., Bamber, J. L., Broeke, M. R. van den, Lenaerts, J. T. M. and Sasgen, I.: Limits in detecting acceleration of ice sheet mass loss due to climate variability, Nat. Geosci., 6(8), 613–616, doi:10.1038/ngeo1874, 2013.

Xu, Z., Schrama, E. J. O., van der Wal, W., van den Broeke, M. and Enderlin, E. M.: Improved GRACE regional mass balance estimates of the Greenland ice sheet cross-validated with the input–output method, The Cryosphere, 10(2), 895–912, doi:10.5194/tc-10-895-2016, 2016.

Yallop, M. L., Anesio, A. M., Perkins, R. G., Cook, J., Telling, J., Fagan, D., MacFarlane, J., Stibal, M., Barker, G., Bellas, C., Hodson, A., Tranter, M., Wadham, J. and Roberts, N. W.: Photophysiology and albedo-changing potential of the ice algal community on the surface of the Greenland ice sheet, ISME J., 6(12), 2302–2313, doi:10.1038/ismej.2012.107, 2012.

Yang, K. and Smith, L. C.: Supraglacial Streams on the Greenland Ice Sheet Delineated From Combined Spectral #x2013;Shape Information in High-Resolution Satellite Imagery, IEEE Geosci. Remote Sens. Lett., 10(4), 801–805, doi:10.1109/LGRS.2012.2224316, 2013.

Yang, K., Smith, L. C., Chu, V. W., Gleason, C. J. and Li, M.: A Caution on the Use of Surface Digital Elevation Models to Simulate Supraglacial Hydrology of the Greenland Ice Sheet, IEEE J. Sel. Top. Appl. Earth Obs. Remote Sens., 8(11), 1–13, doi:10.1109/JSTARS.2015.2483483, 2015.

Yang, K., Karlstrom, L., Smith, L. C. and Li, M.: Automated High-Resolution Satellite Image Registration Using Supraglacial Rivers on the Greenland Ice Sheet, IEEE J. Sel. Top. Appl. Earth Obs. Remote Sens., 10(3), 845–856, doi:10.1109/JSTARS.2016.2617822, 2017a.

Yang, K., Smith, L. C., Karlstrom, L., Cooper, M. G., Tedesco, M., As, D. van, Cheng, X., Chen, Z. and Li, M.: A new surface meltwater routing model for use on the Greenland Ice Sheet surface, The Cryosphere, 12(12), 3791–3811, doi:https://doi.org/10.5194/tc-12-3791-2018, 2018.

Yang, K., Smith, L. C., Sole, A., Livingstone, S. J., Cheng, X., Chen, Z. and Li, M.: Supraglacial rivers on the northwest Greenland Ice Sheet, Devon Ice Cap, and Barnes Ice Cap mapped using Sentinel-2 imagery, Int. J. Appl. Earth Obs. Geoinformation, 78, 1–13, doi:10.1016/j.jag.2019.01.008, 2019a.

Yang, K., Smith, L. C., Fettweis, X., Gleason, C. J., Lu, Y. and Li, M.: Surface meltwater runoff on the Greenland ice sheet estimated from remotely sensed supraglacial lake infilling rate, Remote Sens. Environ., 234, 111459, doi:10.1016/j.rse.2019.111459, 2019b.

Yang, Y., Marshak, A., Han, M., Palm, S. P. and Harding, D. J.: Snow grain size retrieval over the polar ice sheets with the Ice, Cloud, and land Elevation Satellite (ICESat) observations, J. Quant. Spectrosc. Radiat. Transf., 188, 159–164, doi:10.1016/j.jqsrt.2016.03.033, 2017b.

Yi, D., Zwally, H. J. and Sun, X.: ICESat measurement of Greenland ice sheet surface slope and roughness, Ann. Glaciol., 42, 83–89, doi:10.3189/172756405781812691, 2005.

York, D.: Least squares fitting of a straight line with correlated errors, Earth Planet. Sci. Lett., 5, 320–324, doi:10.1016/S0012-821X(68)80059-7, 1968.

York, D., Evensen, N. M., Martínez, M. L. and De Basabe Delgado, J.: Unified equations for the slope, intercept, and standard errors of the best straight line, Am. J. Phys., 72(3), 367–375, doi:10.1119/1.1632486, 2004.

Zebker, H. A. and Weber Hoen, E.: Penetration depths inferred from interferometric volume decorrelation observed over the Greenland Ice Sheet, IEEE Trans. Geosci. Remote Sens., 38(6), 2571–2583, doi:10.1109/36.885204, 2000.

Zege, E., Katsev, I., Malinka, A., Prikhach, A. and Polonsky, I.: New algorithm to retrieve the effective snow grain size and pollution amount from satellite data, Ann. Glaciol., 49, 139–144, doi:10.3189/172756408787815004, 2008.

Zwally, H. J.: Growth of Greenland Ice Sheet: Interpretation, Science, 246(4937), 1589–1591, doi:10.1126/science.246.4937.1589, 1989.

Zwally, H. J., Bindschadler, R. A., Brenner, A. C., Martin, T. V. and Thomas, R. H.: Surface elevation contours of Greenland and Antarctic Ice Sheets, J. Geophys. Res. Oceans, 88(C3), 1589–1596, doi:10.1029/JC088iC03p01589, 1983.

Zwally, H. J., Bindschadler, R. A., Brenner, A. C., Major, J. A. and Marsh, J. G.: Growth of Greenland Ice Sheet: Measurement, Science, 246(4937), 1587–1589, doi:10.1126/science.246.4937.1587, 1989.

Zwally, H. J., Schutz, B., Abdalati, W., Abshire, J., Bentley, C., Brenner, A., Bufton, J., Dezio, J., Hancock, D., Harding, D., Herring, T., Minster, B., Quinn, K., Palm, S., Spinhirne, J. and Thomas, R.: ICESat's laser measurements of polar ice, atmosphere, ocean, and land, J. Geodyn., 34(3), 405–445, doi:10.1016/S0264-3707(02)00042-X, 2002.

Zwally, H. J., Giovinetto, M. B., Li, J., Cornejo, H. G., Beckley, M. A., Brenner, A. C., Saba, J. L. and Yi, D.: Mass changes of the Greenland and Antarctic ice sheets and shelves and contributions to sea-level rise: 1992–2002, J. Glaciol., 51(175), 509–527, doi:10.3189/172756505781829007, 2005.

Zwally, H. J., Li, J., Brenner, A. C., Beckley, M., Cornejo, H. G., DiMarzio, J., Giovinetto, M. B., Neumann, T. A., Robbins, J., Saba, J. L., Yi, D. and Wang, W.: Greenland ice sheet mass balance: distribution of increased mass loss with climate warming; 2003–07 versus 1992–2002, J. Glaciol., 57(201), 88–102, doi:10.3189/002214311795306682, 2011.